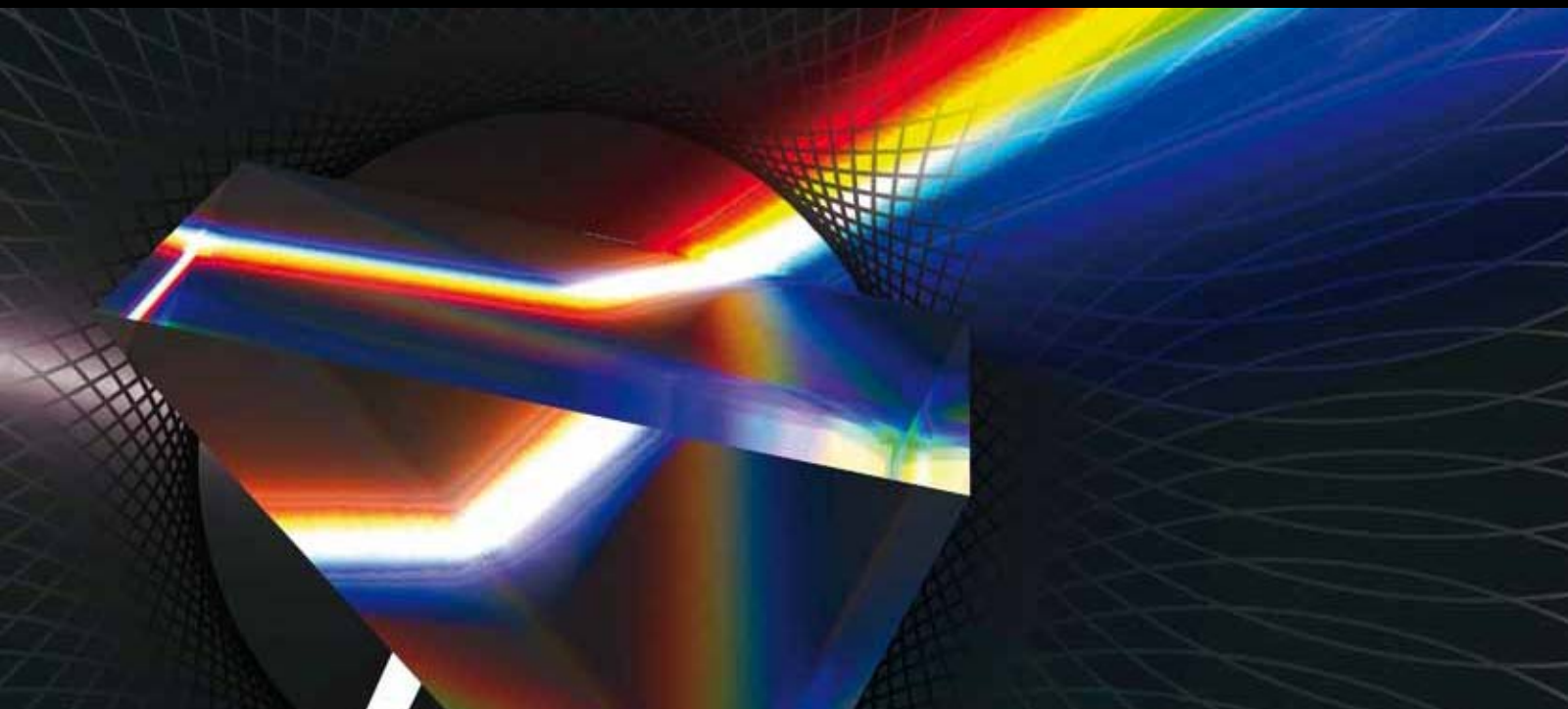


# Singular Optics

GUEST EDITORS: PARAMASIVAM SENTHILKUMARAN, SHUNICHI SATO, AND JAN MASAJADA



---



# **Singular Optics**

International Journal of Optics

---

## **Singular Optics**

Guest Editors: Paramasivam Senthilkumaran, Shunichi Sato,  
and Jan Masajada



---

Copyright © 2012 Hindawi Publishing Corporation. All rights reserved.

This is a special issue published in “International Journal of Optics.” All articles are open access articles distributed under the Creative Commons Attribution License, which permits unrestricted use, distribution, and reproduction in any medium, provided the original work is properly cited.

## Editorial Board

Alejandro Aceves, USA  
Fortunato Tito Arcchi, Italy  
Victor Arrizon, Mexico  
Gaetano Assanto, Italy  
Jose Azana, Canada  
Ole Bang, Denmark  
Randy A. Bartels, USA  
Augusto Belendez, Spain  
E. Bernabeu, Spain  
Le Nguyen Binh, Germany  
Keith J. Blow, UK  
A. D. Boardman, UK  
Wojtek J. Bock, Canada  
Neil Broderick, UK  
Hrvoje Buljan, Croatia  
A. Cartaxo, Portugal  
Giulio Cerullo, Italy  
K. S. Chiang, Hong Kong  
W. C. H. Choy, Hong Kong  
David Coutts, Australia  
Ilaria Cristiani, Italy  
Michael J. Damzen, UK  
Vittorio Degiorgio, Italy  
Cornelia Denz, Germany  
Ivan Djordjevic, USA  
Niloy K. Dutta, USA  
Robert G. Elliman, Australia

Charles M. Falco, USA  
Mahmoud Fallahi, USA  
Pietro Ferraro, Italy  
Mário F. Ferreira, Portugal  
Rashid A. Ganeev, Uzbekistan  
Hooshang Ghafouri-Shiraz, UK  
Ivan Glesk, UK  
Qihuang Gong, China  
N. A. Halliwell, UK  
Sang-Kook Han, Republic of Korea  
Sulaiman Wadi Harun, Malaysia  
W. F. Hsieh, Taiwan  
Mark Humphrey, Australia  
Nicusor Iftimia, USA  
Mohammed N. Islam, USA  
Chennupati Jagadish, Australia  
Wonho Jhe, Korea  
Mirosław A. Karpierz, Poland  
Yu S. Kivshar, Australia  
Wieslaw Krolikowski, Australia  
Nayot Kurukitkoson, Thailand  
R. Leitgeb, Switzerland  
Gong Ru Lin, Taiwan  
Michael E. Marhic, UK  
Lorenzo Marrucci, Italy  
John McInerney, Ireland  
Andrea Melloni, Italy

Adam Miranowicz, Poland  
Roberto Morandotti, Canada  
Uwe Morgner, Germany  
Dragomir Neshev, Australia  
Jean-Michel Nunzi, Canada  
Takashige Omatsu, Japan  
Wolfgang Osten, Germany  
Ben Ovryn, USA  
Nicolae C. Panoiu, UK  
Vittorio M. N. Passaro, Italy  
Gang-Ding Peng, Australia  
Reji Philip, India  
Armando Nolasco Pinto, Portugal  
Adrian Podoleanu, UK  
Jianan Qu, Hong Kong  
Chenggen Quan, Singapore  
Marek Samoc, Poland  
John T. Sheridan, Ireland  
Ping Shum, Singapore  
Mohammad Taghizadeh, UK  
R. P. Tatam, UK  
Markus E. Testorf, USA  
Mustapha Tlidi, Belgium  
Stefano Trillo, Italy  
Stefan Wabnitz, Italy  
Boris Y. Zeldovich, USA

# Contents

**Singular Optics**, Paramasivam Senthilkumaran, Shunichi Sato, and Jan Masajada  
Volume 2012, Article ID 741693, 2 pages

**Experiments on Linear and Nonlinear Localization of Optical Vortices in Optically Induced Photonic Lattices**, Daohong Song, Cibo Lou, Liqin Tang, Zhuoyi Ye, Jingjun Xu, and Zhigang Chen  
Volume 2012, Article ID 273857, 10 pages

**Complex 3D Vortex Lattice Formation by Phase-Engineered Multiple Beam Interference**, Jolly Xavier, Sunil Vyas, Paramasivam Senthilkumaran, and Joby Joseph  
Volume 2012, Article ID 863875, 9 pages

**Generation of a Purely Single Transverse Mode Vortex Beam from a He-Ne Laser Cavity with a Spot-Defect Mirror**, Ken Kano, Yuichi Kozawa, and Shunichi Sato  
Volume 2012, Article ID 359141, 6 pages

**Generation of Optical Vortices by Linear Phase Ramps**, Sunil Vyas  
Volume 2012, Article ID 794259, 6 pages

**Tight Focusing of Partially Coherent Vortex Beams**, Rakesh Kumar Singh  
Volume 2012, Article ID 832086, 6 pages

**Interferometry with Vortices**, P. Senthilkumaran, Jan Masajada, and Shunichi Sato  
Volume 2012, Article ID 517591, 18 pages

**Canonical and Singular Propagation of Ultrashort Pulses in a Nonlinear Medium**, Karl Glasner, Miroslav Kolesik, Jerome V. Moloney, and Alan C. Newell  
Volume 2012, Article ID 868274, 8 pages

**Wavelength Dependence of the Polarization Singularities in a Two-Mode Optical Fiber**, V. V. G. Krishna Inavalli, Vijay Pottapinjara, and Nirmal K. Viswanathan  
Volume 2012, Article ID 358093, 7 pages

**Detector of Optical Vortices as the Main Element of the System of Data Transfer: Principles of Operation, Numerical Model, and Influence of Noise and Atmospheric Turbulence**, Valerii Aksenov, Igor Izmailov, Feodor Kanev, and Boris Poizner  
Volume 2012, Article ID 568485, 14 pages

**Fresnel Lens with Embedded Vortices**, Sunil Vyas, Rakesh Kumar Singh, Devinder Pal Ghai, and P. Senthilkumaran  
Volume 2012, Article ID 249695, 7 pages

**Generation of Optical Vortex Arrays Using Single-Element Reversed-Wavefront Folding Interferometer**, Brijesh Kumar Singh, G. Singh, P. Senthilkumaran, and D. S. Mehta  
Volume 2012, Article ID 689612, 7 pages

## Editorial

# Singular Optics

**Paramasivam Senthilkumaran,<sup>1</sup> Shunichi Sato,<sup>2</sup> and Jan Masajada<sup>3</sup>**

<sup>1</sup> *Department of Physics, Indian Institute of Technology Delhi, New Delhi 110 016, India*

<sup>2</sup> *Institute of Multidisciplinary Research for Advanced Materials, Tohoku University, Katahira 2-1-1, Aoba-ku, Sendai 980-8577, Japan*

<sup>3</sup> *Institute of Physics, Wrocław University of Technology, Wybrzeże Wyspińskiego 27, 50-370 Wrocław, Poland*

Correspondence should be addressed to Paramasivam Senthilkumaran, psenthilk@yahoo.com

Received 12 October 2011; Accepted 12 October 2011

Copyright © 2012 Paramasivam Senthilkumaran et al. This is an open access article distributed under the Creative Commons Attribution License, which permits unrestricted use, distribution, and reproduction in any medium, provided the original work is properly cited.

Recent years have witnessed lots of research activities in the field of singular optics. This special issue is to bring out some of the important research works in this field and to provide a platform to initiate and invite the researchers to share their findings in this relatively new journal. This special issue in an open access journal provides a new dimension in disseminating the new research findings in this field. It also provides the authors and research groups more visibility in the scientific community. After conceiving this idea of bringing out a special issue, we chalked out a time line, for call for papers and the various subsequent processes involved. We have received quite a number of submissions, and after peer-review process 11 articles were selected for this special issue.

Optical vortex also known as optical phase singularity is a point phase defect at which the phase is indeterminate and amplitude is zero. This zero amplitude point draws a curve, called thread of darkness, in space as the singular beam propagates. These dark threads can be tailored to form loops, knots, and other interesting topological structures. The spiraling Poynting vector associated with the vortices in some cases points to backward flow of energy. Singular beams are known to carry orbital angular momentum, and in metrology they are used to lift the degeneracy in peak-valley detection. Special properties of singular beams further lead to many more novel applications in areas as diverse as microparticle manipulation, astrophysics, information technology and processing, beam and polarization shaping, microscopy, and optical testing. Further, singular optics also deals with the presence of singularity in any of the parameters that describe a light field.

A brief introduction given below to the articles would provide an overall idea of the areas covered in this special

issue. There are two review articles “*Interferometry with vortices*” and “*Experiments on linear and nonlinear localization of optical vortices in optically induced photonic lattices*” and nine research articles. The paper by P. Senthilkumaran et al. reviews how interference phenomena involving vortices are useful in optical testing and in polarization optics. The paper by D. Song et al. provides an overview on recent experimental work on linear and nonlinear localization of singly charged vortices (SCVs) and doubly charged vortices (DCVs) in two-dimensional optically induced photonic lattices. Continuing on photonic lattices, the paper “*Complex 3D vortex lattice formation by phase-engineered multiple beam interference*” provides computational results on the formation of diverse complex 3D vortex lattices by a designed superposition of multiple plane waves. Further on 2D vortex lattices, two new interferometric configurations for generating a variety of optical vortex lattices are presented in the paper “*Generation of optical vortex arrays using single-element reversed-wavefront folding interferometer*.” On single-vortex generation, the paper “*Generation of a purely single transverse mode vortex beam from a He-Ne laser cavity with a spot-defect mirror*” elegantly shows an intracavity generation method of Laguerre Gaussian beam with vortex. The authors describe a method in which the spot-defect mirrors replace the conventional rear mirrors of a He-Ne laser cavity with the result that the resonator yielding vortex beams. In the paper “*Generation of optical vortices by linear phase ramps*,” it is shown that vortices can evolve during propagation of a wavefront in which two regions have opposite phase gradients. Vortices of different charges are embedded in a wavefront that has quadratic phase variation, and the intensity distribution near the focal plane is studied in the paper “*Fresnel lens with embedded vortices*.” The paper “*Wavelength dependence*

*of the polarization singularities in a two-mode optical fiber*” shows that the coherent superposition of vector modes results in the generation of phase singular beams, and the polarization character of these beams with dislocation has strong wavelength dependence. The paper *“Tight focusing of partially coherent vortex beams”* investigates the intensity distribution, degree of polarization, and coherence of a tightly focused partially polarized vortex beam. The paper *“Detector of optical vortices as the main element of the system of data transfer: principles of operation, numerical model, and influence of noise and atmospheric turbulence”* deals with the proposal of a method of detection of topological charge of vortex in a turbulent medium in the presence of amplitude and phase noise based on intensity measurements. The paper *“Canonical and singular propagation of ultrashort pulses in a nonlinear medium”* discusses singular behaviors of ultrashort pulses in a nonlinear medium.

This issue consists of articles covering various aspects of singular optics. Many of the articles can be grouped areawise, which means that these articles are not in isolation. The groupings under possible categories are vortex generation, vortex lattice generation polarization singularity, singularity in nonlinear medium, photonic lattices, partially coherent vortex beams, and vortices in atmospheric turbulence.

We hope that the readers will enjoy the collection of articles in this special issue. This issue is realized by the efforts of authors, referees, and the Hindawi editorial team members. We acknowledge their contributions and look forward to more feature issues from this journal.

*Paramasivam Senthilkumaran  
Shunichi Sato  
Jan Masajada*

## Review Article

# Experiments on Linear and Nonlinear Localization of Optical Vortices in Optically Induced Photonic Lattices

Daohong Song,<sup>1</sup> Cibo Lou,<sup>1</sup> Liqin Tang,<sup>1</sup> Zhuoyi Ye,<sup>1</sup> Jingjun Xu,<sup>1</sup> and Zhigang Chen<sup>1,2</sup>

<sup>1</sup>The Key Laboratory of Weak-Light Nonlinear Photonics, Ministry of Education and TEDA Applied Physics School, Nankai University, Tianjin 300457, China

<sup>2</sup>Department of Physics & Astronomy, San Francisco State University, San Francisco, CA 94132, USA

Correspondence should be addressed to Zhigang Chen, biglasers@gmail.com

Received 9 June 2011; Accepted 8 August 2011

Academic Editor: Jan Masajada

Copyright © 2012 Daohong Song et al. This is an open access article distributed under the Creative Commons Attribution License, which permits unrestricted use, distribution, and reproduction in any medium, provided the original work is properly cited.

We provide a brief overview on our recent experimental work on linear and nonlinear localization of singly charged vortices (SCVs) and doubly charged vortices (DCVs) in two-dimensional optically induced photonic lattices. In the nonlinear case, vortex propagation at the lattice surface as well as inside the uniform square-shaped photonic lattices is considered. It is shown that, apart from the fundamental (semi-infinite gap) discrete vortex solitons demonstrated earlier, the SCVs can self-trap into stable gap vortex solitons under the normal four-site excitation with a self-defocusing nonlinearity, while the DCVs can be stable only under an eight-site excitation inside the photonic lattices. Moreover, the SCVs can also turn into stable surface vortex solitons under the four-site excitation at the surface of a semi-infinite photonic lattice with a self-focusing nonlinearity. In the linear case, bandgap guidance of both SCVs and DCVs in photonic lattices with a tunable negative defect is investigated. It is found that the SCVs can be guided at the negative defect as linear vortex defect modes, while the DCVs tend to turn into quadrupole-like defect modes provided that the defect strength is not too strong.

## 1. Introduction

Vortices and vortex solitons are ubiquitous in many branches of sciences such as hydrodynamics, superfluid, high-energy physics, laser and optical systems, and Bose-Einstein condensates [1, 2]. In optics, optical vortices are phase singularities embedded in electromagnetic waves, and the intensity in a singularity point vanishes due to the undetermined phase. The field phase changes by  $2\pi m$  ( $m$  is an integer called topological charge) along any closed loop around the singularity point. The study of linear and nonlinear propagation dynamics of optical vortex beams in continuum media attracted great attentions for decades [1]. In general, a vortex dark ring beam will expand during linear propagation due to the diffraction. However, nonlinearity can compensate the diffraction, leading to the formation of nonlinear localized states called spatial vortex solitons. It is found that an optical vortex can self-trap into a vortex soliton in nonlinear media with a *self-defocusing* nonlinearity [3–7], even the vortex is nested in a partially incoherent optical beam [8]. However,

with a *self-focusing* nonlinearity, optical vortices tend to breakup into filaments due to the azimuthally modulation instabilities [9].

Several different physical mechanisms have been proposed for suppression of the azimuthally instability [10–12]. Guiding the vortices in periodic structures such as photonic crystals or photonic lattices opened a new avenue to stabilize optical vortices in nonlinear media. Generally speaking, the vortices propagation in periodic structures is dominated by the lattice discreteness, nonlinearity, and the phase singularity. Therefore, the localization and stabilization of such vortices exhibit many new phenomena which do not exist in continuous medium. In fact, discrete SCV solitons have been both theoretically predicated and successfully observed experimentally in square photonic lattices with self-focusing nonlinearity under four-site excitation [13–16]. Singly charged high-band vortex solitons are also realized in photonic lattices [17]. On the other hand, DCV propagation in isotropic square photonic lattice leads to periodic charge flipping with a quadrupole-like mediate states [18].

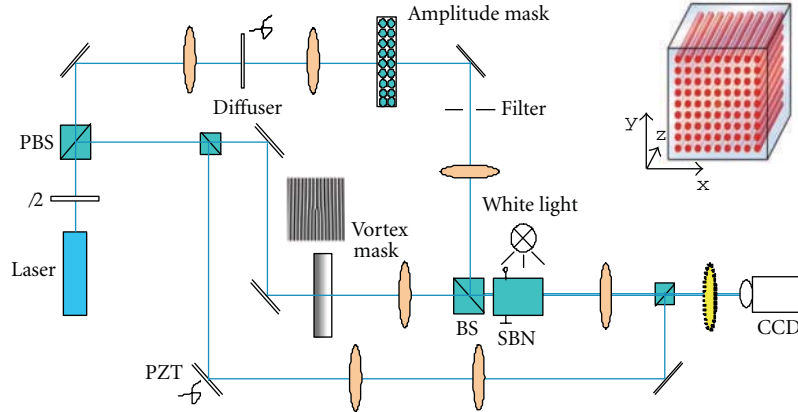


FIGURE 1: Experimental setup for optical induction of photonic lattices in a biased photorefractive crystal by amplitude modulation of a partially coherent beam. PBS: polarizing beam splitter; SBN: strontium barium niobate. Top path is the lattice-inducing beam, the middle path is the probing vortex beam, and the bottom path is the reference beam. The top right insert illustrates the scheme of induced waveguide arrays in the otherwise uniform SBN nonlinear crystal.

Stable SCV, DCV, and multivortex solitons in hexagonal lattices have also been experimentally demonstrated [19–21]. Besides square-like and hexagonal lattices, it has also been proposed that discrete vortex solitons with higher topological charges even exist in photonic quasicrystals [22].

In this paper, we present a brief overview of our recent work on both linear and nonlinear propagation of SCV and DCV beams in 2D photonic lattices in bulk photorefractive material by optical induction. In the nonlinear cases, vortex beam propagation both inside and at the surface of photonic lattices is considered. We show that under appropriate nonlinear conditions both SCV and DCV beams can stably self-trapped into a gap vortex soliton in photonic lattices with self-defocusing nonlinearity. While a SCV beam can turn into a stable gap vortex soliton under four-site excitation, a DCV beam tends to turn into a quadrupole gap soliton which bifurcates from the band edge. However, under geometrically extended eight-site excitation, the DCV can evolve into a stable gap vortex soliton. At the interface between photonics lattice and a homogenous media, under appropriate conditions, the SCV beam can turn into a stable surface discrete vortex soliton under four-site excitation with self-focusing nonlinearity, while it self-traps into a quasi-localized surface state under single site excitation. The stability of such nonlinear localized states is monitored by the numerical simulation to long propagation distance. In the linear case, the SCV beam can also evolve into a linear localized vortex defect mode in photonic lattice with a negative defect, while the DCV beam turns again into a quadrupole-like defect mode, provided that the defect strength is not too deep. Our results may prove to be relevant to the studies of similar phenomena in superfluids and Bose-Einstein condensates.

## 2. Experimental Setup

The experimental setup for our study is similar to those we used earlier for observation of discrete solitons [15, 23, 24],

as shown in Figure 1, except that the input probe beam here can be either a SCV or DCV beam. Our experiments are typically performed in a biased SBN:60 ( $5 \times 5 \times 10 \text{ mm}^3$ ) photorefractive crystal illuminated by a laser beam with wavelength 488 nm from the Argon ion lasers. The biased crystal provides a self-focusing or defocusing non-instantaneous nonlinearity by simply reversing the external biased field. To generate a 2D-waveguide lattice, we use an amplitude mask to spatially modulate the otherwise uniform incoherent beam after the diffuser. The rotating diffuser turns the laser beam into a partially spatially incoherent beam with a controllable degree of spatial coherence. The mask is then imaged onto the input face of the crystal; the periodic intensity pattern is a nearly nondiffracting pattern throughout the crystal after proper spatial filtering. The lattice beam is ordinarily polarized, so it will induce a nearly linear waveguide array that remains invariant during propagation. We can create not only uniform lattices but also lattices with negative defects and lattices with sharp surfaces by simply changing the specially designed amplitude mask. The extraordinarily polarized beam passes through a computer generated hologram to create a ring vortex beam, and then it is focused by a circular lens. The vortex beam is then used as our probe beam or *soliton-forming* beam, propagating collinearly with the *lattice-inducing* beam. In our experiment, the linear propagation of the vortex beam can be realized either by keeping the vortex beam at low intensity or by taking advantage of the noninstantaneous of the photorefractive nonlinearity. A weak reference beam is introduced to interfere with the vortex probe beam after it exits the crystal (bottom path of the Figure 1).

A piezotransduced (PZT) mirror is added to the optical path of the reference beam which can be used to actively vary the relative phase between the plane wave and the vortex beam. In addition, a white-light background beam illuminating from the top of the crystal is typically used for fine-tuning the photorefractive nonlinearity [8, 15].

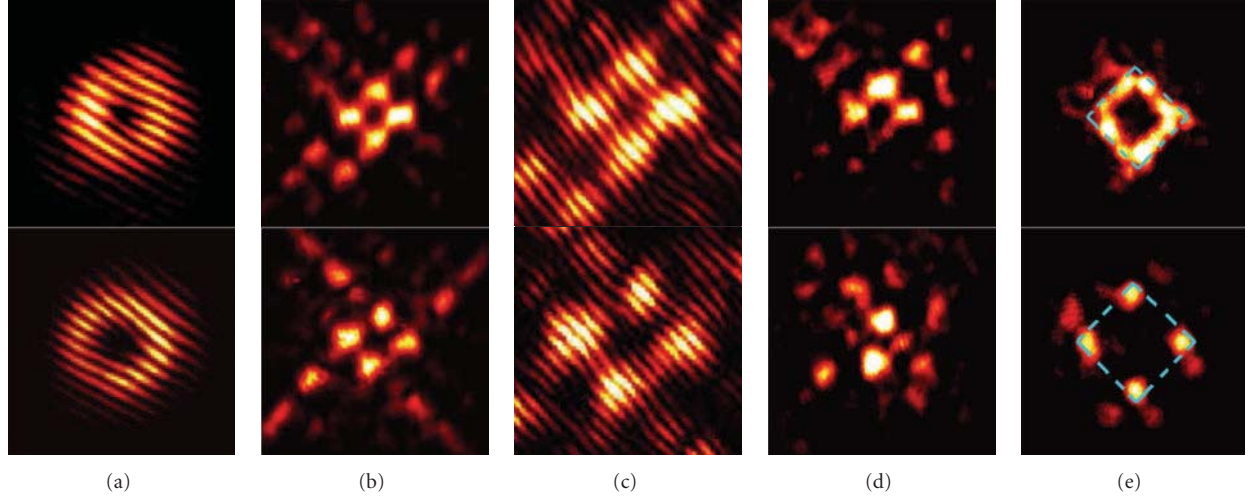


FIGURE 2: Experimental results of self-trapping of SCVs (top) and DCVs (bottom) in a defocusing photonic lattice. (a) Interferograms showing the phase of the input vortex beams, (b) intensity patterns of self-trapped vortex beams at lattice output, (c, d) interferograms between (b) and a tilted plane wave (c) and an on-axis Gaussian beam (d), respectively, and (e) the  $k$ -space spectra of (b) where the dash squares mark the first Brillouin zone of the square lattice. (a, c) are zoomed in with respect to (b, d) for better visualization.

### 3. Nonlinear Localization of Optical Vortices in Photonic Lattices

*3.1. Discrete Gap Vortex Solitons.* First, we study the SCV and DCV beams propagating inside optically induced photonic lattices under the self-defocusing nonlinearity. We find that a donut-shaped SCV beam can self-trap into a stable gap vortex soliton, while the DCV beam evolves into a quadruple soliton under the four-site excitation. Spectrum measurement and numerical analysis suggest that the gap vortex soliton does not bifurcate from the edge of the Bloch band, quite different from previously observed spatial gap solitons.

In our experiment, the lattice beam induces a “backbone” lattice with a self-defocusing nonlinearity where an intensity minimum corresponds to an index maximum [25]. The off-site excitation scheme is used so that the vortex core is on an index minimum, while the donut-like vortex beam covers four adjacent index maxima. Under proper conditions, self-trapping of the vortex beam can be established. Typical experimental results are presented in Figure 2, for which the lattice spacing is about  $27\ \mu\text{m}$ , the intensity ratio of the vortex beam to the lattice beam is about 1 : 4, and the bias field is about  $-1.2\ \text{kV/cm}$ . The interferograms of the input vortex beam with an inclined plane wave are shown in Figure 2, where the central fork in the interference fringes indicates the phase singularity ( $m = 1$  for top panels and  $m = 2$  for bottom panels) of the vortex beam. When the self-trapped state is established in the nonlinear regime, both  $m = 1$  and  $m = 2$  vortices break up into four filaments to cover the initially excited four lattice sites, just as in the self-focusing case [15, 16] except with longer tails along the two principal axes. Although the intensity patterns of self-trapped  $m = 1$  and  $m = 2$  vortices look somewhat similar, significant differences can be found in their phase structure and spatial spectrum. Two different interference techniques are used to

identify the phase structure of self-trapped vortices. One is to send a tilted broad beam (quasiplane wave) to interfere with the output vortex beam (Figure 2(c)). For the limited propagation distance of our crystal length (10 mm), it appears that the vortex singularity (manifested by the central forks in the interferograms) persists after the nonlinear propagation through the crystal, although it seems that charge-flipping (reversal of forks) is associated with the DCV at crystal output. However, from numerical simulations to longer propagation distances, the singularity can maintain only for the  $m = 1$  but not for the  $m = 2$  vortices [26]. In fact, our theoretical analysis shows that a “true” doubly charged gap vortex soliton does not exist under this excitation condition, and a quadrupole-like soliton structure is found instead for the  $m = 2$  vortex [26]. The other technique is to send a coaxial broad Gaussian beam as an interference beam. We can clearly see that the phase structures for self-trapped  $m = 1$  and  $m = 2$  vortices are different (Figure 2(d)). The two diagonal spots are out-of-phase for the  $m = 1$  vortex but in-phase for the  $m = 2$  vortex.

We also measure the spatial spectrum of self-trapped vortices by using the Brillouin Zone (BZ) Spectroscopy technique [27]. Again, dramatic difference between  $m = 1$  and  $m = 2$  vortices can be seen in the  $k$ -space spectra, indicating quite different physical pictures for self-trapping. For the  $m = 1$  vortex, most of the power is located alongside the first BZ, but it would not concentrate just to the four corner points (corresponding to four high-symmetry M points) which mark the edge of the first Bloch band and where the diffraction is anomalous. However, for the  $m = 2$  vortex, the nonlinear spectrum reshaping makes the power spectrum settle into the M-points quickly, similar to those of the fundamental discrete gap solitons and gap soliton trains [28]. Numerical simulations show that such spectrum difference remains for long propagation distance. These results suggest

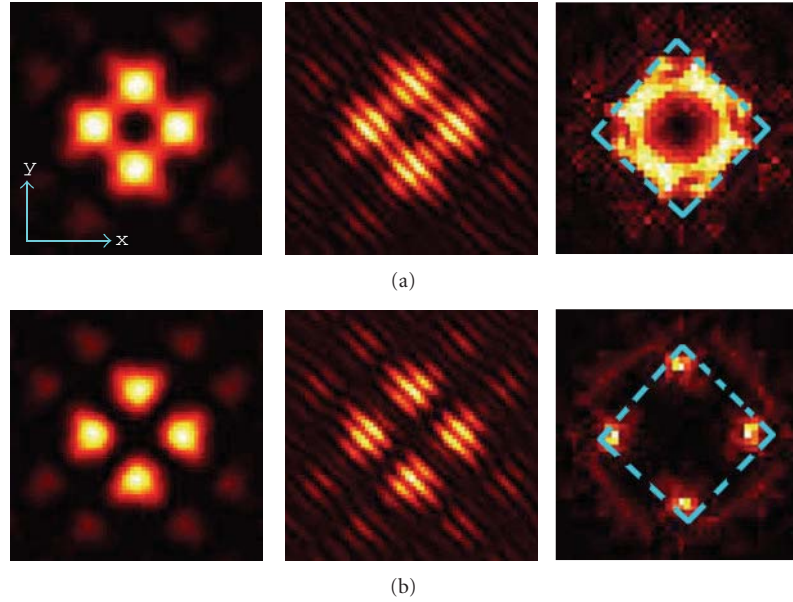


FIGURE 3: Simulation results of singly charged (a) and doubly charged (b) vortex beams propagating to a longer distance of 40 mm. Shown are the output transverse ( $x$ - $y$ ) intensity pattern (left), its interferogram with a tilted plane wave (middle), and its  $k$ -space spectrum (right) in both (a) and (b). Notice that the vortex singularity maintains in (a) but disappears in (b).

that although the  $m = 1$  vortex can evolve into a gap vortex soliton, it does not bifurcate from the edge of the first Bloch band, quite different from all previously observed fundamental, dipole, or quadrupole-like gap soliton in self-defocusing lattices [28, 29]. On the other hand, the  $m = 2$  vortex can evolve into a quadrupole-like localized state, which does seem to bifurcate from the edge of the first Bloch bands as confirmed by numerical analysis [26, 30].

The experimental observations are also compared with the numerical results obtained using beam propagation method with initial conditions similar to that for the experiment. The numerical model is a nonlinear wave equation with a 2D square lattice potential under saturate self-defocusing nonlinearity. Excellent agreement can be found for the propagation distance of 10 mm (i.e., our crystal length) for both  $m = 1$  and  $m = 2$  vortices [26]. To test whether the relevant gap soliton structure can persist for longer propagation distance, simulations are performed with propagation distance up to 40 mm while all other parameters are unchanged. It is found that the phase singularity can maintain for the singly charged vortex, while for the doubly charged vortex at long propagation distance, it turns into a quadrupole-like structures. The simulation results are shown in Figure 3. Notice that the interference patterns of the nonlinear output with a tilted plane wave show that the fork is still in the center for the  $m = 1$  vortex, but this is not the case for the  $m = 2$  vortex which turns into an out-of-phase quadrupole soliton. The power spectrum is also similar to that of 1 cm propagation in experiment: the spectrum for the  $m = 1$  gap vortex soliton does not evolve into the vicinity of the first-band M points, whereas that for the  $m = 2$  vortex does. Intuitively, the nonedge bifurcation of the singly charged gap vortex may be attributed to the nontrivial helical

phase structure of the vortex, which cannot be expressed as a simple superposition of linear Bloch modes near the band edge. Such subtle difference between the SCV and DCV gap solitons is also confirmed by theoretical analysis [26].

It is interesting to explore whether stable doubly charged gap vortex soliton exists in *self-defocusing* square photonic lattices without “decaying” into a quadrupole soliton, although such stable high-order discrete vortex solitons have been observed in hexagonal photonic lattices under a *self-focusing* nonlinearity [20]. Indeed, we find that when the input vortex ring is expanded to cover eight lattice sites as shown in Figure 4(a), under appropriate nonlinear conditions, the phase singularity can maintain and it can evolve into a “true” stable gap vortex soliton. Typical experimental results are shown in Figure 4, where the results were obtained when the lattice spacing is  $25 \mu\text{m}$ , the intensity ratio of the vortex beam to the lattice beam is 1:4, and the bias field is  $-1.4 \text{ kV/cm}$ . When the nonlinear self-trapped state is realized, most of its energy is localized in the initially excited eight lattices (Figure 4(c)). More importantly, the interference pattern between an inclined plane wave and the nonlinear output clearly shows that the two forks along with the bifurcation direction still preserve compared with those of the input vortex shown in Figure 4(b). Again, in such a case, the spectrum is not located in the four M points, different from the nonlinear spectrum under four-site excitation shown in Figure 2(e). Such high-order vortex gap solitons do not bifurcate from the band edge either! We want to mention that the DCV beams can also stably self-trap into solitons in the semi-infinite gap under self-focusing nonlinearity with 8-site excitation. Such geometrical extended stabilization mechanism has also been confirmed by theoretical analysis [31].

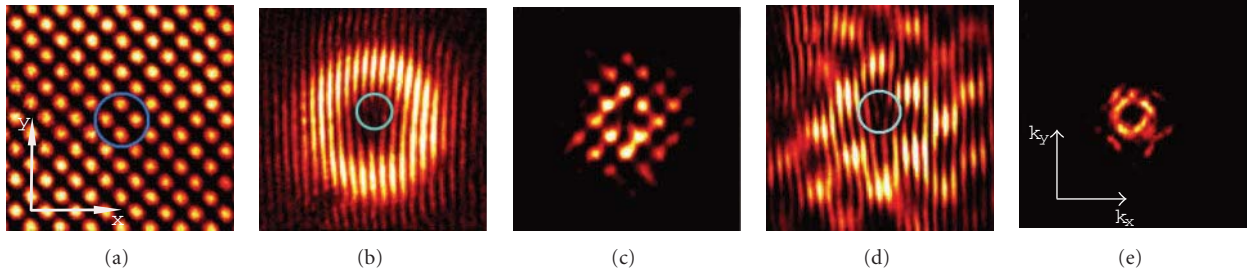


FIGURE 4: Experimental observation of an extended  $m = 2$  gap vortex soliton in photonic lattices with self-defocusing nonlinearity. (a) lattice beam, where the circle shows the location of the input vortex, (b) the interferogram of the input vortex with a tilted plane wave to show the phase singularity, (c) self-trapped vortex pattern, (d) the zoom-in interferogram of (c) with a tilted plane wave, and (e) the Fourier-space spectrum of the  $m = 2$  vortex soliton. The circles in (b) and (d) show the position of the phase singularity.

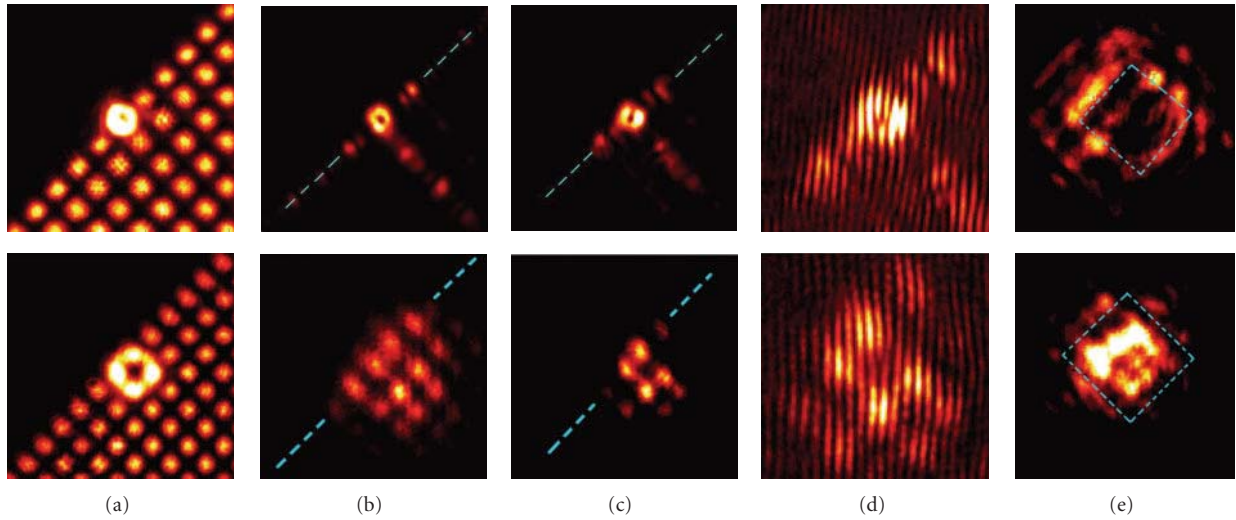


FIGURE 5: Experimental results of vortex self-trapping under single-site surface excitation (top) and four-site surface excitation (bottom). (a) Lattice beam superimposed with the vortex beam, (b) linear and (c) nonlinear output of the vortex beam, where blue dashed line indicates the surface location, (d) zoom-in interferogram of (c) with an inclined plane wave, and (e)  $k$ -space spectrum of (c). The dashed square in (e) marks the boundary of the first Brillouin zone.

**3.2. Discrete Surface Vortex Solitons.** Discrete surface solitons form an important family of discrete solitons that exist at interface between the semi-infinite photonic lattices and a homogenous media [32]. Now, let us use the SCV beam to excite at the surface of the photonic lattice rather than inside the lattice under the self-focusing nonlinearity. Surface vortex solitons have also been theoretically considered [33, 34]. Here, we present our experimental results of discrete surface vortex solitons with different excitation conditions. Both single-site and four-site excitation schemes are considered. We find that a SCV beam under the four-site excitation can evolve into a stable discrete surface vortex soliton in the semi-infinite gap, while under the single-site excitation, it evolves into a unstable quasilocalized surface state in the first photonic bandgap. The stability of such localized surface states depending on their initial excitation has been studied numerically for longer propagation distance [35].

First, we use the single-site excitation so the vortex ring covers only one lattice site at the surface (Figure 5(a) top). The vortex beam exhibits asymmetric discrete diffraction

when its intensity is low but self-traps at the surface site when its intensity is high while keeping the bias field (2.2 kV/cm) unchanged. Typical experimental results are presented in Figure 5. The lattice spacing is about  $30 \mu\text{m}$ . When the nonlinearity is absent (the intensity ratio of vortex-to-lattice is less than 1 : 10), the vortex beam diffracts as shown in Figure 5(b). The diffraction tails have double peak intensity at each lattice site, indicating the excitation of second-band Bloch modes. The tail going into the lattice is much longer than that at the lattice surface, owing to surface enhanced reflection [36, 37]. As we increase the intensity ratio to 1 : 3, self-trapping of the vortex at the lattice surface occurs when the vortex confines more at the initial excitation site, maintaining a donut-shaped pattern (Figure 5(c) top). To verify its phase singularity, a tilted plane wave is introduced to interfere with the surface vortex beam. The single fork remains in the interferogram, indicating that the phase singularity is preserved during the 1 cm experimental propagation length. Since the input vortex beam is tightly focused, its initial  $k$ -space spectrum extends beyond the first BZ (Figure 5(e) top).

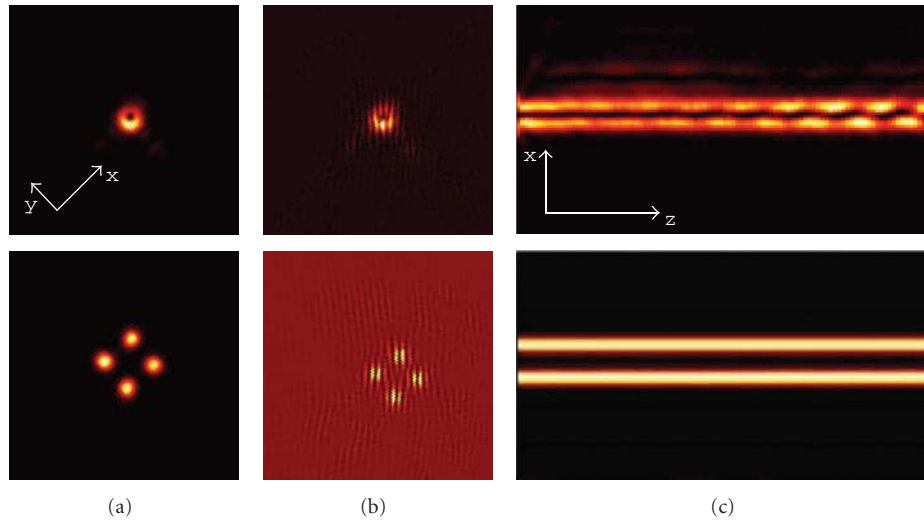


FIGURE 6: Numerical simulation of single-site (top) and four-site (bottom) surface excitation of a SCV after 4-cm of nonlinear propagation. Shown are (a) vortex output intensity pattern and (b) its corresponding interferogram, and (c) side-view of the vortex propagation to  $z = 4$  cm.

Such input condition excites high-band Bloch modes. In the case of the self-focusing nonlinearity, this leads to that the power spectrum is concentrated at the normal diffraction regions outside the first BZ but close to the high-symmetry X-points, as shown in Figure 5(e) top. Apparently, such self-trapped surface vortex states arise from excitation of Bloch modes near the X-points of the second Bloch band. However, numerical results to longer propagation distance (4 cm) shows that these quasilocalized surface states residing in the first photonic bandgap are unstable and thus would break up after long-distance propagation [35].

Next, we use the four-site excitation so the vortex ring is expanded to cover four nearest lattice sites at the surface (the vortex core locates in the index minimum as off-site excitation, as shown in Figure 5(a) bottom). Under appropriate nonlinear conditions, the SCV self-traps into a discrete surface vortex soliton. Typical experimental results are presented in the bottom panels of Figure 5. At a low nonlinearity, the vortex beam exhibits discrete diffraction (Figure 5(b)). Notice that in this case, the diffracted intensity pattern does not have fine features of double-peak in each lattice site, different from that of single-site excitation. This suggests that, under this condition, the expanded vortex excites the first-band Bloch modes. At a high nonlinearity, self-trapping of the vortex beam into a four-spot pattern is achieved (Figure 5(c)).

Due to that the induced surface is slightly deformed, the four-spot does not match a perfect square pattern. To monitor the phase structure of the self-trapped vortex, an inclined plane wave is again introduced for interference. The vortex singularity persists clearly in the nonlinear output (Figure 5(d) bottom). The nonlinear spectrum is also different from that of single-site excitation shown in Figure 5(e), since now most of the energy is concentrated in the central region of the normal diffraction within the first BZ. This indicates that the surface vortex soliton is formed in the semi-

infinite gap with modes primarily from near the  $\Gamma$ -point of the first Bloch band. As shown below, this four-site surface vortex soliton can be stable and thus remains invariant for long distance propagation.

Experimentally, it is difficult to test the stability of the self-trapped surface vortex structures due to the limited crystal length (i.e., 1 cm). Thus, we study the stability of the self-trapped vortex states by numerical simulation with parameters similar to the experimental conditions, but to much longer propagation distance (4 cm). For the four-site excitation vortex in the semi-infinite gap is stable, but for the single-site vortex in the Bragg reflection gap is unstable as shown in Figure 6. The nonlinear output of the SCV under single-site excitation broke up after 4 cm propagation, while the four-site surface soliton is nearly invariant. This stability analysis is also confirmed theoretically [35].

#### 4. Linear Localization of Optical Vortices in Photonic Lattices with Negative Defects

In the previous experiments, the localization of the vortex beam inside and at the surface of the photonic lattice is related to the nonlinearity-induced defect by the vortex beam itself. These self-trapped nonlinear localized topological states can be considered as self-induced *nonlinear* defect modes (DMs). A nature question arises whether vortices can be localized in a fabricated defect as *linear* defect modes within photonic lattices? In fact, band gap guidance of a Gaussian beam in photonic lattice with a negative defect has been realized in optically induced and fs-laser written waveguide arrays [38, 39].

Different from light guided in higher refractive-index region due to the total internal reflection, light guidance in negative defects results from the Bragg reflection in periodic structures. Here, we show that both a SCV and DCV beams

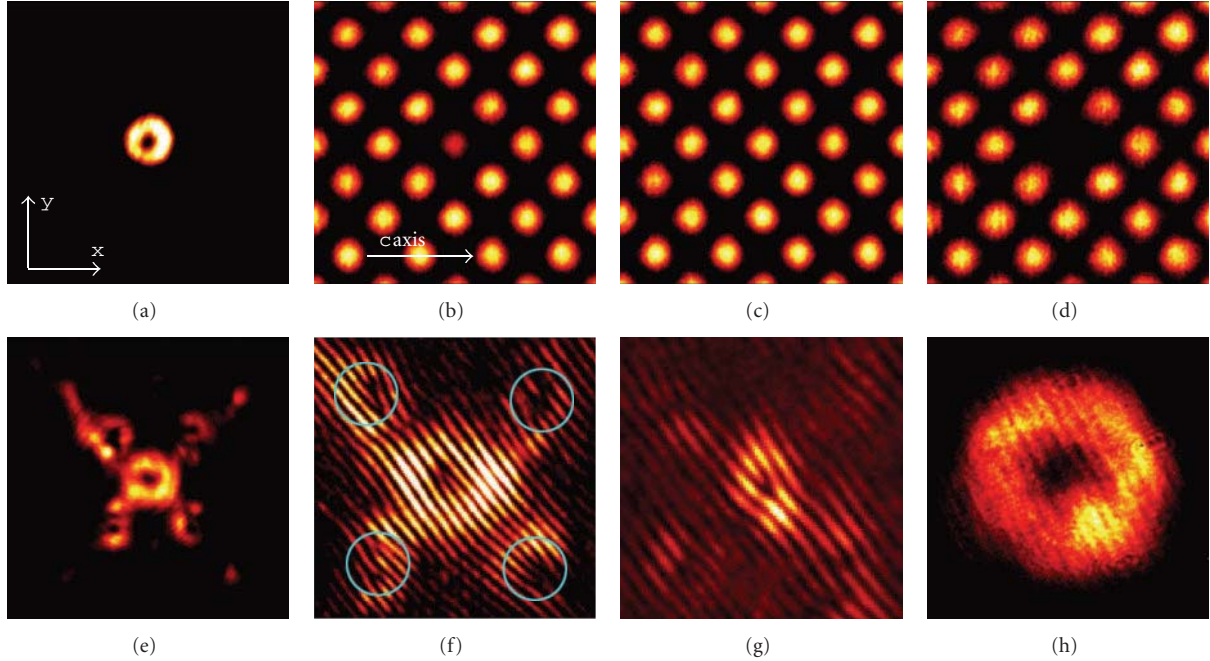


FIGURE 7: Experimental results of bandgap guidance of a vortex beam in a tunable negative defect. (a) Vortex at input. (b)–(d) Induced lattices with nonzero-intensity defect, no defect, and zero-intensity defect, respectively. (e), (f) Vortex output from the defect in (b) and its zoom-in interferogram. The circles in (f) mark the location of the vortex pairs. (g) Interferogram when the vortex is excited at nondefect site. (h) Vortex diffraction output when lattice is absent.

can be guided in the negative defects in 2D photonic lattices provided the defect strength is not too deep. The experimental setup is similar to Figure 1, except that the ordinarily-polarized beam is split again into two lattice-inducing beams: one has an uniform periodic intensity pattern as shown in Figure 7(c) (peak intensity  $I_c$ ), and the other has a zero-intensity defect site on otherwise uniform periodic pattern as shown in Figure 7(d) [peak intensity  $I_d$ ]. Superimposing the two lattice-inducing beams of equal lattice spacing results in a nonzero but tunable defect [an example obtained at  $I_d/I_c = 1/2$  is shown in Figure 7(b)]. The tunability of the defect strength is realized by varying the intensity ratio  $I_d/I_c$  (e.g., at  $I_d/I_c \gg 1$ , the defect is deep or close to zero intensity, but at  $I_d/I_c \ll 1$ , the defect is shallow or close to washout).

Typical experimental results are presented in the bottom panels of Figure 7. Under proper experimental conditions, the input vortex beam ( $20\ \mu\text{m}$  in diameter) is guided into the defect channel, maintaining a donut-shaped pattern in the defect site with “tails” extending along two principal axes of the square lattice. This result was obtained at  $42\ \mu\text{m}$  lattice spacing,  $2.3\ \text{kV/cm}$ , and  $I_d/I_c = 1/2$ . For comparison, the same vortex beam diffracts dramatically when the defect is removed, showing no self-action of the vortex beam under the same bias condition (Figure 7(h)). Fine features can be seen in the interferogram obtained by interference between the output vortex beam and an inclined broad beam (quasipplane wave). While the phase singularity is maintained in the vortex center, additional vortex pairs are evident along the four “tails” away from the defect site, manifested by

two close but separated fork fringes in the interferogram (Figure 7(f)). These fine structures in the “tails” provide us a way to identify the properties of the vortex DMs. By comparing with the theoretical results [40], it is apparent that the input SCV beam has evolved into a high-gap DM, whose propagation constant resides between the second and third Bloch bands. We emphasize that the localization of the vortex beam arises from the linear bandgap guidance, quite different from stationary propagation of second-band vortex solitons where the vortex beam itself creates a positive defect with self-focusing nonlinearity [17]. For comparison, the interferogram from the vortex beam exiting a normal lattice site is shown in Figure 7(g), where a single vortex (instead of vortex pair) is observed along each “tail.”

The formation of the vortex DMs depends on the defect strength. A series of experiments is performed to illustrate the influence of the defect strength. To do so, we keep the bias field and  $I_c$  fixed but tune the defect strength by gradually varying  $I_d$ . We found that the vortex can be guided only when the defect is not too deep (or the intensity in the defect site is not close to zero). Examples of varying the intensity ratio  $I_d/I_c$  or the bias field (both control the induced index change at the defect site) are shown in Figure 8. When the biased field is set at  $2.6\ \text{kV/cm}$ , guidance of the vortex beam is clearly observed at  $I_d/I_c = 1$  (Figure 8(a)) (which corresponds to a half-intensity defect). However, once the uniform lattice beam is removed ( $I_c = 0$ ), the vortex beam cannot be confined in the defect site under the same bias condition (Figure 8(b)). At this zero-intensity defect, the vortex DM cannot form, even at a decreased bias

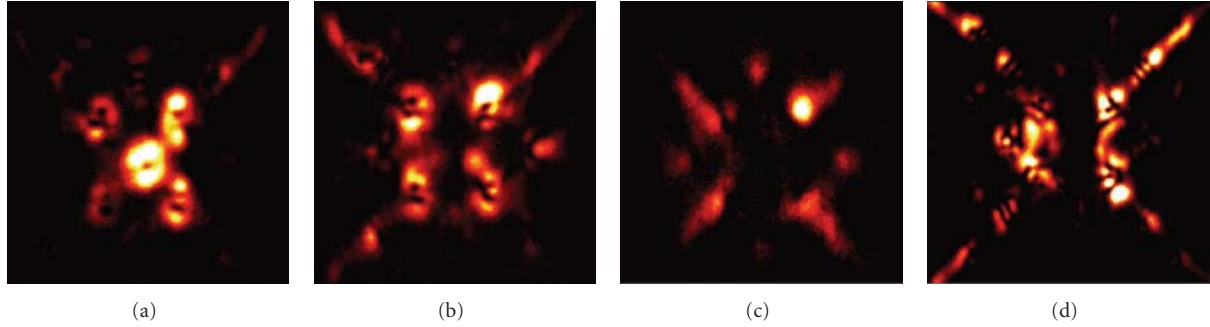


FIGURE 8: Experimental results of SCV beam output after propagating through (a) a half-intensity ( $I_d/I_c = 1/1$ ) defect and (b) a zero-intensity defect at a fixed bias field of 2.6 kV/cm. (c), (d) Output of the vortex beam through the zero-intensity defect when the bias field is decreased to 1.4 kV/cm and increased to 3.2 kV/cm, respectively.

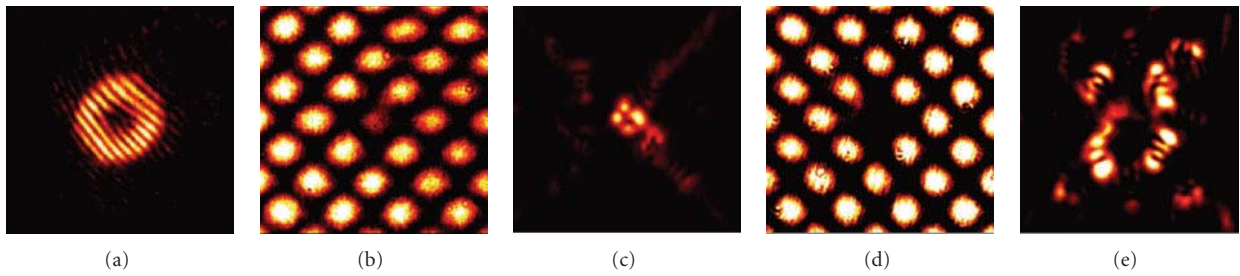


FIGURE 9: Experimental results of bandgap guidance of a DCV beam in a tunable negative defect. (a) interference pattern of input vortex with an inclined plane wave (zoomed in), (b) lattice beam with a nonzero-intensity defect, (c) linear output of the doubly charged vortex beam exiting the defect channel in the lattice (b), (d) lattice beam with a zero-intensity defect, and (e) linear output of the DCV through the defect in lattice (d).

field of 1.4 kV/cm (Figure 8(c)) or an increased bias field of 3.2 kV/cm (Figure 8(d)). Thus, bandgap guidance of the vortex clearly occurs in the half-intensity defect but deteriorates in the zero-intensity defect. There might be a threshold for the defect strength that would support the vortex DM, but experimentally it is difficult to determine such a threshold. Theoretically, it is found that, when the defect gets deeper the propagation constant of the DM moves deeper, toward a higher band-gap. Because of the limited number of fully opened higher gaps, the propagation constant of the DM may move into a higher Bloch band and eventually localized DM disappears [41].

Finally, a DCV beam is used as a probe beam sent into the tunable negative defect to check whether a high-order optical vortex can be guided in it. We find the DCV cannot be guided and it tends to break up again into a quadruple-like structure when the defect strength is not too deep. Typical experimental results are shown in Figure 9. These results were obtained when the lattice spacing is  $42 \mu\text{m}$ , the biased field is about 3.4 kV/cm, and the intensity ratio is  $I_d/I_c = 2$ . As before with nonlinear propagation of DCVs, the linear output is no longer in a donut shape, but rather turns into a quadrupole pattern with the symmetry similar to the lattice as shown in Figure 9(c). However, when the defect strength is very strong (i.e., intensity at the defect site is close to zero as in Figure 9(d)), even the quadrupole-like pattern cannot be maintained (Figure 9(e)). Under this condition, there is no

light guided at the defect site at all when the bias field or the lattice intensity is increased.

## 5. Summary and Conclusions

We have studied experimentally the dynamical propagation of optical vortices in optically induced square photonic lattices under different settings. Inside the uniform photonic lattices, we find that the SCV beams self-trap into stable gap vortex solitons under four-site excitation with a defocusing nonlinearity. However, the DCV beams tend to break up and turn into quadrupole gap solitons. With geometrically extension eight-site excitation, the DCV beams can evolve into stable gap vortex solitons. Both the SCV and DCV gap solitons do not bifurcate from modes at the band edges, which is different from all the previously observed gap solitons. At the lattice surface, the SCV beams turn into stable surface vortex solitons in the semi-infinite gap under the four-site excitation with a self-focusing nonlinearity. However, they evolve into unstable quasivortex solitons with propagation constants in the first Bragg gap under the single-site excitation. In photonic lattices with negative defects, the SCV beams can be guided as linear vortex defect modes under appropriate defect conditions due to the bandgap guidance, while the DCV beams are unstable and evolve into quadrupole-like defect modes. Our results about such linear and nonlinear localized vortex states may prove to be relevant to

similar vortex phenomena in other discrete systems beyond optics.

## Acknowledgments

This work was supported in part by the 973 Program (2007CB613203) and NSFC (10904078) in China and by US National Science Foundation (NSF) and Air Force Office of Scientific Research (AFOSR). The authors thank J. Yang, P. G. Kevrekidis, K. Law, and X. Wang for helpful discussions and assistance.

## References

- [1] A. S. Desyatnikov, Y. S. Kivshar, and L. Torner, "Optical vortices and vortex solitons," in *Progress in Optics*, E. Wolf, Ed., vol. 47, pp. 219–319, North-Holland, Amsterdam, The Netherlands, 2005.
- [2] M. R. Dennis, Y. S. Kivshar, M. S. Soskin, and G. A. Swartzlander Jr., "Singular optics: more ado about nothing," *Journal of Optics A*, vol. 11, no. 9, Article ID 090201, 2009.
- [3] G. A. Swartzlander and C. T. Law, "Optical vortex solitons observed in Kerr nonlinear media," *Physical Review Letters*, vol. 69, no. 17, pp. 2503–2506, 1992.
- [4] J. Christou, V. Tikhonenko, Y. S. Kivshar, and B. Luther-Davies, "Vortex soliton motion and steering," *Optics Letters*, vol. 21, no. 20, pp. 1649–1651, 1996.
- [5] G. Duree, M. Morin, G. Salamo et al., "Dark photorefractive spatial solitons and photorefractive vortex solitons," *Physical Review Letters*, vol. 74, no. 11, pp. 1978–1981, 1995.
- [6] Z. Chen, M. Segev, D. W. Wilson, R. E. Muller, and P. D. Maker, "Self-trapping of an optical vortex by use of the bulk photovoltaic effect," *Physical Review Letters*, vol. 78, no. 15, pp. 2948–2951, 1997.
- [7] Z. Chen, M. F. Shih, M. Segev, D. W. Wilson, R. E. Muller, and P. D. Maker, "Steady-state vortex-screening solitons formed in biased photorefractive media," *Optics Letters*, vol. 22, no. 23, pp. 1751–1753, 1997.
- [8] Z. Chen, M. Mitchell, M. Segev, T. H. Coskun, and D. N. Christodoulides, "Self-trapping of dark incoherent light beams," *Science*, vol. 280, no. 5365, pp. 889–891, 1998.
- [9] W. J. Firth and D. V. Skryabin, "Optical solitons carrying orbital angular momentum," *Physical Review Letters*, vol. 79, no. 13, pp. 2450–2453, 1997.
- [10] C. C. Jeng, M. F. Shih, K. Motzek, and Y. Kivshar, "Partially incoherent optical vortices in self-focusing nonlinear media," *Physical Review Letters*, vol. 92, no. 4, pp. 439041–439044, 2004.
- [11] I. Towers and B. A. Malomed, "Stable (2+1)-dimensional solitons in a layered medium with sign-alternating Kerr nonlinearity," *Journal of the Optical Society of America B*, vol. 19, no. 3, pp. 537–543, 2002.
- [12] D. Briedis, D. E. Petersen, D. Edmundson, W. Krolikowski, and O. Bang, "Ring vortex solitons in nonlocal nonlinear media," *Optics Express*, vol. 13, no. 2, pp. 435–443, 2005.
- [13] B. A. Malomed and P. G. Kevrekidis, "Discrete vortex solitons," *Physical Review E*, vol. 64, no. 2, pp. 266011–266016, 2001.
- [14] J. Yang and Z. H. Musslimani, "Fundamental and vortex solitons in a two-dimensional optical lattice," *Optics Letters*, vol. 28, no. 21, pp. 2094–2096, 2003.
- [15] D. N. Neshev, T. J. Alexander, E. A. Ostrovskaya et al., "Observation of discrete vortex solitons in optically induced photonic lattices," *Physical Review Letters*, vol. 92, no. 12, p. 123903, 2004.
- [16] J. W. Fleischer, G. Bartal, O. Cohen et al., "Observation of vortex-ring "discrete" solitons in 2D photonic lattices," *Physical Review Letters*, vol. 92, no. 12, p. 123904, 2004.
- [17] G. Bartal, O. Manela, O. Cohen, J. W. Fleischer, and M. Segev, "Observation of second-band vortex solitons in 2D photonic lattices," *Physical Review Letters*, vol. 95, no. 5, Article ID 053904, pp. 1–4, 2005.
- [18] A. Bezryadina, E. Eugenieva, and Z. Chen, "Self-trapping and flipping of double-charged vortices in optically induced photonic lattices," *Optics Letters*, vol. 31, no. 16, pp. 2456–2458, 2006.
- [19] B. Terhalle, D. Göries, T. Richter et al., "Anisotropy-controlled topological stability of discrete vortex solitons in optically induced photonic lattices," *Optics Letters*, vol. 35, no. 4, pp. 604–606, 2010.
- [20] B. Terhalle, T. Richter, K. J. H. Law et al., "Observation of double-charge discrete vortex solitons in hexagonal photonic lattices," *Physical Review A*, vol. 79, no. 4, pp. 043821–043828, 2009.
- [21] B. Terhalle, T. Richter, A. S. Desyatnikov et al., "Observation of multivortex solitons in photonic lattices," *Physical Review Letters*, vol. 101, no. 1, pp. 013903–013904, 2008.
- [22] K. J. H. Law, A. Saxena, P. G. Kevrekidis, and A. R. Bishop, "Stable structures with high topological charge in nonlinear photonic quasicrystals," *Physical Review A*, vol. 82, no. 3, Article ID 035802, 2010.
- [23] H. Martin, E. D. Eugenieva, Z. Chen, and D. N. Christodoulides, "Discrete solitons and soliton-induced dislocations in partially coherent photonic lattices," *Physical Review Letters*, vol. 92, no. 12, p. 123902, 2004.
- [24] Z. Chen, H. Martin, E. D. Eugenieva, J. Xu, and A. Bezryadina, "Anisotropic enhancement of discrete diffraction and formation of two-dimensional discrete-soliton trains," *Physical Review Letters*, vol. 92, no. 14, p. 143902, 2004.
- [25] N. K. Efremidis, J. Hudock, D. N. Christodoulides, J. W. Fleischer, O. Cohen, and M. Segev, "Two-dimensional optical lattice solitons," *Physical Review Letters*, vol. 91, no. 21, pp. 213906/1–213906/4, 2003.
- [26] D. Song, C. Lou, L. Tang et al., "Self-trapping of optical vortices in waveguide lattices with a self-defocusing nonlinearity," *Optics Express*, vol. 16, no. 14, pp. 10110–10116, 2008.
- [27] G. Bartal, O. Cohen, H. Buljan, J. W. Fleischer, O. Manela, and M. Segev, "Brillouin zone spectroscopy of nonlinear photonic lattices," *Physical Review Letters*, vol. 94, no. 16, Article ID 163902, 2005.
- [28] C. Lou, X. Wang, J. Xu, Z. Chen, and J. Yang, "Nonlinear spectrum reshaping and gap-soliton-train trapping in optically induced photonic structures," *Physical Review Letters*, vol. 98, no. 21, Article ID 213903, 2007.
- [29] L. Tang, C. Lou, X. Wang et al., "Observation of dipole-like gap solitons in self-defocusing waveguide lattices," *Optics Letters*, vol. 32, no. 20, pp. 3011–3013, 2007.
- [30] J. Wang and J. Yang, "Families of vortex solitons in periodic media," *Physical Review A*, vol. 77, no. 3, Article ID 033834, 2008.
- [31] K. J. H. Law, D. Song, P. G. Kevrekidis, J. Xu, and Z. Chen, "Geometric stabilization of extended S=2 vortices in two-dimensional photonic lattices: theoretical analysis, numerical computation, and experimental results," *Physical Review A*, vol. 80, no. 6, Article ID 063817, 2009.
- [32] S. Suntsov, K. G. Makris, G. A. Siviloglou et al., "Observation of one- and two-dimensional discrete surface spatial solitons,"

- Journal of Nonlinear Optical Physics and Materials*, vol. 16, no. 4, pp. 401–426, 2007.
- [33] H. Susanto, p. G. Kevrekidis, B. A. Malomed, R. Carretero-González, and D. J. Frantzeskakis, “Discrete surface solitons in two dimensions,” *Physical Review E*, vol. 66, Article ID 046602, 2007.
  - [34] Y. V. Kartashov, A. A. Egorov, V. A. Vysloukh, and L. Torner, “Surface vortex solitons,” *Optics Express*, vol. 14, no. 9, pp. 4049–4057, 2006.
  - [35] D. Song, C. Lou, K. J. H. Law et al., “Self-trapping of optical vortices at the surface of an induced semi-infinite photonic lattice,” *Optics Express*, vol. 18, no. 6, pp. 5873–5878, 2010.
  - [36] S. Suntsov, K. G. Makris, D. N. Christodoulides et al., “Observation of discrete surface solitons,” *Physical Review Letters*, vol. 96, no. 6, Article ID 063901, 2005.
  - [37] X. Wang, A. Bezryadina, Z. Chen, K. G. Makris, D. N. Christodoulides, and G. I. Stegeman, “Observation of two-dimensional surface solitons,” *Physical Review Letters*, vol. 98, no. 12, Article ID 123903, 2007.
  - [38] I. Makasyuk, Z. Chen, and J. Yang, “Band-gap guidance in optically induced photonic lattices with a negative defect,” *Physical Review Letters*, vol. 96, no. 22, Article ID 223903, 2006.
  - [39] A. Szameit, Y. V. Kartashov, M. Heinrich et al., “Observation of two-dimensional defect surface solitons,” *Optics Letters*, vol. 34, no. 6, pp. 797–799, 2009.
  - [40] J. Wang, J. Yang, and Z. Chen, “Two-dimensional defect modes in optically induced photonic lattices,” *Physical Review A*, vol. 76, no. 1, Article ID 013828, 2007.
  - [41] D. Song, X. Wang, D. Shuldman et al., “Observation of band-gap guidance of optical vortices in a tunable negative defect,” *Optics Letters*, vol. 35, no. 12, pp. 2106–2108, 2010.

## Research Article

# Complex 3D Vortex Lattice Formation by Phase-Engineered Multiple Beam Interference

**Jolly Xavier, Sunil Vyas, Paramasivam Senthilkumaran, and Joby Joseph**

*Department of Physics, Indian Institute of Technology Delhi, New Delhi 110016, India*

Correspondence should be addressed to Jolly Xavier, jolly.xavierp@physics.iitd.ac.in

Received 8 June 2011; Accepted 20 July 2011

Academic Editor: Shunichi Sato

Copyright © 2012 Jolly Xavier et al. This is an open access article distributed under the Creative Commons Attribution License, which permits unrestricted use, distribution, and reproduction in any medium, provided the original work is properly cited.

We present the computational results on the formation of diverse complex 3D vortex lattices by a designed superposition of multiple plane waves. Special combinations of multiples of three noncoplanar plane waves with a designed relative phase shift between one another are perturbed by a nonsingular beam to generate various complex 3D vortex lattice structures. The formation of complex gyrating lattice structures carrying designed vortices by means of relatively phase-engineered plane waves is also computationally investigated. The generated structures are configured with both periodic as well as transversely quasicrystallographic basis, while these whirling complex lattices possess a long-range order of designed symmetry in a given plane. Various computational analytical tools are used to verify the presence of engineered geometry of vortices in these complex 3D vortex lattices.

## 1. Introduction

Optical wavefront dislocations occur naturally in an interference field during the superposition of three or more coherent plane waves [1–4]. An optical screw dislocation in a given plane, also called as optical vortex or phase singularity, is a point phase defect where the amplitude is zero and the phase is indeterminate [4]. The wavefront of the vortex beam is associated with the spiral flow of the electromagnetic energy. Vortices are thus points or lines of absolute darkness with undefined phase embedded within the spatial structure of the wave field. Regular wave function can have singular points only when the real as well as imaginary parts of the wave function vanishes simultaneously [3]. These two conditions define two surfaces in space whose intersection determines the position of vortex lines. However, the vanishing of the wave function is the necessary but not the sufficient condition for the existence of vortex. They exist only if the circulation of phase around the line, where the wave function vanishes, is different from zero. Diverse approaches are implemented to generate array of optical vortices, called as vortex lattices [1, 4–18]. Vortex lattices possess the property of orbital angular momentum due to spatial distribution of intensity and phase distribution of the optical field. We

find these phenomenal structures and their dynamics also in other physical systems like Bose-Einstein condensates, super fluids, and so forth [19]. Among various fabrication methods for 2D and 3D photonic lattice structures, the fabrication approach involving a designed combination of light fields dynamically sculpting the structures to control the light is proven to be versatile in terms of scalability, tunability, and large area fabrication flexibility in a single step [20–25]. It has also been shown that optical field patterns belonging to all 14 Bravais crystallographic lattice 3D structures can be formed by designed plane wave interference [26, 27]. By means of a spatial light modulator (SLM-) assisted approach, the basic multiple beam interference technique has been extended to reconfigurable single-step fabrication process for both 2D and 3D periodic as well as transversely quasicrystallographic photonic lattices [1, 4, 13–16, 24, 25].

Various periodic as well as transversely quasicrystallographic vortex lattices have been investigated in view of their applications especially in the field of nondiffracting beams [14]. Recently, we demonstrated for the first time by a phase only spatial light modulator (SLM-) assisted reconfigurable optical phase engineering approach, 3D chiral lattices belonging to periodic as well as transversely quasicrystallographic basis which possessed spiraling vortices [13]. We

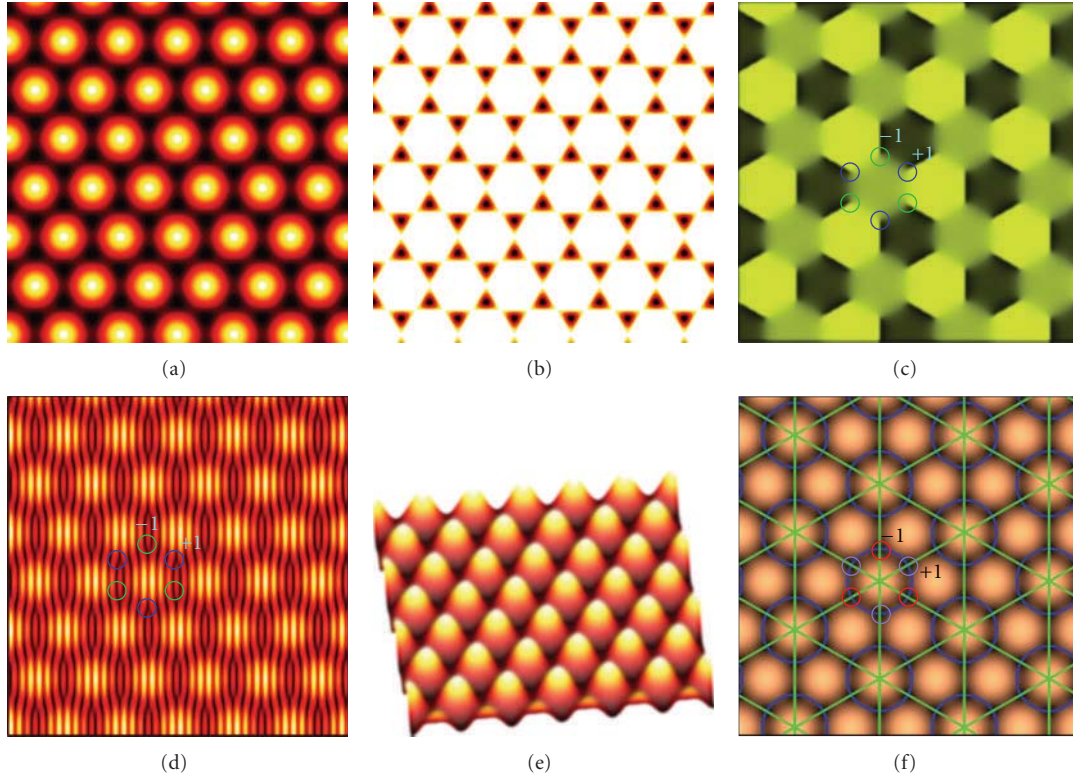


FIGURE 1: Analysis of three noncoplanar beam interference patterns possessing a distribution of single-charged vortices. (a) Intensity distribution in  $x$ - $y$  plane. (b) Intensity distribution with a lower threshold value in order to highlight the darker regions alone. (c) Phase profile. (d) The fork formation while the pattern is interfered with a plane wave launched at a large angle from the axis. (e) Intensity mesh plot. (f) Zero crossing plot (blue line: zeros of  $\text{Re}(E(r))$  and green line: zeros of  $\text{Im}(E(r))$ ).

envisage that the photonic structures with the spiral phase modulation will add a new degree of freedom and would open up the possibility of forming lattices with well-defined phase defects with the special property of orbital angular momentum [1]. In this paper, we present the formation and analysis of 3D vortex lattice structures by means of interbeam relative phase engineering of interfering plane waves. It has been observed that minimum three plane waves are required to form the lattice structure carrying optical vortices in case of multiple plane wave interference [5]. Here, we investigate the combinations of multiples of three plane waves having a designed relative phase between them to form novel 3D chiral vortex superlattice structures with a long-range order of designed symmetry in a given transverse plane. These real-time tunable spiraling vortex superlattice structures are envisaged to find novel applications in advanced multiple particle trapping/manipulation [1, 28], photonic cloaking [29], dense coded satellite communications and dynamic optical vortex meteorology [1, 30], and so forth.

## 2. Wave Design for Complex Vortex Lattices

It has been observed that in the interference field of three or more plane waves, the optical vortices are formed [5]. Recently, we had investigated the fabrication of 3D photonic chiral lattices [13]. In the following, we formulate the wave

design of interfering beams for complex 3D spiraling lattices imbedded with tunable vortex clusters. As three plane waves being the minimum number of interfering plane waves for the resultant vortex-embedded irradiance field, in our wave design, we choose  $n = 3$  plane waves as the basic combination of noncoplanar equidistant side beams. With respect to one another, we introduce an initial phase of  $\varphi_m = (2\pi/3) \times m$  to these beams, where  $m$  is from 1 to 3. Then we define an integer “ $p$ ” as a multiplying factor with  $n$ , leading to  $q = n \times p$  number of axially equidistant noncoplanar plane waves, where  $n = 3$ . Moreover, their Fourier components in turn lie axially equidistantly on a circle [23]. The complex irradiance profile formed by the interference of these coherent beams is subsequently perturbed by means of an axially launched noncoplanar plane wave [4, 13]. Considering the multiples of  $n = 3$ , the overall irradiance profile of the interference pattern of  $q + 1$  linearly polarized plane waves is given by [13, 25],

$$I(\mathbf{r}) = \sum_{i=0}^q |\mathbf{E}_i|^2 + \sum_{i=0}^q \sum_{\substack{j=0 \\ j \neq i}}^q \mathbf{E}_i \mathbf{E}_j^* \cdot \exp[i(\mathbf{k}_i - \mathbf{k}_j) \cdot \mathbf{r} + i\varphi_{ij}], \quad (1)$$

where  $\mathbf{E}_{i,j}$ ,  $\mathbf{k}_{i,j}$ ,  $\mathbf{r}$ , and  $\varphi_{ij}$  are the complex amplitudes, the wave vectors, position vector, and the difference in initial offset phase of the interfering side beams, respectively. It

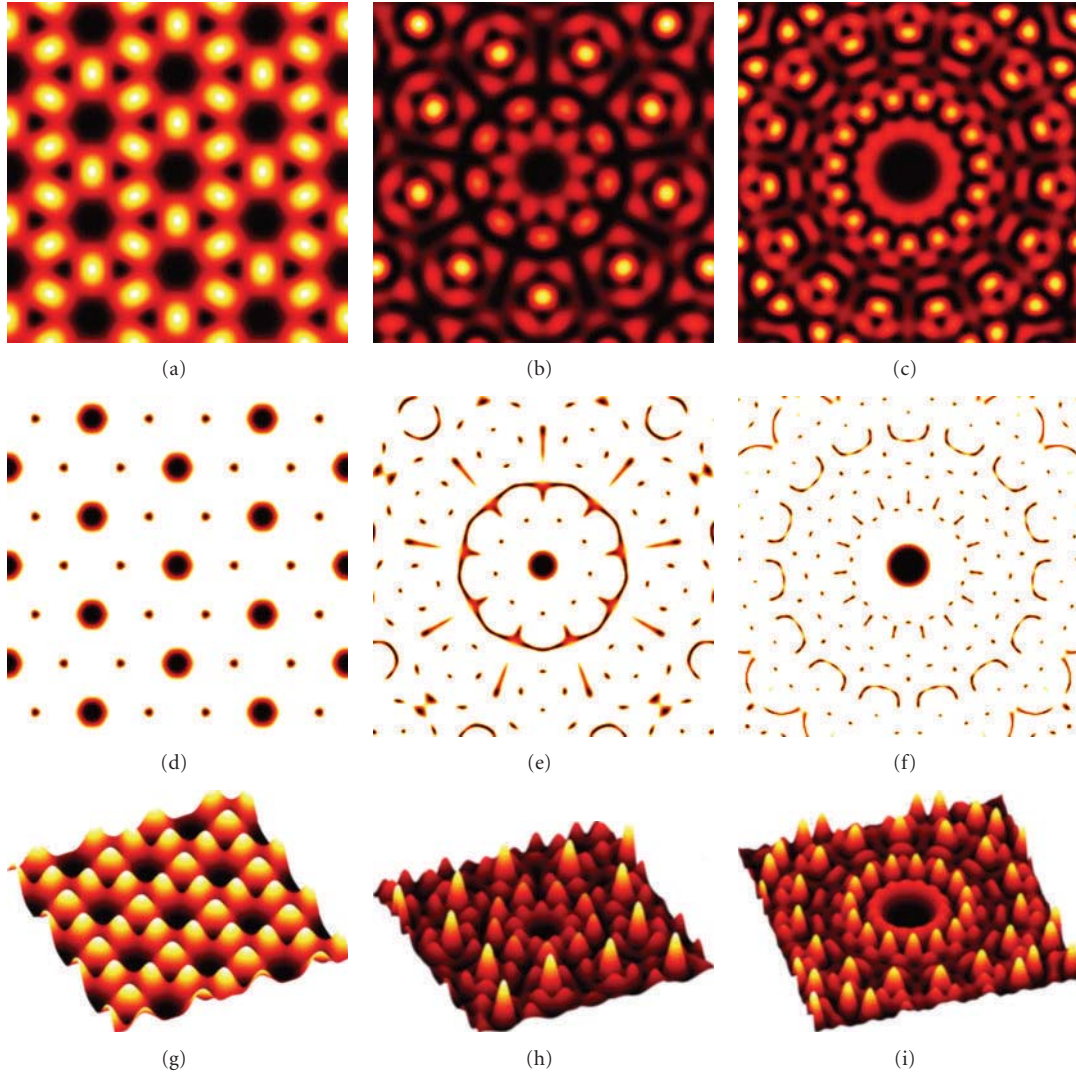


FIGURE 2: Simulation of complex 2D vortex lattice intensity profile possessing a distribution of higher-order topological charged as well as single charged vortices. Taking the multiples of relatively phase-shifted three beams, the numbers of interfering beams involved are, respectively 6 beams (first column), 9 beams (second column), and 15 beams (third column). (a)–(c) Intensity distribution in  $x$ - $y$  plane. (d)–(f) Intensity distribution with a lower threshold value in order to high light the darker regions alone. (g)–(i) Intensity mesh plots.

has been observed that interference between an L-G beam and a plane wave transforms the azimuthal phase variation into an azimuthal intensity variation [28], and in accordance with the “ $p$ ” number of  $2\pi$  phase variations, “ $p$ ” spiral arms could be formed. This is analogous to the unfolding of a vortex of higher-order topological charge “ $p$ ” into “ $p$ ” singly charged vortices with identical sign in the presence of a nonsingular perturbing beam [4]. So in fact, the presence of the perturbing beam shifts the position of the generated vortices in the interference field. Similar behaviour is also applicable in the case of a distribution of vortices under consideration [31, 32]. Moreover, it has also been observed that a distribution of vortices of small localized core function carrying unit charge of identical sign in a host Gaussian beam envelop begin to rotate as a rigid pattern [32]. As given in equation (1), the dynamically generated interference

pattern formed by means of the interference of the designed relatively phase engineered plane waves possesses a designed distribution of vortices within complex spiraling vortex lattices. In the presence of the axially launched perturbing optical field, these  $q + 1$  plane waves with specific beam geometries interfere to sculpt complex 3D photonic lattices embedded with vortices.

### 3. 2D Vortex Lattices: Folded Phase Dislocations

In this section, we analyse our results on complex 2D vortex lattices formed by following the wave design given above. In a 2D vortex lattice structure, the transverse irradiance profile of the interference pattern remains invariant along the  $z$ -direction. So we consider, in this section, the interference of only “ $q$ ” axially equidistant side beams in the absence of a

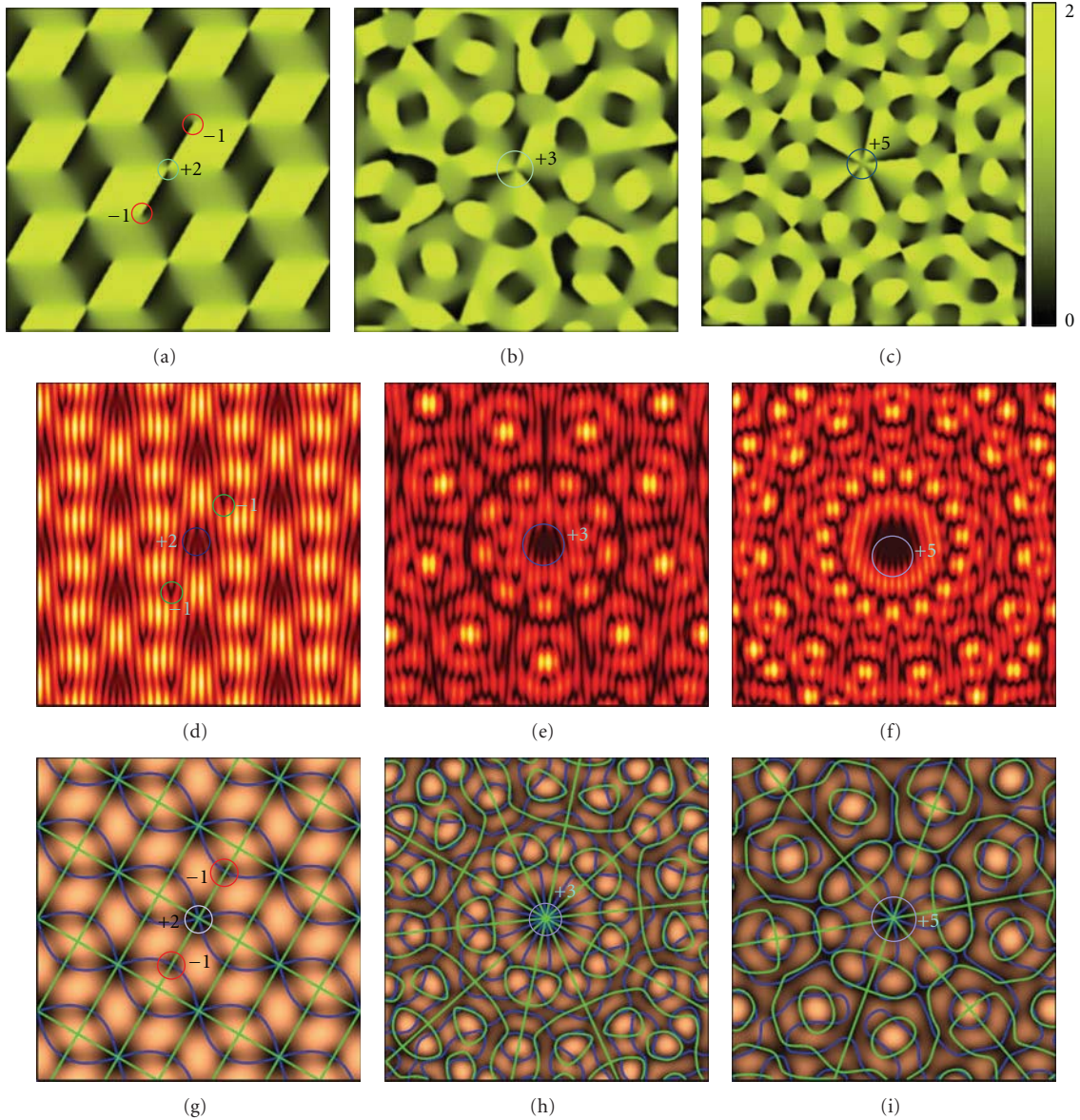


FIGURE 3: Computational analysis of complex 2D vortex lattices. Taking the multiples of relatively phase-shifted three beams, the numbers of interfering beams involved are, respectively, 6 beams (first column), 9 beams (second column), and 15 beams (third column). (a)–(c) Phase profile. (d)–(f) The fork formation while the pattern is interfered with a plane wave launched at a large angle from the axis. (g)–(i) Zero crossing plot (blue line: zeros of  $\text{Re } E(r)$  and green line: zeros of  $\text{Im } E(r)$ ). Circle at the center in cyan color highlights the higher-order vortex.

perturbing central beam. We call such vortices as “folded” [4], as in the absence of an additional nonsingular perturbing beam, they remain in their original higher-order topological charged state without being unfolded into singly charged vortices of identical sign. In Figures 1–3, there are detailed analyses of various 2D vortex lattices for varying values of “ $q$ .” For  $p = 1$ , the lattice structure has a triangular basis embedded with vortex structure of honey comb lattice. The computed phase patterns for respective lattice structures show the  $2\pi$  phase variations leading to phase dislocations as given in Figure 1(c) and Figures 3(a)–3(c). And these phase profiles clearly indicate the presence of vortex distribution.

As given in Figure 1(d) and Figures 3(d)–3(f), as the lattice forming beams are interfered with an additional plane wave, launched with a large angle with respect to the axis, this leads to the formation of forks as the clear classical signature of the positions of the phase dislocations.

Further, the direction of the generated fork structure indicates the relative sign of the topological charge. Considering the resultant complex amplitude  $E(r)$  by the superposition of beams, the optical vortex occurs at the intersection lines of the surfaces given by zeros of  $\text{Re } E(r)$  and  $\text{Im } E(r)$  [3]. These lines are plotted for the case of an  $x$ - $y$  plane of complex amplitude for the unperturbed structure in

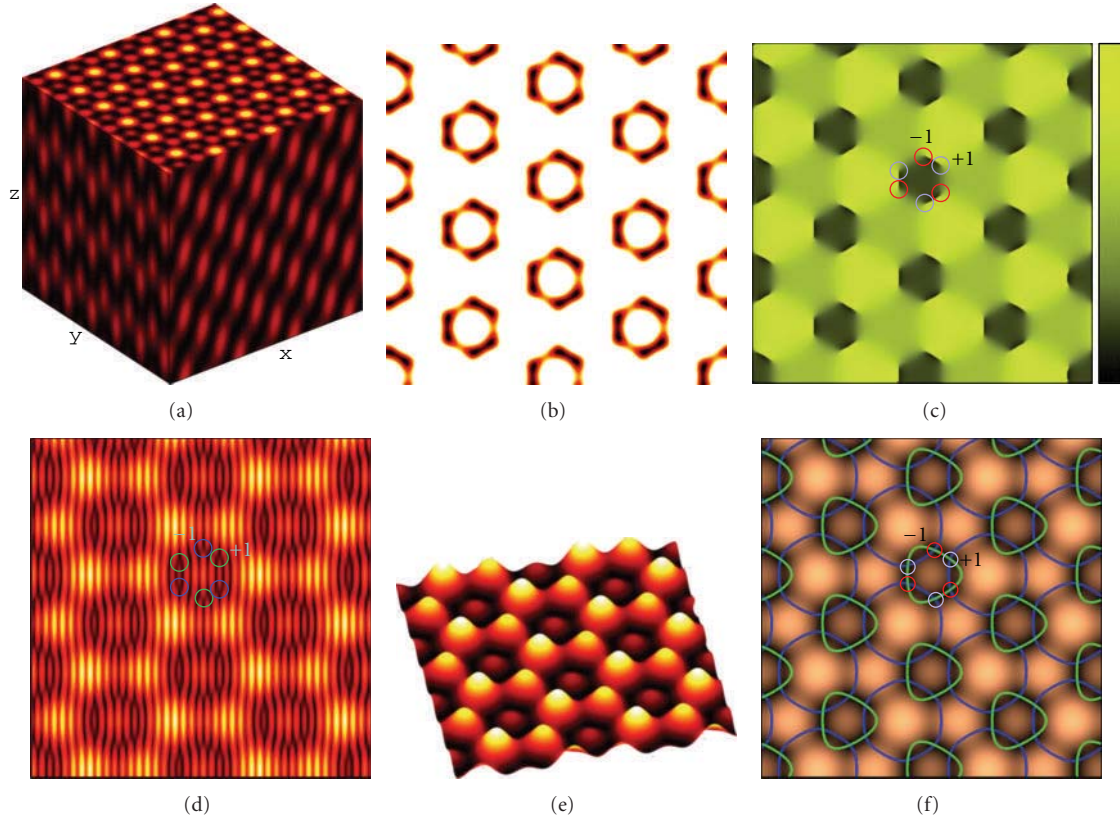


FIGURE 4: Analysis of vortices in a 3D photonic lattice formation by 3 + 1 noncoplanar beam interference. (a) 3D intensity distribution. (b) Intensity distribution of  $x$ - $y$  plane with a lower threshold value in order to highlight the darker regions alone. (c) Phase profile. (d) The fork formation while the pattern is interfered with a plane wave launched at a large angle from the axis. (e) Intensity mesh plot. (f) Zero crossing plot (blue line: zeros of  $\text{Re } E(r)$  and green line: zeros of  $\text{Im } E(r)$ ).

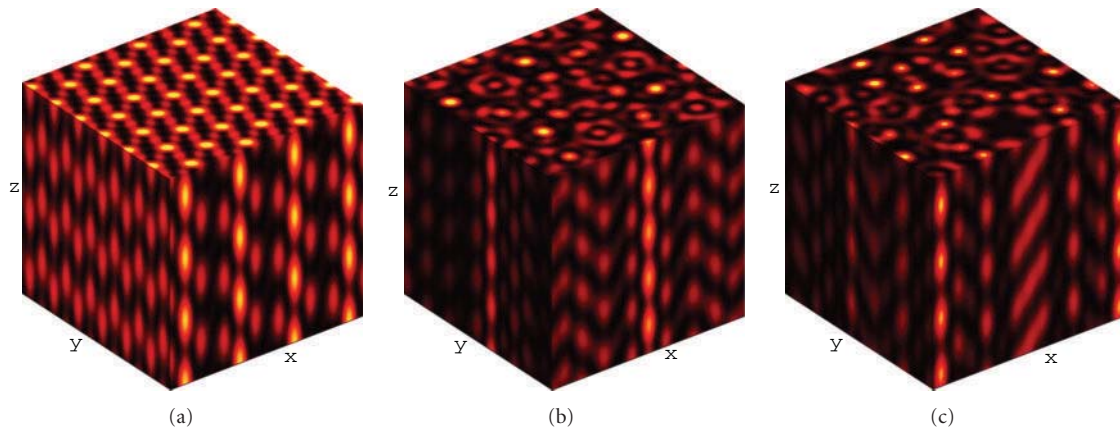


FIGURE 5: Computer simulations of intensity distributions of complex 3D photonic vortex lattices. Taking the multiples of relatively phase-shifted three beams, where the numbers of interfering beams involved are, respectively, (a) 6 + 1 beams, (b) 9 + 1 beams, and (c) 15 + 1 beams.

Figures 3(g)–3(i). By tuning the value of “ $p$ ,” we could design the lattice structures embedded with higher-order vortices, where, in the present case, the higher-order topological charge is directly proportional to the integer multiples of the relatively phase shifted three plane waves. This is being verified in Figures 2 and 3. Unlike the normal transversely

quasicrystallographic photonic lattice formation or photonic vortex lattice formation, in the case of this complex vortex lattice where  $p = 5$ , we get a variant of 15-fold transversely quasicrystallographic structure with a topological charge of charge 5 at the center. We have used five-fold multiple of three beams leading to a 15-beam configurations to realize

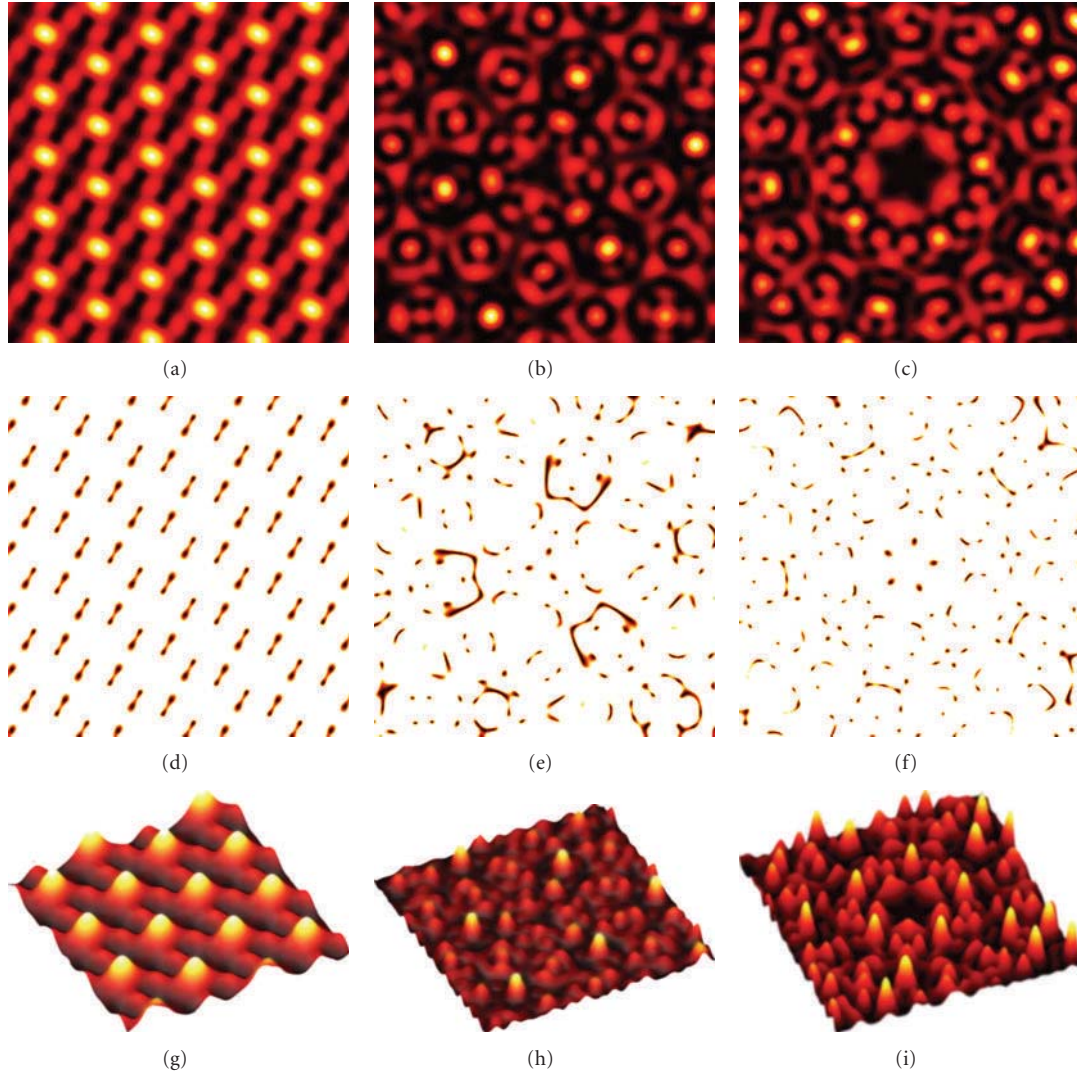


FIGURE 6: Computational analysis of complex 3D complex vortex lattices. Taking the multiples of relatively phase-shifted three beams, where the numbers of interfering beams involved are, respectively,  $6 + 1$  beams (first column),  $9 + 1$  beams (second column), and  $15 + 1$  beams (third column). (a)–(c) Intensity distribution in  $x$ - $y$  plane. (d)–(f) Intensity distribution with a lower threshold value in order to highlight the darker regions alone. (g)–(i) Intensity mesh plots.

this. These complex 2D vortex lattices could be further configured as spiraling vortex lattices in which photonic lattices embedded with vortex spirals could be formed.

#### 4. Complex 3D Spiraling Vortex Lattices: Unfolded Phase Dislocations

In order to generate complex 3D vortex lattices, we perturb the interference field with an axially launched plane wave as per the wave design formula for  $q + 1$  interfering beams given in (1). In the simplest case, by keeping  $p = 1$ , four plane wave interference including the axially launched central beam forms a 3D photonic lattice [23, 24] as depicted in Figure 4. As given in Figures 5, 6, and 7, with various analytical tools, the perturbing central beam “unfolds” the higher-order vortices into singly charged vortices of identical sign and shifts them away from their respective higher-order

vortex core centers [4, 32]. As shown in Figure 5, various 3D vortex lattices could be realized for varying values of  $p$ . In the spiraling vortex 3D photonic lattices as we have designed, a variant of 15-fold transversely quasicrystallographic vortex lattice could be unfolded into a variant of spiraling vortex transversely photonic quasicrystallographic lattice with a 5-fold symmetry distribution of bright lattice points spiraling with respect to the central axis. The identical sign of the unfolded single-charged vortices at the center is also verified by the direction of the multiple forks formed as given in Figures 8(a)–8(c). The complex spiral arms are formed while the generated photonic vortex lattice forming wave is superposed with a spherical wave (Figures 8(d)–8(f)). The interference intensity distribution of different planes along the  $z$ -direction clearly depicts the spiraling vortex lattice as given in Figure 9. As we move from one plane to another for varying values of “ $Z$ ” of a Cartesian coordinate

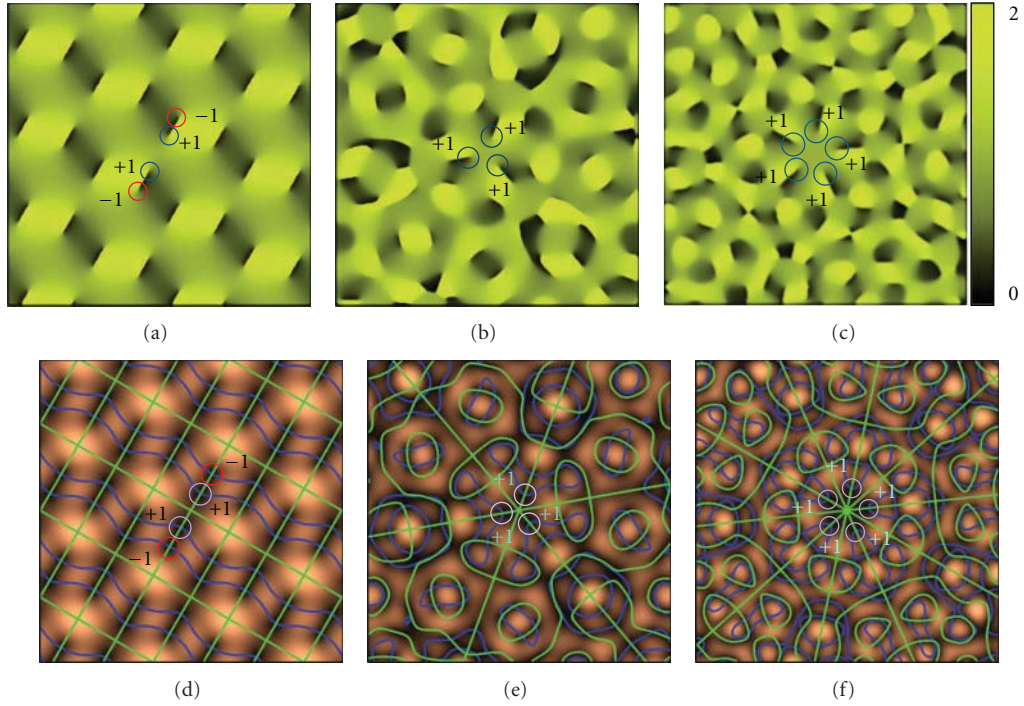


FIGURE 7: Computational analysis of complex 3D vortex lattices. Taking the multiples of relatively phase-shifted three beams, the numbers of interfering beams involved are, respectively, 6 beams (first column), 9 beams (second column), and 15 beams (third column). (a)–(c) Phase profile. (d)–(f) Zero crossing plot (blue line: zeros of  $\text{Re } E(r)$  and green line: zeros of  $\text{Im } E(r)$ ). Under perturbation, the unfolding and shifting of the vortices are clearly visible and circled to identify the position.

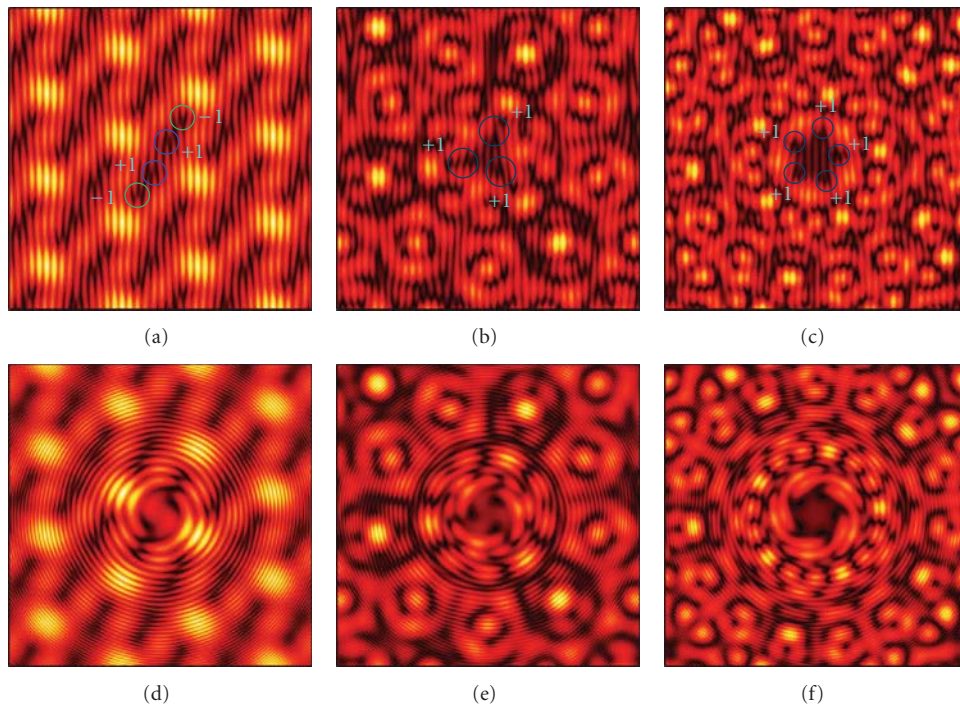


FIGURE 8: Analysis of presence of singularity in complex 3D vortex lattices. Taking the multiples of relatively phase-shifted three beams, the numbers of interfering beams involved are, respectively, 6 beams (first column), 9 beams (second column), and 15 beams (third column). (a)–(c) The fork formation, while the pattern is interfered with a plane wave launched at a large angle from the axis. (d)–(e) The spiral formation while the pattern is interfered with a spherical wave. The points of singularities are clearly visible as the signature of the presence of vortex distribution in the designed symmetry.

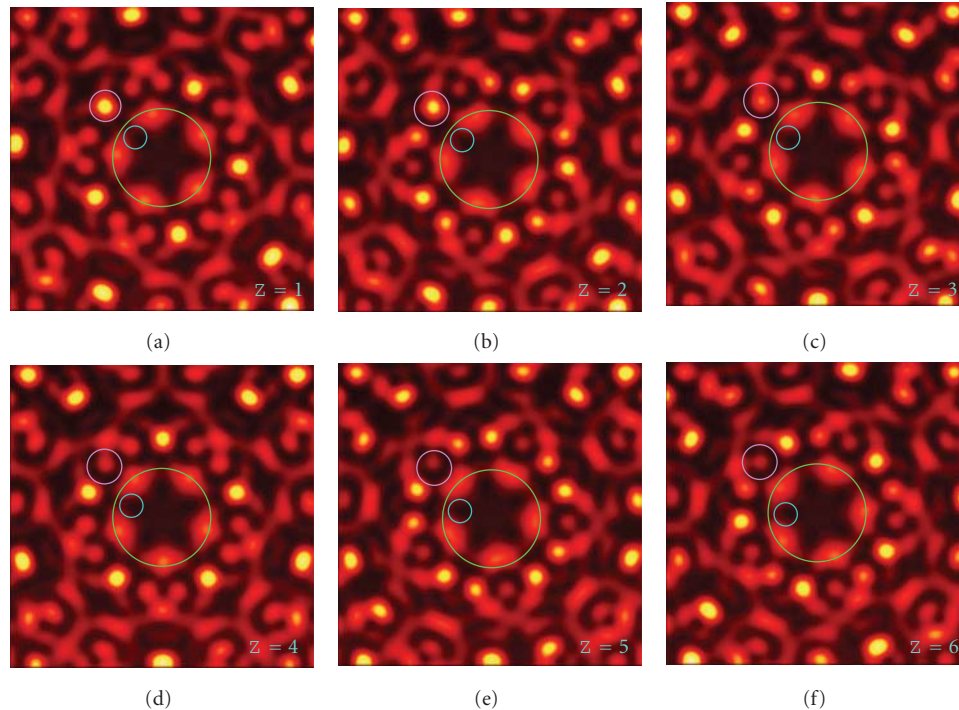


FIGURE 9: Computational analysis of spiraling complex 3D vortex lattice formed in the presence of a perturbing beam and a fivefold multiple of relatively phase-shifted three beams leading to  $15 + 1$  noncoplanar multiple beam interference. (a)–(f) The intensity distributions of  $x$ - $y$  planes while the value of “ $Z$ ” is varied along the direction of propagation. The circled region (cyan) visualizes the spiraling vortex distribution, and the circled region (magenta) depicts how the energy gets coupled to the adjacent region, while the complex vortex lattice structure makes a whirling movement along the direction of propagation.

system, the adjacent dark lattice points become bright as the lattice axially spirals. The spiraling vortices embedded in a centrally-intertwined 3D vortex lattice (Figure 5(c)) are depicted by slicing different  $x$ - $y$  planes as given in Figure 9. By tuning the values of  $p$ , we could even design higher-order transverse rotational symmetry spiraling 3D vortex lattice structures.

## 5. Conclusion

We have presented the formation of diverse complex 3D vortex lattices by a designed superposition of multiple plane waves. By means of multiples of relatively phase-engineered three plane waves, we have formed complex structures with designed phase dislocations. These complex 3D lattice structures carrying even spiraling vortices are computationally investigated with various computational analytical tools. These complex lattices embedded with higher-order topological loci of darkness in folded as well as unfolded forms are envisaged to find applications in various fields of photonics in all-optical high-density information processing, real-time tunable adaptive nulling interferometry, ultra-high-resolution microscopy [1], and so forth.

## References

- [1] D. L. Andrews, *Structured Light and Its Applications: An Introduction to Phase-Structured Beams and Nanoscale Optical Forces*, Academic Press, Waltham, Mass, USA, 2008.
- [2] Y. S. Kivshar and E. A. Ostrovskaya, “Optical vortices: folding and twisting waves of light,” *Optics and Photonics News*, vol. 12, no. 4, pp. 24–29, 2001.
- [3] I. Freund and N. Shvartsman, “Wave-field phase singularities: the sign principle,” *Physical Review A*, vol. 50, no. 6, pp. 5164–5172, 1994.
- [4] M. R. Dennis, K. O’Holleran, and M. J. Padgett, “Singular optics: optical vortices and polarization singularities,” *Progress in Optics*, vol. 53, pp. 293–363, 2009.
- [5] K. O’Holleran, M. J. Padgett, and M. R. Dennis, “Topology of optical vortex lines formed by the interference of three, four, and five plane waves,” *Optics Express*, vol. 14, no. 7, pp. 3039–3044, 2006.
- [6] L. G. Wang, L. Q. Wang, and S. Y. Zhu, “Formation of optical vortices using coherent laser beam arrays,” *Optics Communications*, vol. 282, no. 6, pp. 1088–1094, 2009.
- [7] A. Dreischuh, S. Chervenkov, D. Neshev, G. G. Paulus, and H. Walther, “Generation of lattice structures of optical vortices,” *Journal of the Optical Society of America B*, vol. 19, no. 3, pp. 550–556, 2002.
- [8] S. Vyas and P. Senthilkumaran, “Interferometric optical vortex array generator,” *Applied Optics*, vol. 46, no. 15, pp. 2893–2898, 2007.
- [9] G. Ruben and D. M. Paganin, “Phase vortices from a Young’s three-pinhole interferometer,” *Physical Review E*, vol. 75, no. 6, article 066613, 2007.
- [10] S. Vyas and P. Senthilkumaran, “Vortex array generation by interference of spherical waves,” *Applied Optics*, vol. 46, no. 32, pp. 7862–7867, 2007.
- [11] J. Masajada and B. Dubik, “Optical vortex generation by three plane wave interference,” *Optics Communications*, vol. 198, no. 1–3, pp. 21–27, 2001.

- [12] G. C. G. Berkhout and M. W. Beijersbergen, "Method for probing the orbital angular momentum of optical vortices in electromagnetic waves from astronomical objects," *Physical Review Letters*, vol. 101, no. 10, Article ID 100801, 2008.
- [13] J. Xavier and J. Joseph, "Tunable complex photonic chiral lattices by reconfigurable optical phase engineering," *Optics Letters*, vol. 36, no. 3, pp. 403–405, 2011.
- [14] V. Arrizón, D. Sánchez-De-La-Llave, G. Méndez, and U. Ruiz, "Efficient generation of periodic and quasi-periodic non-diffractive optical fields with phase holograms," *Optics Express*, vol. 19, no. 11, pp. 10553–10562, 2011.
- [15] Y. F. Chen, H. C. Liang, Y. C. Lin et al., "Generation of optical crystals and quasicrystal beams: kaleidoscopic patterns and phase singularity," *Physics Review A*, vol. 83, Article ID 053813, 4 pages, 2011.
- [16] K. J. H. Law, A. Saxena, P. G. Kevrekidis, and A. R. Bishop, "Stable structures with high topological charge in nonlinear photonic quasicrystals," *Physical Review A*, vol. 82, no. 3, Article ID 035802, 2010.
- [17] W. Wang, S. G. Hanson, Y. Miyamoto, and M. Takeda, "Experimental investigation of local properties and statistics of optical vortices in random wave fields," *Physical Review Letters*, vol. 94, no. 10, Article ID 103902, 2005.
- [18] D. Buccoliero, A. S. Desyatnikov, W. Krolikowski, and Y. S. Kivshar, "Spiraling multivortex solitons in nonlocal nonlinear media," *Optics Letters*, vol. 33, no. 2, pp. 198–200, 2008.
- [19] D. V. Freilich, D. M. Bianchi, A. M. Kaufman, T. K. Langin, and D. S. Hall, "Real-time dynamics of single vortex lines and vortex dipoles in a Bose-Einstein condensate," *Science*, vol. 329, no. 5996, pp. 1182–1185, 2010.
- [20] J. D. Joannopoulos, P. R. Villeneuve, and S. Fan, "Photonic crystals: putting a new twist on light," *Nature*, vol. 386, no. 6621, pp. 143–149, 1997.
- [21] K. Busch, S. Loelkes, R. B. Wehrspohn, and H. Foell, *Photonic Crystals: Advances in Design, Fabrication, and Characterization*, Wiley-VCH, Weinheim, Germany, 2004.
- [22] T. Kondo, S. Juodkazis, V. Mizeikis, H. Misawa, and S. Matsuo, "Holographic lithography of periodic two- and three-dimensional microstructures in photoresist SU-8," *Optics Express*, vol. 14, no. 17, pp. 7943–7953, 2006.
- [23] J. Xavier, P. Rose, B. Terhalle, J. Joseph, and C. Denz, "Three-dimensional optically induced reconfigurable photorefractive nonlinear photonic lattices," *Optics Letters*, vol. 34, no. 17, pp. 2625–2627, 2009.
- [24] C. Lu and R. H. Lipson, "Interference lithography: a powerful tool for fabricating periodic structures," *Laser and Photonics Reviews*, vol. 4, no. 4, pp. 568–580, 2010.
- [25] J. Xavier, M. Boguslawski, P. Rose, J. Joseph, and C. Denz, "Reconfigurable optically induced quasicrystallographic three-dimensional complex nonlinear photonic lattice structures," *Advanced Materials*, vol. 22, no. 3, pp. 356–360, 2010.
- [26] L. Z. Cai, X. L. Yang, and Y. R. Wang, "All fourteen Bravais lattices can be formed by interference of four noncoplanar beams," *Optics Letters*, vol. 27, no. 11, pp. 900–902, 2002.
- [27] A. Dwivedi, J. Xavier, J. Joseph, and K. Singh, "Formation of all fourteen Bravais lattices of three dimensional photonic crystal structures by a dual beam multiple-exposure holographic technique," *Applied Optics*, vol. 47, no. 12, pp. 1973–1980, 2008.
- [28] L. Paterson, M. P. MacDonald, J. Arlt, W. Sibbett, P. E. Bryant, and K. Dholakia, "Controlled rotation of optically trapped microscopic particles," *Science*, vol. 292, no. 5518, pp. 912–914, 2001.
- [29] M. Wegener and S. Linden, "Shaping optical space with metamaterials," *Physics Today*, vol. 63, no. 10, pp. 32–36, 2010.
- [30] E. Serabyn, D. Mawet, and R. Burruss, "An image of an exoplanet separated by two diffraction beamwidths from a star," *Nature*, vol. 464, no. 7291, pp. 1018–1020, 2010.
- [31] P. Senthilkumaran, F. Wyrowski, and H. Schimmel, "Vortex Stagnation problem in iterative Fourier transform algorithms," *Optics and Lasers in Engineering*, vol. 43, no. 1, pp. 43–56, 2005.
- [32] G. Indebetouw, "Optical vortices and their propagation," *Journal of Modern Optics*, vol. 40, no. 1, pp. 73–87, 1993.

## Research Article

# Generation of a Purely Single Transverse Mode Vortex Beam from a He-Ne Laser Cavity with a Spot-Defect Mirror

Ken Kano, Yuichi Kozawa, and Shunichi Sato

*Institute of Multidisciplinary Research for Advanced Materials, Tohoku University, Katahira 2-1-1, Aoba-ku, Sendai 980-8577, Japan*

Correspondence should be addressed to Ken Kano, [kkano@mail.tagen.tohoku.ac.jp](mailto:kkano@mail.tagen.tohoku.ac.jp)

Received 7 June 2011; Accepted 3 August 2011

Academic Editor: Paramasivam Senthilkumaran

Copyright © 2012 Ken Kano et al. This is an open access article distributed under the Creative Commons Attribution License, which permits unrestricted use, distribution, and reproduction in any medium, provided the original work is properly cited.

Spot-defect mirrors were fabricated by focusing laser pulses on the surface of conventional dielectric mirrors. These mirrors were used as rear mirrors of a He-Ne laser cavity for generating a vortex beam. The intensity distribution of the beam generated from the cavity with a spot diameter of  $50\ \mu\text{m}$  was in excellent agreement with theory. Comprehensive analysis of the intensity distribution, the beam quality factor, and the interference pattern revealed that the beam obtained was a purely single transverse mode  $\text{LG}_{01}$  beam.

## 1. Introduction

Laguerre-Gaussian (LG) beams have been highlighted due to its dominant feature of carrying optical angular momenta in singular optics [1]. They have brought about many applications such as optical spanners for driving micro-machines, quantum information processing [2], super-resolution microscopy [3], and microneedle fabrication [4]. To enhance the validity of these applications, the generation of a stable and high-quality LG mode beam is inevitable.

LG beams can be produced by extracavity methods such as a mode converter composed of a pair of cylindrical lenses [5], computer-generated holograms [6–8], diffractive optics [9], an adaptive helical mirror [10], and a spatial light modulator [11]. However, the misalignment and the imperfection of the optical elements gave rise to the degradation of LG beams. By contrast, direct generation from a laser cavity is expected to improve the beam quality due to an inherent feedback effect in the cavity. Although many attempts have been reported, for example, a ring-shaped beam pumping [12], the thermal lensing effect in a diode-side-pumped bounce laser cavity [13], the insertion of a spiral phase plate [14], and the use of a circular absorber [15–17], most of them have merely reported the generation of the LG beam without a detailed evaluation of the beam purity and quality. Recently, we have demonstrated the generation of LG beams from a Nd:yttrium aluminum garnet (YAG) laser cavity

using a spot defect mirror [18]. This method is simple, robust, and applicable to many laser systems. In addition, a Gaussian mode will be strongly suppressed by properly choosing a diameter of the defect leading to the generation of a pure single transverse mode.

In this paper, we demonstrate the generation of a purely single transverse mode LG beam from a He-Ne laser cavity with a spot defect mirror. For mirrors with different spot diameters, comprehensive analysis was performed for the intensity distribution, the beam quality factor, and the observed interference pattern. The generation of a purely single transverse mode  $\text{LG}_{01}$  beam was verified.

## 2. Experimental Setup

Spot defect mirrors were fabricated by focusing Ti:Sapphire laser pulses near the surface of a conventional dielectric multilayer mirror. A circular part of the multilayer coating on the mirror surface was ablated to create a spot defect with low reflectivity. By changing the distance between the mirror surface and the focus, spot defects with different diameter  $d$ , of 13, 20, and  $50\ \mu\text{m}$  were fabricated. Figure 1(a) shows a photograph of the fabricated spot defect mirror. A small spot defect exists in the center of the mirror though it is hardly recognized in the photograph. The inset of Figure 1(a) is a reflective optical microscope image of the defect on the mirror surface fabricated by pulsed laser irradiation. The

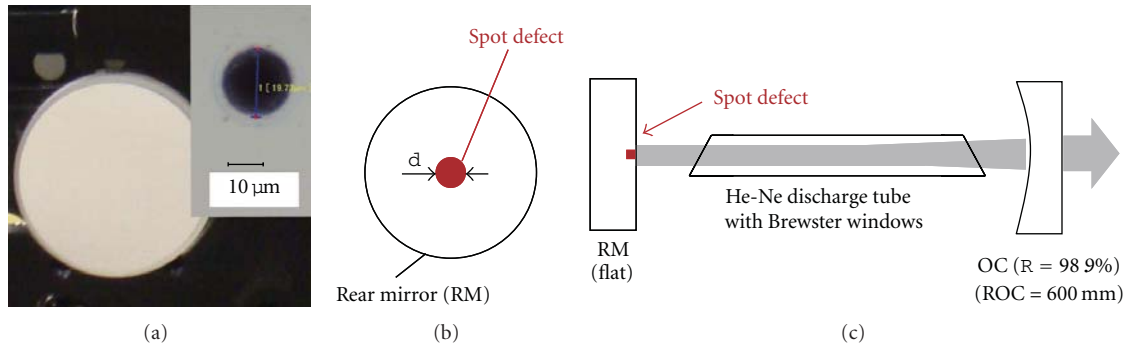


FIGURE 1: (a) A photograph of the fabricated spot defect mirror. The inset is a reflective optical microscope image of the mirror surface with a spot defect diameter of  $20\ \mu\text{m}$ . Schematics of the spot defect mirror (b) and the He-Ne laser cavity (c).

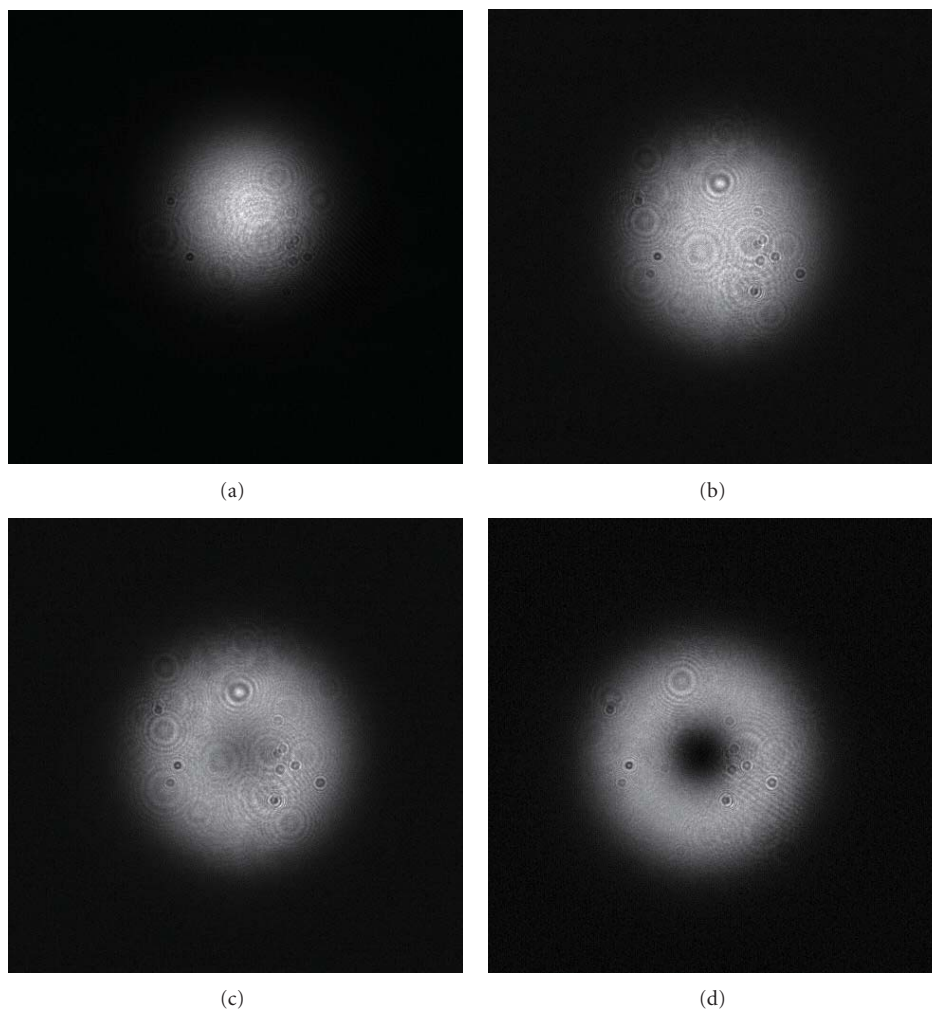


FIGURE 2: Intensity distributions of the generated beams for different spot defect diameters  $d$  of (a)  $0\ \mu\text{m}$ , (b)  $13\ \mu\text{m}$ , (c)  $20\ \mu\text{m}$ , and (d)  $50\ \mu\text{m}$ .

spot is a nearly perfect circle with a diameter of  $20\ \mu\text{m}$ . The shape of other spot defects has similar circularity.

Figure 1(b) illustrates a schematic of the spot defect mirror, which was used as a rear mirror (RM) of a He-Ne laser cavity as shown in Figure 1(c). The RM was mounted on

an X-Y mechanical stage. The cavity length and the distance between the RM and a discharge tube (length:  $192\ \text{mm}$ ; inner diameter:  $3.7\ \text{mm}$ ; terminated by Brewster windows) were  $300\ \text{mm}$  and  $78\ \text{mm}$ , respectively. The radius of curvature ROC and the reflectance  $R$  of an output coupler (OC)

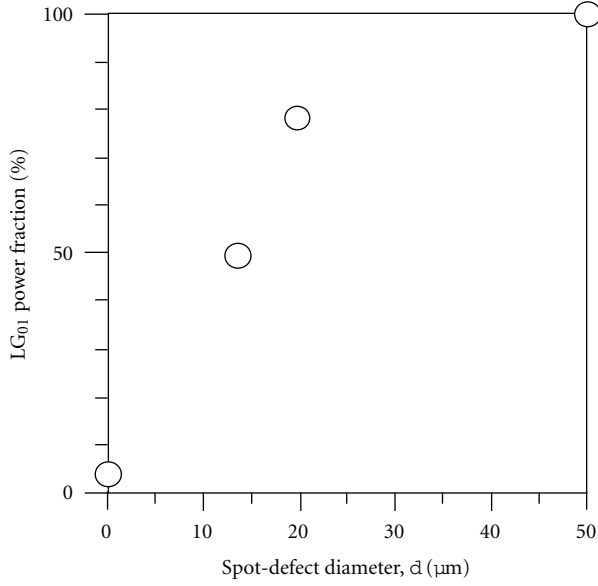


FIGURE 3: LG<sub>01</sub> power fractions for different spot defect diameters  $d$  (open circles).

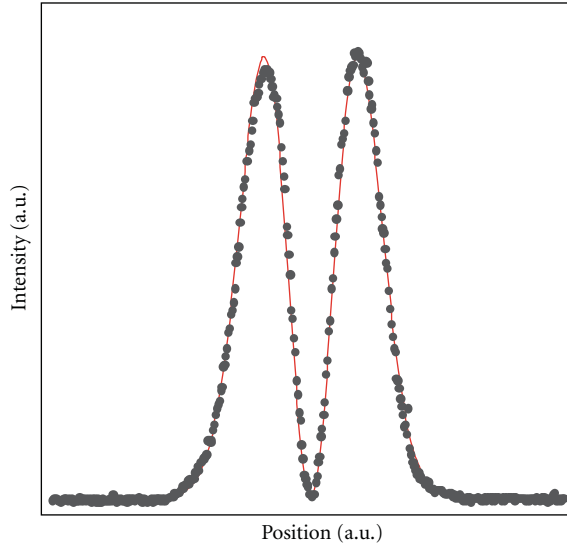


FIGURE 4: A cross-section of the intensity distribution of the beam for  $d = 50 \mu\text{m}$ . Dotted lines and a red solid curve indicate the measured data and fitting result, respectively.

were 600 mm and 98.9%, respectively. Intensity distributions of the laser beams were recorded by a beam profiler. Polarization was verified from the intensity distributions after passing through a linear polarizer. Optical power was measured by an optical power meter.

To align the spot defect just on the cavity axis, the position of the RM was adjusted in the following procedure. First, a normal laser oscillation without a spot defect was achieved by putting the spot defect off the cavity axis. Then, the mirror was carefully moved to make the center of the spot defect coincide with the cavity axis. When the center of the spot defect is exactly on the cavity axis, the generated

beam pattern drastically changed. This procedure was readily conducted by manually translating the X-Y mechanical stage.

Note that the spot defect located on the beam axis is expected to readily generate a doughnut-like beam [18]. In addition, the Brewster plate inside a He-Ne laser cavity ensures the linear polarization. Under this condition, the most probable beam is a linearly polarized LG beam with an optical vortex.

### 3. Results and Discussion

Figure 2 shows the intensity distributions of the generated beams for different  $d$ . Note that all the beams were linearly polarized in the horizontal direction owing to the Brewster windows of the discharge tube. Without a spot defect ( $d = 0 \mu\text{m}$ ), a Gaussian beam was obtained as shown in Figure 2(a). With increasing  $d$ , the intensity distribution changed to doughnut shape as shown in Figures 2(b)–2(d) due to the stronger suppression of a Gaussian mode by a larger spot defect. The output power was 1.0 mW except for the case without a spot defect (1.5 mW).

To evaluate the transverse mode purity of the generated laser beam, two-dimensional fitting analysis to the recorded intensity distribution was performed. A superposition of theoretical intensity distributions of a Gaussian [ $I_{00}(x, y)$ ] and LG<sub>01</sub> mode [ $I_{01}(x, y)$ ] was adopted as a fitting function  $I(x, y)$  and is given by

$$I(x, y) = C_{00} I_{00}(x, y) + C_{01} I_{01}(x, y) + \text{BG}, \quad (1)$$

where  $C_{00}$  and  $C_{01}$  represent power fractions of a Gaussian and a LG<sub>01</sub> mode beam, respectively, and BG is background intensity. An intensity distribution of a LG <sub>$pm$</sub>  mode beam is the square of the absolute value of its complex amplitude, which is expressed in the cylindrical coordinate ( $r, \theta, z$ ) as

$$\begin{aligned} u_{pm}(r, \theta, z) = & \sqrt{\frac{2p!}{\pi(|m|+p)!}} \frac{1}{w(z)} \times \left( \sqrt{2} \frac{r}{w(z)} \right)^{|m|} \\ & \times L_p^{|m|} \left( \frac{2r^2}{w^2(z)} \right) \exp\left( -\frac{r^2}{w^2(z)} \right) \\ & \times \exp\left( -\frac{ikr^2}{2R(z)} - ikz - im\theta \right. \\ & \left. + i(2p + |m| + 1)\Psi(z) \right), \end{aligned} \quad (2)$$

where  $p$  and  $m$  are the radial and azimuthal mode indices, respectively.  $k$  is the wave number and  $w(z)$  is the Gaussian beam width defined as  $w(z) = w_0 \sqrt{1 + (z/z_R)^2}$ , with the minimum beam radius  $w_0$  at  $z = 0$  and the Rayleigh length  $z_R = kw_0^2/2$ .  $R(z) = z + (z_R^2/z)$  is the wave-front radius of curvature,  $(2p + |m| + 1)\Psi(z)$  is the Gouy phase shift with  $\Psi(z) = \arctan(z/z_R)$ , and  $L_p^{|m|}$  is the generalized Laguerre polynomial. Note that fitting analysis was performed in the Cartesian coordinate system. Complex amplitude  $u_{pm}(r, \theta)$  was transformed into  $u_{pm}(x, y)$  by using following relationships  $x = r \cos(\theta)$  and  $y = r \sin(\theta)$ . By the two-dimensional fitting, the parameters including  $C_{00}$ ,  $C_{01}$ , BG,

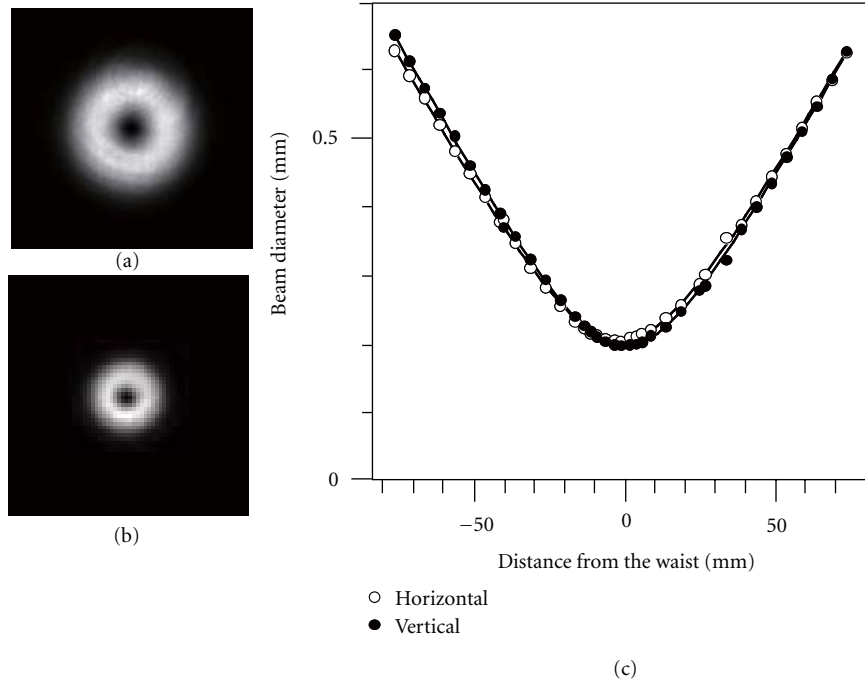


FIGURE 5: Recorded intensity distributions (a) before the waist by 4 times of Rayleigh length and (b) at the waist, respectively. (c) The variations of the beam diameters as a function of the distance from the waist. Open and filled circles indicate the horizontal and vertical beam widths, respectively. Fitting curves are depicted by solid lines.

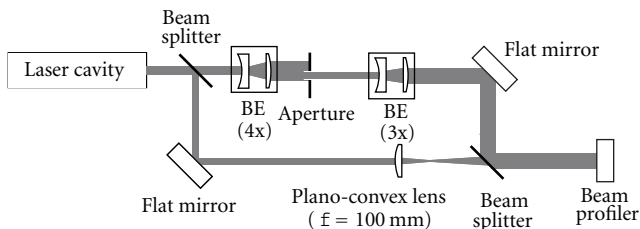


FIGURE 6: Optical schematic of the Mach-Zehnder interferometer.

center position, and the beam radius were determined. Two-dimensional analysis enables direct and rigorous comparison between the theoretical profiles and the observed patterns avoiding ambiguity caused by an intentional selection of an intensity profile for the one-dimensional fitting. Figure 3 shows the  $LG_{01}$  power fraction estimated by  $C_{01}/(C_{00}+C_{01})$  as a function of  $d$ . The  $LG_{01}$  power fraction was about 4% for  $d = 0 \mu\text{m}$ . With increasing  $d$ , the  $LG_{01}$  power fraction increased and reached 99.99% for  $d = 50 \mu\text{m}$ . Note that the selection of proper size of the spot defect is important to eliminate a Gaussian mode component.

Figure 4 shows a typical intensity distribution profile for  $d = 50 \mu\text{m}$  (dotted lines) and the fitting curve of a theoretical  $LG_{01}$  mode (red solid line). The profile was in excellent agreement with that of a  $LG_{01}$  mode beam. Note that the intensity on the beam axis was almost zero meaning that a Gaussian mode component was negligibly small. A small difference of the peak height between two lobes may arise from the residual misalignment of the laser cavity mirrors.

Theoretical values of beam quality factor  $M^2$  are 1 and 2 for Gaussian and  $LG_{01}$  mode beams, respectively. The value is between 1 and 2 when a laser beam contains both Gaussian and  $LG_{01}$  components. The  $M^2$  of the beam generated for  $d = 50 \mu\text{m}$  was measured by using a planoconvex lens with a focal length  $f$  of 250 mm. Recorded images of the beam cross-section before the waist by 4 times of Rayleigh length and at the waist are shown in Figures 5(a) and 5(b), respectively. The doughnut-shaped pattern was maintained throughout the focusing suggesting that the beam is an eigen mode. Figure 5(c) shows the variations of the beam diameter along the horizontal (open circle) and vertical (filled circle) axes as a function of the distance from the waist. Fitting curves are depicted by solid curves. Both of the beam quality factors for the horizontal and vertical axes were determined to 2.0. This value is exactly the same with the theoretical value for a  $LG_{01}$  mode beam.

The phase structure (spiral phase front) of the beam generated for  $d = 50 \mu\text{m}$  was confirmed by measuring an interference pattern with a reference plane wave using a Mach-Zehnder interferometer. Figure 6 shows a schematic of a Mach-Zehnder interferometer. The output beam from the He-Ne laser cavity with a spot defect was divided into two beams by a beam splitter. The upper beam shown in Figure 6 was expanded by a beam expander (BE) with a pair of lenses, clipping a small portion of the beam through a small aperture and then expanded again by a BE to generate a reference plane wave. At the camera position, the reference beam had a Gaussian-like intensity distribution with some fringes due to diffraction by the aperture. In the lower arm,

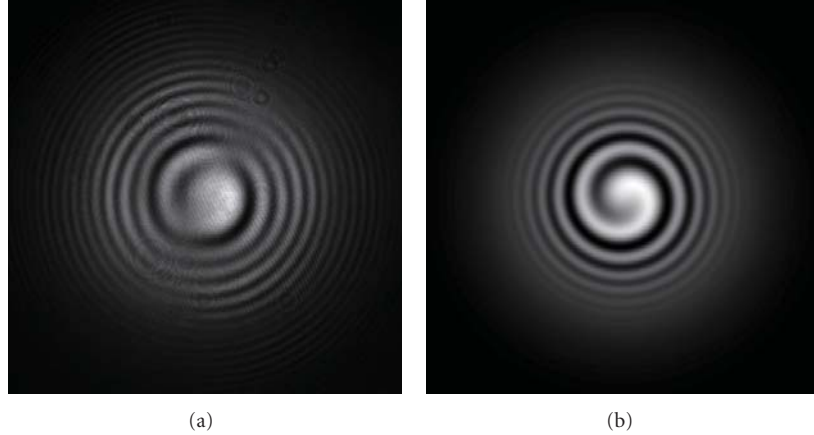


FIGURE 7: (a) Measured interference pattern between the beam generated for  $d = 50 \mu\text{m}$  and a plane reference wave. (b) Calculated interference pattern between corresponding beams to (a).

the wave front of the signal wave was converted to a spherical one by a planoconvex lens with  $f = 100 \text{ mm}$ . Figure 7(a) shows the observed interference pattern. Figure 7(b) depicts a calculated interference pattern of an ideal spherical  $\text{LG}_{01}$  mode beam with a collimated Gaussian beam. The interference fringe becomes obscure beyond the first three rings in Figure 7 (b) due to the inherent mismatch of intensity distributions between a doughnut-shaped  $\text{LG}_{01}$  mode beam and a Gaussian beam. The comparison of Figures 7(a) and 7(b) strongly suggests that the beam generated for  $d = 50 \mu\text{m}$  is a purely single transverse  $\text{LG}_{01}$  mode beam with the phase dependence of  $\exp(-i\theta)$ , namely, the topological charge of 1. The imperfection of the contrast of the interference pattern and the continuity of the spiral in Figure 7(a) compared with Figure 7(b) may be attributed to the distortion of the reference wave generated by clipping a small portion of the  $\text{LG}_{01}$  mode beam through many optical elements as shown in Figure 6.

The comparison of power fraction of  $\text{LG}_{01}$  mode to higher order modes may be suitable to discuss the mode purity of the beam generated in this experiment. The power fractions of  $\text{LG}_{01}$  mode generated by using a computer-generated hologram and diffractive optics have been reported to be 93% [8] and 92.9% [9], respectively. Following Kennedy et al. [9], the power fraction in our case was calculated to be 96.5%, which is much higher than those ever reported indicating that the mode purity of the  $\text{LG}_{01}$  mode obtained in this experiment was quite high. In this calculation, higher order modes up to 6th order were considered.

The generated  $\text{LG}_{01}$  mode was quite stable. The doughnut-shaped intensity pattern was maintained over several hours. Mechanical vibrations produced in a normal laboratory resulted in no notable effects in our experimental condition in which the laser cavity was constructed on a vibration isolated table. The helicity of the  $\text{LG}_{01}$  beam mode was robust against a slight change of the alignment of the cavity mirrors. In addition, the  $\text{LG}_{01}$  beam with the same helicity was reproducibly generated after switching off and on the power source of the discharge or inserting an

obstacle into the cavity to stop the oscillation. The stability and reproducibility observed here have been reported for a Nd:YAG laser cavity with a spot defect mirror [18].

A beam radius  $w$  on the RM was estimated to be  $0.246 \text{ mm}$  by the  $ABCD$  matrix formalism. The ratio of the spot defect diameter ( $d = 50 \mu\text{m}$ ) to the beam diameter  $[= d/(2w)]$  was 0.102 in contrast to 0.207 observed for a Nd:YAG laser [18]. This difference can be attributed to the smaller gain of a He-Ne laser compared to a Nd:YAG laser.

#### 4. Conclusion

Spot defect mirrors with the diameters  $d$  of 13, 20, and  $50 \mu\text{m}$  were fabricated by focusing laser pulses on the surface of commercially available dielectric mirrors used as rear mirrors of a He-Ne laser cavity. With increasing  $d$ , the intensity distribution of the generated beam changed from a Gaussian beam to a doughnut-shaped pattern. The intensity distribution obtained for  $d = 50 \mu\text{m}$  was in excellent agreement with that of a  $\text{LG}_{01}$  mode beam. The beam quality factor also agreed well with the theoretical value of a  $\text{LG}_{01}$  beam mode. The spiral interference pattern indicates that the generated beam had an  $\exp(-i\theta)$  phase-front structure. By the careful analysis of the intensity distributions, the value of a beam quality factor, and observed interference pattern, the beam was verified to be a purely single transverse  $\text{LG}_{01}$  mode beam.

#### References

- [1] L. Allen, S. M. Barnett, and M. J. Padgett, *Optical Angular Momentum*, Institute of Physics, Bristol, UK, 2003.
- [2] S. Franke-Arnold, L. Allen, and M. Padgett, "Advances in optical angular momentum," *Laser and Photonics Reviews*, vol. 2, no. 4, pp. 299–313, 2008.
- [3] E. Rittweger, K. Y. Han, S. E. Irvine, C. Eggeling, and S. W. Hell, "STED microscopy reveals crystal colour centres with nanometric resolution," *Nature Photonics*, vol. 3, no. 3, pp. 144–147, 2009.

- [4] T. Omatsu, K. Chujo, K. Miyamoto et al., "Metal microneedle fabrication using twisted light with spin," *Optics Express*, vol. 18, no. 17, pp. 17967–17973, 2010.
- [5] M. W. Beijersbergen, L. Allen, H. E. L. O. van der Veen, and J. P. Woerdman, "Astigmatic laser mode converters and transfer of orbital angular momentum," *Optics Communications*, vol. 96, no. 1–3, pp. 123–132, 1993.
- [6] N. R. Heckenberg, R. McDuff, C. P. Smith, and A. G. White, "Generation of optical phase singularities by computer-generated holograms," *Optics Letters*, vol. 17, no. 3, pp. 221–223, 1992.
- [7] J. Arlt, K. Dholakia, L. Allen, and M. J. Padgett, "The production of multiringed Laguerre-Gaussian modes by computer-generated holograms," *Journal of Modern Optics*, vol. 45, no. 6, pp. 1231–1237, 1998.
- [8] M. A. Clifford, J. Arlt, J. Courtial, and K. Dholakia, "High-order Laguerre-Gaussian laser modes for studies of cold atoms," *Optics Communications*, vol. 156, no. 4–6, pp. 300–306, 1998.
- [9] S. A. Kennedy, M. J. Szabo, H. Teslow, J. Z. Porterfield, and E. R. I. Abraham, "Creation of Laguerre-Gaussian laser modes using diffractive optics," *Physical Review A*, vol. 66, no. 4, Article ID 43801, pp. 43801/1–43801/5, 2002.
- [10] D. P. Ghai, "Generation of optical vortices with an adaptive helical mirror," *Applied Optics*, vol. 50, no. 10, pp. 1374–1381, 2011.
- [11] N. Matsumoto, T. Ando, T. Inoue, Y. Ohtake, N. Fukuchi, and T. Hara, "Generation of high-quality higher-order Laguerre-Gaussian beams using liquid-crystal-on-silicon spatial light modulators," *Journal of the Optical Society of America A*, vol. 25, no. 7, pp. 1642–1651, 2008.
- [12] Y. F. Chen and Y. P. Lan, "Dynamics of the Laguerre Gaussian  $TEM_{0,l}^*$  mode in a solid-state laser," *Physical Review A*, vol. 63, no. 6, Article ID 063807, pp. 063807/1–063807/9, 2001.
- [13] S. P. Chard, P. C. Shardlow, and M. J. Damzen, "High-power non-astigmatic  $TEM_{00}$  and vortex mode generation in a compact bounce laser design," *Applied Physics B*, vol. 97, no. 2, pp. 275–280, 2009.
- [14] R. Oron, Y. Danziger, N. Davidson, A. A. Friesem, and E. Hasman, "Laser mode discrimination with intra-cavity spiral phase elements," *Optics Communications*, vol. 169, no. 1–6, pp. 115–121, 1999.
- [15] C. Tamm, "Frequency locking of two transverse optical modes of a laser," *Physical Review A*, vol. 38, no. 11, pp. 5960–5963, 1988.
- [16] L. E. Grin, P. V. Korolenko, and N. N. Fedotov, "Laser beams with a helical wavefront structure," *Optics and Spectroscopy*, vol. 73, no. 5, pp. 604–605, 1992.
- [17] M. Harris, C. A. Hill, and J. M. Vaughan, "Optical helices and spiral interference fringes," *Optics Communications*, vol. 106, no. 4–6, pp. 161–166, 1994.
- [18] A. Ito, Y. Kozawa, and S. Sato, "Generation of hollow scalar and vector beams using a spot-defect mirror," *Journal of the Optical Society of America A*, vol. 27, no. 9, pp. 2072–2077, 2010.

## Research Article

# Generation of Optical Vortices by Linear Phase Ramps

**Sunil Vyas**

*Institute of Multidisciplinary Research for Advanced Materials, Tohoku University, Katahira 2-1-1, Aoba-ku, Sendai 980-8577, Japan*

Correspondence should be addressed to Sunil Vyas, sunilk\_vyas@yahoo.com

Received 11 May 2011; Accepted 17 July 2011

Academic Editor: Paramasivam Senthilkumaran

Copyright © 2012 Sunil Vyas. This is an open access article distributed under the Creative Commons Attribution License, which permits unrestricted use, distribution, and reproduction in any medium, provided the original work is properly cited.

Generation of optical vortices using linear phase ramps is experimentally demonstrated. When two regions of a wavefront have opposite phase gradients then along the line of phase discontinuity vortices can be generated. It is shown that vortices can evolve during propagation even with the unequal magnitude of tilt in the two regions of the wavefront. The number of vortices and their location depend upon the magnitude of tilt. Vortex generation is experimentally realized by encoding phase mask on spatial light modulator and their presence is detected interferometrically. Numerical simulation has been performed to calculate the diffracted intensity distribution from the phase mask, and presence of vortices in the diffracted field is detected by computational techniques.

## 1. Introduction

Optical fields possessing phase singularities or wavefront dislocations have received great deal of attention in recent years because of their fascinating properties and potential applications. The study of phenomena associated with phase singularities has generated a new branch of physical optics called singular optics, which reveals their basic properties and possible applications. Phase singularities also known as optical vortices are the points where the real and imaginary part of wave function vanishes. At phase singular points amplitude is zero and the phase is indeterminate. As a result, the wave front acquires the shape of helicoids, causing the precession of the Poynting vector. Nye and Berry showed that vortices in scalar field are strongly connected with the phase discontinuities or singularities [1]. Near the dislocation centers the phase gradients line is found to form closed vortex-like structures. Optical vortices can appear spontaneously or can be created in one of several ways, such as by the manipulation of laser cavity [2], transforming Gaussian beams into helical beams [3], computer generated holograms [4], cylindrical lenses [5], and spiral phase plates [6]. In recent years several important applications of optical vortices have been demonstrated. For example vortices have been used in optical tweezers [7], wave guiding [8], astronomy as coronagraph [9], optical testing [10], and so forth.

In this paper, experimental and simulation studies are performed to show the formation of vortices along the line of phase discontinuity which arises due to the different phase gradients in the wavefront. To explain the concept of vortex evolution we first discussed a simple case in which the two parts of the wavefront are given equal and opposite phase variations. Diffracted field is analyzed for the vortex evolution using experiments and numerical simulation. Various cases of tilt combinations are also discussed in which the different parts of the wavefront have different magnitude of the phase variations. To check the presence of vortices computational and interferometric techniques have been used. In experiments spatial light modulator is used to provide opposite constant phase gradients of small magnitude at two different regions of the wavefront. It is shown that the generation of single vortex and linear array of vortices using this method is possible. The major advantage of this method is that a vortex of unit charge having phase variation of  $2\pi$  can be comfortably realized by the SLM that can retard wavefront between  $\pi$  and  $2\pi$ .

## 2. Study of Phase Gradients

*2.1. Tilted Plane Wave.* A unit amplitude plane wave with tilt is given by

$$\psi = \exp\{j2\pi(\alpha x + \beta y + \gamma z)\}, \quad (1)$$

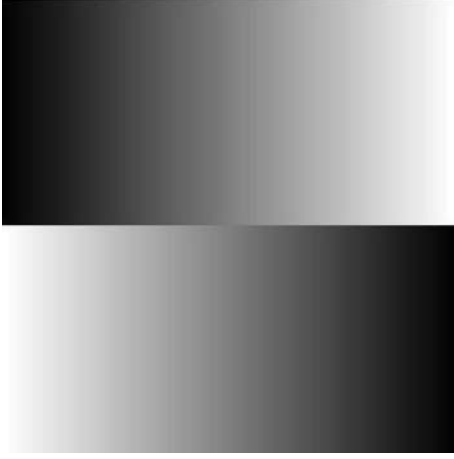


FIGURE 1: Two linear phase variations in equal and opposite directions in the upper and the lower regions of the wavefront.

where  $\alpha$ ,  $\beta$ , and  $\gamma$  are spatial frequencies along  $x$ ,  $y$ , and  $z$  directions, respectively.  $\lambda$  is wavelength of light.

The phase gradient for a tilted wavefront is

$$\nabla\phi = 2\pi(\alpha\hat{x} + \beta\hat{y} + \gamma\hat{z}). \quad (2)$$

Transverse components of phase gradient for tilted plane wave are given by

$$\nabla_{\perp}\phi = 2\pi(\alpha\hat{x} + \beta\hat{y}). \quad (3)$$

Unlike an optical vortex, here the phase gradient is constant and does not depend on the location.

**2.2. Wavefronts with Equal and Opposite Tilts.** Consider the case when the two regions in the wavefront have equal and opposite phase variations and the maximum phase variation of the two regions of wavefront is restricted to  $\leq 2\pi$ . These two regions are separated by a line of phase discontinuity. The complex amplitude in the two regions is given by

$$\psi = \begin{cases} \exp(2\pi\alpha x) & \text{when } y > 0 \\ \exp\{2\pi\alpha(1-x)\} & \text{when } y < 0, \end{cases} \quad (4)$$

where  $\alpha$  is a constant which decides the slope of the phase variation across the wavefront. If the wavefront is tilted by angle  $\theta$ , then  $\alpha = \sin\theta/\lambda$  and  $\lambda$  is the wavelength of light used. There is a line of phase discontinuity at  $y = 0$ . Figure 1 shows the linear phase distribution of function  $\psi_1$ . Tilt  $\alpha$  gives rate at which the linear phase variation occurs across the beam. Experimentally realizing such small phase variation is easier by using SLM. Detailed study of phase distribution and gradient of phase around the points where the vortices can be evolved is given in [11]. The main objective of this work is to explore the new wavefront tilt configurations for vortex generation.

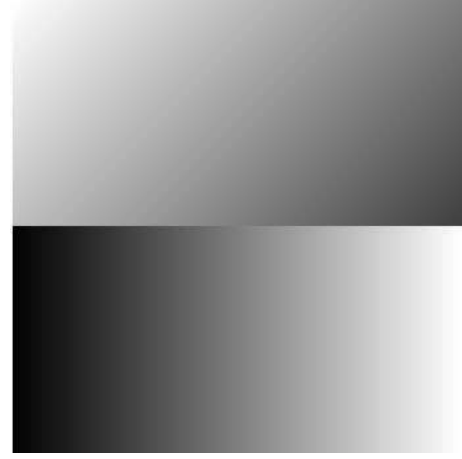


FIGURE 2: Phase distribution of two wavefronts with unequal and opposite tilts.

**2.3. Wavefronts with Unequal and Opposite Tilts.** Consider the case when two regions of the wavefront is having unequal and opposite tilts. The complex field can be given as

$$\psi = \begin{cases} \exp(j2\pi\alpha_1 x) & \text{when } y \geq 0 \\ \exp(j2\pi\alpha_2(1-x)) & \text{when } y \leq 0. \end{cases} \quad (5)$$

The out-of-phase condition for the neighborhood points is well met when opposite phase gradients are present. In this case the  $\Delta\phi = \pm\pi$  condition can occur at locations along the line of phase discontinuity  $y = 0$ , whose  $x$  coordinates can be given by

$$\begin{aligned} x_0 &= \frac{1 + 2\alpha_2}{2(\alpha_1 + \alpha_2)}, \\ x_1 &= \frac{1 - 2\alpha_2}{2(\alpha_1 + \alpha_2)}. \end{aligned} \quad (6)$$

One can see the position of points  $x_0$  and  $x_1$  has changed when compared with that of previous configuration of wavefront tilts. Figure 2 shows the phase distribution corresponding to tilt equation (5), where  $\alpha_1$  and  $\alpha_2$  are constants with different values.

**2.4. New Configurations of Phase Structures for Vortex Generation.** In the previous cases the phase gradients in the upper and lower parts of the beam point to opposite directions. It is also possible to generate vortices with other configurations of wavefront tilts. To do this let us consider complex field given by

$$\psi(x, y) = \begin{cases} \exp\{j2\pi(\alpha_1 x + \beta_1 y)\} & \text{for } y > 0 \\ \exp\{j2\pi(1 - (\alpha_2 x + \beta_2 y))\} & \text{for } y < 0. \end{cases} \quad (7)$$

In the neighborhood of the phase discontinuity line  $y = 0$ , if the  $x$ -components of the phase gradients are opposite in  $y > 0$  and  $y < 0$  regions, it is possible to generate vortices.  $\beta_1$  and  $\beta_2$  are constants.

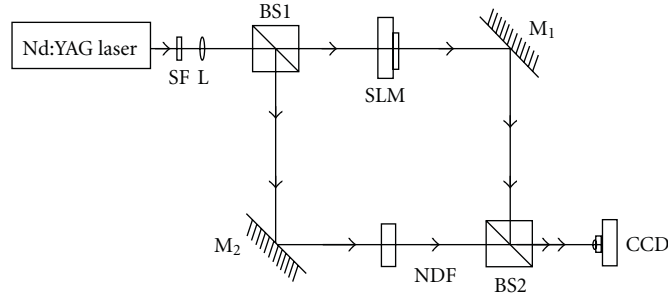


FIGURE 3: Mach-Zehnder interferometer. SF: spatial filter, BS1 and BS2: beam splitters, L: lens,  $M_1$  and  $M_2$ : mirrors, NDF: neutral density filter, CCD: camera, and SLM: spatial light modulator assembly.

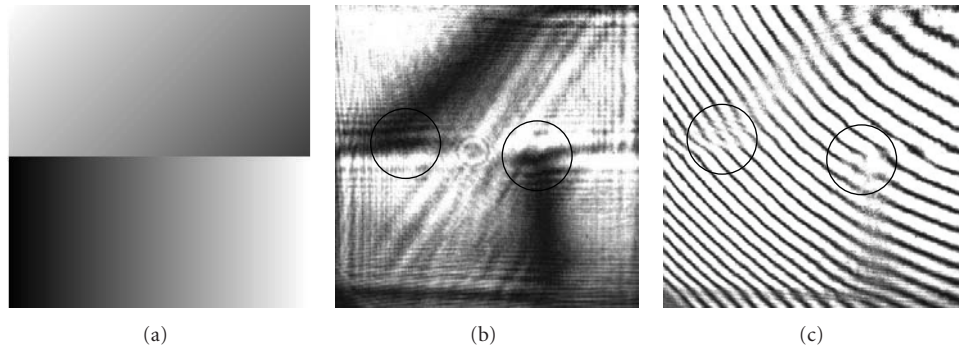


FIGURE 4: (a) Phase distribution for one oblique and one linear phase ramp. (b) Experimentally observed intensity distribution of propagated field when phase mask corresponding to (a) is displayed onto the SLM. (c) Formation of fork fringes when the propagated field interferes with a plane wave coming from the other arm of the Mach-Zehnder interferometer.

### 3. Experimental

Experiments have been performed to demonstrate the validity of the proposed approach. Optical setup used is shown in Figure 3 in which a Mach-Zehnder interferometer has been used. Output beam of linearly polarized light from a diode pumped solid-state (DPSS) Nd:Yag laser at  $532\text{ nm}$  is spatially filtered, expanded, and collimated by spatial filter and collimating lens, respectively. This light is incident on beam splitter BS1. It splits the incident beam into two parts. One beam is reflected by the mirror  $M_1$ , which is served as reference beam. The other beam illuminates a programmable spatial light modulator (Holoeye LC-2002 with  $832 \times 624$  numbers of pixel and pixel pitch  $32\ \mu\text{m}$ ) which is operated in phase modulation mode. SLM in phase modulation mode acts like a phase only diffractive optical element. The desired local tilt in the different parts of the wavefront is created by designing the phase mask as grey level images. When the phase masks are encoded onto the SLM and illuminated with the light, it will diffract the light into the different orders. The superposition of the diffracted light from the SLM and the reference plane wave produces interference fringes. To enhance the quality of the interference fringes a neutral density filter is used which makes the amplitude of the reference wave equal to that of the vortex beam.

### 4. Experimental Results

In [11] the phase gradients in the upper and lower parts of the beam point are in opposite directions. In the neighborhood of the phase discontinuity line  $y = 0$ , if the  $x$ -components of the phase gradients are opposite in  $y > 0$  and  $y < 0$  regions, it is possible to generate vortices. Some of the following tilt configurations can generate vortex arrays.

*4.1. One Oblique and One Linear Phase Ramp.* In this configuration two phase ramps are grouped, one is the slanted and the other is linear as shown in Figure 4(a). The phase distribution in Figure 4 can be obtained by putting  $\alpha_1 \neq 0$ ,  $\beta_1 \neq 0$ , and  $\beta_2 = 0$  in (5). Vortices are positioned at the point where the component of gradient of phase of the slanted wavefront cancels the phase gradient of the linear phase variation. Formation of vortices can be seen as the fork fringes where the exact phase cancellation occurs. It reveals the fact that even if one of the two parts of the wavefront has the different orientation then vortex formation is also possible.

The complex field corresponding to Figure 4(a) is displayed on the SLM, and the intensity distribution obtained is shown in Figure 4(b) which contains two vortices as the interference pattern in Figure 4(c) reveals.

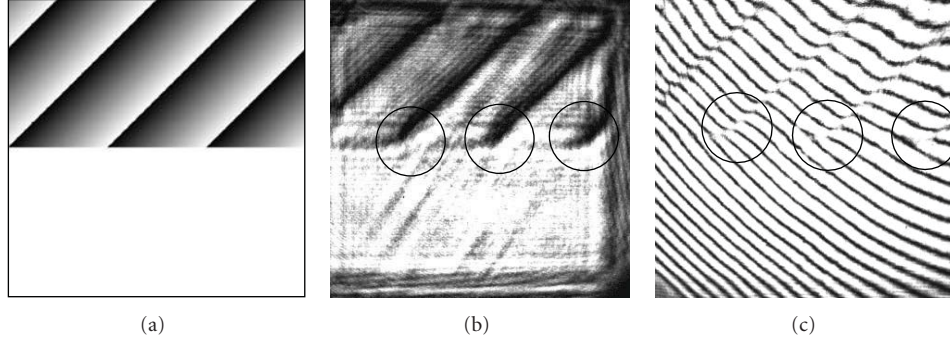


FIGURE 5: (a) Phase distribution for linear array of inclined phase ramps with constant background. (b) Experimentally observed intensity distribution of propagated field when phase mask corresponding to (a) is displayed onto the SLM. (c) Formation of fork fringes when the propagated field interferes with a plane wave coming from the other arm of the Mach-Zehnder interferometer.

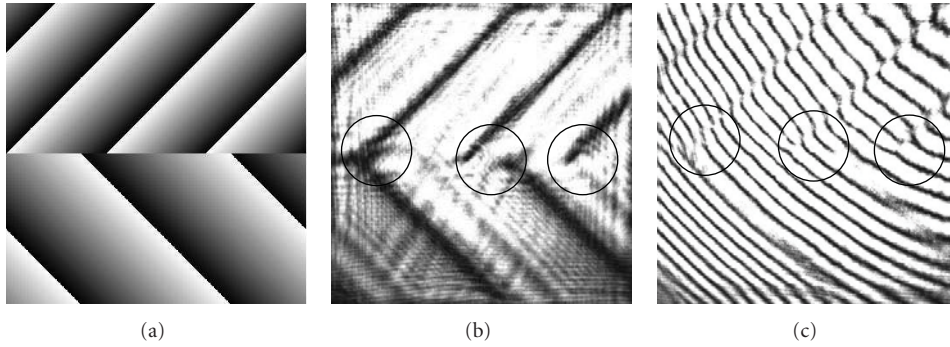


FIGURE 6: (a) Phase distribution for oppositely inclined linear phase ramps with different tilts. (b) Experimentally observed intensity distribution of propagated field when phase mask corresponding to (a) is displayed onto the SLM. (c) Formation of fork fringes when the propagated field interferes with a plane wave coming from the other arm of the Mach-Zehnder interferometer.

**4.2. Linear Array of Inclined Phase Ramps with Constant Background.** In this configuration linear array of vortices is produced by wavefront which has only one part inclined and the other part having constant phase. This case is similar to the case of linear array discussed previously [12]. In this case the number of phase ramps will determine the number of vortices and the slope of the phase ramp will determine the position of vortices.

To obtain phase distribution corresponding to Figure 5(a)  $\alpha_1 \neq 0$ ,  $\beta_1 \neq 0$ , and  $\alpha_2 = \beta_2 = 0$  are needed. Experimentally observed intensity distribution of propagated field when phase mask corresponding to Figure 5(a) is displayed onto the SLM is shown in Figure 5(b), and the corresponding fork fringes are shown in Figure 5(c), respectively.

**4.3. Oppositely Inclined Linear Phase Ramps with Different Tilts.** Extending the earlier arrangements one more combination of phase ramps is also possible in which two parts of the wavefronts have unequal phase gradients in opposite directions. In this case the formation of three vortices at the point where the components of phase gradients of two parts of the wavefront exactly cancel each others is expected and confirmed. Vortices are detected by the fork fringes in the interference pattern.

In phase distribution for Figure 6(a)  $\alpha_1 \neq 0$ ,  $\beta_1 \neq 0$  and  $\alpha_2 \neq 0$ ,  $\beta_2 \neq 0$  and further  $\alpha_1 \neq \alpha_2$  and  $\beta_1 \neq \beta_2$  in (7). Experimentally observed intensity distribution of propagated field when phase mask corresponding to Figure 6(a) is displayed onto the SLM is shown in Figure 6(b), and the corresponding fork fringes are shown in Figure 6(c), respectively. From the above cases it can be seen that at the boundary line separating two regions of wavefront the required opposite gradients can be achieved by component tilts rather than the ones presented earlier in [11].

## 5. Simulation Study

To verify the experimental results numerical studies have been performed. Intensity distribution is computed using Fresnel diffraction formula. The propagation of the complex field from the phase mask is computed by the Fresnel Kirchhoff diffraction integration which is given by [13]

$$\tilde{U}(x, y) = \frac{e^{jkz}}{j\lambda z} \iint_{-\infty}^{\infty} \psi \times \exp\left\{j\frac{k}{2z}[(x-\xi)^2 + (y-\eta)^2]\right\} d\xi d\eta, \quad (8)$$

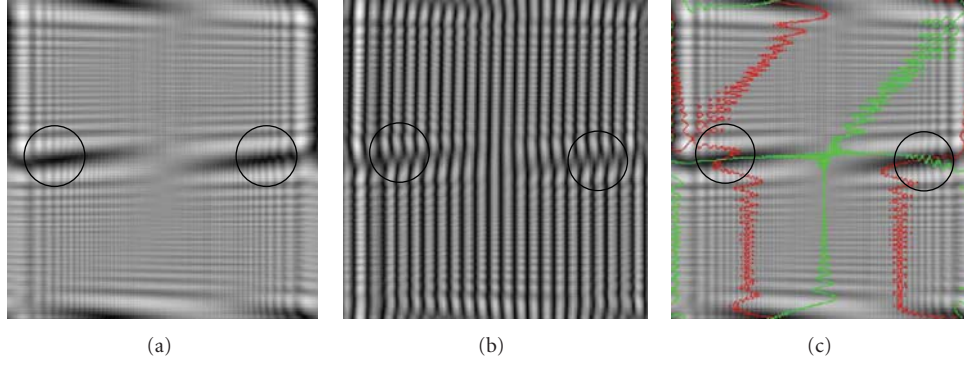


FIGURE 7: (a) Simulated intensity distribution for one oblique and one linear phase ramp. (b) Simulated interference patterns to check formation of optical vortices. (c) Simulated results for zero crossing of real and imaginary lines one oblique and one linear phase ramp.

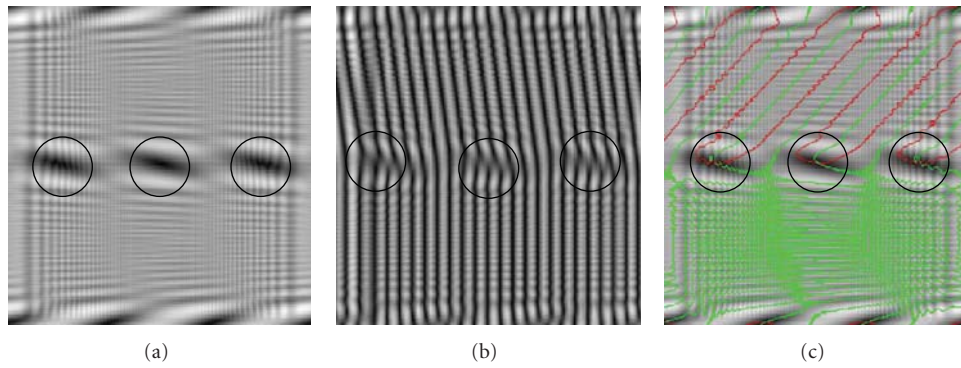


FIGURE 8: (a) Simulated intensity distribution for linear array of inclined phase ramps with constant background. (b) Simulated interference patterns to check formation of optical vortices. (c) Simulated results for zero crossing of real and imaginary lines for linear array of inclined phase ramps with constant background. Green line represents real part and red line represents imaginary part of the wave function.

where  $(x, y)$  and  $(\xi, \eta)$  correspond to the object and the diffracted field planes, respectively.  $|k| = 2\pi/\lambda$  is the magnitude of propagation vector, and  $z$  is the distance between object and the diffracted plane. Since line phase discontinuity is present in the complex field presented in (8), closed analytical solution of (8) may not be possible for arbitrary values of spatial frequencies in  $x$ - and  $y$ -directions and hence numerical solutions are attempted to view the propagated (diffracted) field. Intensity at the observation plane is

$$I(x, y) = |\tilde{U}(x, y)|^2. \quad (9)$$

Figures 7(a), 8(a), and 9(a) show simulated results for intensity distribution corresponding to the experimentally recorded intensity distribution for unequal tilt configurations. Vortices are located by interfering the vortex beam with a tilted plane wave which forms fork fringes at the singular points which are shown in Figures 7(b), 8(b), and 9(b). The exact location of the vortices in the optical field can be obtained by computational methods. One of the important computational methods of vortex detection is the zero crossing method. The zero crossing method is based on the fact that the wave function of the vortex field

comprises of real and imaginary parts, both of which vanish simultaneously at the vortex point [14].

Consider a complex field

$$\tilde{U}(x, y) = a(x, y)e^{i\phi(x, y)}. \quad (10)$$

The real zero  $\text{Re}(0)$  and  $\text{Im}(0)$  contours of  $\tilde{U}(x, y)$  are given, respectively, as

$$\begin{aligned} a(x, y) \cos(\phi(x, y)) &= 0, \\ a(x, y) \sin(\phi(x, y)) &= 0. \end{aligned} \quad (11)$$

At the vortex point

$$a(x, y) \cos(\phi(x, y)) = a(x, y) \sin(\phi(x, y)) = 0. \quad (12)$$

By plotting  $\text{Re}(0)$  and  $\text{Im}(0)$  lines the presence of vortices can be found by locating the intersection of these lines. Simulated results for zero crossing for Figures 7(a), 8(a), and 9(a) are shown in Figures 7(c), 8(c), and 9(c), respectively. These simulated results match with the experimental results that confirm the presence of vortices at the predicted points.

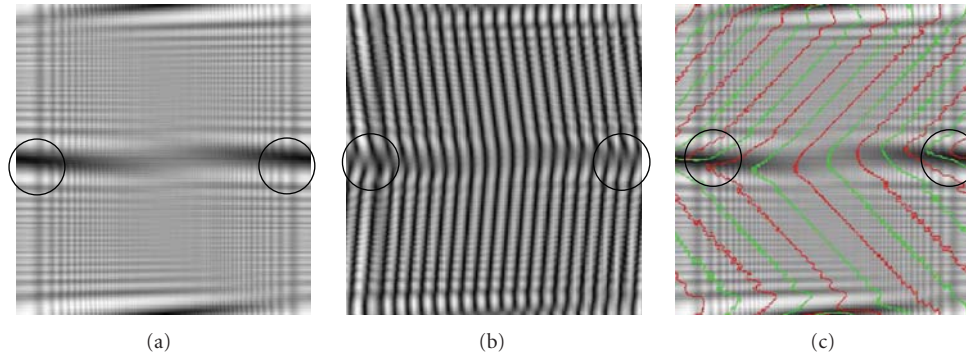


FIGURE 9: (a) Simulated intensity distribution for linear array for two oppositely inclined phase ramps with different tilt. (b) Simulated interference patterns to check formation of optical vortices. (c) Simulated results for zero crossing of real and imaginary for two oppositely inclined phase ramps with different tilt. In the figure green line represents real part and red line represents imaginary part of the wave function.

## 6. Conclusion

Evolution of vortices in the beam by providing different tilts to the two parts of the wavefront is experimentally demonstrated. For experimental verification tilted wavefronts are generated by encoding the phase mask with linear phase variations on spatial light modulator, and the presence of the vortices in the output field is conformed by formation of characteristic fork and spiral fringes. Different combination of tilts to produce vortices has been described to show the adaptability of the proposed method for vortex array generation. One of the key advantages of this method is the ability to modify optical beam into a symmetric array of vortices dynamically.

## Acknowledgment

The author would like to express his sincere thanks to Professor P. Senthilkumaran for useful discussions and correction of the paper.

## References

- [1] J. F. Nye and M. V. Berry, "Dislocations in wave trains," *Proceedings of the Royal Society of London Series A*, vol. 336, pp. 165–190, 1974.
- [2] J. M. Vaughan and D. V. Willetts, "Temporal and interference fringe analysis of TEM<sub>01</sub>\* laser modes," *Journal of the Optical Society of America*, vol. 73, no. 8, pp. 1018–1021, 1983.
- [3] C. Tamm, "Frequency locking of two transverse optical modes of a laser," *Physical Review A*, vol. 38, no. 11, pp. 5960–5963, 1988.
- [4] N. R. Heckenberg, R. McDuff, C. P. Smith, and A. G. White, "Generation of optical phase singularities by computer generated hologram," *Optics Letters*, vol. 17, pp. 221–223, 1992.
- [5] M. W. Beijersbergen, L. Allen, H. E. L. O. van der Veen, and J. P. Woerdman, "Astigmatic laser mode converters and transfer of orbital angular momentum," *Optics Communications*, vol. 96, pp. 123–132, 1993.
- [6] M. W. Beijersbergen, R. P. C. Coerwinkel, M. Kristensen, and J. P. Woerdman, "Helical-wavefront laser beams produced with a spiral phase plate," *Optics Communications*, vol. 112, no. 5–6, pp. 321–327, 1994.
- [7] K. T. Gahagan and G. A. Swartzlander Jr., "Trapping of low-index microparticles in an optical vortex," *Journal of the Optical Society of America B*, vol. 15, no. 2, pp. 524–534, 1998.
- [8] G. A. Swartzlander Jr. and C. T. Law, "Optical vortex solitons observed in Kerr nonlinear media," *Physical Review Letters*, vol. 69, no. 17, pp. 2503–2506, 1992.
- [9] J. H. Lee, G. Foo, E. G. Johnson, and G. A. Swartzlander Jr., "Experimental verification of an optical vortex coronagraph," *Physical Review Letters*, vol. 97, no. 5, article 053901, 2006.
- [10] P. Senthilkumaran, "Optical phase singularities in detection of laser beam collimation," *Applied Optics*, vol. 42, no. 31, pp. 6314–6320, 2003.
- [11] S. Vyas and P. Senthilkumaran, "Vortices from wavefront tilts," *Optics and Lasers in Engineering*, vol. 48, no. 9, pp. 834–840, 2010.
- [12] S. Vyas and P. Senthilkumaran, "Two dimensional vortex lattices from pure wavefront tilts," *Optics Communications*, vol. 283, pp. 2767–2771, 2010.
- [13] J. W. Goodman, *Introduction to Fourier Optics*, The McGraw-Hill Companies, 2nd edition, 1996.
- [14] I. Freund, "Saddles, singularities, and extrema in random phase fields," *Physical Review E*, vol. 52, no. 3, pp. 2348–2360, 1995.

## Research Article

# Tight Focusing of Partially Coherent Vortex Beams

**Rakesh Kumar Singh**

*Department of Engineering Science, The University of Electro-Communications, 1-5-1 Chofugaoka, Chofu-shi, Tokyo 182-8585, Japan*

Correspondence should be addressed to Rakesh Kumar Singh, krakeshsingh@gmail.com

Received 29 May 2011; Accepted 11 July 2011

Academic Editor: Paramasivam Senthilkumaran

Copyright © 2012 Rakesh Kumar Singh. This is an open access article distributed under the Creative Commons Attribution License, which permits unrestricted use, distribution, and reproduction in any medium, provided the original work is properly cited.

Tight focusing of partially polarized vortex beams has been studied. Compact form of the coherence matrix has been derived for polarized vortex beams. Effects of topological charge and polarization distribution of the incident beam on intensity distribution, degree of polarization, and coherence have been investigated.

## 1. Introduction

Polarization distribution of tightly focused optical beams has drawn considerable interest in recent years and recent advances in the field of nanophotonics have contributed much to the rapid progress of the field [1–7]. Tightly focused structure of the optical field possesses three-dimensional structure, and  $x$ -,  $y$ -, and  $z$ -polarization components are involved in shaping the focal structure [1]. Role of longitudinal polarization component becomes significant in shaping the focused structure in contrast to low NA-focusing system where contribution of  $z$  component is negligible in comparison to that of transverse polarization components [1]. Input polarization of the beam becomes a dominating factor apart from complex amplitude in shaping the focused structure. For example, optical vortex produces doughnut structure in the low NA focusing, whereas existence of the doughnut in tightly focused structure of vortex beam depends on its topological charge as well as on its polarization distribution [6, 8–12].

A vortex beam has a helical phase structure with a point of undefined phase in the heart of the surface, and this point is referred to as “phase singularity.” Accumulated phase variation around the singularity is an integral multiple of  $2\pi$  and is referred to as “topological charge” [13]. Doughnut structure is useful in several applications ranging from optical trapping, microscopy to lithography [13–15]. Scattered vortex beam from the sample or object provides important information about the sample, and this sensing property of the optical beam is named as “singular

microscopy” [16]. Helical phase structure in association with polarization distribution is also used to generate optical beams with nonuniform polarization distributions [17–19]. Optical beams with non-uniform polarization distribution are a solution of the wave equation in the cylindrical coordinates, and this family of optical beams is referred cylindrically polarized (CV) beams [19]. Azimuthally and radially polarized beams are examples of CV beams, and have been exploited in shaping the focal spot in recent years due to their unique characteristics and applications [20–23].

The azimuthally polarized nonvortex beam possesses a sharp doughnut structure and less susceptible to azimuthal aberration in comparison to circularly polarized unit-charged vortex beam [11]. However, doughnut structure with on-axis intensity null ceases to exist for the unit-charged azimuthally polarized vortex beam due to contribution from the longitudinal polarization component [11]. Focal spot may be extremely small when the incident beam possesses radial polarization distribution and such kind of beam has been used for various purposes. Therefore, the state of polarization in the focal region of an optical beam decides its shape and size. Polarization distribution of focused singular beam can play an important role in singular microscopy due to significant role of the scattered light in sensing the object.

Investigations on polarization and coherence properties of the randomly fluctuating field have also been area of interest from many years [24–28]. A fair amount of literature is available on the coherence matrix to deal with such situation. Modification has also been made in the coherence matrix to take consideration of the vectorial nature and

3D characteristics of the tightly focused beam [29–31]. Detailed study on the tight focusing of uniformly partially polarized radiation has been carried out in the past [30]. Such investigations for partially coherent vortex beams have been carried out recently [32, 33]. With increasing importance of polarized vortex beams in several applications and in physical optics, it is also important to carry out such investigations. In this paper, we have investigated effect of coherence and polarization on the intensity distribution, degree of polarization, and coherence in the focal region of a high numerical aperture systems.

## 2. Theory

Complex field distribution of incident quasimonochromatic beam in the focal region of a high NA aplanatic lens is given [1] as

$$E(r, z) = \left( -i \frac{A}{\lambda f} \right) \int_0^\alpha \int_0^{2\pi} A_2(\theta) e^{im\phi} P(\theta, \phi), \quad (1)$$

$$\times \begin{bmatrix} E_{xo} \\ E_{yo} \end{bmatrix} e^{ik\vec{s} \cdot \vec{r}} \sin \theta d\phi d\theta,$$

where  $A$  is related to the optical system parameters and  $\lambda$  is wavelength of light in the medium with refractive index  $n$  in the focal region.  $\theta$  is the focusing angle,  $\phi$  is azimuthal angle on the incident plane,  $\alpha$  is maximum angle of convergence ( $\alpha = \theta_{\max}$ ), and the numerical aperture  $NA = n \sin \vartheta$ .  $P$  represents the polarization matrix distribution at the exit pupil, and  $A_2(\vartheta)$  is apodization factor and is equal to  $\cos^{1/2}\vartheta$  for an aplanatic system.

The polarization distribution matrix  $P(\theta, \phi)$  at the exit pupil plane is written [9] as

$$P(\theta, \phi) = \begin{bmatrix} a[\cos \theta \cos^2 \phi + \sin^2 \phi] & \\ +b[\cos \theta \sin \phi \cos \phi - \sin \phi \cos \phi] & \\ a[\cos \theta \cos \phi \sin \phi - \sin \phi \cos \phi] & \\ +b[\cos \theta \sin^2 \phi + \cos^2 \phi] & \\ -a \sin \theta \cos \phi - b \sin \theta \sin \phi & \end{bmatrix}, \quad (2)$$

where  $a$  and  $b$  are the strengths of the  $x$ -, and  $y$ -polarized incident beams, respectively. Strength factors are position dependent in the case of nonuniformly polarized or CV beams and constant in the case of uniformly polarized beam.

The second-order coherence properties of the vector field in the focal region of a high NA system can be studied using the coherence matrix. Compact form of the  $3 \times 3$  coherence-polarization matrix can be written using  $2 \times 2$  CP matrix of the incident field, and given [30] as

$$W(r_1, r_2, z) = M^*(r_1, z) W_o M^T(r_2, z), \quad (3)$$

where  $W$  is  $3 \times 3$  CP matrix, and element of this matrix is written as  $W_{\alpha\beta}(r_1, r_2, z) = \langle E_\alpha^*(r_1, z) E_\beta(r_2, z) \rangle$ .  $\alpha, \beta = x, y, z$  and  $r_1, r_2$  are position coordinates in the observation plane. Angle bracket and asterisk denote ensemble average and complex conjugate, respectively.  $M$  is  $3 \times 2$  matrix and  $T$  represents transpose of the matrix. Complete form of matrix depends on the input polarization distribution.

The CP matrix of the incident field  $W_o$  takes on the form

$$W_o(r_{1o}, r_{2o}) = \begin{bmatrix} W_{xxo} & |\mu_{xyo}| [W_{xxo} W_{yyo}]^{1/2} \exp(i\beta_o) \\ |\mu_{xyo}| [W_{xxo} W_{yyo}]^{1/2} \exp(-i\beta_o) & W_{yyo} \end{bmatrix}, \quad (4)$$

where  $W_{xxo}$  and  $W_{yyo}$  are the intensities of the  $x$  and  $y$  components; respectively, and  $|\mu_{xyo}|$  and  $\beta_o$  are the magnitude and phase of their complex correlation coefficients.  $W_{pqo}(r_{1o}, r_{2o}) = \langle E_p^*(r_{1o}) E_q(r_{2o}) \rangle$  is the CP matrix of order  $2 \times 2$  at the input plane, and  $p, q = x, y$ .

Degree of coherence and degree of polarization are the important parameters in addition to intensity distribution for the evaluation of effect of partial coherence and partial polarization. These parameters at a point  $r$  in the focal plane of high NA system are given [30] as

$$I(r_P, r_P, z) = W_{xx}(r_P, r_P, z) + W_{yy}(r_P, r_P, z) + W_{zz}(r_P, r_P, z), \quad (5)$$

$$ptP_3^2(r_P, r_P, z) = \frac{3}{2} \left[ \frac{tr[W^2(r_P, r_P, z)]}{tr^2[W(r_P, r_P, z)]} - \frac{1}{3} \right], \quad (6)$$

$$\mu_{ij}(r_P, r_P, z) = \frac{W_{ij}(r_P, r_P, z)}{[W_i(r_P, r_P, z) W_j(r_P, r_P, z)]^{1/2}}, \quad (7)$$

where  $I$ ,  $\mu$ , and  $P$  are, respectively, intensity distribution, degree of coherence, and degree of polarization in the focal region at point  $r$ .

Strength factors of  $x$ - and  $y$ -polarized component of the incident beam are independent of the position coordinate and beam referred to as uniformly or homogeneously polarized beam. Complex field distribution in the focal region for uniformly polarized beam can be obtained by substituting proper strength factor into (2) and subsequently using (1). Using trigonometric identities Matrix  $M$  for homogeneously or uniformly polarized vortex beam can be written [10, 11] as

$$M = \begin{bmatrix} \left( I_m e^{im\phi_p} - 0.5 \{ I_{m-2} e^{i(m-2)\phi_p} + I_{m+2} e^{i(m+2)\phi_p} \} \right) & 0.5i \left( -I_{m-2} e^{i(m-2)\phi_p} + I_{m+2} e^{i(m+2)\phi_p} \right) \\ 0.5i \left( I_{m+2} e^{i(m+2)\phi_p} - I_{m-2} e^{i(m-2)\phi_p} \right) & \left( I_m e^{im\phi_p} + 0.5 \{ I_{m-2} e^{i(m-2)\phi_p} + I_{m+2} e^{i(m+2)\phi_p} \} \right) \\ - \left( I_{m-1} e^{i(m-1)\phi_p} + I_{m+1} e^{i(m+1)\phi_p} \right) & i \left( -I_{m-1} e^{i(m-1)\phi_p} + I_{m+1} e^{i(m+1)\phi_p} \right) \end{bmatrix},$$

$$I_m(\nu, u) = \left( \frac{1}{2} \right) 2\pi i^m \int_0^\alpha \cos^{1/2} \theta (1 + \cos \theta) J_m \left[ \frac{\nu}{\sin \alpha} \sin \theta \right] \exp \left[ i \frac{u}{\sin^2 \alpha} \cos \theta \right] \sin \theta d\theta, \quad (8)$$

$$I_{m\pm 1}(\nu, u) = \left( \frac{1}{2} \right) 2\pi i^{(m\pm 1)} \int_0^\alpha \cos^{1/2} \theta J_{m\pm 1} \left[ \frac{\nu}{\sin \alpha} \sin \theta \right] \exp \left[ i \frac{u}{\sin^2 \alpha} \cos \theta \right] \sin^2 \theta d\theta,$$

$$I_{m\pm 2}(\nu, u) = \left( \frac{1}{2} \right) 2\pi i^{(m\pm 2)} \int_0^\alpha \cos^{1/2} \theta (1 - \cos \theta) J_{m\pm 2} \left[ \frac{\nu}{\sin \alpha} \sin \theta \right] \exp \left[ i \frac{u}{\sin^2 \alpha} \cos \theta \right] \sin \theta d\theta.$$

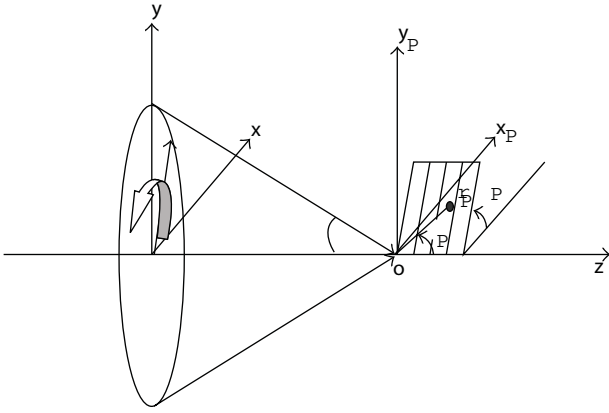


FIGURE 1: Focusing geometry of optical beams.

Here  $\nu = kr_p \sin \theta_p \sin \alpha$ ,  $u = kr_p \cos \theta_p \sin^2 \alpha$  and  $J_m(\cdot)$  is Bessel Function.

In the case of nonvortex beam ( $m = 0$ ), (7) corresponds to the matrix  $M$  for uniformly partially polarized beam [30]. In our study, we have assumed incident field as completely coherent and only focused on the partially polarized beam.

### 3. Results

Intensity distribution, degree of polarization, and coherence in the focal region of an aplanatic system can be obtained using (5)–(7) with proper polarization matrix for different input cases for input coherence matrix given by (3). We have presented results at the focal plane ( $u = 0$ ) of an air aplanatic lens with  $NA = 0.9$ . Results were evaluated for homogeneously polarized [30] and completely unpolarized [31] cases of nonvortex beam compared, and good agreement is found between both.

Results of intensity distribution and degree of polarization for polarized vortex beams are shown in Figure 2 and for two values of topological charge with  $\mu_o = 0.5$  and  $\mu_o = 0.8$  for  $\beta = \pi/2$ . Figures 2(a) and 2(b) represent intensity distribution for vortex beam with  $m = 1$ , whereas intensity

distribution for beam with  $m = 2$  is shown in Figures 2(c) and 2(d). Intensity possesses circular symmetry with lowest value at the center, and it decreases even to zero for fully correlated case. Size of low-intensity region increases with an increase in the topological charge. The distribution of degree of polarization as shown in second row of Figure 2 shows circular symmetry with rings with fully polarized at the center, and degree of polarization fluctuates around center. Figures 2(e)–2(h) represent change in degree of polarization due to change in topological charge and coherence. Intensity profiles of vortex beams with  $m = 0, 1$ , and  $2$  in the focal plane are shown by curves  $a, b$ , and  $c$  in Figure 3 for  $\mu = 0.5$  and  $\beta = \pi/2$ . Intensity value at the focal point decreased with an increase in the topological charge and also decreases with an increase in the correlation coefficient. Figure 4 shows distribution of degree of polarization for non-vortex ( $m = 0$ ) and vortex beams with  $m = 1$  and  $2$ . Degree of polarization for vortex beams possesses unit value at the center, and its variation around the center is sharp for unit-charged beam. However non-vortex beam possesses unit value away from the center. Degree of coherence for unit-charged vortex beam with  $\beta = \pi/2$  and two values of correlation coefficients are shown in Figure 5 in the focal plane along  $\phi = \pi/4$ . Curves  $a$  and  $b$  in Figure 5 represent profile of  $\mu_{xy}$  and  $\mu_{xz}$  for  $\mu_o = 0.5$ , whereas curves  $c$  and  $d$  show results for  $\mu_o = 0.8$ . Results of  $\mu_{yz}$  match with results of  $\mu_{xz}$  for both cases.

### 4. Conclusions

Investigations on the tightly focused vortex beams have been carried out using the vectorial diffraction integral. Contribution of different polarization components in the focal region according to the incident beam polarization and vortex characteristics have direct impact on the intensity distribution, degree of polarization, and degree of coherence in the focal region.

### Acknowledgment

The author is highly thankful to Japanese Society of promotion of Science (JSPS) for fellowship.

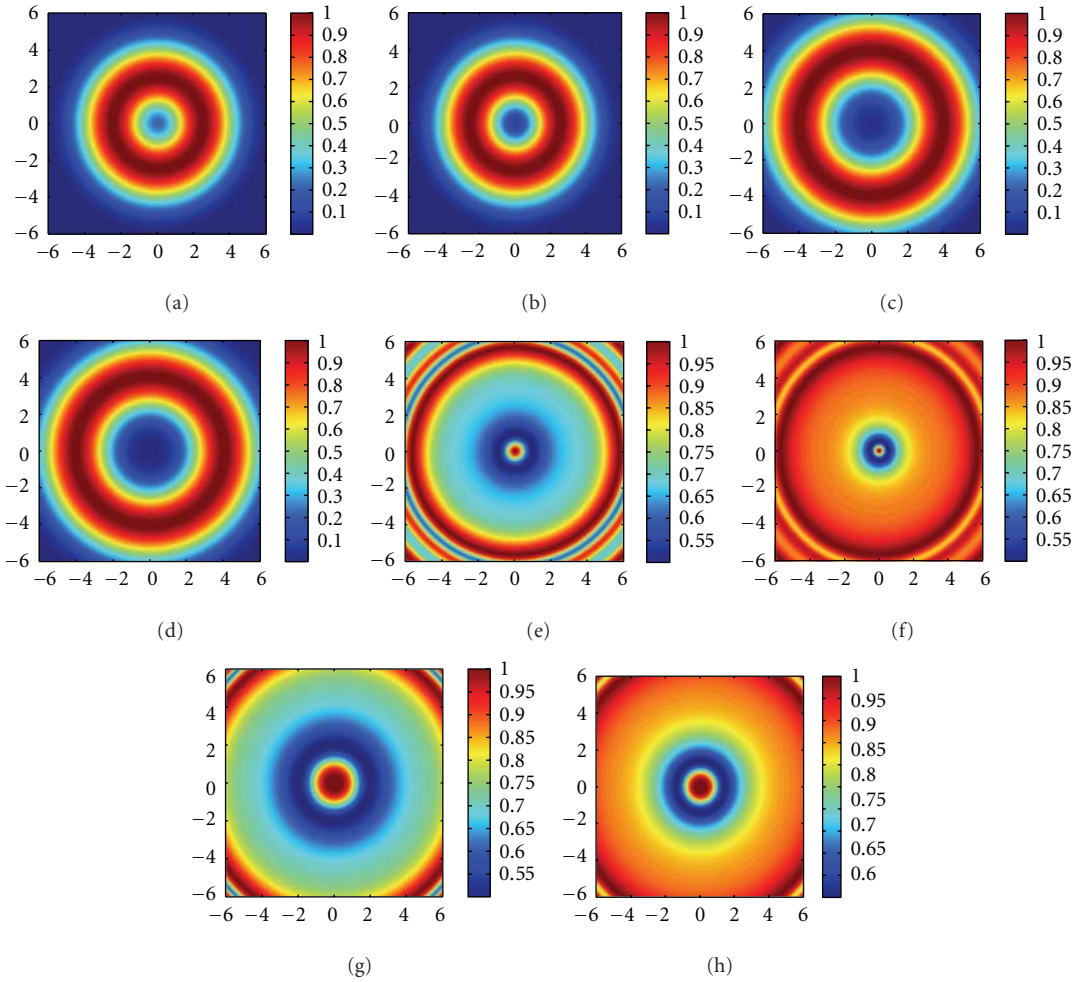


FIGURE 2: Intensity distribution of uniformly polarized vortex beams at the focal plane of an aplanatic lens with  $NA = 0.9$ : with  $m = 1$  and  $\beta = \pi/2$  for (a)  $\mu_o = 0.5$  (b)  $\mu_o = 0.8$ ; for  $m = 2$  and  $\beta = \pi/2$  with (c)  $\mu_o = 0.5$  (d)  $\mu_o = 0.8$ ; degree of polarization for  $m = 1$  and  $\beta = \pi/2$  for (e)  $\mu_o = 0.5$  (f)  $\mu_o = 0.8$ ; for  $m = 2$  and  $\beta = \pi/2$  with (g)  $\mu_o = 0.5$  (h)  $\mu_o = 0.8$ .

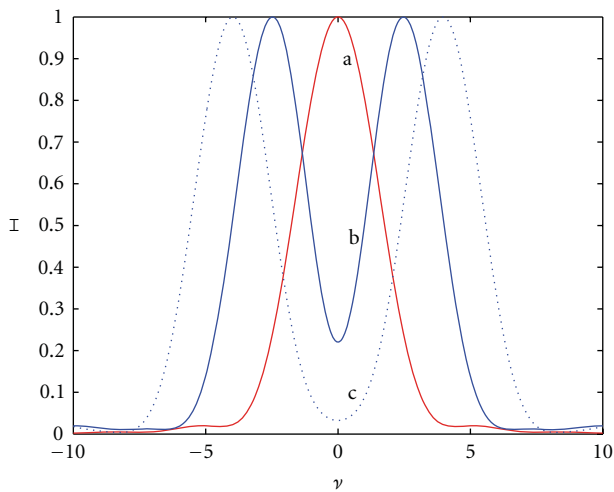


FIGURE 3: Intensity profile of uniformly polarized vortex beams with  $NA = 0.9$ ,  $\mu_o = 0.5$ ,  $\beta = \pi/2$ , for  $m$  (a) 0, (b) 1, and (c) 2.

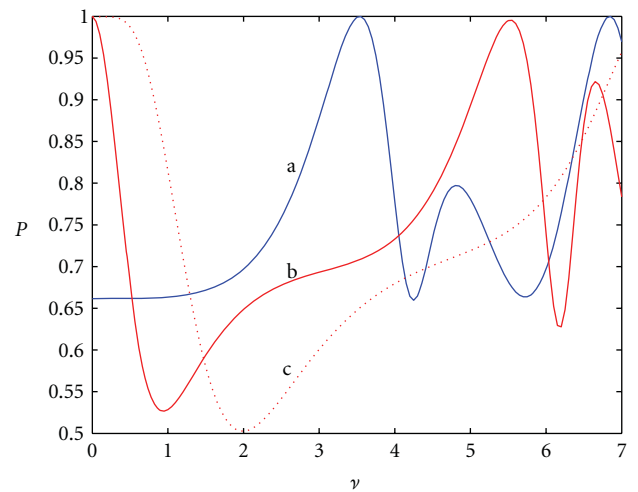


FIGURE 4: Degree of polarization along  $\pi/4$  in focal plane of an aplanatic lens with  $NA = 0.9$  of uniformly polarized vortex beams  $\mu_o = 0.5$ ,  $\beta = \pi/2$ , for  $m$  (a) 0 (b) 1, and (c) 2.

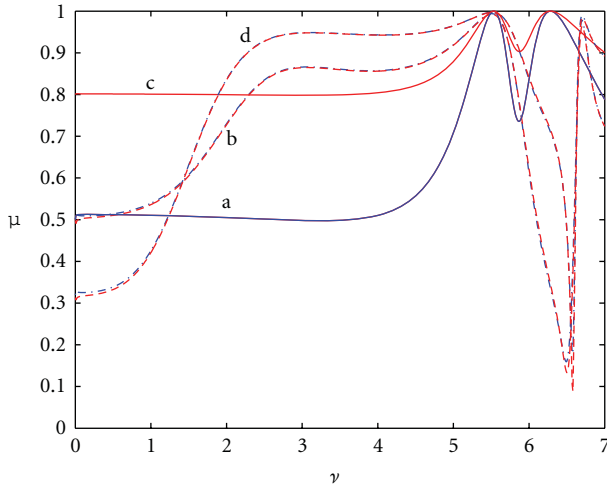


FIGURE 5: Degree of coherence along  $\pi/4$  in focal plane of aplanatic lens with  $NA = 0.9$  for uniformly polarized vortex beams with  $m = 1$   $\mu_o = 0.5$ ,  $\beta = \pi/2$ ; (a)  $\mu_{xy}$  (b)  $\mu_{xz}$ ; for  $\mu_o = 0.8$  (c)  $\mu_{xy}$  (d)  $\mu_{xz}$ .

## References

- [1] B. Richards and E. Wolf, "Electromagnetic diffraction in optical systems II. Structure of the image field in an aplanatic system," *Proceedings of the Royal Society of London A*, vol. 253, no. 1274, pp. 358–379, 1959.
- [2] L. Novotny, M. R. Beversluis, K. S. Youngworth, and T. G. Brown, "Longitudinal field modes probed by single molecules," *Physical Review Letters*, vol. 86, no. 23, pp. 5251–5254, 2001.
- [3] M. Totzeck, "Numerical simulation of high-NA quantitative polarization microscopy and corresponding near-fields," *Optik*, vol. 112, no. 9, pp. 399–406, 2001.
- [4] M. A. Lieb and A. J. Meixner, "A high numerical aperture parabolic mirror as imaging device for confocal microscopy," *Optics Express*, vol. 8, no. 7, pp. 458–474, 2001.
- [5] N. Huse, A. Schönle, and S. W. Hell, "Z-polarized confocal microscopy," *Journal of Biomedical Optics*, vol. 6, no. 3, pp. 273–276, 2001.
- [6] N. Bokor, Y. Iketaki, T. Watanabe, and M. Fujii, "Investigation of polarization effects for high-numerical-aperture first-order Laguerre-Gaussian beams by 2D scanning with a single fluorescent microbead," *Optics Express*, vol. 13, no. 26, pp. 10440–10447, 2005.
- [7] Z. Bomzon, M. Gu, and J. Shamir, "Angular momentum and geometrical phases in tight-focused circularly polarized plane waves," *Applied Physics Letters*, vol. 89, no. 24, Article ID 241104, 3 pages, 2006.
- [8] D. Ganic, X. Gan, and M. Gu, "Focusing of doughnut laser beams by a high numerical-aperture objective in free space," *Optics Express*, vol. 11, no. 21, pp. 2747–2752, 2003.
- [9] L. E. Helseth, "Optical vortices in focal regions," *Optics Communications*, vol. 229, no. 1–6, pp. 85–91, 2004.
- [10] R. K. Singh, P. Senthilkumaran, and K. Singh, "Effect of primary spherical aberration on high-numerical-aperture focusing of a Laguerre-Gaussian beam," *Journal of the Optical Society of America A*, vol. 25, no. 6, pp. 1307–1318, 2008.
- [11] R. K. Singh, P. Senthilkumaran, and K. Singh, "Tight focusing of vortex beams in presence of primary astigmatism," *Journal of the Optical Society of America A*, vol. 26, no. 3, pp. 576–588, 2009.
- [12] Z. Zhang, J. Pu, and X. Wang, "Distribution of phase and orbital angular momentum of tightly focused vortex beams," *Optical Engineering*, vol. 47, no. 6, Article ID 068001, 2008.
- [13] L. Allen, S. M. Barnett, and M. J. Padgett, Eds., *Optical Angular Momentum*, Institute of Physics, 2003.
- [14] P. Török and P. R. T. Mimro, "The use of Gauss-Laguerre vector beams in STED microscopy," *Optics Express*, vol. 12, no. 15, pp. 3605–3617, 2004.
- [15] M. D. Levenson, T. Ebihara, G. Dai, Y. Morikawa, N. Hayashi, and S. M. Tan, "Optical vortex masks for via levels," *Journal of Microlithography, Microfabrication and Microsystems*, vol. 3, no. 2, pp. 293–304, 2004.
- [16] B. Spektor, A. Normatov, and J. Shamir, "Singular beam microscopy," *Applied Optics*, vol. 47, no. 4, pp. A78–A87, 2008.
- [17] D. G. Hall, "Vector-beam solutions of Maxwell's wave equation," *Optics Letters*, vol. 21, no. 1, pp. 9–11, 1996.
- [18] K. S. Youngworth and T. G. Brown, "Focusing of high numerical aperture cylindrical-vector beams," *Optics Express*, vol. 7, no. 2, pp. 77–87, 2000.
- [19] Q. Zhan and J. R. Leger, "Focus shaping using cylindrical vector beams," *Optics Express*, vol. 10, no. 7, pp. 324–331, 2002.
- [20] R. Dorn, S. Quabis, and G. Leuchs, "Sharper focus for a radially polarized light beam," *Physical Review Letters*, vol. 91, no. 23, Article ID 233901, 4 pages, 2003.
- [21] C. J. R. Sheppard and A. Choudhury, "Annular pupils, radial polarization, and superresolution," *Applied Optics*, vol. 43, no. 22, pp. 4322–4327, 2004.
- [22] S. F. Pereira and A. S. Van de Nes, "Superresolution by means of polarisation, phase and amplitude pupil masks," *Optics Communications*, vol. 234, no. 1–6, pp. 119–124, 2004.
- [23] G. M. Lerman and U. Levy, "Effect of radial polarization and apodization on spot size under tight focusing conditions," *Optics Express*, vol. 16, no. 7, pp. 4567–4581, 2008.
- [24] W. Wang, A. T. Friberg, and E. Wolf, "Focusing of partially coherent light in systems of large Fresnel numbers," *Journal of the Optical Society of America A*, vol. 14, no. 2, pp. 491–496, 1997.
- [25] G. P. Agrawal and E. Wolf, "Propagation-induced polarization changes in partially coherent optical beams," *Journal of the Optical Society of America A*, vol. 17, no. 11, pp. 2019–2023, 2000.
- [26] K. Duan and B. Lü, "Partially coherent vectorial nonparaxial beams," *Journal of the Optical Society of America A*, vol. 21, no. 10, pp. 1924–1932, 2004.
- [27] T. van Dijk, G. Gbur, and T. D. Visser, "Shaping the focal intensity distribution using spatial coherence," *Journal of the Optical Society of America A*, vol. 25, no. 3, pp. 575–581, 2008.
- [28] Y. Cai, Q. Lin, H. T. Eyyuboğlu, and Y. Baykal, "Average irradiance and polarization properties of a radially or azimuthally polarized beam in a turbulent atmosphere," *Optics Express*, vol. 16, no. 11, pp. 7665–7673, 2008.
- [29] T. Setälä, A. Shevchenko, M. Kaivola, and A. T. Friberg, "Degree of polarization for optical near fields," *Physical Review E*, vol. 66, no. 1, Article ID 016615, 7 pages, 2002.
- [30] K. Lindfors, T. Setälä, M. Kaivola, and A. T. Friberg, "Degree of polarization in tightly focused optical fields," *Journal of the Optical Society of America A*, vol. 22, no. 3, pp. 561–568, 2005.
- [31] K. Lindfors, A. Priimagi, T. Setälä, A. Shevchenko, A. T. Friberg, and M. Kaivola, "Local polarization of tightly focused unpolarized light," *Nature Photonics*, vol. 1, no. 4, pp. 228–231, 2007.

- [32] Z. Zhang, J. Pu, and X. Wang, "Focusing of partially coherent Bessel-Gaussian beams through a high-numerical-aperture, objective," *Optics Letters*, vol. 33, no. 1, pp. 49–51, 2008.
- [33] B. Chen, Z. Zhang, and J. Pu, "Tight focusing of partially coherent and circularly polarized vortex beams," *Journal of the Optical Society of America A*, vol. 26, no. 4, pp. 862–869, 2009.

## Review Article

# Interferometry with Vortices

**P. Senthilkumaran,<sup>1</sup> Jan Masajada,<sup>2</sup> and Shunichi Sato<sup>3</sup>**

<sup>1</sup>Department of Physics, Indian Institute of Technology-Delhi, New Delhi 110 016, India

<sup>2</sup>Institute of Physics, Wrocław University of Technology, Wybrzeże Wyspińskiego 27, 50-370 Wrocław, Poland

<sup>3</sup>Institute of Multidisciplinary Research for Advanced Materials, Tohoku University, Katahira 2-1-1, Aoba-ku, Sendai 980-8577, Japan

Correspondence should be addressed to P. Senthilkumaran, psenthilk@yahoo.com

Received 15 April 2011; Revised 24 June 2011; Accepted 4 July 2011

Academic Editor: Takashige Omatsu

Copyright © 2012 P. Senthilkumaran et al. This is an open access article distributed under the Creative Commons Attribution License, which permits unrestricted use, distribution, and reproduction in any medium, provided the original work is properly cited.

Interference of optical beams with optical vortices is often encountered in singular optics. Since interferometry makes the phase observable by intensity measurement, it brings out a host of applications and helps to understand the optical vortex. In this article we present an optical vortex interferometer that can be used in optical testing and has the potential to increase the accuracy of measurements. In an optical vortex interferometer (OVI), a lattice of vortices is formed, and the movement of the cores of these vortices is tracked when one of the interfering beams is deformed. Instead of multiple vortices in an OVI, an isolated single vortex also finds applications in optical testing. Finally, singularity in scalar and vector fields is presented, and the relation between them is illustrated by the superposition of these beams.

## 1. Introduction

Phase singularities in light waves appear at points or lines in a beam cross section, where the phase of the wave changes abruptly [1–6]. When this abrupt phase change occurs along a line, it is called edge dislocation, and when it occurs at a point, it is called a screw dislocation. Screw dislocation type phase singularity is also called an optical vortex. The singular point with undefined phase and zero amplitude forms the vortex core. A wavefront with optical vortex (OV) has a characteristic helical geometry. As the vortex beam propagates, this zero amplitude point draws a curve in space. The helical wavefront winds about this dark thread of amplitude. The helix may be left- or right-handed, and accordingly the vortex is considered to possess positive or negative topological charge. Optical vortices possess a number of interesting features. On the flip side, they can cause stagnation problems in phase retrieval where wavefront geometry is reconstructed [7, 8] and in diffractive optics [9, 10]. On the positive side, since the seminal work published by Nye and Berry [1], hundreds of papers have been published on various aspects of the OVs. Large number of papers is devoted to optical vortex applications. In a vortex coronagraph an optical vortex lens is used as a filter that

enables detection of a feeble star in bright background [11–13]. Optical vortices are useful in optical tweezers with dark traps [14–17]. They are useful in fluorescence microscopy where the STED (stimulated emission depletion) pulse is used for dumping the fluorescence response of the molecule located outside the dark core of the optical vortex [18–20]. Vortices are useful in collimation testing and in the detection of elevation and depression of surfaces from a single interferogram. Further vortex interferograms can be used as signatures of vortices in the detection process. Optical recording of these interferograms can also be used as holograms for the generation of OVs. Vortices can be used to generate inhomogeneously polarized beams. OVs carry non-zero orbital angular momentum (OAM) in addition to the momentum related to polarization [21, 22]. The OAM arises due to the spiraling of Poynting vector in the singular beam. This makes optical vortices stable features of the wavefront.

In this paper we present the use of OVs in interferometry. In part I, we present optical vortex interferometer (OVI), which refers to interferometric system in which OV lattice plays a crucial role in the measurement process. In part II, we present the use of isolated single vortex in optical metrology. In the last section of part II, we discuss the role of

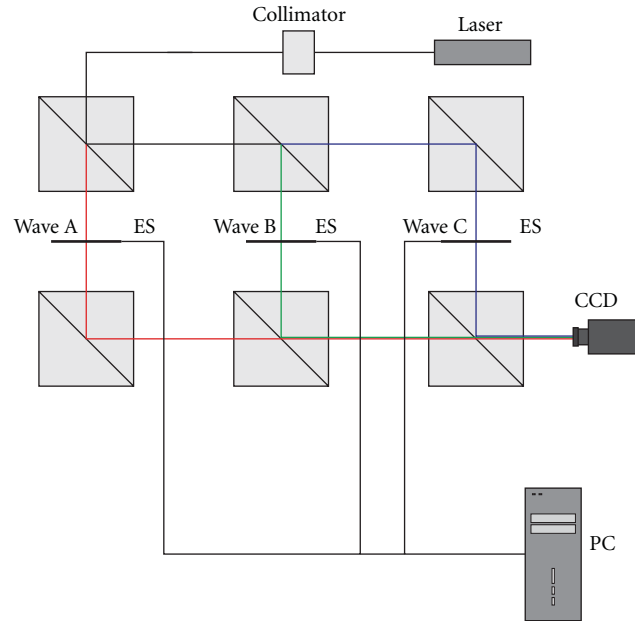


FIGURE 1: Six cubic beam splitters generate a set of three plane waves:  $A$ ,  $B$ ,  $C$ . These beams interfere and generate regular lattice of optical vortices. ESs are electronic shutters, which enable to capture the following interferograms:  $A + B$ ,  $A + C$ ,  $B + C$ ,  $A + B + C$ . The electronic shutters are not necessary when using one-frame ( $A + B + C$ ) measurement procedure.

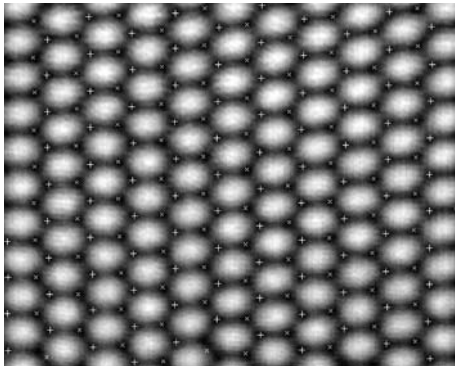


FIGURE 2: The Intensity distribution of the interference field obtained by three-plane waves (experiment). The position of vortex points is marked by plus signs or crosses to distinguish between two different topological charges.

vortex interferometry in the realization of inhomogeneously polarized beams.

## 2. Part I

**2.1. Optical Vortex Lattice Interferometer.** When two beams interfere in space, bright and dark surfaces due to interference are formed in the volume of overlap. When viewed at an observation plane, these surfaces appear as interference fringes in a conventional interferometer. When one of the interfering beams is modified, the fringe pattern undergoes a change, and this is tracked in conventional optical testing. But when three or more waves interfere, light vanishes at lines rather than on surfaces. In 2D, these lines appear as dark

points instead of fringes. The central part of each such dark point is a vortex point, that is, an isolated point where phase is undetermined. The OVI focuses on the distribution and dynamics of these dark points.

The regular lattice of optical vortices generated by wave interference was a subject of interest prior to the work on OVI. The first papers focused on physical questions concerning the properties of electromagnetic field or more specifically the phase singularity itself [23–25]. In a multiple-beam interference, it is possible to shape and tailor the geometry of these dark threads of light in the form of loops, links and knots [26–28]. The relations between vortex lattices and polarization singularities have also been described [29]. The papers concerning general questions in the theory of electromagnetic fields have also been published in the last decade [30, 31]. The three- or more plane waves interference can also be used for photonics crystal manufacturing [32, 33].

Here we want to focus our attention on metrological aspects of vortex lattice in interference fields [34–49]. Our first goal is to show specific basic properties of the vortex lattice formed by the interference of three-plane waves [34, 35]. Figure 1 shows the basic optical setup for three-plane-wave OVI, and Figure 2 shows an interference pattern obtained in such an interferometer.

The resultant field, due to the interference, consists of vortices arranged in a regular fashion. The net charge in the pattern is zero, which means that there is an equal number of positive and negative charges in the lattice. The vortex lattice can be decomposed into two sublattices each consisting of vortex points having the same topological charge (Figure 2). It is useful to use phasors and constant angle lines (CALs) [37, 38] to have better understanding on vortex lattice creation and properties. The CALs of two

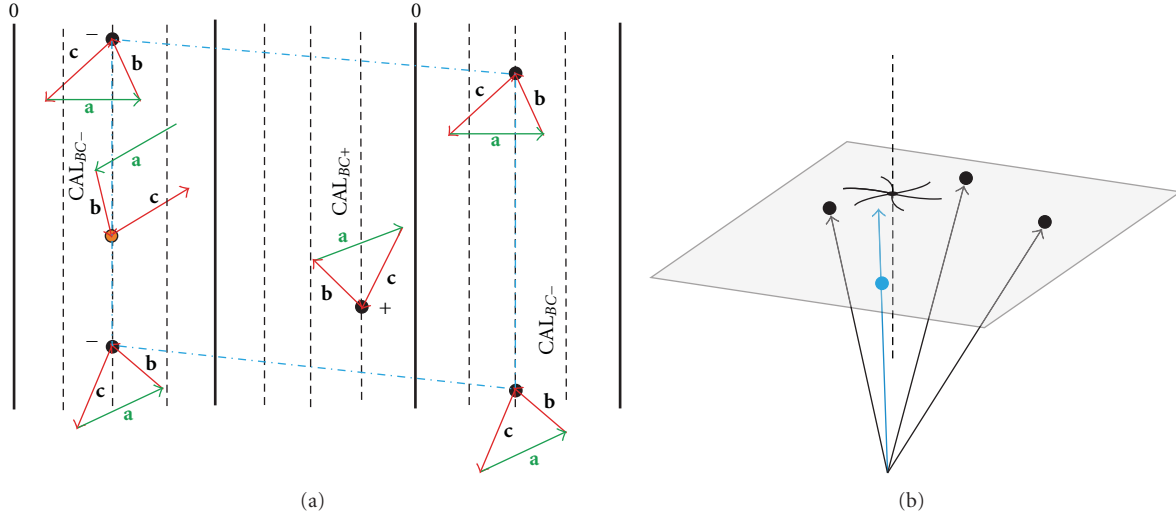


FIGURE 3: (a) A set of CALs (dashed lines) of two interfering waves  $B$  and  $C$ . By adding the third wave—wave  $A$ —a regular vortex lattice is generated. The arrows  $\mathbf{a}$ ,  $\mathbf{b}$ , and  $\mathbf{c}$  are phasors of wave  $A$ ,  $B$ , and  $C$ , respectively. The OV's appear at points where the three phasors form a triangle. The whole pattern can be divided into two subsequently appearing regions: the region with positive vortices and the region with negative vortices, respectively. The  $CAL_{BC}$  representing angle value  $0$  and  $\pi$  (bold lines) are borders between these two regions. Vortex points are marked by black dots. The four neighboring vortices of the same topological charge form an equilateral basic cell (dash dotted blue line). (b) The ends of three non-collinear wave vectors define the OVI plane. The optical vortex generated by the three-plane waves moves along the straight line (dashed line) perpendicular to the OVI plane. When adding one more wavevector (blue in this Figure) the OVI plane cannot be defined, but in very specific cases.

waves  $B$  and  $C$  ( $CAL_{BC}$ ) is a line of constant phase angle between these two waves. The CALs are defined at the plane at which interference pattern is observed. Figure 3 explains why the regular vortex lattice is created when three-plane waves interfere [34, 35, 37–39].

The vortex lattice shown in Figure 2 has a number of interesting properties, which result from two facts [38]. First, the ends of three non collinear wave vectors determine a plane uniquely (OVI plane (Figure 3(b))), and, second, the relative phases between interfering waves are defined by their amplitudes (at vortex points). It can be concluded from the above that (a) the vortex lattice moves as a rigid body, when the phase of one or more of three waves is changed, (b) changing the amplitude of the interfering waves has no influence on the vortex positive (negative) sublattice geometry; however, both sublattices change their relative positions, (c) in space optical vortices travel along lines perpendicular to the OVI plane (Figure 3(b)), and (d) it is easy to determine formulas for vortex points positions [38] as follows:

$$\begin{aligned}
 x_P &= \frac{(-\delta_{AB} + \pi - \gamma_{AB} + 2\pi l)k'_{yC}}{k'_{xB}k'_{yC} - k'_{xC}k'_{yB}} \\
 &+ \frac{(\delta_{CA} - \pi - \gamma_{AC} - 2\pi m)k'_{yB}}{k'_{xB}k'_{yC} - k'_{xC}k'_{yB}}, \\
 x_N &= \frac{(-\delta_{AB} + \pi + \gamma_{AC} + 2\pi l)k'_{yC}}{k'_{xB}k'_{yC} - k'_{xC}k'_{yB}} \\
 &+ \frac{(\delta_{CA} - \pi + \gamma_{AC} - 2\pi m)k'_{yB}}{k'_{xB}k'_{yC} - k'_{xC}k'_{yB}}.
 \end{aligned} \tag{1}$$

In the above formulas, index  $N$  and  $P$  indicate negative and positive sublattices, respectively.  $\delta_{QR}$  is a relative phase difference between waves  $Q$  and  $R$  at the origin of the reference frame,  $\gamma_{qr}$  is a triangle angle between phasor  $q$  and  $r$ ;  $q, r \in [a, b, c]$  (see Figure 3),  $k_{\mu Q}$  is the  $\mu$ -coordinate of the wavevector of wave  $Q$ ,  $\mu \in [x, y, z]$ ,  $Q, R \in [A, B, C]$ , and

$$\begin{aligned}
 k'_{xQ} &= k_{xQ} - k_{xA}, \\
 k'_{yQ} &= k_{yQ} - k_{yA}.
 \end{aligned} \tag{2}$$

The  $y$ -coordinates may be expressed by  $x$ -coordinates as follows:

$$\begin{aligned}
 y_P &= \frac{-k'_{xB}}{k'_{yB}}x_P + \frac{\delta_A - \delta_B + \pi - \gamma_{ab} + 2\pi l}{k'_{yB}}, \\
 y_N &= \frac{-k'_{xC}}{k'_{yC}}x_N + \frac{\delta_A - \delta_C + \pi + \gamma_{ac} + 2\pi m}{k'_{yB}}.
 \end{aligned} \tag{3}$$

When placing subsequent integer numbers  $m$  and  $l$  into formulas (1) and (3), the position of the same vortex point may be obtained many times, especially for highly symmetrical arrangement of interfering waves. Special reduction procedures must be applied to avoid such a multiplication. Vortex points move along straight lines perpendicular to the OVI plane. The direction of this path can be determined by formulas [37, 38]

$$\begin{aligned}
 \Delta x &= \frac{k'_{zC}k'_{yB} - k'_{yC}k'_{zB}}{k'_{xB}k'_{yC} - k'_{xC}k'_{yB}}\Delta z, \\
 \Delta y &= \frac{k'_{zB}k'_{xC} - k'_{xB}k'_{zC}}{k'_{xB}k'_{yC} - k'_{xC}k'_{yB}}\Delta z.
 \end{aligned} \tag{4}$$

Adding more than three-plane waves results in a less regular vortex lattice, and the special properties described above are no longer valid [38]. More precisely, the regular vortex lattice can still be generated but only in case of very specific wavevector configurations (for example, when the ends of wavevectors touch the same plane).

After presenting the specific basic properties of the vortex lattice formed by the interference of three-plane waves, let us present how OVI is useful in optical testing. The sample under measurement is introduced in one or more beams of the OVI. This in turn disturbs the vortex lattice geometry. These changes can be related to the value of the physical quantity being measured. The most basic example is wave tilt measurement [39–43]. The direction of propagation of the wave  $A$ , for example, can be changed by inserting an optical wedge. Figure 4 shows the response of the vortex lattice due to wedge insertion in wave  $A$  [42].

Using the properties listed above, we can derive formulas for the wave tilt through  $x$  and  $y$  axes separately. Only one measurement step is necessary for that. Instead of calculating these two angles, we can calculate the wedge angle and its orientation.

Two methods have been proposed to analyze vortex lattice dynamics. The first method is based on the analysis of vortex triplet geometry. Vortex triplet consists of three vortex points which do not lie along a single line [37, 40–42]. Having 300–400 vortex points, we can find about one million vortex triplets. The second method uses elementary cells [42] as shown in Figure 5.

Both methods are compared, and proper formulas for computing wave tilt are derived in [42]. The interesting point is that OVI enables a sound statistical analysis of the measurement, which usually is not possible in interferometric measurements. Figure 6 shows these results.

Promising versions of the OVI are compact setups using one [44, 45] or two Wollaston prisms (one-way OVI) [46]. They support a limited access to the interfering waves but are smaller and more stable. Simple and compact one-way OVI is equivalent to a four-wave OVI. As was mentioned above, the four-wave system generates less regular vortex lattice. However, this two Wollaston prism setup generates waves at very symmetrical distribution. As a result, the vortex lattice is more regular. The one-way OVI can be used for tracing the dynamic changes of light polarization or birefringent sample properties [47, 48]. In a single measurement, both azimuth angle and ellipticity or ellipticity and phase difference between fast and slow axes of the birefringent medium can be determined. Figure 7 shows exemplary results of such a measurement.

A more sophisticated setup is shown in Figure 8. One version of these systems generates a rectangular table of all polarization states of light [36]. Along the horizontal line, the polarization states of subsequent points differ in their azimuth while going along the vertical line they differ in their ellipticity. Using the system in the reverse way, the optical vortex is generated in the observation plane. The coordinates of this vortex point identify the polarization state of the incoming light (i.e., azimuth angle and ellipticity). Joining the two one-way setups, a compact spatial

polarimeter has been proposed. In a single measurement, this instrument allows the measurement of azimuth and ellipticity of the fast and slow beams and also the retardation introduced by the birefringent medium. When applying the carrier frequency method for interferogram analysis all these parameters can be determined at each pixel of the camera. This is the most ascetic polarimetric system ever proposed.

The OVI was also applied for the wavefront reconstruction [37, 39, 49]. By knowing the charge of the vortices in the vortex lattice, we can reconstruct the wavefront geometry without any ambiguities, for instance, the phase unwrapping problem, which is a characteristic of classical interferometry. There are many methods available to identify optical vortex charge for a single beam [50–53]. The methods for determining the charge sign distribution at vortex lattice are described in [54–56]. These methods can be used before measurement (as system calibration methods), and as such do not change the results of the measurements.

The accuracy and resolution of the OVI strongly depends on the accuracy of vortex point's localization. A few localization methods have been specifically designed for the OVI. The most basic is the one which searches intensity minima [57]. When supported by modern image processing techniques, this minima method can result in precise vortex localization. Moreover, more advanced methods too begin with the minima method. When compared with classical interferometry, minima method has a resolution of around  $\lambda/30$ . Nevertheless, we realize that by applying a more professional approach, this resolution can be improved. The big advantage of the minima method is that it works on a single interferogram. More precise methods require more than one interferogram, which means that the optical system must be stable [58]. The “triangle” method described in [57] requires four interferograms:  $A + B$ ,  $A + C$ ,  $B + C$ , and  $A + B + C$ , so the OVI must be equipped with fast shutters. The triangle methods result in a resolution twice as good as the minima method. An even more precise method is the phase-shifting method [59]. This method needs an extra reference wave with a phase shifter. This ensures that the vortex lattice remains undisturbed during the process. Since the topic is new, we hope that remarkable progress is still possible.

*2.2. Vortex Lattices from Spherical Waves.* Other ways of vortex lattice generation are also possible. We describe here the use of amplitude splitting and wavefront splitting interferometers for the same. Three pinholes on an opaque screen are illuminated by a plane wave, or a spherical wave and the diffracted waves behind the pinholes interfere to form the vortex lattice. The schematic of the experimental setup is shown in Figure 9. If the distance between the  $xy$  plane and the observation plane ( $x_1, y_1$  plane) is large enough to treat the diffraction as Fraunhofer, the spherical waves from the three pinholes will be seen as plane waves in the observation plane which interfere to form the vortex lattice. The geometry of the lattice is decided by the relative positions of the pinholes. The positions of the vortices in the lattices

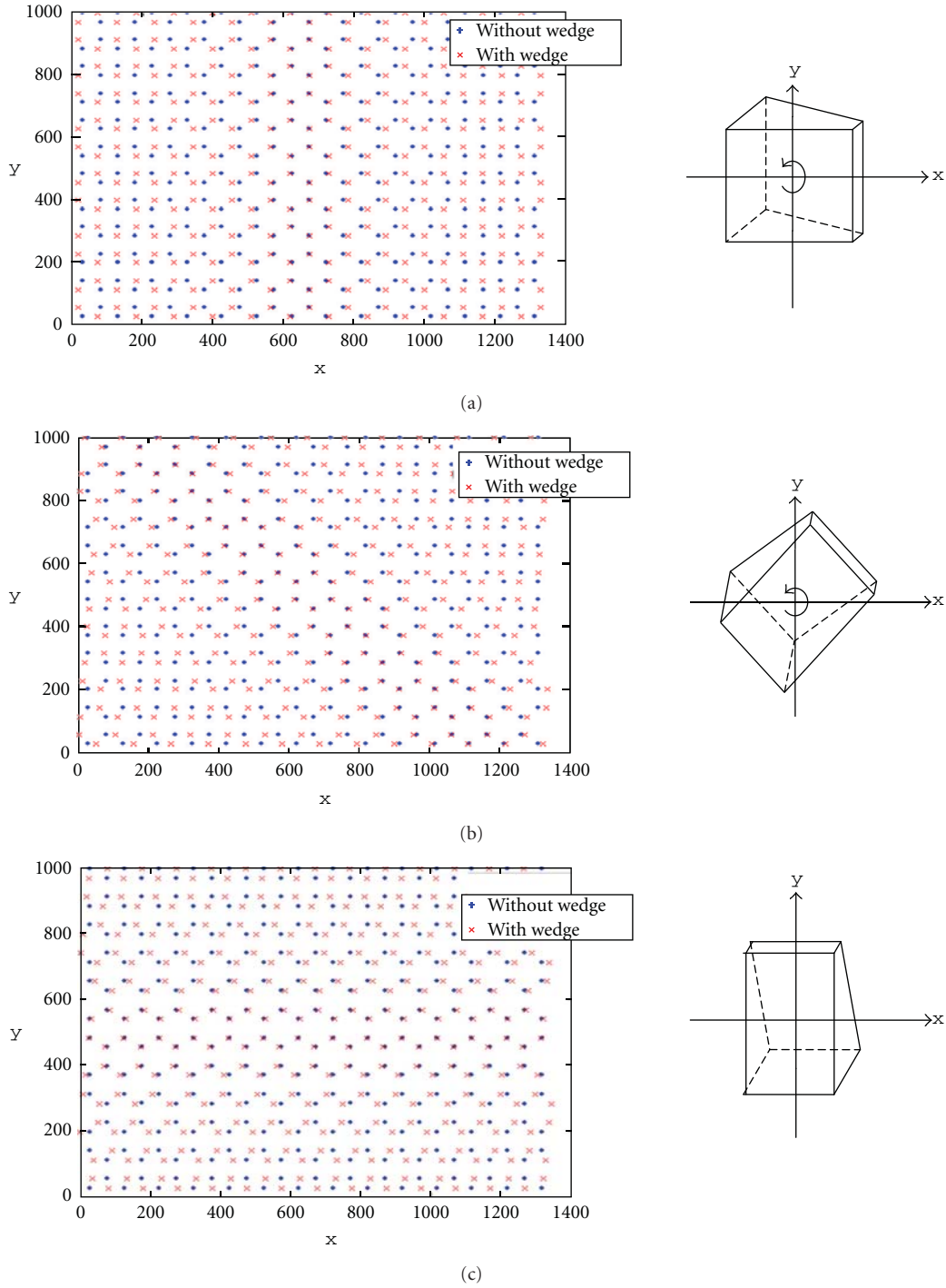


FIGURE 4: The position of the vortex points (expressed in pixel number) as measured without the wedge (circles) and with the wedge (crosses), (a) wedge inserted horizontally, (b) wedge inserted at  $\beta = 45^\circ$ , (c) wedge inserted vertically as presented in the right corners. Deflection angle  $\alpha = 20$  arcsec.

have been derived both in far- and near-field approximations and presented by Masajada et al. [60]. When the distance  $z$  between the two planes is small or when spherical waves are involved, the formation of vortex lattice still occurs and has been dealt with by Masajada et al. [60] and Ruben and Paganin [61]. Finding of analytical expression for the

position of vortex points in the lattice becomes complicated when one more pinhole is added. Technically the three pinholes setup is the simplest version of OVI interferometers. The three pinholes experiment can be considered as an extension of the classical Young's double-slit experiment. We can derive formulas for the intensity minima in a simple way

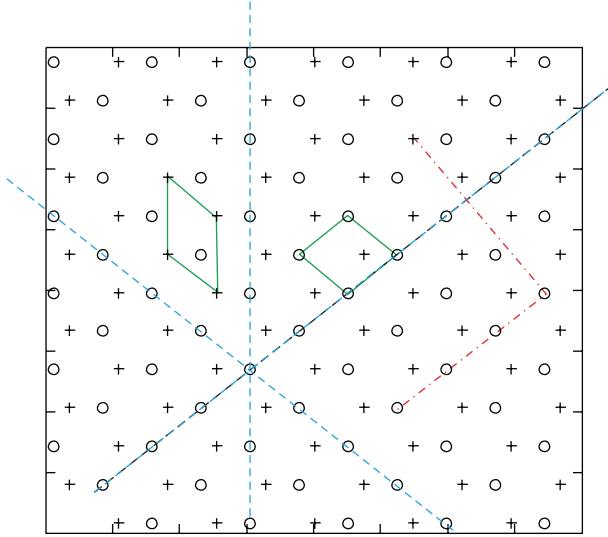


FIGURE 5: The vortex lattice consists of two sublattices which are marked by plus signs and circles. The CALs of wave pairs  $A$  and  $B$ ,  $B$  and  $C$ ,  $A$  and  $C$  are marked by dashed blue lines and are parallel to the corresponding  $A+B$ ,  $B+C$ , and  $A+C$  fringe systems. Figure shows an example of two cells, whose sides are determined by CALs and one triplet (red dashed-dot line). The vortex cells must be occupied by the vortex points having the same topological charge, while the triplets can be composed of any three vortex points, which are not collinear.

as in case of the later. Adding one more pinhole makes the whole problem complex.

Diffraction through the pinhole arrangement falls under the category of interference by wavefront splitting. It is also possible to generate vortex lattices by shear interferometers in which amplitude splitting of spherical waves is employed [62, 63]. In a lateral shear interferometer, interference is obtained between a test wavefront and its displaced replica. The most common configuration of lateral shear interferometer uses a plane parallel plate also called shear plate. When a test wavefront is incident on the plane parallel plate at an oblique angle, the beams reflected from the front and back surfaces of the plate are laterally displaced (sheared). The sheared wavefronts form an interference pattern in the region of overlap in the observation plane, as shown in Figure 10.

The fringes in the interference pattern represent phase gradients of the test wavefront. If the test wavefront has a small curvature, the interference pattern exhibits straight fringes, perpendicular to the direction of shear. The number of fringes in the interference pattern is a function of both the curvature and magnitude of shear.

In the vortex lattice generation by interference of three-plane waves, the phase difference between any two waves at the observation plane is found to vary in a linear way. Linearly varying phase difference leads to straight fringes. Hence, for a given interference pattern  $I(x, y)$  involving two waves with constant amplitude distribution, we have absolute freedom on choosing the phase  $\psi(x, y)$  of the first wave as long as we are able to realize the other interfering wave, which can produce the required phase difference  $\Delta\psi$

(which is linear) at the interference plane. This can be verified for any two-plane waves or spherical waves:

$$\begin{aligned} & |1 + \exp(-i2\pi\mu x)|^2 \\ &= \left| \exp\left(\frac{ik}{2R}(x^2 + y^2)\right) + \exp\left(\frac{ik}{2R}((x + \Delta x)^2 + y^2)\right) \right|^2 \end{aligned} \quad (5)$$

provided  $(\Delta x)^2$  is negligible and  $2\pi\mu = (k/R)\Delta x$ . Here  $R$  is the radius of curvature of the beam. In this example, the first term on the left hand side is the complex amplitude distribution at the  $z$  plane for an on-axis plane wave, and the second term is for a plane wave with tilt to the  $z$  axis at an angle given by  $\theta = \sin^{-1}(\mu\lambda)$  where  $\mu$  is the spatial frequency and  $\lambda$  is the wavelength of the light. On the right hand side of (5), the first term is a spherical wave under quadratic phase approximation, and the second term is the spherical wave which is sheared in the  $x$  direction by  $\Delta x$ . Hence, in case of the interference of spherical waves, the linear phase difference variations  $\Delta\psi$  in the  $x$  and  $y$  directions are brought about by shears in the  $x$  and  $y$  directions, respectively. The amplitude of the interfering waves is kept constant, and this provides a better contrast of fringes. It is important to note that when the beam is perfectly collimated, parallel plate will not give any fringes. Fringes are formed only when the lens is decollimated and spherical wavefronts are formed [63]. Another striking and interesting aspect observed is that while interference fringes are described by phase differences, the phase distribution of the resultant field is completely different when compared with the case of vortex generation by plane wave interference. But, a regular grid of vortex dipoles is generated in both the cases. One possible configuration of the interferometer for vortex lattice generation is given in Figure 11. The observed intensity pattern at the output of the interferometer is shown in Figure 12(a). To reveal the vortex lattice in the interference pattern, a fourth beam is superposed to obtain fork fringes at the vortex points as shown in Figure 12(b).

There is also another area of research, namely, the vortex metrology. In vortex metrology [64–67], vortices which are randomly distributed in a speckle field, are tracked for metrological applications. This is different from OVI, because in OVI the regular grid of vortices act as a reference and the movement of vortex cores upon deformation of one of the interfering beams is tracked. This method has been used for measuring small displacements and also in fluid dynamics. In the [68], a similar problem for a laser beam probing the atmosphere was solved. The obtained speckle pattern was investigated through the optical vortex localization.

The study of optical vortices in microscopy was started with Tychinsky [69–72]. He proposed to measure the phase dislocations propagating in the zero-order diffraction beam. The beam was highly magnified (up to 10000 times) and interfered with a reference beam whose phase was controlled by moving mirror (phase-shifting interferometry). The other approach was to introduce the vortex into a scanning microscope and analyze the behavior of vortex after reflection

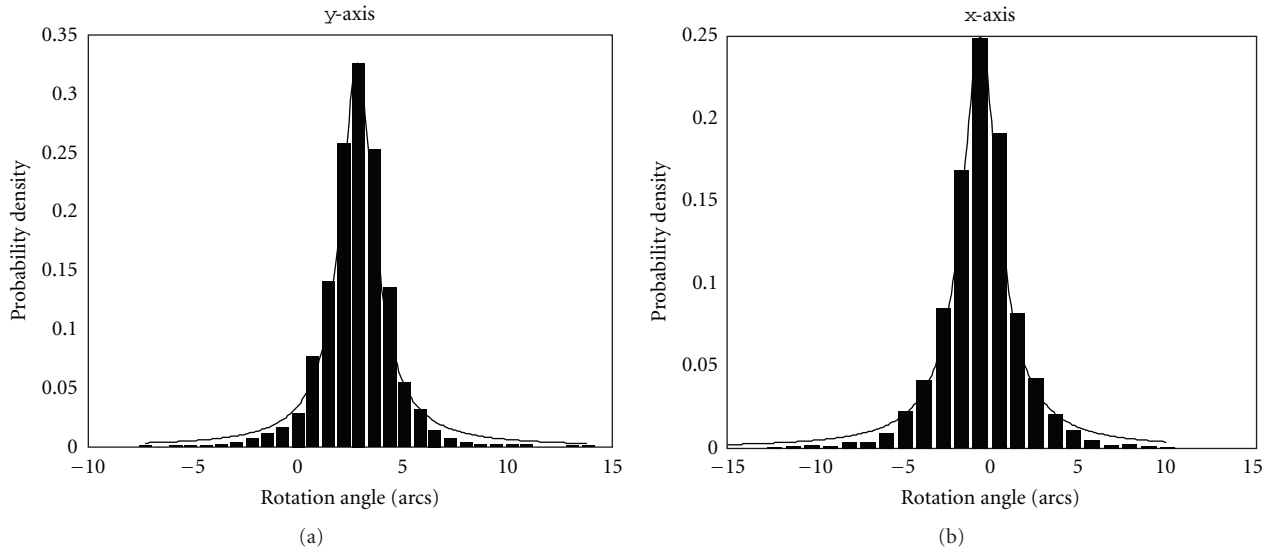


FIGURE 6: The angle of wave tilt (wave rotation) determined for  $x$  and  $y$  axes by analyzing the vortex triplets geometry. The expected values were 2.5 second of arc through  $y$ -axis and 0 second of arc through  $x$ -axes. In this example, around 350 vortices were observed at the image area. The statistics were made for 3500 triplets. Probability density function can be described by the Lorentz distribution (when using cells instead of triplets, we get the Gaussian distribution).

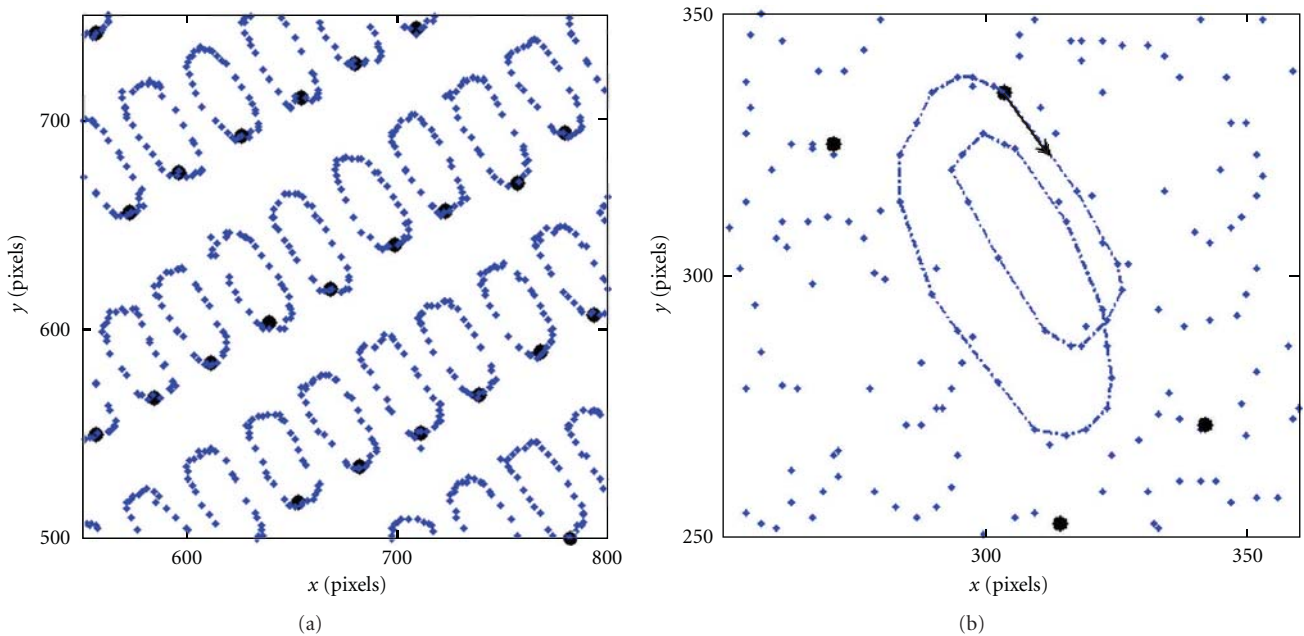


FIGURE 7: The trajectory of vortex points measured when a quarter wave plate is inserted between the Wollaston prism and rotated (a). The same situation applies but the quarter wave plate is wedge-like. Figure on the right shows part of the whole image.

from the sample. Since the OV may be identified by means of interference with reference beam this solution can be considered as a kind of vortex interference microscopy. This new solution has been presented in [73–79].

### 3. Part II

3.1. *Interferometry in Polar Coordinates.* The interference fringes obtained in an interferometer represent contour

lines of phase difference between a test and a reference wave. By using suitable reference waves in conventional interferometers, interference fringes that are functions of polar coordinates can be obtained [80]. Such interferograms are useful since most optical elements for imaging are rotational symmetric, and it is valuable if the data is directly presented in polar coordinates. When the phase of the test wavefront varies in the radial direction, radial interferograms are advantageous, and, when the phase variation occurs

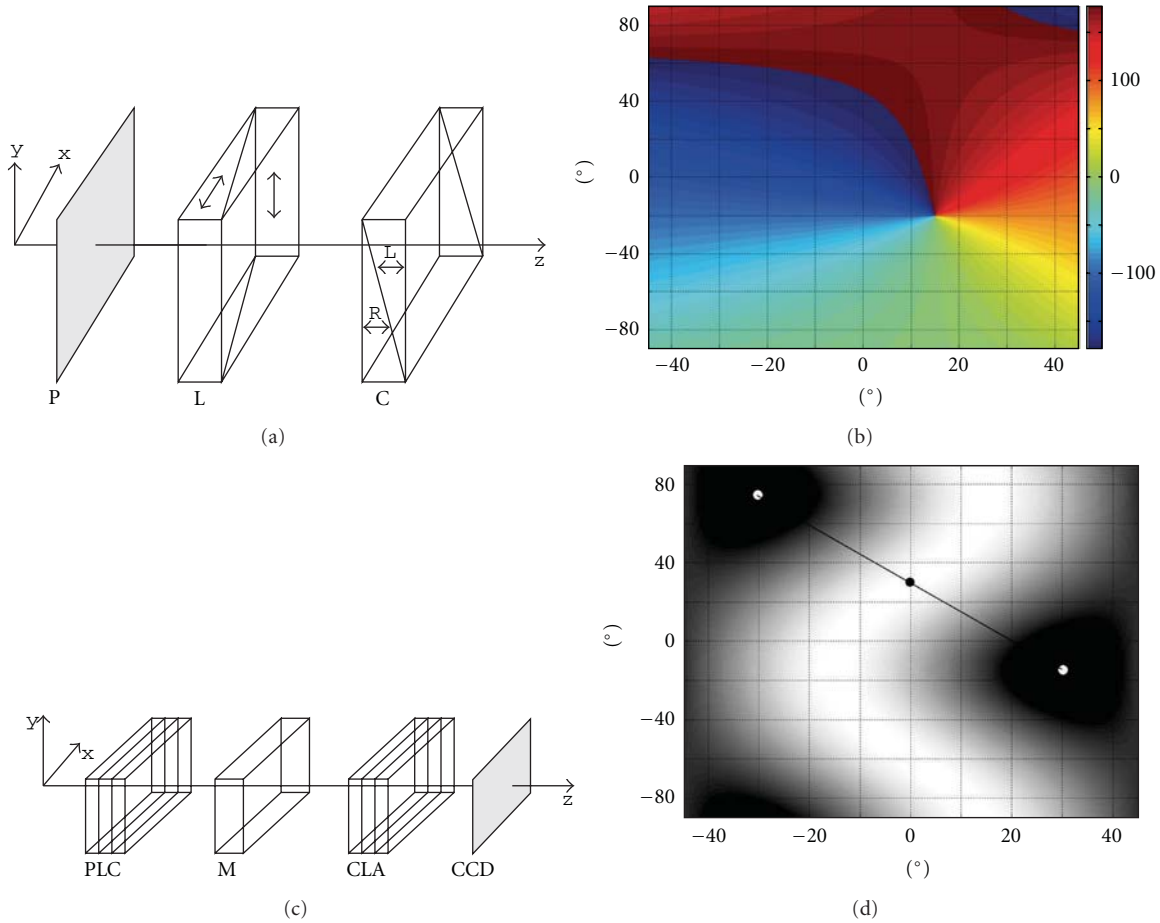


FIGURE 8: (a) A new polarimetric system consists of polarizer P, Wollaston prism L, and a circular wedge compensator C. This setup produces a table of all polarization states. When working in reverse direction (light incident on circular wedge compensator C), the optical vortex appears as shown (as a phase map) in part (b). Having the position of this vortex point, it is easy to read the polarization state of the incident light; (c) a more complex system named “spatial elliptical polariscope”. Here M is a birefringent medium under measurement. Figure (d) shows the intensity distribution with two dark points where optical vortices are seeded. Each vortex points (white points) indicate the state of the polarization of fast and slow beams, respectively. The black points show the position of maximum intensity. The distribution of these points enable determining the azimuth and ellipticity of both the beams and also the retardation between them [36].

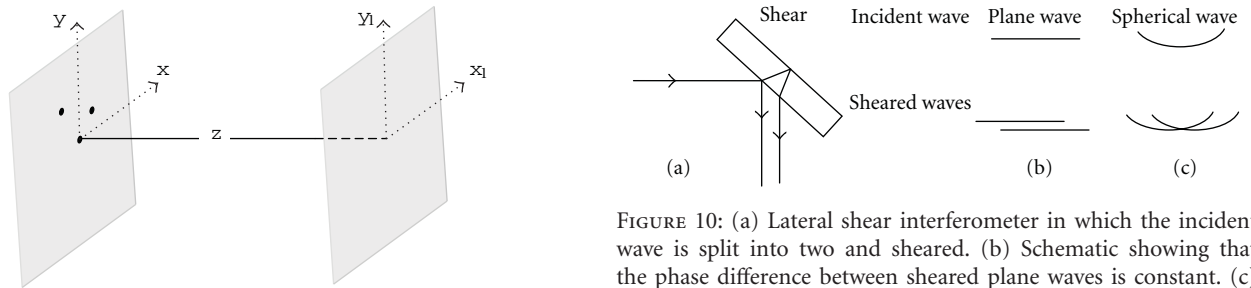


FIGURE 9: Schematic of the three pinholes arrangement for vortex lattice generation.

FIGURE 10: (a) Lateral shear interferometer in which the incident wave is split into two and sheared. (b) Schematic showing that the phase difference between sheared plane waves is constant. (c) Schematic showing the phase difference between sheared spherical waves is not constant and varies linearly in the direction of shear.

in the azimuthal direction, circular fringe interferograms are useful. It is much similar to the use of an appropriate coordinate system depending upon a variable in the problem which is also a function of some coordinate system.

Optical vortices play a crucial role in obtaining interferograms that are radial or spiral. The reference wave used in these interferometers consists of vortex-like phase variation. To obtain radial interferograms, reference wave consisting of

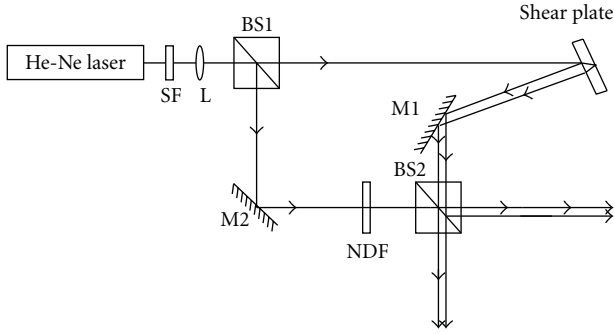


FIGURE 11: Experimental setup for the Mach-Zehnder interferometer configuration with shear plate inducted in one arm.

an optical vortex of multiple charge is useful. The reference wave that is used to get radial interferogram is given by  $\phi_{r1} = m\theta$ . To obtain spiral fringe interferograms, the reference wave phase distribution is of the form  $\phi_{r2} = m\theta + Cr$ , where  $m$  is the charge and  $C$  is a constant. The reference wave here is a conical wave in which vortex phase distribution is embedded. Figures 13(a) and 13(b) show the reference beams where optical vortices are used. Figures 13(c) and 13(d) are two test wavefronts in which the phase variations are azimuthal and radial respectively. In the phase distributions, dark represents zero phase, and white represents  $2\pi$  phase with grey levels representing other intermediate phase values.

The phase variations of the two simulated test wavefronts are  $\phi_{t1} = \pi \sin(6\theta)$  and  $\phi_{t2} = \pi \cos(\alpha r^3)$ , respectively.

The interferogram of Figure 14(b) is useful as the test wavefront  $\phi_{t1}$  has an azimuthal phase variation. The spiral interferogram that would have resulted in an interference with a plane wave has a constant period in the radial direction. The fringe shift in the radial direction is a function of phase variation of the test wavefront.

The interferogram of Figure 15(a) is useful as in this case the test wavefront  $\phi_{t2}$  has radial phase variation and the shift in the radial fringes depends on this phase variation. The advantages of polar interferograms are reported by Bryngdahl [80].

**3.2. Shear Interferometry in Polar Coordinates.** Shear interferometer eliminates the need for a known reference as the interference is between the test wavefront and a sheared copy of it. The fringes obtained give the phase gradient of the wavefront if the test wavefront is appropriately sheared.

While the lateral shear interferometer reveals phase gradients in Cartesian coordinates, it is essential to modify the way shear is applied for obtaining gradient in polar coordinates. The gradient of the complex amplitude  $u$  in polar coordinates is given by

$$\nabla u = \frac{\partial u}{\partial r} \hat{r} + \frac{1}{r} \frac{\partial u}{\partial \phi} \hat{\phi}. \quad (6)$$

Thus, to study gradients with shearing interferometers, we need to introduce wavefront displacements that are constant in both the radial and azimuthal directions. In order to realize a shearing interferometer that displays gradients in

the azimuthal direction, all of the object points in one of the wavefronts need to be displaced by the same distance relative to the corresponding points in the other, along circular arcs, with the origin as center. Thus, rotation of the wavefront, with the amount of rotation dependent on the radius, is required. Points near to the origin are rotated by larger amount where as points away from the origin are rotated by less amount, but, in each case, the displacement along the circular arc is of equal length.

Bryngdahl and Lee [81] have used computer-generated gratings as shown in Figures 16 and 17 to achieve constant azimuthal and constant radial displacements to the wavefronts. These gratings have spiral and segmented spiral grating elements that are associated with optical vortices.

In the grating shown in Figure 16, the superimposed red arrows are indicating the directions of the local grating vectors at two different locations. The diffracted orders of the wavefront behind the grating will be shifted in the radial direction. This way, radial shear between the diffracted beams can be achieved.

For constant azimuthal displacement, simple rotation about the centre of the beam will not suffice as in, simple rotation, the azimuthal displacement is different at different radial locations. In the grating shown in Figure 17, the superimposed red arrows indicate the local grating vector directions. Each of these shows that the grating vector has both radial and angular components. For the points on a circle of constant radius, the rate of change of rotation of the grating vector is faster (with respect to  $\theta$ ) than those points on a circle of larger radius. It can be seen that the component of the grating vector in the azimuth direction between two vectors in the same segment is the same which ensures that the diffracted light from the grating acquires a constant azimuthal shear. The segmentation has been done to reduce distortion in the sheared wavefronts.

### 3.3. Interferograms of Various Wavefronts with Vortex Beam.

Knowledge about the nature of interferograms formed by the interference of various types of wavefronts with vortex beams is useful in many situations. Fringes obtained by the interference of vortex beams are characterized by the birth of new fringes from the middle of the interferogram. In conventional interferograms, extrema are surrounded by closed fringes, and no fringe terminates or originates at the centre of the interferogram.

When the vortex-bearing wavefronts are plane and their vortex cores coincide, purely radial fringes occur as in Figure 18(a). The number of new fringes that originate is indicative of the charges present in the interfering beams. When the locations of the vortices in the interfering beams coincide, star like, fringes are obtained [82]. The number of new fringes indicates the difference between the vortex charges in the individual interfering beams (Figures 18(a) and 18(b)). Hence, a fringe-free pattern results when both interfering beams have equal number of charges with the same polarity. The interference pattern between a tilted plane wave and a vortex results in fork fringes (Figure 18(c)). Fork fringes are commonly used in the detection of vortices. If

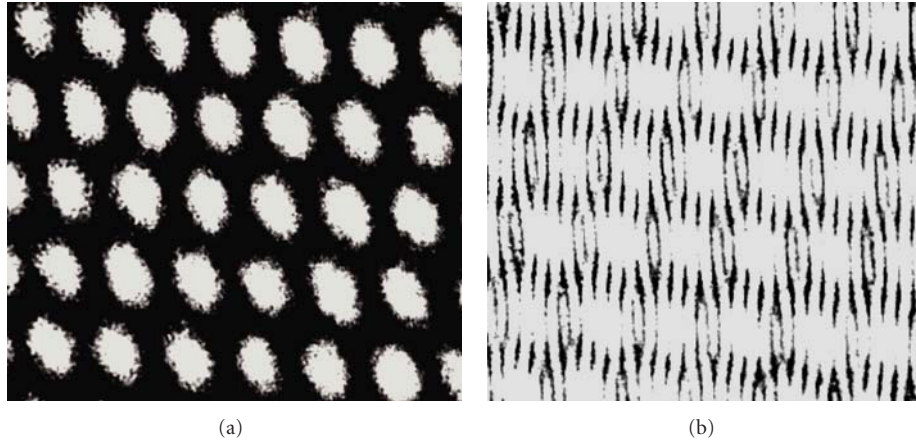


FIGURE 12: (a). Interferogram recorded with the Mach-Zehnder interferometer configuration, (b) Formation of fork fringe pattern when fourth beam is added, indicating the presence of vortex dipole arrays.

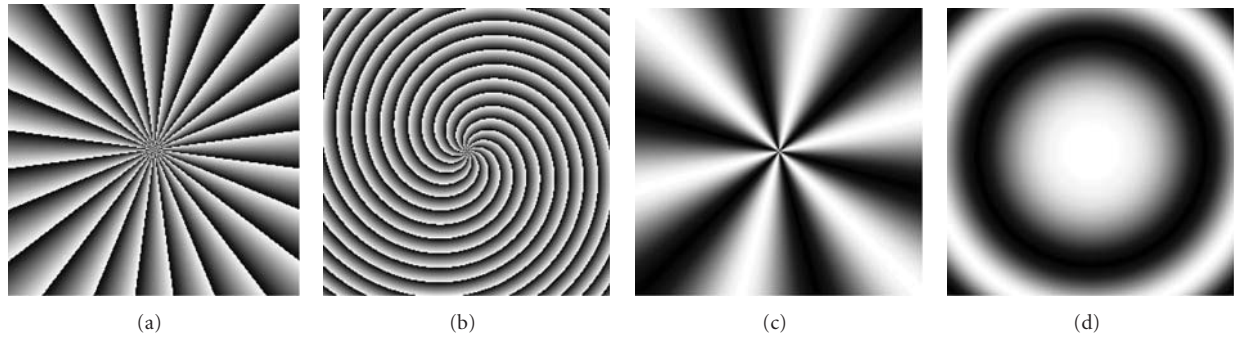


FIGURE 13: The phase distributions of (a) reference wave  $\phi_{r1} = m\theta$  and (b) reference wave  $\phi_{r2} = m\theta + Cr$ . (c) Test wave with azimuthal phase variation. (d) Test wave with radial phase variation.

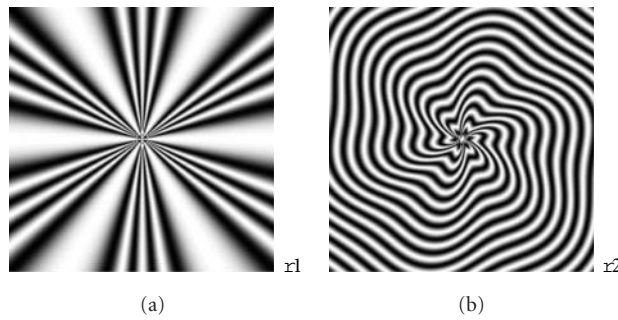


FIGURE 14: Interferogram when the test wave  $\phi_{r1}$  of Figure 13(c) interferes with (a) reference wave  $\phi_{r1} = m\theta$  and (b) reference wave  $\phi_{r2} = m\theta + Cr$ .

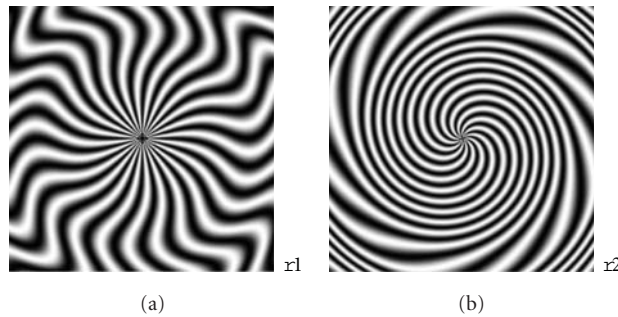


FIGURE 15: Interferogram when the test wave  $\phi_{r2}$  of Figure 13(d) interferes with (a) reference wave  $\phi_{r1} = m\theta$  (b) reference wave  $\phi_{r2} = m\theta + Cr$ .

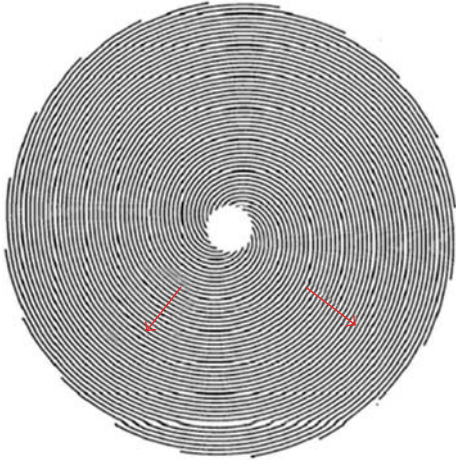


FIGURE 16: Grating that introduces a constant radial displacement between sheared wavefronts [81].

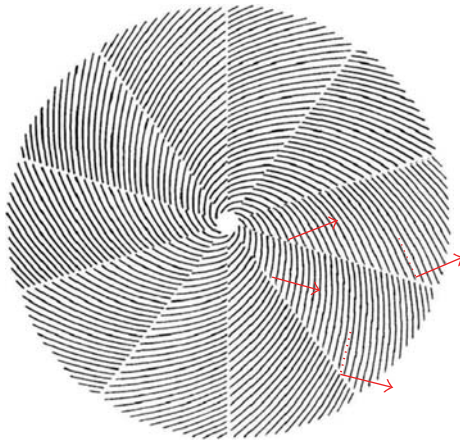


FIGURE 17: Segmented spiral grating that can be used to introduce a constant azimuthal displacement between sheared wavefronts [81].

the interferogram consists of a fork pattern anywhere in the field of view, it is inferred that one of the interfering waves has a singularity. Diffraction phenomenon can also be used for the detection of vortices [83]. When the cores of the vortices of the interfering waves do not coincide, the total number of fringes obtained is different in the cases of beams with opposite and similar polarity. In the former case, it is exactly equal to the charge of the beam with the higher charge value (Figure 18(d)), whereas, in the latter case, it equals the sum of the charges of the two (Figure 18(e)). Interferograms shown in Figure 18(d) are due to interference of two singular beams having charges  $+8$  and  $-2$ , respectively, whereas in Figure 18(e), the interfering beams have charges  $+8$  and  $+2$ , respectively.

The radial fringes shown in Figure 18(b) start to spiral in the anticlockwise direction when the interfering beam acquires a positive curvature (Figure 19(a)) and spiral clockwise direction (Figure 19(b)) when the interfering beam acquires a negative curvature. This phenomenon can be used to detect beam collimation. At collimation, radial fringes

can be obtained [82]. Interference of spherical beam with a plane reference wave gives rise to concentric circular fringes irrespective of the sign of the curvature of the spherical wave. If the plane reference beam is replaced by a vortex beam, spiral interferograms can be obtained. This enables us to distinguish the extremum between peak and valley [84]. When the interfering wave is a conical wave, the resulting spiral interferogram will have a fringe spacing that is constant in the radial direction (Figure 19(c)). Such interferogram can be recorded to make gratings that are useful in obtaining radial shear [80]. When the extrema (in the phase map) of the spiral wavefront do not coincide with the core of the vortex during interference, fringes as shown in Figure 19(d) are obtained [85]. One of the circular fringes at the vortex point branches (forks). As a result fringes start to spiral only from this point, and we see both circular and spiral fringes in the same interferogram. Thus, we see, in Figure 19(d), two circular fringes at the center of the interferogram and spiral fringes thereafter. Such recorded interferograms can be used as holograms, which reconstruct the vortex beam when illuminated by a beam free of vortices. When sinusoidal amplitude fork grating (with charge  $+m$ ) is illuminated by a plane wave, the different diffraction orders  $-1$ ,  $0$ , and  $+1$  produce beams with topological charge  $-m$ ,  $0$  and  $+m$ , respectively. If the fork grating (with charge  $+m$ ) is a binary amplitude or a phase grating, beams in each of the multiple diffraction orders contain vortices of charge  $mp$ , where  $p$  is the integral diffraction order number. Recordings of the interferograms shown in Figures 19(a) and 19(b) yield spiral zone plates [86], and recording of interferogram shown in Figure 18(c) yields fork grating. These elements are commonly used for vortex generation. In the recording of Figure 19(b), if the signs of the curvature of the spherical beam and the charge of the vortex are simultaneously reversed, interferogram shown in Figure 19(e) can be obtained. Equivalently, we can say that a fork grating with its fork up can be generated either by the interference of a singular beam with a positive vortex and an off-axis beam with positive tilt or by the interference of a singular beam with a negative vortex and an off-axis beam with a negative tilt.

**3.4. Vortex Interferometry with Orthogonally Polarized Light Waves.** In this section, we show the synthesis of a vortex beam by a superposition of beams with a polarization singularity using an interferometer. In other words, scalar beams with a phase singularity and vector beams with a polarization singularity can be mutually converted.

**3.4.1. Laguerre-Gaussian Beams.** The optical beam generated in an optical resonator is a solution of the wave equation. When the scalar wave equation, commonly referred to as the Helmholtz equation, is solved, the solution is a linearly polarized optical beam with homogeneous spatial distribution across the beam cross section. Hermite-Gaussian (HG) beams are the typical paraxial solutions obtained in the orthogonal coordinate system. In the cylindrical coordinate system, Laguerre-Gaussian (LG) and Bessel-Gaussian (BG)

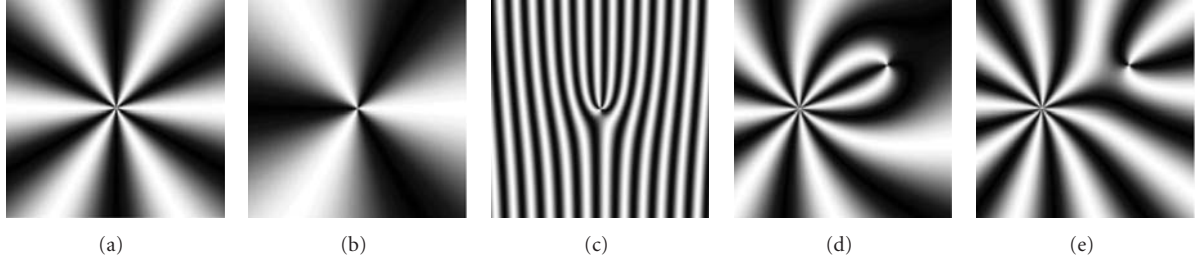


FIGURE 18: Fringes obtained due to interference between a vortex of charge +3 with (a) another beam with charge  $-3$  (b) an on-axis plane wave (c) an off-axis plane wave. Interferograms obtained when both the interfering beams have off centred vortices of (d) opposite unequal charges (e) same signed unequal charges.

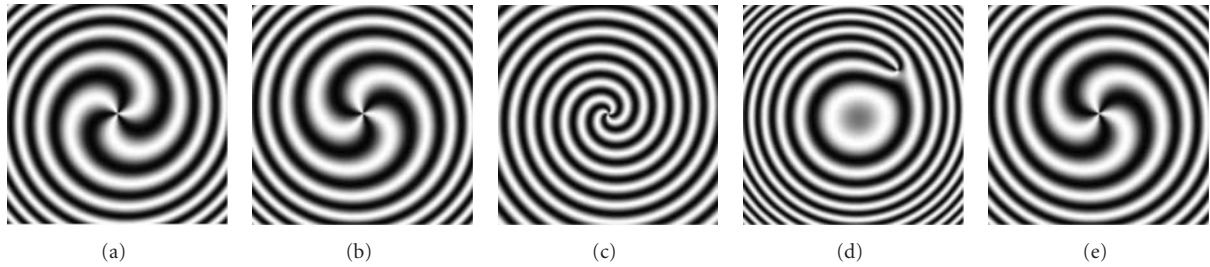


FIGURE 19: Fringes obtained due to interference between a vortex of charge 3 with (a) Spherical beam of positive curvature (b) spherical beam of negative curvature (c) conical beam. (d) Interference between an off centred vortex and a spherical wave (e) Interference between negatively charged vortex and a spherical beam with positive curvature.

beams are derived and are well known as vortex beams. The electric field of scalar LG beam of degree  $p$  and order  $m$  is expressed by

$$E_{p,m}^{(s)}(r, \phi, z) \propto Y_{p,m}(r, \phi, z) \exp(im\phi), \quad (7)$$

$$Y_{p,m}(r, \phi, z) = \frac{\omega_0}{\omega(z)} \left[ \frac{\sqrt{2}r}{\omega(z)} \right]^{|m|} L_p^{|m|} \left[ \frac{2r^2}{\omega^2(z)} \right] \times \exp[ikz - i(2p + |m| + 1)\psi(z)] \times \exp\left\{-r^2 \left[ \frac{1}{\omega^2(z)} - \frac{ik}{2R(z)} \right]\right\}, \quad (8)$$

where  $r$  is the radius,  $\phi$  is the azimuthal angle,  $z$  is the distance from the beam waist,  $\omega_0$  is the minimum beam radius at  $z = 0$ ,  $R = (z^2 + z_0^2)/z$  is the radius of curvature of the wave front,  $k$  is the wave number,  $(2p + |m| + 1)\psi(z)$  is the Gouy phase shift with  $\psi(z) = \arctan(z/z_0)$ , and  $\omega(z)$  is the Gaussian beam width defined as  $\omega(z) = \omega_0 \sqrt{1 + (z/z_0)^2}$  with  $z_0 = k\omega_0^2/2$ .  $L_p^m(t)$  is the Laguerre polynomial of degree  $p$  and order  $m$ . The beam is assumed to propagate in the  $z$  direction. The last term of (7),  $\exp(im\phi)$ , indicates that the beams have a spiral phase shift with  $m$  revolutions about the axis of the optical beam. The number  $m$  is the topological charge and is indicative of the beam carrying an orbital angular momentum [21]. This equation implies that beams with  $m \geq 1$  have an intensity null on the beam axis, which corresponds to a point phase singularity. The Bessel-Gaussian beams also have a spiral phase shift and, hence, a point phase singularity.

If the polarization of the optical beam is inhomogeneous, optical beams must be derived by solving the vector wave equation. The solutions of this equation are different from those of the Helmholtz equation. LG [87], BG [88], and modified BG [89] beams are the solutions in the cylindrical coordinate system. The electric field of vector LG beam of degree  $p$  and order  $m \pm 1$  is expressed by

$$\mathbf{E}_{p,m\pm 1}^{(v)}(r, \phi, z) \propto Y_{p,m\pm 1}(r, \phi, z) \begin{cases} \mp \sin(m\phi)\boldsymbol{\rho} + \cos(m\phi)\boldsymbol{\phi} \\ \cos(m\phi)\boldsymbol{\rho} \pm \sin(m\phi)\boldsymbol{\phi} \end{cases}, \quad (9)$$

where  $\boldsymbol{\rho}$  and  $\boldsymbol{\phi}$  are the unit vectors of the electric field for the radial and azimuthal directions, respectively. Equation (9) shows that these beams do not have a spiral phase shift but a complicated distribution of polarization as shown by the last term. All beams also have an intensity null on the beam axis due to the presence of a point singularity. Note that this is not a phase singularity but a singularity of polarization. Thus, there is an inherent difference of singularities between scalar and vector LG beams.

The lowest-order mode of vector LG beams is obtained for  $m = 0$ . In this case, the beam carries pure azimuthal and radial polarizations for upper and lower rows of (9), respectively. The temporal electric field distributions of these two lowest order LG beams are depicted in Figure 20. An azimuthally polarized beam is shown in Figure 20(a), which is called TE<sub>01</sub> mode because there is no electric field in the direction of beam propagation. The other beam shown in Figure 20(b) is a radially polarized beam, which has no

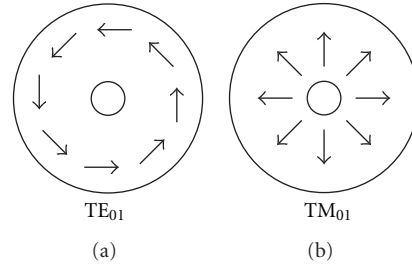


FIGURE 20: The lowest-order vector LG beams. (a) Azimuthally ( $TE_{01}$ ) and (b) radially ( $TM_{01}$ ) polarized, respectively. The arrows indicate the direction of the temporal electric field.

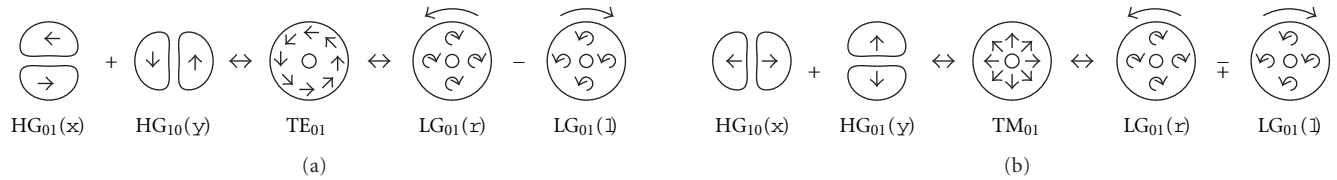


FIGURE 21: The conversion between scalar and vector LG beams. (a) Azimuthally and (b) radially polarized beams.  $x$  and  $y$  in the parentheses for linearly polarized HG beams indicate the polarization direction.  $r$  and  $l$  in the parentheses for circularly polarized LG beams indicate right- and left-hand polarizations, respectively. HG: Hermite-Gaussian beam, LG: Laguerre-Gaussian beam.

magnetic field in the direction of propagation ( $TM_{01}$  mode). The small circle in the center is the dark area due to the polarization singularity on the beam axis. In what follows, we will show that these beams can also be synthesized by a superposition of scalar beams with a phase singularity.

As shown in Figure 21(a), an azimuthally polarized beam can be expressed by a superposition of two linearly polarized HG beams with orthogonal polarizations, that is,  $HG_{01}$  mode with  $x$ -polarization and  $HG_{10}$  mode with  $y$ -polarization. Note that these HG beams have a line phase singularity. Similarly, a radially polarized beam can be expressed by a superposition of  $HG_{10}$  mode with  $x$ -polarization and  $HG_{01}$  mode with  $y$ -polarization as shown in Figure 21(b). Another superposition is possible as shown in the right-hand side of Figure 21. In these cases, radially and azimuthally polarized beams are superpositions of circularly polarized  $LG_{01}$  beams with inverse handedness of both spin and orbital angular momenta, that is, right- and left-hand circularly polarized  $LG_{01}$  beams superposed with beams carrying left- and right-hand orbital angular momenta, respectively. Note that there is  $\pi$ , phase shift between two left-handed circularly polarized  $LG_{01}$  beams, namely, subtraction and addition in Figures 21(a) and 21(b), respectively.

These transformations between scalar and vector LG beams have been experimentally demonstrated by Tidwell et al. [90] using a Mach-Zehnder interferometer and a linearly polarized Ar ion laser beam with a Gaussian intensity profile ( $TEM_{00}$  mode). Although the manipulation of polarization is not difficult, the production of higher transverse modes such as  $HG_{01}$  and  $LG_{01}$  modes needed the use of unconventional phase elements. For the  $HG_{01}$  mode, a half part of a  $TEM_{00}$  mode beam was passed through a tilted glass plate, whose angle was adjusted to obtain a  $\pi$  phase shift between the two semicircular parts of the beam.  $LG_{01}$  mode beams were

produced by passing a  $TEM_{00}$  mode beam through a spiral phase delay plate, which had a spiral ramp made from thin-film-coated glass plate resulting in the relative phase shift of  $\pi$ . Although the synthesis of radially and azimuthally polarized beams has been verified, there have still been some drawbacks. The first method using two linearly polarized  $HG_{01}$  beams was sensitive to the intensity profile error of an input  $TEM_{00}$  mode beam. The second one using  $LG_{01}$  beams had a low conversion efficiency ( $<50\%$ ) because two circularly polarized beams were combined by a conventional polarization beam splitter for linear polarization. These problems have been solved based on the fact that a linearly polarized  $HG_{01}$  mode is a superposition of two linearly polarized  $LG_{01}$  modes carrying inverse orbital angular momenta [91]. Figure 22 shows the case for the generation of an azimuthally polarized beam shown in Figure 20(a). In Figure 22(a), a  $HG_{01}$  mode is expressed by a superposition of two  $LG_{01}$  modes with inverse orbital angular momenta and  $\pi$ -phase shift (subtraction). In the same manner, a  $HG_{10}$  mode is expressed by an addition of two  $LG_{01}$  modes. Since the polarizations are linear and the intensity patterns are doughnut, the drawbacks in the previous methods are improved. In addition, this method implies that vector  $LG_{01}$  beams with a polarization singularity on the beam axis can be converted from scalar  $LG_{01}$  beams with a phase singularity on the beam axis similar to the conversion shown on the right-hand side of Figure 21. Some improvements based on a similar principle have been demonstrated using a simpler phase element [92] and a Sagnac's interferometer [93].

The generation of pure radially and azimuthally polarized beams directly from a laser cavity has also been demonstrated [94] based on the same principle as shown in Figure 21(b). In this experiment,  $HG_{01}$  and  $HG_{10}$  beams are generated and combined in a laser cavity using linear

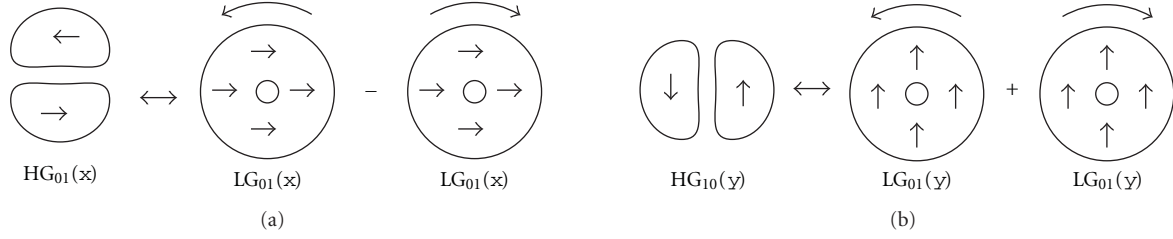


FIGURE 22: Conversion between linearly polarized HG and LG modes.

polarization optics and a  $\pi$ -phase shifter. Recent progresses on vector beams are reviewed [95].

In the following, we show that the conversion between scalar and vector LG beams mentioned above is generally concluded. The upper row of (9) can be expressed by a superposition of two  $LG_{01}$  modes with opposite spin and orbital angular momenta in the following way:

$$\begin{aligned}
& E_{p,\mp(m\pm 1)}^{(s)}(\mathbf{x} + i\mathbf{y}) - E_{p,\pm(m\pm 1)}^{(s)}(\mathbf{x} - i\mathbf{y}) \\
& \propto Y_{p,m\pm 1} \{ \exp[\mp i(m\pm 1)\phi](\mathbf{x} + i\mathbf{y}) \\
& \quad - \exp[\pm i(m\pm 1)\phi](\mathbf{x} - i\mathbf{y}) \} \\
& = Y_{p,m\pm 1} \{ \exp[\mp i(m\pm 1)\phi] \exp(i\phi)(\boldsymbol{\rho} + i\boldsymbol{\varphi}) \\
& \quad - \exp[\pm i(m\pm 1)\phi] \exp(-i\phi)(\boldsymbol{\rho} - i\boldsymbol{\varphi}) \} \\
& = Y_{p,m\pm 1} \{ \mp [\exp(im\phi) - \exp(-im\phi)]\boldsymbol{\rho} \\
& \quad + i[\exp(im\phi) + \exp(-im\phi)]\boldsymbol{\varphi} \} \\
& = 2iY_{p,m\pm 1} [\mp \sin(m\phi)\boldsymbol{\rho} + \cos(m\phi)\boldsymbol{\varphi}] \\
& \propto \mathbf{E}_{p,m\pm 1}^{(v)}(\text{upper row}),
\end{aligned} \tag{10}$$

where  $\mathbf{x}$  and  $\mathbf{y}$  are the unit vectors of the electric field for the  $x$  and  $y$  directions in the orthogonal coordinate system, respectively. In the same way, the lower row of (9) can be expressed as

$$\begin{aligned}
& E_{p,\mp(m\pm 1)}^{(s)}(\mathbf{x} + i\mathbf{y}) + E_{p,\pm(m\pm 1)}^{(s)}(\mathbf{x} - i\mathbf{y}) \\
& \propto Y_{p,m\pm 1} \{ \exp[\mp i(m\pm 1)\phi](\mathbf{x} + i\mathbf{y}) \\
& \quad + \exp[\pm i(m\pm 1)\phi](\mathbf{x} - i\mathbf{y}) \} \\
& = Y_{p,m\pm 1} \{ \exp[\mp i(m\pm 1)\phi] \exp(i\phi)(\boldsymbol{\rho} + i\boldsymbol{\varphi}) \\
& \quad + \exp[\pm i(m\pm 1)\phi] \exp(-i\phi)(\boldsymbol{\rho} - i\boldsymbol{\varphi}) \} \\
& = Y_{p,m\pm 1} \{ [\exp(im\phi) + \exp(-im\phi)]\boldsymbol{\rho} \\
& \quad \mp i[\exp(im\phi) - \exp(-im\phi)]\boldsymbol{\varphi} \} \\
& = 2Y_{p,m\pm 1} [\cos(m\phi)\boldsymbol{\rho} \pm \sin(m\phi)\boldsymbol{\varphi}] \\
& \propto \mathbf{E}_{p,m\pm 1}^{(v)}(\text{lower row}).
\end{aligned} \tag{11}$$

The relation,  $\mathbf{x} \pm i\mathbf{y} = (\boldsymbol{\rho} \cos \phi - \boldsymbol{\varphi} \sin \phi) \pm i(\boldsymbol{\rho} \sin \phi + \boldsymbol{\varphi} \cos \phi) = \exp(\pm i\phi)(\boldsymbol{\rho} \pm i\boldsymbol{\varphi})$ , played an important role in the above conversion. The expression is indicative that a spin angular momentum can be represented by an orbital angular momentum, in other words, a polarization singularity is related to a phase singularity. While (10) and (11) are the derivation of a vector LG mode from scalar LG modes, the derivation in the opposite way is also possible as shown in the following:

$$\begin{aligned}
& \mathbf{E}_{p,m+1}^{(v)}(\text{upper row}) \pm i\mathbf{E}_{p,m+1}^{(v)}(\text{lower row}) \\
& = \pm iE_{p,\pm(m+1)}^{(s)}(\mathbf{x} \mp i\mathbf{y}), \\
& \mathbf{E}_{p,m-1}^{(v)}(\text{upper row}) \pm i\mathbf{E}_{p,m-1}^{(v)}(\text{lower row}) \\
& = \pm iE_{p,\mp(m-1)}^{(s)}(\mathbf{x} \mp i\mathbf{y}).
\end{aligned} \tag{12}$$

In the above expressions, circularly polarized LG modes are derived by a superposition of two vector LG modes.

**3.4.2. Bessel-Gaussian Beams.** The electric fields of scalar and vector BG beams,  $E_m^{s-BG}(r, \phi, z)$  and  $\mathbf{E}_m^{v-BG}(r, \phi, z)$ , respectively, are expressed by

$$E_m^{s-BG}(r, \phi, z) \propto Z(r, \phi, z) i^m J_m(u) \exp(im\phi), \tag{13}$$

$$\mathbf{E}_m^{v-BG}(r, \phi, z) \propto Z(r, \phi, z) \mathbf{T}_m(r, \phi, z), \tag{14}$$

$$\begin{aligned}
& Z(r, \phi, z) \\
& = \frac{\omega_0}{\omega(z)} \exp[ikz - i\psi(z)] \exp\left\{-r^2 \left[ \frac{1}{\omega^2(z)} - \frac{ik}{2R(z)} \right]\right\}, \\
& \quad \times \exp\left\{-\frac{i\beta^2 z}{2k(1 + iz/z_0)}\right\},
\end{aligned} \tag{15}$$

where  $\beta$  is a constant,  $J_m(u)$  is the Bessel function of the first kind of order  $m$ , and  $u = \beta r / (1 + iz/z_0)$ .  $\mathbf{T}_m(r, \phi, z)$  has two

families transverse electric field solutions  $\mathbf{TE}_m$  and transverse magnetic field solution  $\mathbf{TM}_m$  [88], expressed by

$$\begin{aligned}\mathbf{TE}_m(r, \phi, z) &= [J_{m-1}(u) - J_{m+1}(u)] \begin{bmatrix} -\sin(m\phi) \\ \cos(m\phi) \end{bmatrix} \boldsymbol{\varphi} \\ &+ [J_{m-1}(u) + J_{m+1}(u)] \begin{bmatrix} \cos(m\phi) \\ \sin(m\phi) \end{bmatrix} \boldsymbol{\rho}, \\ \mathbf{TM}_m(r, \phi, z) &= -[J_{m-1}(u) + J_{m+1}(u)] \begin{bmatrix} \cos(m\phi) \\ \sin(m\phi) \end{bmatrix} \boldsymbol{\varphi} \\ &+ [J_{m-1}(u) - J_{m+1}(u)] \begin{bmatrix} -\sin(m\phi) \\ \cos(m\phi) \end{bmatrix} \boldsymbol{\rho}.\end{aligned}\quad (16)$$

Equation (13) shows that a scalar BG beam with the Bessel function of order  $m$  has a topological charge of  $m$  and a point phase singularity on the beam axis except for  $m = 0$ . On the other hand, vector BG beams have a point polarization singularity on the beam axis except for  $m = 1$ , where the order of the Bessel function is zero, and the beam has a finite intensity on the beam axis. Although the intensity distribution of vector BG beams is more complicated compared to that of a vector LG beam, the conversion between scalar and vector BG beams is also possible. For example, the equation in the upper row of  $\mathbf{TE}_m$  is derived by a superposition of four scalar BG beams with circular polarization as mentioned below.

$$\begin{aligned}& [E_{m-1}^{s-BG} - E_{-(m+1)}^{s-BG}](\mathbf{x} + i\mathbf{y}) + [E_{-(m-1)}^{s-BG} - E_{m+1}^{s-BG}](\mathbf{x} - i\mathbf{y}) \\ & \propto Zi^{m-1} \{ J_{m-1} \exp[i(m-1)\phi] \\ & \quad + J_{m+1} \exp[-i(m+1)\phi] \} (\mathbf{x} + i\mathbf{y}) \\ & \quad + Zi^{m-1} \{ J_{m-1} \exp[-i(m-1)\phi] \\ & \quad + J_{m+1} \exp[i(m+1)\phi] \} (\mathbf{x} - i\mathbf{y}) \\ & = Zi^{m-1} J_{m-1} \{ \exp[i(m-1)\phi] (\mathbf{x} + i\mathbf{y}) \\ & \quad + \exp[-i(m-1)\phi] (\mathbf{x} - i\mathbf{y}) \} \\ & \quad + Zi^{m-1} J_{m+1} \{ \exp[-i(m+1)\phi] (\mathbf{x} + i\mathbf{y}) \\ & \quad + \exp[i(m+1)\phi] (\mathbf{x} - i\mathbf{y}) \} \\ & = 2Zi^{m-1} J_{m-1} [\cos(m\phi)\boldsymbol{\rho} - \sin(m\phi)\boldsymbol{\varphi}] \\ & \quad + 2Zi^{m-1} J_{m+1} [\cos(m\phi)\boldsymbol{\rho} + \sin(m\phi)\boldsymbol{\varphi}] \\ & = 2Zi^{m-1} \{ (J_{m-1} - J_{m+1}) [-\sin(m\phi)\boldsymbol{\varphi}] \\ & \quad + (J_{m-1} + J_{m+1}) \cos(m\phi)\boldsymbol{\rho} \} \\ & \propto \mathbf{TE}_m(\text{upper row}).\end{aligned}\quad (17)$$

Here we used the relation,

$$\begin{aligned}E_{-m}^{s-BG}(r, \phi, z) &\propto Z(r, \phi, z) i^{-m} J_{-m}(u) \exp(-im\phi) \\ &= Z(r, \phi, z) i^m J_m(u) \exp(-im\phi).\end{aligned}\quad (18)$$

In the similar way, other components of  $\mathbf{TE}_m$  and  $\mathbf{TM}_m$  are represented by

$$\begin{aligned}& [E_{m-1}^{s-BG} + E_{-(m+1)}^{s-BG}](\mathbf{x} + i\mathbf{y}) - [E_{-(m-1)}^{s-BG} + E_{m+1}^{s-BG}](\mathbf{x} - i\mathbf{y}) \\ & \propto \mathbf{TE}_m(\text{lower row}), \\ & - [E_{m-1}^{s-BG} - E_{-(m+1)}^{s-BG}](\mathbf{x} + i\mathbf{y}) + [E_{-(m-1)}^{s-BG} - E_{m+1}^{s-BG}](\mathbf{x} - i\mathbf{y}) \\ & \propto \mathbf{TM}_m(\text{upper row}), \\ & [E_{m-1}^{s-BG} + E_{-(m+1)}^{s-BG}](\mathbf{x} + i\mathbf{y}) + [E_{-(m-1)}^{s-BG} + E_{m+1}^{s-BG}](\mathbf{x} - i\mathbf{y}) \\ & \propto \mathbf{TM}_m(\text{lower row}).\end{aligned}\quad (19)$$

For  $m = 0$ , vector BG beams have pure azimuthal and radial polarizations corresponding to  $\mathbf{TE}_0$  and  $\mathbf{TM}_0$  components, respectively. In this case, the electric fields of both scalar and vector BG beams include  $J_1(u)$  only. Experimental demonstration has been reported by a superposition of two scalar BG beams with orthogonal polarization generated by using a spatial light modulator [93].

## 4. Conclusion

In this paper we present a detailed analysis about the interferograms that form optical vortex lattices and also how these vortex lattices are used in the measurement process. An example of the displacement of the vortex cores in the lattice by the introduction of a wedge plate in the interferometer is illustrated. The various vortex lattice generation methods including the one based on multiple pinhole diffraction and another using a shear interferometer are presented. As far as beams with single optical vortex are concerned, the role played by a single vortex in realizing interferograms in polar coordinates and shear interferometry in polar coordinates are dealt with. Interferograms of vortex-infested beams with plane, spherical, and conical beams and their applications are discussed. Finally, scalar beams with phase singularity and vector beams with polarization singularity are presented. The conversion between scalar and vector LG beams and the conversion between linearly polarized HG and LG modes are also illustrated. Realization of radial and azimuthal polarization states by superposition of orthogonally polarized beams are also discussed.

## References

- [1] J. F. Nye and M. V. Berry, "Dislocations in wave trains," *Proc. Roy. Soc. Lond. A*, vol. 336, pp. 165–190, 1974.
- [2] J. F. Nye, *Natural Focusing and Fine Structure of Light*, Institute of Physics Publishing, 1999.
- [3] M. Vasnetsov and K. Staliunas, Eds., *Optical Vortices*, Nova Science, Huntington, NY, USA, 1999.

- [4] M. S. Soskin and M. V. Vasnetsov, "Singular optics," *Progress in Optics*, vol. 42, pp. 219–276, 2001.
- [5] M. R. Dennis, K. O'Holleran, and M. J. Padgett, "singular optics: optical vortices and polarization singularities," *Progress in Optics*, vol. 53, pp. 293–363, 2009.
- [6] A. S. Desyatnikov, Y. S. Kivshar, and L. Torner, "Optical vortices and vortex solitons," *Progress in Optics*, vol. 47, pp. 291–391, 2005.
- [7] K. G. Larkin, D. J. Bone, and M. A. Oldfield, "Natural demodulation of two-dimensional fringe patterns. I. General background of the spiral phase quadrature transform," *The Journal of the Optical Society of America A*, vol. 18, no. 8, pp. 1862–1870, 2001.
- [8] K. G. Larkin, "Natural demodulation of two-dimensional fringe patterns. II. Stationary phase analysis of the spiral phase quadrature transform," *The Journal of the Optical Society of America A*, vol. 18, no. 8, pp. 1871–1881, 2001.
- [9] D. C. Ghiglia and M. D. Pritt, *Two-Dimensional Phase Unwrapping Theory, Algorithms and Software*, John Wiley & Sons, New York, NY, USA, 1998.
- [10] P. Senthikumar, F. Wyrowski, and H. Schimmel, "Vortex Stagnation problem in iterative Fourier transform algorithms," *Optics and Lasers in Engineering*, vol. 43, no. 1, pp. 43–56, 2005.
- [11] G. A. Swartzlander Jr., "Peering into darkness with a vortex spatial filter," *Optics Letters*, vol. 26, no. 8, pp. 497–499, 2001.
- [12] D. Mawet, P. Riaud, O. Absil, and J. Surdej, "Annular groove phase mask coronagraph," *The Astrophysical Journal*, vol. 633, no. 2 I, pp. 1191–1200, 2005.
- [13] G. A. Swartzlander Jr., E. L. Ford, R. S. Abdul-Malik et al., "Astronomical demonstration of an optical vortex coronagraph," *Optics Express*, vol. 16, no. 14, pp. 10200–10207, 2008.
- [14] K. T. Gahagan and G. A. Swartzlander Jr., "Optical vortex trapping of particles," *Optics Letters*, vol. 21, no. 11, pp. 827–829, 1996.
- [15] D. G. Grier, "A revolution in optical manipulation," *Nature*, vol. 424, no. 6950, pp. 810–816, 2003.
- [16] N. Friedman, A. Kaplan, and N. Davidson, "Dark optical traps for cold atoms," *Advances in Atomic, Molecular and Optical Physics*, vol. 48, pp. 99–151, 2002.
- [17] D. Cojoc, V. Garbin, E. Ferrari, L. Businaro, F. Romanato, and E. D. Fabrizio, "Laser trapping and micro-manipulation using optical vortices," *Microelectronic Engineering*, vol. 78–79, no. 1–4, pp. 125–131, 2005.
- [18] S. W. Hell and J. Wichmann, "Breaking the diffraction resolution limit by stimulated emission: stimulated-emission-depletion fluorescence microscopy," *Optics Letters*, vol. 19, no. 11, pp. 780–782, 1994.
- [19] S. W. Hell, "Increasing the resolution of far-field fluorescence microscopy by point-spread-function engineering, topics," in *Fluorescence Spectroscopy; 5: Nonlinear and Two-Photon-Induced Fluorescence*, J. Lakowicz, Ed., pp. 361–426, Plenum Press, New York, NY, USA, 1997.
- [20] T. A. Klar, E. Engel, and S. W. Hell, "Breaking Abbe's diffraction resolution limit in fluorescence microscopy with stimulated emission depletion beams of various shapes," *Physical Review E*, vol. 64, no. 6, part 2, Article ID 066613, 9 pages, 2001.
- [21] L. Allen, S. M. Barnett, and M. J. Padgett, Eds., *Optical Angular Momentum*, Institute of Physics Publishing, 2003.
- [22] L. Allen, M. J. Padgett, and M. Babiker, "IV the orbital angular momentum of light," *Progress in Optics*, vol. 39, pp. 291–372, 1999.
- [23] K. W. Nicholls and J. F. Nye, "Three-beam model for studying dislocations in wave pulses," *Journal of Physics A*, vol. 20, no. 14, article 013, pp. 4673–4696, 1987.
- [24] I. Freund, N. Shvartsman, and V. Freilikh, "Optical dislocation networks in highly random media," *Optics Communications*, vol. 101, no. 3–4, pp. 247–264, 1993.
- [25] O. V. Angelsky, R. N. Besaha, and I. I. Mokhun, "Appearance of wave front dislocations under interference among beams with simple wave fronts," *Optica Applicata*, vol. 27, no. 4, pp. 273–278, 1997.
- [26] M. V. Berry and M. R. Dennis, "Knotting and unknotting of phase singularities: helmholtz waves, paraxial waves and waves in  $2 + 1$  spacetime," *Journal of Physics A*, vol. 34, no. 42, pp. 8877–8888, 2001.
- [27] M. V. Berry and M. R. Dennis, "Topological events on wave dislocation lines: birth and death of loops, and reconnection," *Journal of Physics A*, vol. 40, no. 1, pp. 65–74, 2007.
- [28] K. O'Holleran, M. J. Padgett, and M. R. Dennis, "Topology of optical vortex lines formed by the interference of three, four, and five plane waves," *Optics Express*, vol. 14, no. 7, pp. 3039–3044, 2006.
- [29] P. Kurzynowski, W. A. Woźniak, and M. Borwińska, "Regular lattices of polarization singularities: their generation and properties," *Journal of Optics*, vol. 12, no. 3, Article ID 035406, 2010.
- [30] I. Bialynicki-Birula and S. Bialynicka-Birula, "Vortex lines in electromagnetic field," *Physical Review A*, vol. 67, Article ID 062114, 2003.
- [31] I. Bialynicki-Birula, "Electromagnetic vortex lines riding atop null solutions of the Maxwell equations," *Journal of Optics A*, vol. 6, no. 5, pp. S181–S183, 2004.
- [32] Y. Lin, D. Rivera, Z. Poole, and K. P. Chen, "Five-beam interference pattern controlled through phases and wave vectors for diamondlike photonic crystals," *Applied Optics*, vol. 45, no. 31, pp. 7971–7976, 2006.
- [33] J. Becker, P. Rose, M. Boguslawski, and C. Denz, "Systematic approach to complex periodic vortex and helix lattices," *Optics Express*, vol. 19, no. 10, pp. 9848–9862, 2011.
- [34] J. Masajada and B. Dubik, "Optical vortex generation by three plane wave interference," *Optics Communications*, vol. 198, no. 1–3, pp. 21–27, 2001.
- [35] S. Vyas and P. Senthikumar, "Interferometric optical vortex array generator," *Applied Optics*, vol. 46, no. 15, pp. 2893–2898, 2007.
- [36] W. A. Woźniak and P. Kurzynowski, "Compact spatial polariscope for light polarization state analysis," *Optics Express*, vol. 16, no. 14, pp. 10471–10479, 2008.
- [37] J. Masajada, *Optical Vortices and Their Application to Interferometry*, Oficyna Wydawnicza Politechniki Wrocławskiej, Wrocław, Poland, 2004.
- [38] J. Masajada, "The interferometry based on regular lattice of optical vortices," *Optica Applicata*, vol. 37, no. 1–2, pp. 167–185, 2007.
- [39] J. Masajada, A. Popiołek-Masajada, and D. M. Wieliczka, "The interferometric system using optical vortices as phase markers," *Optics Communications*, vol. 207, no. 1–6, pp. 85–93, 2002.
- [40] J. Masajada, "Small-angle rotations measurement using optical vortex interferometer," *Optics Communications*, vol. 239, no. 4–6, pp. 373–381, 2004.
- [41] A. Popiołek-Masajada, M. Borwińska, and W. Frączek, "Testing a new method for small-angle rotation measurements with the optical vortex interferometer," *Measurement Science and Technology*, vol. 17, no. 4, pp. 653–658, 2006.

- [42] M. Borwińska, A. Popiołek-Masajada, and B. Dubik, "Reconstruction of a plane wave's tilt and orientation using an optical vortex interferometer," *Optical Engineering*, vol. 46, no. 7, Article ID 073604, 2007.
- [43] E. Frączek and J. Mrocza, "An accuracy analysis of small angle measurement using the Optical Vortex Interferometer," *Metrology and Measurement Systems*, vol. 16, no. 2, pp. 249–258, 2009.
- [44] P. Kurzynowski, W. A. Woźniak, and E. Frączek, "Optical vortices generation using the Wollaston prism," *Applied Optics*, vol. 45, no. 30, pp. 7898–7903, 2006.
- [45] A. Popiołek-Masajada, P. Kurzynowski, W. A. Wozniak, and M. Borwińska, "Measurements of the small wave tilt using the optical vortex interferometer with the Wollaston compensator," *Applied Optics*, vol. 46, no. 33, pp. 8039–8044, 2007.
- [46] P. Kurzynowski and M. Borwińska, "Generation of vortex-type markers in a one-wave setup," *Applied Optics*, vol. 46, no. 5, pp. 676–679, 2007.
- [47] M. Borwińska, A. Popiołek-Masajada, and P. Kurzynowski, "Measurements of birefringent media properties using optical vortex birefringence compensator," *Applied Optics*, vol. 46, no. 25, pp. 6419–6426, 2007.
- [48] W. A. Woźniak and M. Banach, "Measurements of linearly birefringent media parameters using the optical vortex interferometer with the Wollaston compensator," *Journal of Optics A*, vol. 11, no. 9, Article ID 094024, 2009.
- [49] W. Frączek and J. Mrocza, "Optical vortices as phase markers to wave-front deformation measurement," *Metrology and Measurement Systems*, vol. 15, no. 4, pp. 433–440, 2008.
- [50] C. V. Felde, P. V. Polyanski, and H. V. Bogatyryova, "Comparative analysis of techniques for diagnostics of phase singularities," *Ukrainian Journal of Physical Optics*, vol. 9, no. 2, pp. 82–90, 2008.
- [51] I. Mokhun and Y. Galushko, "Detection of vortex sign for scalar speckle fields," *Ukrainian Journal of Physical Optics*, vol. 9, no. 4, pp. 246–255, 2008.
- [52] V. G. Denisenko, A. Minovich, A. S. Desyatnikov, W. Krolikowski, M. S. Soskin, and Y. S. Kivshar, "Mapping phases of singular scalar light fields," *Optics Letters*, vol. 33, no. 1, pp. 89–91, 2008.
- [53] L. E. E. De Araujo and M. E. Anderson, "Measuring vortex charge with a triangular aperture," *Optics Letters*, vol. 36, no. 6, pp. 787–789, 2011.
- [54] E. Frączek, W. Frączek, and J. Masajada, "The new method of topological charge determination of optical vortices in the interference field of the optical vortex interferometer," *Optik*, vol. 117, no. 9, pp. 423–425, 2006.
- [55] E. Frączek, W. Frączek, and J. Mrocza, "The Experimental method for topological charge determination of optical vortices in a regular net," *Optical Engineering*, vol. 44, no. 2, Article ID 025601, 2005.
- [56] P. Kurzynowski, M. Borwinska, and J. Masajada, "Optical vortex sign determination using self-interference methods," *Optica Applicata*, vol. 40, no. 1, pp. 165–175, 2010.
- [57] J. Masajada, A. Popiołek, E. Frączek, and W. Frączek, "Vortex points localization problem in optical vortices interferometry," *Optics Communications*, vol. 234, no. 1–6, pp. 23–28, 2004.
- [58] G. Budzyń, E. Frączek, W. Frączek, and J. Mrocza, "Influence of a laser beam's frequency stability on dislocation of vortex points in an optical vortex interferometer," *Applied Optics*, vol. 45, no. 17, pp. 3982–3984, 2006.
- [59] A. Popiołek-Masajada and W. Frączek, "Evaluation of phase shifting method for vortex localization in optical vortex interferometry," *Journal of Optics & Laser Technology*, vol. 43, pp. 1219–1224, 2011.
- [60] J. Masajada, A. Popiołek-Masajada, and M. Leniec, "Creation of vortex lattices by a wavefront division," *Optics Express*, vol. 15, no. 8, pp. 5196–5207, 2007.
- [61] G. Ruben and D. M. Paganin, "Phase vortices from a Young's three-pinhole interferometer," *Physical Review E*, vol. 75, no. 2, Article ID 066613, 2007.
- [62] D. P. Ghai, S. Vyas, P. Senthilkumaran, and R. S. Sirohi, "Vortex lattice generation using interferometric techniques based on lateral shearing," *Optics Communications*, vol. 282, no. 14, pp. 2692–2698, 2009.
- [63] S. Vyas and P. Senthilkumaran, "Vortex array generation by interference of spherical waves," *Applied Optics*, vol. 46, no. 32, pp. 7862–7867, 2007.
- [64] W. Wang, S. G. Hanson, Y. Miyamoto, and M. Takeda, "Experimental investigation of local properties and statistics of optical vortices in random wave fields," *Physical Review Letters*, vol. 94, no. 10, Article ID 103902, 2005.
- [65] W. Wang, T. Yokozeki, R. Ishijima, M. Takeda, and S. G. Hanson, "Optical vortex metrology based on the core structures of phase singularities in Laguerre-Gauss transform of a speckle pattern," *Optics Express*, vol. 14, no. 22, pp. 10195–10206, 2006.
- [66] W. Wang, N. Ishii, S. G. Hanson, Y. Miyamoto, and M. Takeda, "Phase singularities in analytic signal of white-light speckle pattern with application to micro-displacement measurement," *Optics Communications*, vol. 248, no. 1–3, pp. 59–68, 2005.
- [67] W. Wang, T. Yokozeki, R. Ishijima et al., "Optical vortex metrology for nanometric speckle displacement measurement," *Optics Express*, vol. 14, no. 1, pp. 120–127, 2006.
- [68] V. P. Aksenov and O. V. Tikhomirova, "Theory of singular-phase reconstruction for an optical speckle field in the turbulent atmosphere," *The Journal of the Optical Society of America A*, vol. 19, no. 2, pp. 345–355, 2002.
- [69] V. P. Tychinsky, I. N. Masalov, V. L. Pankov, and D. V. Ublinsky, "Computerized phase microscope for investigation of submicron structures," *Optics Communications*, vol. 74, no. 1–2, pp. 37–40, 1989.
- [70] V. P. Tychinsky, "On superresolution of phase objects," *Optics Communications*, vol. 74, no. 1–2, pp. 41–45, 1989.
- [71] V. P. Tychinsky and C. H. F. Velzel, "Super-resolution in microscopy," in *Current Trends in Optics*, chapter 18, Academic Press, New York, NY, USA, 1994.
- [72] C. Velzel and J. Masajada, "Superresolution phase image microscope," *Optica Applicata*, vol. 29, no. 3, pp. 293–300, 1999.
- [73] B. Spektor, A. Normatov, and J. Shamir, "Experimental validation of 20nm sensitivity of Singular Beam Microscopy," in *Optical Measurement Systems for Industrial Inspection*, vol. 6616 of *Proceedings of SPIE*, Munich, Germany, June 2007.
- [74] B. Spektor, A. Normatov, and J. Shamir, "Singular beam microscopy," *Applied Optics*, vol. 47, no. 4, pp. A78–A87, 2008.
- [75] B. Spektor, A. Normatov, and J. Shamir, "Singular beam scanning microscopy: preliminary experimental results," *Optical Engineering*, vol. 49, no. 4, Article ID 048001, 2010.
- [76] J. Masajada, M. Leniec, E. Jankowska, H. Thienpont, H. Ottevaere, and V. Gomez, "Deep microstructure topography characterization with optical vortex interferometer," *Optics Express*, vol. 16, no. 23, pp. 19179–19191, 2008.
- [77] J. Masajada, M. Leniec, S. Bczyński, H. Thienpont, and B. Kress, "Micro-step localization using double charge optical vortex interferometer," *Optics Express*, vol. 17, no. 18, pp. 16144–16159, 2009.

- [78] J. Masajada, M. Leniec, and I. Augustyniak, "Optical vortex scanning inside Gaussian beam," *Journal of Optics*, vol. 13, Article ID 035714, 2011.
- [79] E. Frączek and G. Budzyn, "An analysis of an optical vortices interferometer with focused beam," *Optica Applicata*, vol. 39, no. 1, pp. 91–99, 2009.
- [80] O. Bryngdahl, "Radial and Circular fringe interferograms," *The Journal of the Optical Society of America A*, vol. 63, pp. 1098–1104, 1973.
- [81] O. Bryngdahl and W. H. Lee, "Shearing interferometry in polar coordinates," *The Journal of the Optical Society of America A*, vol. 64, no. 12, pp. 1606–1615, 1974.
- [82] P. Senthilkumaran, "Optical phase singularities in detection of laser beam collimation," *Applied Optics*, vol. 42, no. 31, pp. 6314–6320, 2003.
- [83] D. P. Ghai, P. Senthilkumaran, and R. S. Sirohi, "Single-slit diffraction of an optical beam with phase singularity," *Optics and Lasers in Engineering*, vol. 47, no. 1, pp. 123–126, 2009.
- [84] S. Fürhapter, A. Jesacher, S. Bernet, and M. Ritsch-Marte, "Spiral interferometry," *Optics Letters*, vol. 30, no. 15, pp. 1953–1955, 2005.
- [85] F. S. Roux, "Diffractive lens with a null in the center of its focal point," *Applied Optics*, vol. 32, no. 22, pp. 4191–4192, 1993.
- [86] N. R. Heckenberg, R. McDuff, C. P. Smith, and A. G. White, "Generation of optical phase singularities by computer generated hologram," *Optics Letters*, vol. 17, pp. 221–223, 1992.
- [87] A. A. Tovar, "Production and propagation of cylindrically polarized Laguerre-Gaussian laser beams," *The Journal of the Optical Society of America A*, vol. 15, no. 10, pp. 2705–2711, 1998.
- [88] D. G. Hall, "Vector-beam solutions of Maxwell's wave equation," *Optics Letters*, vol. 21, no. 1, pp. 9–11, 1996.
- [89] C. F. Li, "Integral transformation solution of free-space cylindrical vector beams and prediction of modified Bessel-Gaussian vector beams," *Optics Letters*, vol. 32, no. 24, pp. 3543–3545, 2007.
- [90] W. C. Tidwell, D. H. Ford, and W. D. Kimura, "Generating radially polarized beams interferometrically," *Applied Optics*, vol. 29, pp. 2234–2239, 1990.
- [91] S. C. Tidwell, G. H. Kim, and W. D. Kimura, "Efficient radially polarized laser beam generation with a double interferometer," *Applied Optics*, vol. 32, no. 27, pp. 5222–5229, 1993.
- [92] N. Passilly, R. de Saint Denis, K. Aït-Ameur, F. Treussart, R. Hierle, and J. F. Roch, "Simple interferometric technique for generation of a radially polarized light beam," *The Journal of the Optical Society of America A*, vol. 22, no. 5, pp. 984–991, 2005.
- [93] P. H. Jones, M. Rashid, M. Makita, and O. M. Maragò, "Sagnac interferometer method for synthesis of fractional polarization vortices," *Optics Letters*, vol. 34, no. 17, pp. 2560–2562, 2009.
- [94] R. Oron, S. Blit, N. Davidson, A. A. Friesem, Z. Bomzon, and E. Hasman, "The formation of laser beams with pure azimuthal or radial polarization," *Applied Physics Letters*, vol. 77, no. 21, pp. 3322–3324, 2000.
- [95] Q. Zhan, "Cylindrical vector beams: from mathematical concepts to applications," *Advances in Optics and Photonics*, vol. 1, no. 1, pp. 1–57, 2009.

## Research Article

# Canonical and Singular Propagation of Ultrashort Pulses in a Nonlinear Medium

Karl Glasner,<sup>1</sup> Miroslav Kolesik,<sup>2,3,4</sup> Jerome V. Moloney,<sup>1,2,3</sup> and Alan C. Newell<sup>1,2</sup>

<sup>1</sup> Department of Mathematics, University of Arizona, Tucson, AZ 85721-0089, USA

<sup>2</sup> Arizona Center for Mathematical Sciences, University of Arizona, Tucson, AZ 85721-0089, USA

<sup>3</sup> College of Optical Sciences, University of Arizona, Tucson, AZ 85721, USA

<sup>4</sup> Department of Physics, Constantine the Philosopher University, Nitra 94974, Slovakia

Correspondence should be addressed to Jerome V. Moloney, jml@acms.arizona.edu

Received 14 May 2011; Revised 13 July 2011; Accepted 14 July 2011

Academic Editor: Shunichi Sato

Copyright © 2012 Karl Glasner et al. This is an open access article distributed under the Creative Commons Attribution License, which permits unrestricted use, distribution, and reproduction in any medium, provided the original work is properly cited.

We examine the two types of singular behaviors of ultrashort pulses in a nonlinear medium, pulse steepening if the weak longitudinal dispersion is normal and collapse if it is anomalous. Connections with analogous behaviors of wave packets of almost monochromatic waves in strongly dispersive media are discussed.

## 1. Introduction

The drive to achieve ever higher local intensities with finite amounts of energy is the main reason that has led to much interest into the propagation characteristics of ultrashort pulses whose spectrum is broad, and whose widths are no more than several wavelengths of light. A second reason is that they exhibit novel singular behaviors, behaviors which are worth contrasting with those of “rogue” waves, familiar from ocean contexts and the “collapses” associated with the envelopes of almost monochromatic waves associated with singular solutions of equations of nonlinear Schrödinger type. A third reason is the ongoing program of attempting to create suitable conditions under which one might effectively propagate high intensity short pulses over long distances through gases such as the atmosphere.

Our aim in this short paper is to provide a unified mathematical description via a nonlinear partial differential equation that captures both type of singularity while avoiding the usual envelope approximations utilized in the nonlinear optics literature. Many of the ideas and some of the equation derivations, albeit in different formats, have appeared already in the literature; for example, in the recent works of Balakin et al. (BLMS; [1]) which in turn were informed by results going back to the eighties [2, 3]; the papers of Alterman and Rauch [4] and Schaffer and Wayne

[5], and the results of Kolesik and Moloney [6]. Indeed, in many cases the authors appeared to be unaware of each other's results. Our goals here are as follows.

We want to show that the series of governing equations (UPPE, an acronym for unidirectional pulse propagation equation) derived by Kolesik and Moloney [6] directly from Maxwell's equations using a Fourier decomposition of the electromagnetic fields can be reduced by asymptotic analysis to an equation for the dominant electric field in which all wavelength (short,  $\mu\text{m}$ ) scales have been removed, essentially by averaging over wavelength scales. We call the reduced equation RUPPE. In RUPPE, the electric field varies over distances associated with nonlinearity, diffraction, dispersion, and attenuation. The Fourier representation is particularly valuable because it shows clearly the circumstances in which nonlinearity has long distance cumulative, order one, effects. It will let us see, for example, how, if the pulse is broadband, dispersion in the direction of propagation (longitudinal dispersion) must necessarily be weak. This contrasts with the situation in which the pulse is almost monochromatic with a narrowband spectrum, in which case, with strong dispersion, the propagation equation will be more of nonlinear Schrödinger type.

We show how, by taking the inverse Fourier transform of RUPPE, we arrive at the modified Kadomtsev-Petviashvili

equation (MKPI) of type I which is closely related to the equation derived in the early eighties by Kuznetsov for acoustic waves [2], for which equation with cubic nonlinearity, various “blowup” results were found by Turitsyn and Falkovich [3], and which is the main equation used by BLMS in their analysis. If  $E_0(x, y, z, \tau = t - (n_0/c)z)$  is the dominant (either linearly or azimuthally polarized) component of the electric field, then the MKPI equation in nondimensional form is

$$\frac{\partial}{\partial \tau} \left( \frac{\partial E_0}{\partial z} + \frac{z_0 E_0^2}{z_{\text{NL}}} \frac{\partial E_0}{\partial \tau} - \frac{z_0 s}{z_{\text{disp}}} \frac{\partial^3 E_0}{\partial \tau^3} - \frac{z_0}{z_{\text{att}}} \frac{\partial^2 E_0}{\partial \tau^2} \right) = \frac{z_0}{z_{\text{diff}}} \delta^2 E_0. \quad (1)$$

Equation (1) shows how the right going Riemann invariant  $E_0$  of the underlying wave equation is deformed over long distances by a combination of nonlinear, diffraction, dispersion, and attenuation influences.

In (1),  $z_{\text{NL}}$ ,  $z_{\text{disp}}$ ,  $z_{\text{att}}$ , and  $z_{\text{diff}}$  are the nonlinear, dispersion, attenuation, and diffraction distances defined by

$$z_{\text{NL}} = \frac{n_0 c t_0}{3\pi \chi^{(3)} e_0^2}, \quad z_{\text{disp}} = \frac{2n_0 c t_0}{|B|}, \quad (2)$$

$$z_{\text{att}} = \frac{2n_0 c t_0}{A}, \quad z_{\text{diff}} = \frac{2n_0 L^2}{c t_0},$$

where  $s = \text{sgn } B$  and  $\chi^{(3)} e_0^2 = (8/3)n_0 n_2 I$  is related to the nondimensional pulse intensity,  $n_0, n_2$  the linear and nonlinear refractive indices,  $t_0$  pulse width,  $L$  beam width and  $z_0$  is the shortest distance (usually  $z_{\text{NL}}$  or  $z_{\text{diff}}$  over which  $E_0$  changes. The nondimensional coefficients  $B$  and  $A$  describe how the real and imaginary parts of the linear susceptibility deviate from constant values. The operator  $\delta^2$  is the Laplacian  $\partial^2/\partial x^2 + \partial^2/\partial y^2 = \partial^2/\partial r^2 + (1/r)(\partial/\partial r)$  if the field is asymmetric and linearly polarized and  $\partial^2/\partial r^2 + (1/r)(\partial/\partial r) - 1/r^2$  for the azimuthally polarized case.

We explore singular behavior in (1). By singular behavior, we mean that there will be a finite time singularity, namely unbounded growth tending to infinity in a finite time, in either the amplitude or the slope of the electric field. Dispersion, as indeed does dissipation, regularizes the singularity in that either the amplitude or slope becomes very large before the unbounded growth gets arrested. For example, if the singularity is in the slope, the pulse steepens until the dispersion or dissipation terms become sufficiently large so as to bring about a balance between the nonlinear steepening effect, manifested by the time derivative of the electric field cubed and the dissipation or dispersion. If the singularity is in the amplitude, then the arrest is a bit more subtle and involves the property that in two transverse space dimensions the collapsing pulse carries exactly the critical amount of energy (power) required to affect collapse. Any loss, through dissipation or radiative dispersion will have the effect of bringing the power below critical, and then the collapse slowly radiates away in waves. The point of the paper is to emphasize that because dispersion and dissipation are small when applied to the original pulse shape, the pulse

will evolve a long way towards the collapse state before being arrested, as indeed our numerics show.

We find that there are two distinct types of singular behavior exhibited by solutions of (1). If the dispersion is normal, namely  $B > 0$ , then the evolution of the electric field is dominated by the first two terms. The leading part of the pulse (it is the rear part if viewed from a fixed frame of reference) steepens until either dispersion causes the steepening front to form oscillations, or diffusion causes the front to develop a shock. This is the case studied by BLMS [1]. We make a very important point. Unlike KPI, namely where the nonlinearity is quadratic, the MKPI whose behavior in the longitudinal direction satisfies the modified Korteweg-de Vries equation, the difference in signs of nonlinearity and dispersion is crucial. For  $B > 0$ , the oscillations, which the steepening front produces, never become solitons. They are purely radiative and eventually disperse. Indeed what we show is that they behave rather like normal dispersion does in arresting the collapse of the two dimensional nonlinear Schrödinger equation discussed by us in the mid nineties [7]. Thus, the energy of the oscillating waves spreads into the transverse direction by four-wave resonant interactions. This behavior is clearly seen in our simulations and was extensively reported in the simulations of Kolesik and Moloney [6]. On the other hand, if dispersion is anomalous,  $B < 0$ , then solitons do form and destabilize into local collapses with an amplitude singularity when diffractive effects become important. By diffractive effects, we are referring to the dispersion brought about by the diffraction term which causes pulses whose carrier wavevector is not quite along the  $z$  axis to spread. We show that each collapse follows a self-similar form given by  $E \sim (Z - z)^{-1/3}$ ,  $r \sim (Z - z)^{2/3}$ , and  $\tau - \tau^*(z) \sim (Z - z)^{1/3}$ , where  $Z$  is the blowup point and  $\tau^*(z)$  follows the maximum of  $E_0$ .

We also point out that there is a distinct difference in collapse behavior between the linearly and azimuthally polarized cases but we leave it to a later paper [8] to report details.

Finally, we briefly describe how, in the case of strong longitudinal dispersion, a much weaker nonlinearity, and an almost monochromatic rather than broadband pulse, (1) takes on nonlinear Schrödinger form with normal ( $B > 0$ ) and anomalous ( $B < 0$ ) longitudinal dispersion. In that case, the behavior of the electric field envelope follows that discussed by Luther et al. [7].

## 2. Derivation of RUPPE and MKPI

To make the presentation as simple as possible and to postpone approximations until absolutely necessary, we start with an azimuthally polarized field  $E = \hat{\theta} E(r, z, t)$ , where  $\hat{\theta}$  is the unit vector in the angular direction and  $z$  is the direction of propagation. The result we obtain for a linearly polarized wave  $\vec{E} = \hat{e} E_0(x, y, z, t) + \dots$  will be almost the same except that it is necessary to include a small electric field component in the propagation direction  $z$  in order to satisfy the divergence free condition. In addition, the diffraction

operator will be the Laplacian  $\partial^2/\partial r^2 + (1/r)(\partial/\partial r)$  rather than  $\delta^2 = \partial^2/\partial r^2 + (1/r)(\partial/\partial r) - 1/r^2$ .

We take as constitutive relations  $\vec{B} = \mu\vec{H}$  and

$$\vec{D} = \varepsilon_0\vec{\theta}\left(E + \int_{-\infty}^t \chi(t-\tau)E(\tau)d\tau + \int_{-\infty}^t \chi^{(3)} \times (t-\tau_1, t-\tau_2, t-\tau_3)E(\tau_1)E(\tau_2)E(\tau_3)d\tau_1d\tau_2d\tau_3\right). \quad (3)$$

We write the Fourier transforms of  $E(r, z, t)$ , the linear and nonlinear susceptibility  $\chi(t)$  and  $\chi^{(3)}(t_1, t_2, t_3)$  to be  $e(r, z, \omega) = \int_{-\infty}^{\infty} E(r, z, t)e^{i\omega t}dt$ ,  $\hat{\chi}(\omega)$  and  $\hat{\chi}^{(3)}(\omega_1, \omega_2, \omega_3)$ , respectively. From Maxwell's equation  $\nabla \times \nabla \times \vec{E} = \mu(\partial^2\vec{D}/\partial t^2)$  and  $\mu\varepsilon_0 = 1/c^2$ , we obtain the exact relation

$$\begin{aligned} \frac{\partial^2 e}{\partial z^2} + \delta^2 e + \frac{\omega^2}{c^2}(1 + \hat{\chi}(\omega))e \\ = -\frac{2\pi\omega^2}{c^2} \int \chi^{(3)}(\omega_1, \omega_2, \omega_3)e(\omega_1)e(\omega_2)e(\omega_3) \\ \times \delta(\omega - \omega_1 - \omega_2 - \omega_3)d\omega_1d\omega_2d\omega_3, \end{aligned} \quad (4)$$

where  $\delta(x)$  is the Dirac delta function. Anticipating that we will be taking nonlinearity and diffraction to be small when compared to the linear response  $(n^2(\omega)\omega^2/c^2)e$ ,  $n^2(\omega) = 1 + \hat{\chi}(\omega)$ , we write  $e(r, z, \omega)$  as the sum of forward and backward fields. Let

$$e(r, z, \omega) = A(r, z, \omega)e^{ik_0(\omega)z} + B(r, z, \omega)e^{-ik_0(\omega)z}, \quad (5)$$

where  $k_0^2(\omega) = (\omega^2/c^2)(1 + \hat{\chi}_r(\omega))$ ,  $\hat{\chi}_r(\omega)$  the real part of  $\hat{\chi}(\omega)$  and make the free choice of a relation between  $A$  and  $B$  to be  $(\partial A/\partial z)e^{ik_0(\omega)z} + (\partial B/\partial z)e^{-ik_0(\omega)z} = 0$  (cf. method of variation of parameters). Then substituting (5) into (4), and adding and subtracting the free choice, we obtain the exact relations:

$$\begin{aligned} 2ik_0(\omega)\frac{\partial A}{\partial z} = -\frac{i\omega^2}{c^2}\hat{\chi}_i(\omega)A - \frac{i\omega^2}{c^2}\hat{\chi}_i(\omega)Be^{-2ik_0(\omega)z} \\ - \delta^2 A - \delta^2 Be^{-2ik_0(\omega)z} - \frac{2\pi}{c^2}\omega^2 Pe^{-ik_0(\omega)z}, \end{aligned} \quad (6)$$

where

$$\begin{aligned} P = \int \chi^{(3)}(\omega_1, \omega_2, \omega_3)\delta(\omega - \omega_1 - \omega_2 - \omega_3)d\omega_1d\omega_2d\omega_3 \\ \times (A(\omega_1)e^{-ik_0(\omega_1)z} + B(\omega_1)e^{-ik_0(\omega_1)z}) \\ \times (\omega_1 \rightarrow \omega_2)(\omega_1 \rightarrow \omega_3), \end{aligned} \quad (7)$$

and an equivalent equation for  $\partial B/\partial z$ . These equations are exact. There have been no approximations thus far. Note that the parameters  $A$  and  $B$  introduced here and discussed in the following are different from those introduced in (2).

We will now ask how can we approximate solutions to (6), and (7) if their right hand sides are small? Suppose we set  $A = A_0 + A_1 + \dots$ ,  $B = B_0 + B_1 + \dots$ . To leading

order,  $A_0$  and  $B_0$  will be independent of  $z$  but, in order to remove secular terms (terms growing as  $z$ ) in the iterates  $A_1, B_1, \dots$ , we will have to choose their slow variations  $\partial A_0/\partial z$  and  $\partial B_0/\partial z$  accordingly. So the first task is to identify the secular terms in  $A_1$  and  $B_1$ . The equation for  $A_1$  is

$$\begin{aligned} 2ik_0(\omega)\frac{\partial A_1}{\partial z} = -\frac{i\omega^2}{c^2}\hat{\chi}_i(\omega)A_0 - \frac{i\omega^2}{c^2}\hat{\chi}_i(\omega)B_0e^{-2ik_0(\omega)z} \\ - \delta^2 A_0 - \delta^2 B_0e^{-2ik_0(\omega)z} + P_0e^{-ik_0(\omega)z}, \end{aligned} \quad (8)$$

where  $P_0$  is  $P$  given in (7) with  $A$  replaced by  $A_0$ . Since, to leading order,  $A_0$  and  $B_0$  are  $z$  independent, it is clear that by direct integration from  $z = 0$  to  $z = z$ , the first and third terms on the right hand side of (8) are secular whereas the second and fourth, each of whose fast dependence is  $((e^{-ik_0(\omega)z} - 1)/ik_0(\omega))$ , are not. The more interesting discussion involves the nonlinear term one member of which, when integrated from 0 to  $z$ , is

$$\begin{aligned} \int \chi^{(3)}(\omega_1, \omega_2, \omega_3)A_0(\omega_1)A_0(\omega_2)A_0(\omega_3) \\ \times \left( \frac{e^{i(k_0(\omega_1)+k_0(\omega_2)+k_0(\omega_3)-k_0(\omega))z} - 1}{i(k_0(\omega_1) + k_0(\omega_2) + k_0(\omega_3) - k_0(\omega))} \right) \\ \times \delta(\omega - \omega_1 - \omega_2 - \omega_3)d\omega_1d\omega_2d\omega_3. \end{aligned} \quad (9)$$

In order to assess whether this term gives rise to secular behavior, we must ask what is its limiting behavior as  $z$  becomes large. To answer this, we require a little mathematics. We state two important results. If  $f(x)$  is an ordinary (measurable) function which is absolutely integrable and  $h(x)$  is not identically zero over a finite interval in the domain of integration, we know that  $\lim_{z \rightarrow \infty} \int f(x)\exp(ih(x)z)dx = 0$  (the Riemann-Lebesgue lemma) and that  $\lim_{z \rightarrow \infty} \int f(x)\Delta(h(x))dx = \int \pi \operatorname{sgn} z \delta(h(x)) + iP(1/h(x))f(x)dx$  where  $\Delta(h) = (e^{ihz} - 1)/ih$  and  $P$  denotes the Cauchy Principal Value. This means that as long as the amplitudes  $A_0(\omega), B_0(\omega)$  are ordinary (as opposed to, say, Dirac delta) functions and are absolutely integrable, the nonlinear terms will give a bounded contribution to  $A_1$  and be therefore nonsecular unless  $h(\omega_1, \omega_2, \omega_3) = k_0(\omega_1) + k_0(\omega_2) + k_0(\omega_3) - k_0(\omega)$  is identically zero over finite regions of  $\omega_2, \omega_3$  space (note:  $\omega_1 = \omega - \omega_2 - \omega_3$ ). Namely, the nonlinear term will give no cumulative long distance effect unless  $h$  is identically zero. This occurs only when there is no (at least to leading order) longitudinal dispersion.

This realization makes the propagation of narrow pulses with broadband spectrum for which the Fourier transforms are smooth very different from that of almost monochromatic pulses for which the Fourier amplitudes  $A_0(\omega)$  and  $B_0(\omega)$  are close to Dirac delta functions centered on some finite set of carrier frequencies. In the latter case, the nonlinear term can be secular either because of modal interactions leading to a nonlinear Schrödinger type nonlinearity or resonant interactions leading to coupled wave packets. Namely, if the amplitudes  $A_0(\omega)$  can be Dirac delta functions, the integral (9) becomes a sum and  $\Delta(h)$  will be equal to  $z$  at any points in  $\omega_1, \omega_2, \omega_3$  space with  $\omega_1 + \omega_2 + \omega_3 = \omega$  where the

resonant condition  $h \equiv k_0(\omega_1) + k_0(\omega_2) + k_0(\omega_3) - k_0(\omega) = 0$  holds. We return to this situation at the end of this section. For now, we focus on the case of narrow pulses for which the Fourier transforms  $e(r, z, \omega)$  are smooth in  $\omega$  and for which (9) is only secular when  $k_0(\omega_1) + k_0(\omega_2) + k_0(\omega_3) - k_0(\omega)$  is (almost) identically zero; namely, when  $k_0(\omega) = n_0(\omega/c)$  for constant  $n_0 = \sqrt{1 + \hat{\chi}_r}$ . It should now also be clear that any of the other products in  $P_0$  such as those involving  $A_0(\omega_1)A_0(\omega_2)B_0(\omega_3)$  with fast  $z$  behavior  $\Delta(k_0(\omega_1) + k_0(\omega_2) - k_0(\omega_3) - k_0(\omega))$  never give rise to secular terms. Thus, the interaction between right and left going pulses is small and does not affect their deformations.

We now return to (4) and write  $\hat{\chi}(\omega)$  as  $\hat{\chi}(\omega) - \hat{\chi}(0) + \hat{\chi}(0)$  and assume that  $\hat{\chi}(\omega) - \hat{\chi}(0)$  is small compared to  $\hat{\chi}(0)$ . This small difference will give rise to weak dispersion and attenuation. We recall that since  $E(r, z, t)$  and  $D(r, z, t)$  are real,  $\hat{\chi}(-\omega) = \hat{\chi}^*(\omega)$  so that  $\hat{\chi}_r(\omega)$  is even in  $\omega$  and  $\hat{\chi}_i(\omega)$  is odd in  $\omega$ . We will then obtain an equation (6) for  $A(r, z, \omega)$  in which  $k_0(\omega) = n_0(\omega/c)$ ,  $n_0 = \sqrt{1 + \hat{\chi}_r(0)}$  and the susceptibility deviation from  $\hat{\chi}(0)$  will manifest itself as the term  $((\hat{\chi}(0) - \hat{\chi}(\omega))/c^2)\omega^2 A$  on the right hand side of (6). When we now repeat the analysis, we find the only secular terms arising in  $A_1$  are those for which all fast dependence on  $z$  have been removed. To suppress these secular terms in  $A_1$ , we allow  $A_0$  to be slowly varying. We find the equation we call RUPPE,

$$\begin{aligned} 2in_0 \frac{\omega}{c} \frac{\partial A_0}{\partial z} &= \frac{\hat{\chi}(0) - \hat{\chi}(\omega)}{c^2} \omega^2 A_0 - \delta^2 A_0 \\ &- \frac{2\pi\omega^2}{c^2} \int \chi^{(3)}(\omega_1, \omega_2, \omega_3) A_0(\omega_1) A_0(\omega_2) A_0(\omega_3) \\ &\times \delta(\omega - \omega_1 - \omega_2 - \omega_3) d\omega_1 d\omega_2 d\omega_3. \end{aligned} \quad (10)$$

It says, in effect, that the evolution of the right going Fourier amplitude of the electric field in frequency space travels without deformation on distances of the order of many wavelengths but is distorted over much longer distances by a combination of dispersion and attenuation, diffraction and nonlinearity. It has several very important properties.

**2.1. Analogue of the Turitsyn-Falkovich Theorem.** In its simplest form, we take  $\hat{\chi}^{(3)}(\omega_1, \omega_2, \omega_3)$  constant and ignore  $(\hat{\chi}(0) - \hat{\chi}(\omega))$ . We define the flux, variance, current, and Hamiltonian to be

$$\begin{aligned} (a) \quad F(z) &= \int_z^\infty A_0 A_0^* r dr d\omega, \\ (b) \quad V(z) &= \int_0^\infty r^2 A_0 A_0^* r dr d\omega, \\ (c) \quad C(z) &= 2i \int_0^\infty \frac{r}{\omega} \left( A_0 \frac{\partial A_0^*}{\partial r} - A_0^* \frac{\partial A_0}{\partial r} \right) r dr d\omega, \end{aligned}$$

$$\begin{aligned} (d) \quad H(z) &= \delta \int r dr d\omega \frac{1}{\omega^2} \left( \frac{\partial A_0}{\partial r} + \frac{1}{r} A_0 \right) \left( \frac{\partial A_0^*}{\partial r} + \frac{1}{r} A_0^* \right) \\ &- \frac{8\pi}{c^2} \int r dr d\omega d\omega_1 d\omega_2 d\omega_3 \\ &\times A_0(\omega) A_0(\omega_1) A_0(\omega_2) A_0(\omega_3) \\ &\times \delta(\omega + \omega_1 + \omega_2 + \omega_3), \end{aligned} \quad (11)$$

where  $A_0(r, z, \omega)$  tends to zero at  $r = 0$  and  $r = \infty$ .

The azimuthally polarized case demands that the electric field be zero at  $r = 0$  in order that the magnetic field is zero (strictly speaking, the magnetic field will be very weak and longitudinally polarized but has no azimuthal component.) Then, we can easily show

$$\frac{dF}{dz} = 0, \quad \frac{dV}{dz} = C, \quad \frac{dC}{dz} = H, \quad \frac{dH}{dz} = 0. \quad (12)$$

Thus,  $d^2V/dz^2 = H$ , and if the constant (in  $z$ )  $H$  is negative at  $z = 0$ , then the positive definite variance  $V$  would become negative in a finite distance  $z$ . The only conclusion is that  $A_0(r, z, \omega)$  must develop a singularity before then.

If we include dispersion and ignore attenuation, then for  $\hat{\chi}(0) - \hat{\chi}(\omega) < 0$ , the case of anomalous dispersion, a similar conclusion holds. For normal dispersion, we will shortly see that a different kind of singularity occurs. It is not known for which class of nonconstant nonlinear susceptibilities  $\chi^{(3)}(\omega_1, \omega_2, \omega_3)$ , singularities must form.

**2.2. The MKPI Equation.** The facts that the forward and backward going components can be separated and that  $\hat{\chi}(\omega)$  is almost constant suggest that we rewrite (10) as an equation for the leading order component of the electric field

$$E_0 \left( r, z, \tau = t - \frac{n_0 z}{c} \right) = \frac{1}{2\pi} \int A_0(r, z, \omega) e^{-i\omega(t - (n_0 z/c))} d\omega. \quad (13)$$

We note that  $-i\omega A_0$  has its Fourier transform  $\partial E_0 / \partial \tau$ . Then if we take  $\hat{\chi}^{(3)}$  constant, (10) becomes

$$\frac{2n_0}{c} \frac{\partial^2 E_0}{\partial \tau \partial z} + \frac{2\pi \hat{\chi}^{(3)}}{c^2} \frac{\partial^2 E_0^3}{\partial \tau^2} + FT \left\{ \frac{\hat{\chi}(0) - \hat{\chi}(\omega)}{c^2} \omega^2 A_0 \right\} = \delta^2 E_0. \quad (14)$$

If we further approximate  $\hat{\chi}(0) - \hat{\chi}(\omega) = -iA\omega t_0 - B\omega^2 t_0^2$ ,  $A, B$  dimensionless, which is not unreasonable over a large frequency range for air, then (14) becomes

$$\frac{\partial}{\partial \tau} \left( \frac{\partial E_0}{\partial z} + \frac{3\pi \hat{\chi}^{(3)} E_0^2}{n_0 c} \frac{\partial E_0}{\partial \tau} - \frac{B t_0^2}{2n_0 c} \frac{\partial^3 E_0}{\partial \tau^3} - \frac{A t_0}{2n_0 c} \frac{\partial^2 E_0}{\partial \tau^2} \right) = \frac{c}{2n_0} \delta^2 E_0. \quad (15)$$

We introduce the nondimensional scalings

$$E_0 \rightarrow e_0 E_0, \quad \tau \rightarrow t_0 \tau, \quad z \rightarrow z_0 z, \quad x, y \rightarrow L(x, y) \quad (16)$$

and define

$$z_{\text{NL}} = \frac{n_0 c t_0}{3\pi \chi^{(3)} e_0^2}, \quad z_{\text{diff}} = \frac{2n_0 L^2}{c t_0}, \quad z_{\text{disp}} = \frac{2n_0 c t_0}{|B|},$$

$$z_{\text{att}} = \frac{2n_0 c t_0}{A}, \quad (17)$$

then (15) is ( $s = \text{sgn } B$ )

$$\frac{\partial}{\partial \tau} \left( \frac{\partial E_0}{\partial z} + \frac{z_0}{z_{\text{NL}}} E_0^2 \frac{\partial E_0}{\partial \tau} - \frac{s z_0}{z_{\text{disp}}} \frac{\partial^3 E_0}{\partial \tau^3} - \frac{z_0}{z_{\text{att}}} \frac{\partial^2 E_0}{\partial \tau^2} \right) = \frac{z_0}{z_{\text{diff}}} \delta^2 E_0 \quad (18)$$

which is the modified Kadomtsev-Petviashvili equation of type 1. If we include a plasma oscillation to account for low-frequency behavior, this is exactly the equation used by BLMS [1] and derived in other contexts by Kuznetsov and collaborators in the nineteen eighties. It is also connected with the work of both Alterman and Rauch [4] and Schaffer and Wayne [5] who realized that, to leading order, the propagation characteristics of short pulses are captured by looking at the deformation of the right going Riemann invariant  $E_0$ .

Depending on which effect is dominant, we will choose  $z_0$  accordingly. For air, for pulses of dimensionless power  $n_2 I (e = (3/8n_0)\chi^{(3)}e_0^2)$  of about  $10^{-4}$ , and for  $c t_0 \sim 10 \mu\text{m}$ , for beam widths of between  $100 \mu\text{m}$  and  $1 \text{mm}$ , the nonlinear and diffraction distances are of the order of  $10 \text{mm}$ , the dispersion length about  $100 \text{mm}$ . Attenuation is negligibly small. In this case, we choose  $z_0 = z_{\text{NL}}$ .

The behaviors in the two cases  $s = 1$  and  $s = -1$  corresponding to normal and anomalous dispersion are markedly different. For normal dispersion, as BLMS have shown, the forward slope (in  $\tau$ ; rear part in a fixed frame) steepens. Before it becomes multivalued, it is arrested by an outburst of regularizing oscillations. The BLMS analysis of the onset of this singular behavior captures the beginning of this behavior. The dimensional frequency range of these waves is given by  $\Omega \sim (1/t_0)\sqrt{z_{\text{disp}}/z_{\text{NL}}}$ . These waves, with wavevector  $\vec{k}_0 = (0, 0, k_0(\Omega))$ , pick up resonant four wave partners  $\vec{k}_{\pm} = (\pm \vec{k}_1, k_0(\Omega))$  via the resonance  $2\vec{k}_0 = \vec{k}_+ + \vec{k}_-$  and eventually disperse the energy transversely. The initial behavior is captured by the scaling  $\tau - (\rho_z/4\rho)r^2$  variable in BLMS (see their equation (29)).

This behavior is reminiscent of what happens for the three-dimensional nonlinear Schrödinger equation with a self-focusing nonlinearity, diffraction, and normal dispersion in the propagation direction. There, if normal dispersion is initially weak, the cross sectional part of the pulse with the greatest power begins to focus into a collapse as a result of the balance between diffraction and self focusing nonlinearity. By following the evolution in  $z$ , the propagation direction, of the self-similar scaling variables describing the collapse, we see the effect of normal dispersion is to arrest the collapse and spread the energy of the failed collapse via four-wave resonant interactions.

For anomalous dispersion, the behavior is very different. For linearly polarized waves, the electric field concentrates in

the vicinity of  $r = 0, z = Z$  at a retarded time  $\tau = \tau^*(Z)$ . For azimuthally polarized waves, the energy concentrates in a collapsing ring about  $r = 0$ . In the following section, we show the results of simulations in the normal and anomalous dispersion cases.

As the final remark of this section, we briefly describe what happens to an almost monochromatic pulse in the case where dispersion is strong, namely, where  $z_{\text{NL}} \gg z_{\text{disp}}$ . In that case, the envelope  $C(x, y, z, \tau)$  of a carrier wave  $\exp(-i\omega_0 \tau + ik_0(\omega_0)z)$  will evolve along its group velocity trajectory and deform under the joint action of a nonlinear Schrödinger nonlinearity  $C^2 C^*$ , diffraction  $(\partial^2 k_z / \partial k_x^2) \nabla^2 C$ , and dispersion  $(\partial^2 k_z / \partial \omega^2)(\delta^2 C / \delta \tau^2)$ .

A natural question to ask is: if, in a medium which contains a strong resonant band about  $\omega \sim \omega_0$ , is it possible that an initially broad band pulse can peel off an almost monochromatic wave packet which separates from the main pulse and whose further propagation behavior is determined by a nonlinear Schrödinger type equation describing its deformation due to dispersion and nonlinearity along its local group velocity trajectory  $t = k'_0(\omega_0)z$ ?

### 3. Numerical Study of the MKPI Equation

With the choice  $z_0 = z_{\text{NL}}$ , equation (18) can be written

$$\frac{\partial}{\partial \tau} \left( \frac{\partial E_0}{\partial z} + \frac{\partial E_0^3}{\partial \tau} - B \frac{\partial^3 E_0}{\partial \tau^3} - A \frac{\partial^2 E_0}{\partial \tau^2} \right) = D \Delta_{\perp} E_0, \quad (19)$$

where

$$B = \frac{z_{\text{NL}}}{z_{\text{disp}}}, \quad A = \frac{z_{\text{NL}}}{z_{\text{att}}}, \quad D = \frac{z_{\text{NL}}}{z_{\text{diff}}}. \quad (20)$$

The discussion will be limited to the case of plane polarization  $\Delta_{\perp} = \partial^2 / \partial x^2 + \partial^2 / \partial y^2$ .

The focus of this section is to study the qualitative aspects of (19), with particular attention on the role of dispersion in preventing or promoting singular behavior. It is notable that for the case of one transverse dimension ( $\Delta_{\perp} = \partial^2 / \partial y^2$ ), much is already understood about the MKP equation (see e.g., Klein and Saut [9]). To our knowledge, the only detailed study of the three dimensional case in the nonlinear optics context was conducted by Balakin et al. [1]. We will compare their findings to ours below.

Numerical simulations are used to illustrate the behavior of solutions of (19). Our method is fairly standard, employing spectral (Fourier and Hankel transform) representations of  $\tau$  and  $r$  derivatives. Approximation of the  $z$ -derivative employs fourth-order exponential time differencing [10, 11]. The computational domain is periodic in  $\tau$ , which has the effect of cutting off small, physically irrelevant frequencies.

Our main attention will focus on the effects of large frequency dispersion encoded in the parameter  $B$ . To this end we fix  $A = 0$  and  $D = 1$ , and assume radial symmetry ( $\Delta_{\perp} E_0 = r^{-1}(r[E_0]_r)_r$ ). It is particularly instructive to compare normal ( $B > 0$ ) to anomalous ( $B < 0$ ) dispersion. While the former is expected for optical pulses, the latter case demonstrates the significance of high frequency dispersion and the need for normal dispersion as a regularizing mechanism.

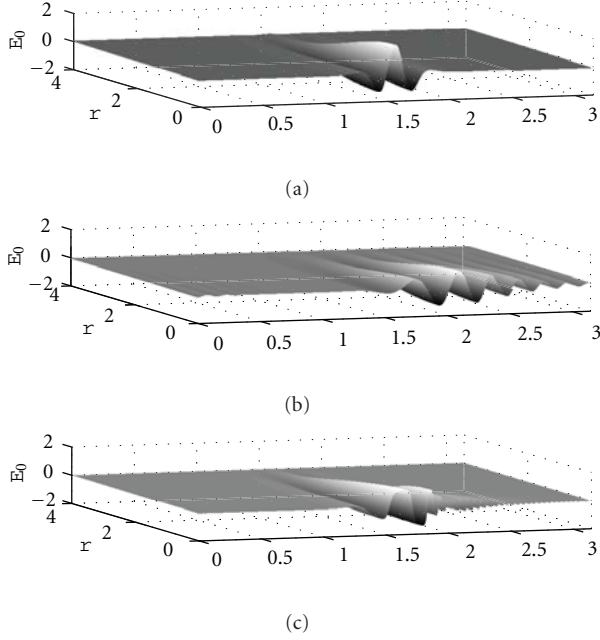


FIGURE 1: Evolution of a narrow pulse (a) for large ( $B = 0.1$ ), (b) and small ( $B = 0.0001$ ), (c) normal dispersion at early stages ( $z = 0.2$ ). In the latter case, the profile steepens, corresponding to the generation of higher frequency components.

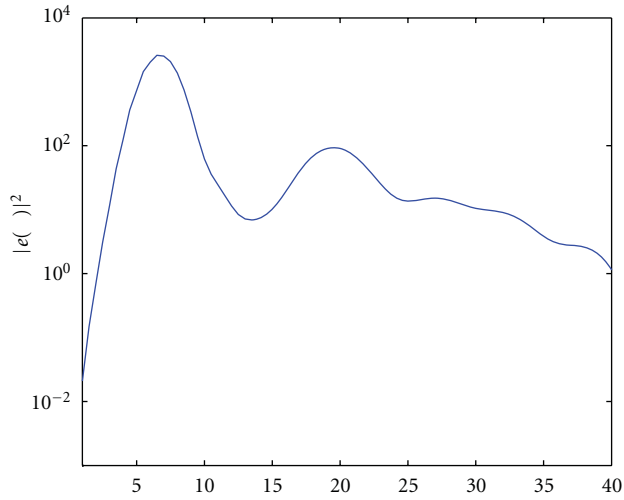


FIGURE 2: Spectral content of a pulse at early stages of evolution, showing generation of third harmonics ( $B = 0.0001$ ).  $e(\omega)$  is the Fourier transform of the centerline profile  $E_0(r = 0)$ .

**3.1. Normal Dispersion.** We consider initial data corresponding to a short pulse of unit width

$$E_0(r, z = 0, \tau) = \exp(-r^2)f(\tau), \quad (21)$$

where  $f$  has Fourier transform  $f_0 \exp(-(\omega - 2\pi)^2)$  and  $f_0$  is chosen so that the maximum amplitude of  $E_0(r, z = 0, \tau)$  is equal to one.

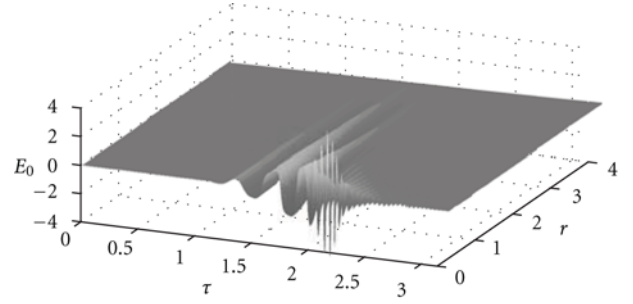


FIGURE 3: Self-focusing of a pulse for small normal dispersion ( $B = 0.0001$ ) when  $z = 1$ . Compression in the transverse direction is apparent in the back ( $\tau$  large) of the pulse.

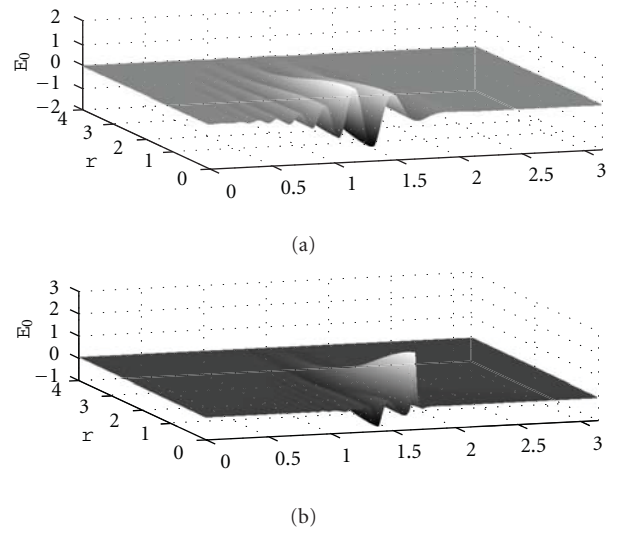


FIGURE 4: Evolution of a pulse for large ( $B = -1$ ), (a) and small ( $B = -0.001$ ), (b) anomalous dispersion. In the latter case, there is compression both temporally and in the transverse direction. The bottom figure shows an incipient collapse event that will develop into a singularity with infinite amplitude.

Consider first the case of large normal dispersion  $B = 0.1$ . In this situation, the pulse does not retain its structure, but rather disintegrates into a wave train dominated by a small band of frequencies (Figure 1, middle).

When the effect of dispersion is smaller ( $B = 0.0001$ ), one observes steepening of the pulse (Figure 1(c)). This coincides with generation of harmonics by four-wave interactions (Figure 2). By comparing the effective size of nonlinear and dispersive terms, one sees that formation of a shock will be arrested when steepening reaches a dimensional timescale  $\tau_{\max} \approx t_0 B^{-1/2}$ . By virtue of  $B$  depending inversely on initial amplitude, it follows that stronger pulses generate higher frequencies.

At a propagation distance comparable to  $z_0$ , self-focusing is apparent (Figure 3). We observe that compression in the transverse direction is stronger when normal dispersion is smaller. This might be expected, since normal dispersion is

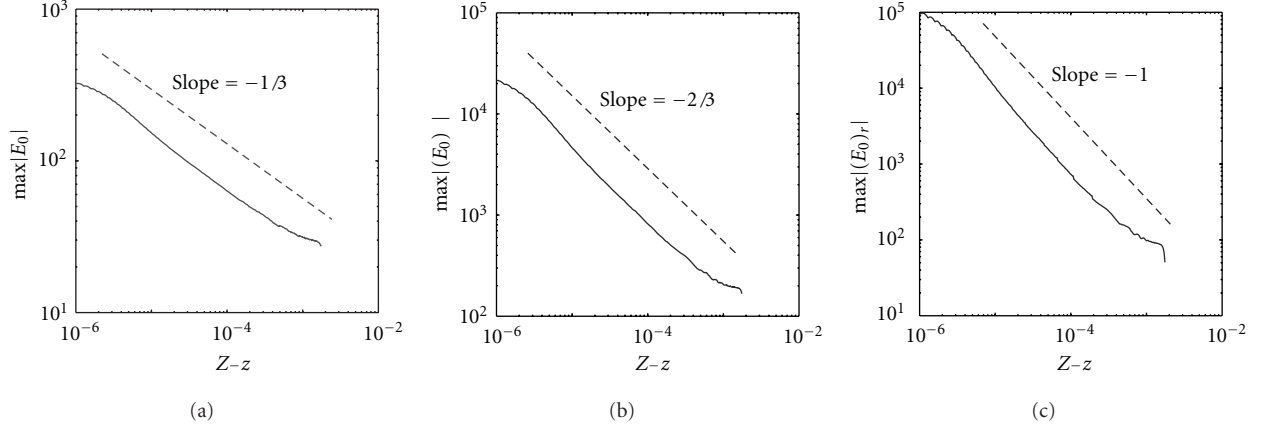


FIGURE 5: The maximum amplitude of  $E_0$  and its derivative during the collapse. The results are consistent with the power law behavior (22) derived in the text.

known to prevent self-focusing collapse in the monochromatic limit described by the nonlinear Schrödinger equation [7].

**3.2. Anomalous Dispersion and Singular Collapse.** The case  $B < 0$  was also studied using the same initial data. This is expected to be different since finite time singularities may occur. In analogy to the focusing nonlinear Schrödinger equation, one can show this by use of a virial-type argument [1, 3].

When  $B = -1$ , no singular behavior is observed. Rather, breakup of the pulse into a wave train occurs much like the large normal dispersion case. (Figure 4(a)). This is analogous to the situation in the nonlinear Schrödinger equation where solutions do not have sufficient power for collapse.

In contrast, when  $B = -0.001$ , the pulse collapses (Figure 4(b)) in both  $\tau$  and  $r$ , and the amplitude grows without bound. This occurs at a point where  $(E_0)_\tau$  is large, suggesting that blowup is initiated when dispersive effects become significant.

The quantitative aspects of this singularity can be analyzed by assuming that scales behave as power laws

$$E_0 \sim (Z-z)^\alpha, \quad \tau \sim (Z-z)^\beta, \quad r \sim (Z-z)^\gamma, \quad (22)$$

where  $z = Z$  is the blowup point. Balancing dispersion, nonlinearity and diffractive effects for  $z \rightarrow Z$  requires

$$\alpha - \beta - 1 = 3\alpha - 2\beta = \alpha - 4\beta = \alpha - 2\gamma, \quad (23)$$

which means  $\alpha = -1/3$ ,  $\beta = 1/3$ ,  $\gamma = 2/3$ . These scalings were confirmed numerically (Figure 5).

Numerical evidence also suggests that collapse occurs in a universal, self-similar fashion (Figure 6). One may derive an equation for the profile by using the ansatz

$$E_0 = (Z-z)^{-1/3} U(\xi, \eta), \quad \xi = (Z-z)^{-1/3}(\tau - \tau^*(z)), \\ \eta = (Z-z)^{-2/3} r, \quad (24)$$

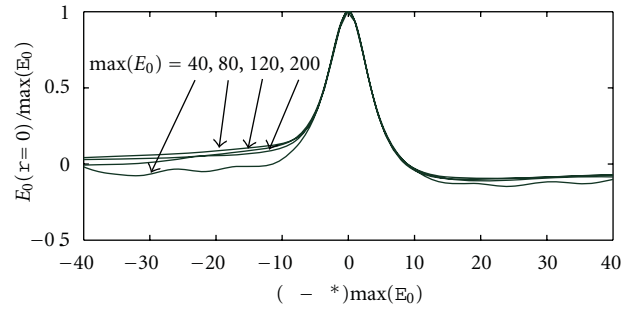


FIGURE 6: Scaled profiles of  $E_0$  along the centerline  $\eta = (Z-z)^{-2/3}r = 0$ , showing collapse onto a single self-similar profile. Similar results hold for  $\eta \neq 0$ .

where the blowup point is at  $(\tau, r, z) = (\tau^*(Z), 0, Z)$ . Inserting (24) into (19) gives the similarity equation (ignoring the attenuation term)

$$\left( \frac{1}{3} [U + \xi U_\xi + 2\eta U_\eta] + U^2 U_\xi + B U_{\xi\xi\xi} \right)_\xi - \frac{D}{\eta} (\eta U_\eta)_\eta = 0. \quad (25)$$

Properties of (25) are still under investigation.

**3.3. Shock Formation Versus Blowup.** Our numerical findings indicate two types of singular or nearly singular behavior. The first type is characterized by steepening of the pulse front. Normal dispersion always appears to arrest steepening that would lead to a shock-type solution. The other candidate for singular behavior is blowup, that is, unbounded growth in amplitude. This appears to only occur for anomalous dispersion.

Balakin et al. [1] make a theoretical prediction of the nature of collapse in (19). The crux of their argument is that dispersion at high frequencies (represented by our  $B$  term) can be ignored as the pulse amplitude grows. This leads to

the assertion that the dominant behavior is described by the equation ( $\xi, \theta$  are modified coordinates [1])

$$w_\xi + 3w^2 w_\theta = 0. \quad (26)$$

They conclude that shock formation should preempt collapse.

In contrast, we find that unless dispersion is exactly zero, there is no circumstance which leads to shock formation. We note that there is an inconsistency in the argument that leads to (26). During such an event,  $E_\tau$  and higher order derivatives grow without bound. This means that the fourth-order dispersive term in (19) should in fact become stronger, not weaker, relative to the size of the nonlinear term. On the other hand, (26) probably does capture the steepening behavior during the early phase of pulse evolution.

#### 4. Summary and Conclusion

In this paper, we have derived an ultra-broadband electromagnetic propagator as a limiting form of the UPPE equation of Kolesik and Moloney [6]. The resulting MKPI equation, derived using asymptotic analysis, allows us to isolate two key singularities, namely, blowup and shock formation and their regularization due to weak linear dispersion. Our results are related to and extend those of Balakin et al. [1]. The MKPI equation derived here captures the nonlinear evolution of the full electromagnetic field in contrast to narrowband nonlinear envelope NLSE equation. Consequently, it should be relevant to the generation of higher harmonic waves during filamentation in extended gaseous media. However, many open questions remain to be addressed. For example, in this ultra-broadband limit, the linear dispersion and absorption spectral landscape spans the ultraviolet to far infrared portion of the electromagnetic spectrum and will need to be represented by a more general form than that used here. Additionally, as a spectrum broadens due to nonlinear propagation, it will be necessary to include real absorption (and associated dispersion) features associated with real resonances at both ends of this broad electromagnetic spectrum—it is anticipated that such resonances will provide a novel nonlocal regularization mechanism for the singularities discussed here. Moreover, a switch in sign of the group velocity dispersion from normal to anomalous as such resonance features are traversed suggests the possibility of novel dispersive waves or possibly soliton-like structures being emitted. Furthermore, at the very high field intensities under consideration here, strong field ionization becomes important and coupling to an electron-ion plasma will need to be included. This question is controversial in the current literature, and there are arguments to support “ionization-free” nonlinear saturation of the cubic nonlinearity in the case of ultrashort pulse propagation in air [12].

#### Acknowledgment

This work was supported by an Air Force Office of Scientific Research Multidisciplinary University Research Initiative (MURI) Grant FA9550-10-1-0561.

#### References

- [1] A. A. Balakin, A. G. Litvak, V. A. Mironov, and S. A. Skobelev, “Structural features of the self-action dynamics of ultrashort electromagnetic pulses,” *Journal of Experimental and Theoretical Physics*, vol. 104, no. 3, pp. 363–378, 2007.
- [2] E. A. Kuznetsov, S. L. Muske, and A. V. Shafarenko, “Collapse of acoustic waves in media with positive dispersion,” *JETP Letters*, vol. 37, no. 5, pp. 241–247, 1983.
- [3] S. K. Turitsyn and E. G. Falkovich, “Stability of of magnetoelastic solitons and self-focusing of sound in antiferromagnets,” *Soviet Physics—JETP*, vol. 62, pp. 146–152, 1985.
- [4] D. Alterman and J. Rauch, “Diffractive short pulse asymptotics for nonlinear wave equations,” *Physics Letters A*, vol. 264, no. 5, pp. 390–395, 2000.
- [5] T. Schaffer and C. E. Wayne, “Propagation of ultra-short optical pulses in cubic nonlinear media,” *Physica D*, vol. 196, no. 1-2, pp. 90–105, 2004.
- [6] M. Kolesik and J. V. Moloney, “Nonlinear optical pulse propagation simulation: from Maxwell’s to unidirectional equations,” *Physical Review E*, vol. 70, no. 3, Article ID 036604, 11 pages, 2004.
- [7] G. Luther, J. V. Moloney, and A. C. Newell, “The effects of normal dispersion on collapse events,” *Physica D*, vol. 74, no. 1-2, pp. 59–73, 1996.
- [8] J. Allen-Flowers and K. G. Glasner, *in preparation*.
- [9] C. Klein and J.-C. Saut, “Numerical study of blow up and stability of solutions of generalized Kadomtsev-petviashvili equations,” [http://arxiv.org/PS\\_cache/arxiv/pdf/1010/1010.5510v1.pdf](http://arxiv.org/PS_cache/arxiv/pdf/1010/1010.5510v1.pdf).
- [10] S. M. Cox and P. C. Matthews, “Exponential time differencing for stiff systems,” *Journal of Computational Physics*, vol. 176, no. 2, pp. 430–455, 2002.
- [11] A.-K. Kassam and L. N. Trefethen, “Fourth-order time-stepping for stiff PDEs,” *SIAM Journal on Scientific Computing*, vol. 26, no. 4, pp. 1214–1233, 2005.
- [12] P. Bejot, J. Kasparian, S. Henin et al., “Higher-order kerr terms allow ionization-free filamentation in gases,” *Physical Review Letters*, vol. 104, no. 10, article 103903, 2010.

## Research Article

# Wavelength Dependence of the Polarization Singularities in a Two-Mode Optical Fiber

V. V. G. Krishna Inavalli, Vijay Pottapinjara, and Nirmal K. Viswanathan

*School of Physics, University of Hyderabad, Hyderabad 500 046, India*

Correspondence should be addressed to Nirmal K. Viswanathan, nirmalkv@hotmail.com

Received 14 May 2011; Revised 3 July 2011; Accepted 7 July 2011

Academic Editor: Shunichi Sato

Copyright © 2012 V. V. G. Krishna Inavalli et al. This is an open access article distributed under the Creative Commons Attribution License, which permits unrestricted use, distribution, and reproduction in any medium, provided the original work is properly cited.

We present here an experimental demonstration of the wavelength dependence of the polarization singularities due to linear combination of the vector modes excited directly in a two-mode optical fiber. The coherent superposition of the vector modes excited by linearly polarized Gaussian beam as offset skew rays propagated in a helical path inside the fiber results in the generation of phase singular beams with edge dislocation in the fiber output. The polarization character of these beams is found to change dramatically with wavelength—from left-handed elliptically polarized edge dislocation to right-handed elliptically polarized edge-dislocation through disclinations. The measured behaviour is understood as being due to intermodal dispersion of the polarization corrections to the propagating vector modes, as the wavelength of the input beam is scanned.

## 1. Introduction

Singular optics is the new branch of modern physical optics that deals with a wide class of effects associated with phase singularities in wave fields and topology of wave fronts [1]. There are three levels of optical singularities: ray singularities (caustics), singularities of plane polarized waves (scalar fields), and polarization singularities of vector light fields that are extensively researched in the recent times as several new possibilities for applications are being explored [2, 3]. Among the most interesting objects of research in singular optics are the polarization singularities (PS), arising in spatially inhomogeneously polarized light fields [2, 3]. The singular structure of such a field is formed by the disclination of the wavefront ( $d$ -singularities), as well as by  $C$ -points and  $L$ -contours observed in the plane perpendicular to the direction of propagation of a paraxial optical beam [4]. PSs are studied extensively in fully developed speckle (random) fields, either from a highly scattering medium or in the output from a multimode optical fiber [3, 5]. Though the random fields are a research area of fundamental importance to study the generic features of optical singularities, their properties are highly statistical in nature and at this point appear to have limited applications [2, 3].

First realized by Zel'dovich et al., the output radiation field from a multimode optical fiber is replete with fork-like interference structure, indicative of its vortical nature [6]. In 2002 Volyar demonstrated that the appearance of optical vortices in the low-mode fiber output are due to the existence of guided modes and discussed their main features [5]. Based on their extensive work on fiber singular optics and subsequently extended by Alexeyev et al., to study the propagation of optical vortices in weakly guiding perturbed fibers [7] it is now well established that the radiation field of low-mode optical fibers exhibit singularity points, whose position depends on the excitation conditions [8, 9], external perturbations, and orientation of polarizer at the output of the fiber [10]. The number of guided modes excited in the fiber and their weights are important to understand and analyze the formation of singularity in the fiber output. One of the methods is where the mode composition is analyzed qualitatively by comparing the output radiation pattern with numerically simulated intensity distributions [11]. In the case of two-mode fibers the mode groups with same azimuthal ( $l$ ) and radial ( $m$ ) indices are excited and the mode weights from within the group of same index " $l$ " with a singularity in the radiation field are considered [5]. It is also

important to remember that the intensity distributions in the fiber output are affected by the mode dispersion arising from within the mode group [12].

In addition, in optical fibers, as a rule, the input polarization changes by virtue of the birefringence of the medium [13]. For a fixed linear input polarization the evolution of polarization along the fiber with residual linear birefringence is measured either by cutback technique or wavelength scanning method [14, 15]. The measured wavelength dependence of the output polarization state moves along a trajectory on the Poincaré sphere [16, 17]. In addition, for skew rays launched into the fiber, the polarization vector of the light ray rotates as it propagates along a twisted path in the inhomogeneous fiber medium [18]. Skew rays are launched into the fiber by adjusting the position and the angle of illumination at the fiber input end to predominantly excite rays with right or left helicity  $\exp(\pm il\phi)$  modes of the axially symmetric fiber [19]. The birefringence properties of the step-index optical fiber are observed as a difference in the polarization corrections  $\delta\beta$  to the propagation constants  $\tilde{\beta}$  of the azimuthally symmetric linearly polarized OV (LV) or circularly polarized (CP) mode [20]. The intermodal dispersion due to the difference in the propagation constants of the fiber modes and their polarization correction leads to vector inhomogeneity of the output field from the fiber [7, 20].

In this paper we present our experimental results on the wavelength dependence of the vector inhomogeneity and hence of the polarization singularity generated in the output of a two-mode optical fiber (TMF). The input excitation conditions are so chosen to result in a combination of right and left elliptically polarized two-lobe output intensity pattern via selective excitation of the guided vector-vortex modes of opposite charges. The elliptically polarized singular beam is formed due to coherent coaxial mixing of weighted orthogonally polarized single-charged Laguerre-Gauss (LG) modes of the fiber. As the wavelength of the input beam is scanned over a range from 740–760 nm we track the changes in the intensity, phase, and polarization of the output beam from the TMF. The phase and polarization character of the output beam from the TMF are characterized using the interferometer and Stokes parameter measurements. A custom Matlab code is developed to map the polarization ellipses, calculated from the measured Stokes parameters, directly onto the output beam to follow the polarization evolution of different parts of the beam as the input beam wavelength is scanned. Using the normalized Stokes parameters ( $S_1/s_0$ ,  $S_2/s_0$ , and  $S_3/s_0$ ) the trajectory at a point of the elliptically polarized output beam from the TMF is tracked on the Poincaré sphere as a function of input wavelength. The output beam intensity and the polarization ellipse parameters ( $b$ ,  $\psi$ ) show periodic behaviour, clearly indicating change in the rotation direction of the polarization ellipse from right to left through linear polarization as a function of wavelength of the input beam, in the linear regime of operation. Thus, the polarization character of the output beam from the TMF is found to change dramatically—from left-handed elliptically polarized edge-dislocation into a

right-handed elliptically polarized-edge dislocation through disclinations. The measured behaviour is understood to be as due to intermodal dispersion of the vector modes and their polarization correction as the wavelength of the input beam is scanned. The wavelength scanning method for such measurements has the added advantage that the orientation of the fiber is not altered during the measurements and is a nondestructive method.

## 2. Experimental Details

Schematic of the experimental setup used for the generation of polarization singular beams using a TMF is shown in Figure 1 along with the setup to characterize the phase and polarization singularities of the beam. We first generate the desired singular beam at a given wavelength, carry out the required interference and Stokes parameters measurements on the beam, and repeat the same for different wavelengths spaced uniformly. A tuneable continuous-wave (CW) Ti: Sapphire laser (MBR 110, Coherent, USA) is used as the source of light. The overall wavelength range of operation of the laser is 700 nm–1000 nm and the range of interest to us here is 740–760 nm, which is in the middle of the two-mode regime ( $2.4048 < V < 3.8317$ ) of the fiber. The laser output is linearly polarized (500:1) TEM<sub>00</sub> mode. A 4% reflection from the glass plate is taken and coupled to an Optical Spectrum Analyzer (AQ 6370B, Yokogawa, Japan) to monitor the wavelength of the light. A Glan-Thomson polarizer (GTP) ( $>10^5:1$ ) and a half-wave plate (HWP) are used to have a better control on the polarization of the input beam launched into the TMF (HI 980 fiber of length 32.2 cm) thereby controlling the output beam characteristics. A modified Mach-Zender interferometer is constructed in parallel to measure the phase characteristics of the generated beam. An  $R/T = 50/50$  beam splitter is used to split the incoming light beam into two beams of almost equal intensity. The beam passing through the beam-splitter (BS<sub>1</sub>) is focused using a microscope objective lens L<sub>1</sub> (0.20 NA and 10x) to couple the light into the fiber, whose input end is fixed on a 3-axis precision launching mount. The output end of the fiber is held using a v-groove clamp and the light output from the fiber is collimated using another objective lens L<sub>2</sub> (0.40 NA and 20x) as shown in Figure 1. The reference beam that is reflected off the BS<sub>1</sub> and the output beam from the fiber are made almost collinear using the beam splitter (BS<sub>2</sub>). A CCD camera connected to computer via IEEE 1394 card is used to capture the images of the light beam at the fiber and the interferometer output. A stop (S) is used to block the reference beam whenever it is not required.

The desired output beam (with embedded dislocations and disclinations) from the TMF is produced by adjusting the controls—HWP orientation angle, and the launching conditions at a given wavelength of the input beam and for a fixed fiber length, as discussed in [9]. The images of the direct output beam from the TMF and the corresponding interference pattern are first captured using the CCD camera. The Stokes parameter of the beam is calculated using the six images captured by first introducing a polarizer (with its axis

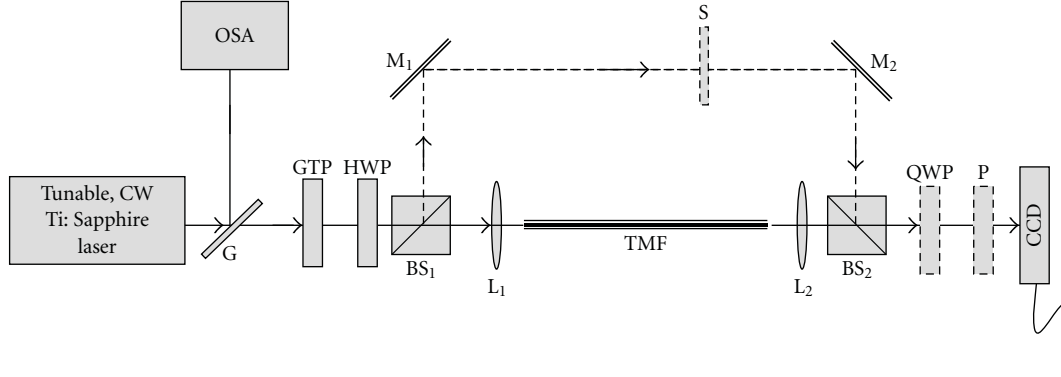


FIGURE 1: Schematic of the experimental setup use to generate and manipulate polarization singular beams using a two-mode optical fiber. G: Glass Plate; GTP: Glan-Thomson Polarizer; HWP: Half-Wave Plate; BS: Beam-splitter; L: Objective Lens; S: Stop; QWP: Quarter-Wave Plate; P: Polarizer; CCD: Camera.

oriented at  $0^\circ$ ,  $45^\circ$ ,  $90^\circ$ , and  $135^\circ$ ) and then with the QWP (at  $45^\circ$  and  $135^\circ$ ) and polarizer (oriented at  $90^\circ$ ) combination. Without disturbing the launching conditions or the orientation of the polarization sensitive optical components in the setup, the wavelength of the laser is scanned from 740–760 nm in steps of 1 nm (by tuning the birefringent filter in the laser cavity) and the above-mentioned measurements are repeated for all the output beams. From the measurements we observe that the modal characteristics (both intensity and polarization) of the beam changes dramatically with the input laser wavelength as the propagation constants ( $\beta_i$ ) of the vector modes are wavelength dependent.

### 3. Results and Discussion

For the input wavelength of the Ti: Sapphire laser tuned to  $\lambda_1 = 740$  nm and the HWP oriented at  $0^\circ$ , the linear vertically polarized Gaussian beam is coupled into the cleaved input end of the TMF. By placing the fiber at the focal point of the objective lens  $L_1$  and adjusting the “x” and “y” positions of the fiber we launch offset skew rays into the fiber. The output two-lobe intensity pattern is similar to the  $HG_{01}$  mode of laser resonators with a  $\pi$ -phase shifted interference pattern between the lobes measured using the CCD camera and shown in Figures 2(a) and 2(b). Assuming that the linear vertically polarized Gaussian input beam coupled into the TMF excites the CP mode  $|\text{CP}(0)\rangle = \begin{pmatrix} 1 \\ 0 \end{pmatrix} \cos\varphi$  within the first few millimetre of the fiber, the mode at the output of the fiber of length “ $l$ ” can be written as being due to the superposition of the fiber’s modes as [20]

$$|\text{CP}(z=l)\rangle = \frac{1}{2} \left[ |1, 1, 1\rangle e^{i\beta_1 l} + |\text{TM}_{01}\rangle e^{i\beta_4 l} + i|\text{TE}_{01}\rangle e^{i\beta_3 l} \right]. \quad (1)$$

Assuming that there is no spin-orbit interaction between the excited modes the distribution of the field corresponding to the field looks like  $I_{\text{CP}}(z) \propto 2\cos^2(\varphi - \alpha l)$  and rotates by an angle “ $\alpha l$ ” during the propagation through the fiber or when the wavelength is changed due to the dispersion of the propagation constants of the modes excited [20]. However, the propagation of the excited fiber modes along a twisted

path also changes the polarization distribution of the ideal linearly polarized modes due to the fiber birefringence.

Next, from the six polarization measurements on the output beam we calculate the Stokes parameters as shown in Figure 2(c). The scale of each Stokes parameter map (Figure 2(c)) is custom set to highlight that even small differences in the data will not be lost. As can be seen from the  $S_3$  Stokes parameter map, there is a small part of the left lobe which is right circularly polarized and the same is true for the other lobe and these portions are on diagonally opposite parts of the mode. The orientation of the ellipses is read from the  $S_1$  and  $S_2$  Stokes parameters. Overall, the part right- and left-handed elliptically polarized (REP/LEP) beam measured at the fiber output shown in Figure 1(d) is the resultant of the superposition between the vector modes excited in the fiber by linearly polarized rotating beam inside the fiber, akin to the propagation of linearly polarized optical vortex  $|\text{LV}(z)\rangle$  in the TMF given by [20]

$$|\text{LV}(z=l)\rangle = \frac{1}{2} \left[ |1, 1, 1\rangle e^{i\beta_1 l} + |\text{TM}_{01}\rangle e^{i\beta_4 l} - i|\text{TE}_{01}\rangle e^{i\beta_3 l} \right]. \quad (2)$$

The resulting polarization distribution in the output beam is complicated due to the presence of spin-orbit interaction, especially as our fiber length  $l \geq z_0$  [20].

From the six polarization measurements we calculate the Stokes parameters ( $S_0 - S_3$ ) (Figure 2(c)) using which we construct the pointwise state of polarization (SOP) of the entire beam. The polarization ellipse parameters are given by  $a = 1$ ,  $b = \pm \tan \chi$ ,  $\psi = 0.5 \tan^{-1}(S_2/S_1)$ , where “ $a$ ”, “ $b$ ”, and “ $\psi$ ” are the lengths of semimajor and semiminor axes and the orientation angle of the ellipse with respect to major axes, respectively [21]. From the intensity values at each pixel in the images captured by the CCD camera the Matlab code written for the purpose of calculating the polarization ellipse reads the image as a matrix with intensity values as its elements. The Stokes parameters and polarization ellipse parameters calculations are performed using these intensity values in the data images. The ellipse parameters are calculated at each point in the resized (based on the source correlation parameters) image,

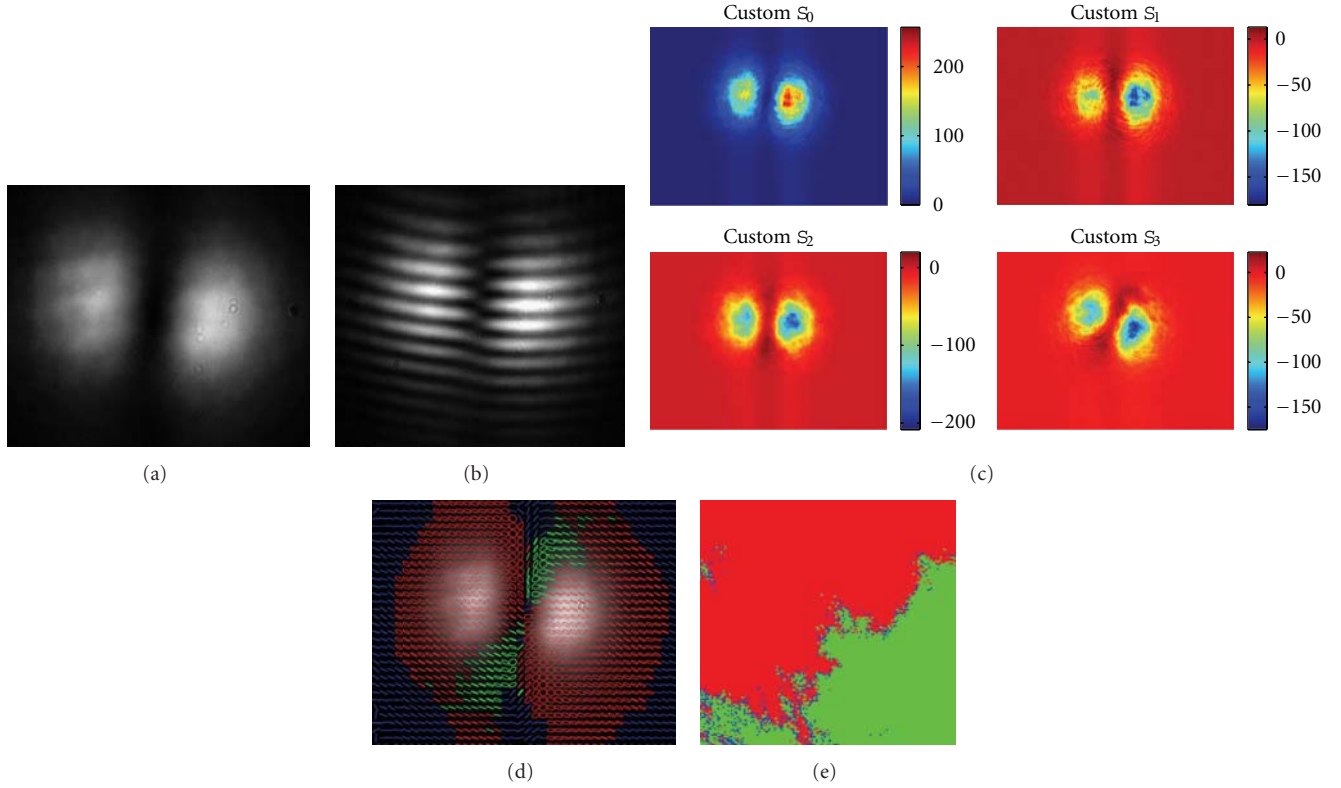


FIGURE 2: Intensity, phase, and polarization characteristics of the output beam from the TMF. (a) Two-lobe intensity profile, (b)  $\pi$ -phase shifted interference pattern of the output beam with unpolarized reference beam, (c) calculated Stokes parameters of the output beam from the six related measurements, (d) calculated polarization ellipse overlapped on the beam intensity pattern: green-right elliptical polarized, red-left elliptical polarized, and blue-linear polarization or no light, (e) high-resolution polarization ellipse map of a small portion of the pattern in (d).

and polarization ellipse is plotted overlaying the image that is of the same size as the original images. The point-wise polarization ellipses are mapped onto the direct beam images at fiber output for all input wavelengths of the laser. Also, as plotting the polarization ellipse at each pixel will make the polarization map blurred, we average the data over a block of  $16 \times 16$  pixels (dimensions less than the source correlation length) and then the ellipse parameters are calculated at each point in the resized image. The fiber output intensity overlapped with the polarization ellipse calculated from the Stokes parameters is shown in Figure 2(d) to be left-handed elliptically polarized mode mixed with right-handed elliptically polarized mode. The high-resolution calculation of the SOP of the beam at the interface between the two opposite elliptically polarization state shows linear polarized boundary (Figure 2(e)), as expected.

The output beam from the TMF is elliptically polarized due to the intramodal phase difference accumulated by the excited and propagated modes due to the fiber birefringence. In addition, the orientation of the polarization ellipse depends on the weight factor of the modes superposed to generate the output beam. These are governed by the overall residual linear birefringence of the TMF which includes inhomogeneities in the core shape, doping inhomogeneities which in turn give rise to nonuniform refractive index profile

along the propagation direction, and so forth. The phase change introduced by the birefringence is given by  $\Phi = (2\pi l/\lambda)\Delta n$ , where  $\Delta n$  is the birefringence (assumed wavelength independent, for closely spaced input wavelengths),  $\lambda$  is the input wavelength, and  $l$  is the fiber length. In the wavelength scanning method used here the wavelength dependence of the birefringence is neglected [16].

Next, without changing the input launch conditions we tune the laser wavelength in steps of 1 nm up to  $\lambda_f = 760$  nm. As the wavelength of the input laser is increased, part of the beam that is right elliptically polarized gradually increases in size, that is, the handedness change is happening from left to right in some parts of the output beam. From  $\lambda = 740$  nm to 758 nm the above-mentioned change from LEP to REP over the entire beam is complete and at  $\lambda = 758$  nm the entire beam is right elliptically polarized (Figure 3(a)). Now moving beyond, at  $\lambda = 760$  nm we see parts of the beam that are REP begin to turn around to being LEP. This confirms that the change in the polarization content (or change in the handedness) of the output beam is periodic. The boundary between the left-handed ellipse and right-handed ellipse, the  $L_x$  and  $L_y$  disclinations are measured by making the Stokes parameter  $S_3 = 0$  (without the pixel average). For all input wavelengths we measure the SOP and the disclinations  $L_x$  and  $L_y$  of the output modes. The formation of elliptically

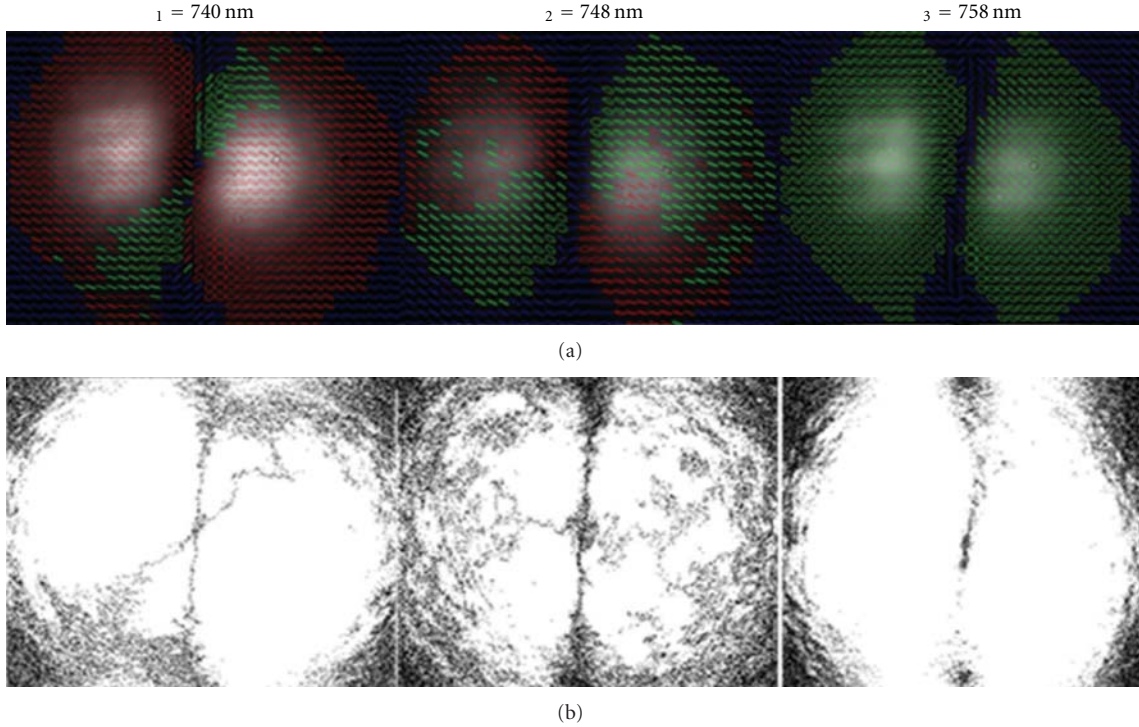


FIGURE 3: (a) Evolution of the polarization ellipse of the output beam from the TMF as a function of the input wavelength, (b) polarization line singularity (L-line) map as a function of the wavelength, indicating the evolution of dislocation via disclinations in the output beam from the TMF.

polarized edge dislocation due to the cyclic changes in the fiber modes are as shown in Figure 3(a) for three different input wavelengths of 740, 748, and 758 nm, respectively. The evolutions of linearly polarized disclinations are shown as dark lines in Figure 3(b). It is interesting to note that when the input wavelength is tuned to 758 nm, the linearly polarized disclinations are oriented in the same axis to form pure edge dislocation as shown in Figure 3.

In addition to plotting the polarization ellipse in the beam cross section we also plot the change in the output beam intensity along a fixed line across the beam for all the wavelengths (Figure 4). It is important to note here that the line profile of the two-lobe beam output from the fiber at the starting wavelength ( $\lambda_i$ ) has a slight asymmetry in its peak intensity, possibly due to the simultaneous presence of the fundamental fiber mode,  $HE_{11}$ . However, a closer look at the polarization ellipse map (Figure 2(d)) does not indicate the presence of vectorial topological dipole and the output beam is free of any coarse speckle structure, a strong indication that there is no measurable residual fundamental  $HE_{11}$  mode leaking into the fiber output [22]. We believe that an almost complete filtering of the  $HE_{11}$  fiber mode was achieved in our experiment via a combination of off-axis launch [12], fiber v-clamp in the output, and a slight bend in the fiber along its length, which causes a slight asymmetry in the output two-lobe intensity pattern. A plot of the line profile of the output beam as a function of wavelength emphasizes that the beam intensity variation is periodic with wavelength (inset in Figure 4), possibly due to the dispersion of the polarization

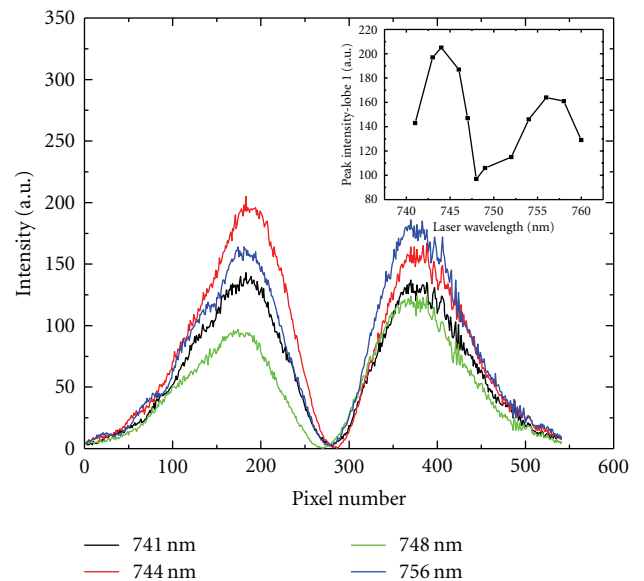


FIGURE 4: Line intensity plot of the output beam from the TMF as a function of the input wavelength. Inset shows the oscillating behaviour of the peak intensity of the left lobe as a function of the laser wavelength.

correction of the vector modes contributing to the output beam from the weakly birefringent elliptic TMF. Also, as the fiber vector modes are excited by offset and skew (linearly

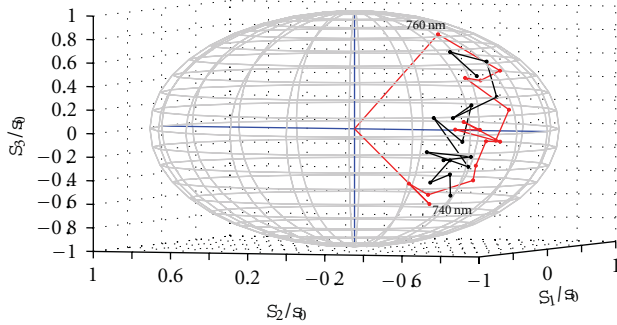


FIGURE 5: Poincaré representation of the Stokes parameters measured in the TMF output as a function of the input laser wavelength. The two sets of data are for the left and right lobes of the output beam.

polarized) Gaussian beam that travels along a twisted path inside the fiber, the role of transverse energy flow in the field resulting in the rotation of the instantaneous energy distribution with wavelength cannot be ruled out [23]. Also, the small modulation contrast ( $\sim 100$  counts) in the two-lobe intensity pattern due to wavelength scanning further emphasizes that the dispersion in the polarization correction terms is of consequence here rather than the  $HE_{11}$  mode influence [24]. Thus it is clear from our observations that both the handedness of the polarization ellipse and intensity of the output beam changes periodically as the wavelength of the input beam is increased.

It is known that graphic representation of the polarization data permit a clear insight into a complex situation where the SOP evolution is tracked as a function of the wavelength. Based on the Stokes parameters calculated for the different input wavelengths we extract necessary information to plot the evolution in the Poincaré sphere representation for both lobes of the output beam (Figure 5) [17]. For the fixed input linear polarization, scanning the input wavelength from 740 nm to 760 nm at a fixed point on the output beam, the SOP moves from REP to LEP, that is, from the bottom half of the sphere to the top half through the equator, corresponding to linear polarization state. As our wavelength scan range covers only a phase change of  $\pi$  between the superposed vector modes, we have plotted only one half of the curve. However, proceeding with the increasing wavelength, we expect to cover the second half of the trajectory as well, which should correspond to the evolution of elliptically polarized light on a Poincaré sphere [25]. A plot of the polarization ellipse parameters ( $b$  and  $\psi$ ) extracted from the above measurements and calculations also shows periodic behaviour with wavelength as shown in Figure 6.

#### 4. Conclusion

We presented here, to the best of our knowledge, a first experimental demonstration of the wavelength dependence of optical beams with polarization singularity generated using a two-mode fiber. The evolution of left elliptically polarized edge dislocation to pure right elliptically polarized

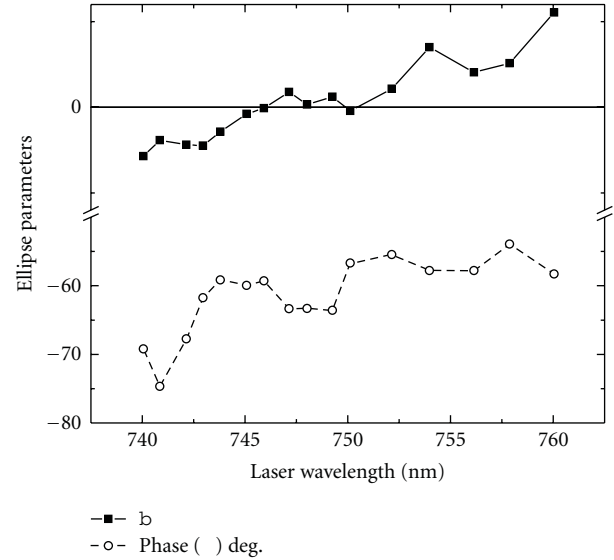


FIGURE 6: Ellipse parameters of the output beam from the TMF showing periodic behaviour as a function of input laser wavelength.

edge dislocation through disclinations is achieved by tuning the input laser wavelength in steps of 1 nm. The changes in the polarization characteristics of these beams with the change in the wavelength occur through the dispersion of the propagation constant ( $\beta_i$ ) and the polarization correction ( $\delta\beta_i$ ) of the vector modes excited and propagated in the fiber. Some evidence is also shown to emphasize that these changes in addition to the intensity variations of the two-lobe intensity pattern and the polarization ellipse parameters are cyclic with wavelength of the input beam. We anticipate that the work will be useful in the advancement of the applicability of the polarization singular beams, especially in polarization tweezers.

#### Acknowledgments

The authors acknowledge Department of Science and Technology (DST), Government of India for financial support for the project. V. V. G. K. Inavalli acknowledges CAS-RFSMS, UoH for research fellowship.

#### References

- [1] M. S. Soskin and M. V. Vasnetsov, "Singular optics," in *Progress in Optics*, E. Wolf, Ed., vol. 42, chapter 4, pp. 219–276, Elsevier, Amsterdam, The Netherlands, 2001.
- [2] M. R. Dennis, K. O. Holleran, and M. J. Padgett, "Singular optics: optical vortices and polarization singularities," in *Progress in Optics*, E. Wolf, Ed., vol. 53, chapter 5, pp. 293–359, Elsevier, Amsterdam, The Netherlands, 2009.
- [3] O. V. Angelsky, *Optical Correlation: Techniques and Applications*, SPIE Press, Washington, Wash, USA, 2007.
- [4] J. Nye, *Natural Focusing and the Fine Structure of Light: Caustics and Wave Dislocations*, IOP, Bristol, UK, 1999.
- [5] A. V. Vol'yar, "Fiber singular optics," *Ukrainian Journal of Physical Optics*, vol. 3, no. 2, pp. 69–96, 2002.

- [6] B. Ya Zel'dovich, N. F. Pilipetsky, and V. V. Shkunov, *Principles of Phase Conjugation*, Springer Series in Optical Sciences, chapter 3, Springer, New York, NY, USA, 1985.
- [7] C. N. Alexeyev, A. V. Volyar, and M. A. Yavorsky, "Fiber optical vortices," in *Lasers, Optics and Electro-Optics Research*, L. I. Chen, Ed., Nova Science Publishers, 2007.
- [8] A. N. Alekseev, A. V. Volyar, and T. A. Fadeeva, "Eigenmode geometry in a high-birefringence optical fiber," *Technical Physics Letters*, vol. 31, no. 5, pp. 374–377, 2005.
- [9] N. K. Viswanathan and V. V. G. K. Inavalli, "Generation of optical vector beams using a two-mode fiber," *Optics Letters*, vol. 34, no. 8, pp. 1189–1191, 2009.
- [10] T. A. Fadeyeva and A. V. Volyar, "Tunneling selection of optical vortices," *Technical Physics Letters*, vol. 29, pp. 594–597, 2003.
- [11] C. Kerbage, P. S. Westbrook, R. S. Windeler, and B. J. Eggleton, "Modal characteristics of an air-silica microstructure fiber," *Optics and Photonics News*, vol. 12, no. 12, p. 18, 2001.
- [12] A. W. Snyder and J. D. Love, *Optical Waveguide Theory*, Chapman and Hall, London, UK, 1983.
- [13] I. Kaminow, "Polarization in optical fibers," *IEEE Journal of Quantum Electronics*, vol. 17, no. 1, pp. 15–22, 1981.
- [14] K. Kikuchi and T. Okoshi, "Wavelength-sweeping technique for measuring the beat length of linearly birefringent optical fibers," *Optics Letters*, vol. 8, pp. 122–123, 1983.
- [15] T. I. Su and L. Wang, "A cutback method for measuring low linear fibre birefringence using an electro-optic modulator," *Optical and Quantum Electronics*, vol. 28, no. 10, pp. 1395–1405, 1996.
- [16] W. Eickhoff, Y. Yen, and R. Ulrich, "Wavelength dependence of birefringence in single-mode fiber," *Applied Optics*, vol. 20, no. 19, pp. 3428–3435, 1981.
- [17] F. T. Martinez, D. Tentori, C. A. Diaz, and F. J. M. Jimenez, "Birefringence assessment of single-mode optical fibers," *Optics Express*, vol. 13, no. 7, pp. 2556–2563, 2005.
- [18] A. Y. Savchenko and B. Y. Zel'dovich, "Wave propagation in a guiding structure: one step beyond the paraxial approximation," *Journal of the Optical Society of America B*, vol. 13, no. 2, pp. 273–281, 1996.
- [19] M. A. Bolshtyansky, A. Y. Savchenko, and B. Y. Zel'dovich, "Use of skew rays in multimode fibers to generate speckle field with nonzero vorticity," *Optics Letters*, vol. 24, no. 7, pp. 433–435, 1999.
- [20] C. N. Alexeyev, A. V. Volyar, and M. A. Yavorsky, "Optical vortices in twisted optical fibres with torsional stress," *Journal of Optics A*, vol. 10, no. 9, Article ID 095007, 2008.
- [21] M. Born and E. Wolf, *Principles of Optics*, Cambridge University Press, Cambridge, UK, 6th edition, 1999.
- [22] T. A. Fadeeva and A. V. Volyar, "Vectorial topological dipole in output radiation of a fiber optical coupler," *Technical Physics Letters*, vol. 30, no. 7, pp. 553–556, 2004.
- [23] C. N. Alexeyev, E. V. Borshak, A. V. Volyar, and M. A. Yavorsky, "Angular momentum conservation and coupled vortex modes in twisted optical fibres with torsional stress," *Journal of Optics A*, vol. 11, no. 9, Article ID 094011, 2009.
- [24] A. S. Jazi and J. C. McKeeman, "Synthesis of intensity patterns in few-mode optical fibers," *Journal of Lightwave Technology*, vol. 9, no. 9, pp. 1047–1052, 1991.
- [25] F. Treviño-Martínez, D. Tentori, C. Ayala-Díaz, and F. J. Mendieta-Jiménez, "Birefringence assessment of single-mode optical fibers," *Optics Express*, vol. 13, no. 7, pp. 2556–2563, 2005.

## Research Article

# Detector of Optical Vortices as the Main Element of the System of Data Transfer: Principles of Operation, Numerical Model, and Influence of Noise and Atmospheric Turbulence

Valerii Aksenov,<sup>1</sup> Igor Izmailov,<sup>2</sup> Feodor Kanev,<sup>1</sup> and Boris Poizner<sup>2</sup>

<sup>1</sup>Institute of Atmospheric Optics, Academician Zuev Square, Tomsk 634021, Russia

<sup>2</sup>Tomsk State University, Tomsk, Russia

Correspondence should be addressed to Feodor Kanev, mna@iao.ru

Received 11 April 2011; Accepted 13 May 2011

Academic Editor: Paramasivam Senthilkumaran

Copyright © 2012 Valerii Aksenov et al. This is an open access article distributed under the Creative Commons Attribution License, which permits unrestricted use, distribution, and reproduction in any medium, provided the original work is properly cited.

The method is proposed of optical vortex topological charge detection along with a design of a corresponding detector. The developed technique is based on measurements of light field intensity. Mathematical model simulating performance of the detector is described in the paper, and results of numerical experiments are presented which illustrate recognition of a vortex in a turbulent medium and in the presence of amplitude and phase noise in the registered radiation. Influence of shifts of the system optical axis on precision of registration is also considered in the paper.

## 1. Introduction

As it is well known, optical beams not only can transmit energy, but also possess linear and angular momentum. The total angular momentum includes a spin component, associated with polarization of light, and orbital component, related with phase and amplitude profiles [1]. In the vicinity of a singular point, the complex amplitude of a beam carrying an optical vortex can be described by the equation [1]:

$$A = C \cdot r^{V_d} \exp(jV_d\vartheta), \quad (1)$$

where  $C$  is a constant,  $V_d$  is the topological charge of vortex,  $\mathbf{r} \equiv (x, y)$  is the radius vector of a point in a cross-section of the beam,  $r \equiv |\mathbf{r}|$  is the distance between the vortex and the given point,  $\vartheta$  is an azimuth angle, and  $j = \sqrt{-1}$  is an imaginary unit. The orbital angular momentum of such a beam reduced to one photon is equal to  $\hbar V_d$ . A topological charge  $V_d$  can be associated with a bit of data. For example,  $V_d = 0$  can be considered as a logical zero, while  $V_d = 1$  is a logical unit. On the base of these properties the authors of [2, 3] proposed to use optical angular momentum to code and transfer information in optical communication systems.

Usually a laser beam propagating in a medium acquires some distortions, which reduce precision of data transfer. Intensity of distortions and probability of errors in communication line should be considered for each particular situation. But it is possible to presume that these errors depend on properties of the medium, on parameters of communication system, its design, principles of operation, and its practical realization. Obviously, influence of atmospheric turbulence and other factors on performance of the system using optical vortices to transfer information should be thoroughly considered. As an example of such analysis [4] can be taken where influence of distortions was discussed.

If construction of the communication system is chosen as the objective of investigation, structure of the system and influence of each element on its quality must be considered. Results of such investigation were published by the authors of [5]. The schematic of system discussed in this paper included transmitter, formed by generator of optical vortices, and initial wavefront corrector which includes adaptive receiver with a sensor of wavefront  $S(\mathbf{r}, t)$ , a second corrector, and comparator. The key element of the system is a sensor that registers topological charge  $V_d(\mathbf{r}, t)$  of the vortex and its

location  $\mathbf{r}_d(t)$ . Reconstruction of the wavefront is not always required in the algorithm of system performance; ordinarily the sensor is employed as a detector of vortices.

Such a detector can be built on the base of a unit measuring or reconstructing

- (1) distributions of phase gradients (Shack-Hartmann sensor [6–8] or a pyramid wavefront sensor [9–11]),
- (2) interference patterns (with subsequent analysis of it) [12, 13],
- (3) distributions of white light intensity (with analysis of chromatic patterns) [14–16],
- (4) phase distributions obtained out of local tilts measured by a wavefront sensor [17, 18].

But requirements to modern communication systems cannot be met with devices whose speed of response is less than a thousand Hz. In what follows we demonstrate the possibility to construct a detector of vortex topological charges using only measurements of beam intensity with registration speed of several GHz.

## 2. Detection of Optical Vortices with the Use of Interferometer

In this part of the paper we illustrate theoretically the possibility to employ an interferometer as a detector of optical vortices in communication system. The obtained results show that existence and order of an optical vortex can be revealed with high precision even in the presence of additive phase noise with amplitude of  $0.4\pi$ .

If a light field in a ring interferometer rotates on angle  $\Delta = 2\pi M/m$ , where the ratio of  $M$  and  $m$  is an even number, optical vortices of different topological charges included into the input field form different optical patterns in the output field. So the interferometer “sorts out” vortices into  $m$  groups according to the rule [19]:

$$N_s = (m + [(V_d + L) \bmod m]) \bmod m, \quad (2)$$

$$\varphi_{\cos} = \varphi_{\cos 0} + \frac{2\pi(LM)}{m},$$

where  $N_s$  is the number of a group (or a structure), expression “mod” signifies operation of a modulus calculation,  $L$  is an even number,  $\varphi_{\cos}$  is a phase shift in feedback contour, and  $\varphi_{\cos 0}$  is a value of  $\varphi_{\cos}$  corresponding to  $L = 0$  or  $M = 0$ .

The described properties of the interferometer allow us to consider it as a detector of optical vortices, and especially suitable to this purpose is the Rozhdestvenskii interferometer with a unit of light field rotation included into an arm (unit  $G$ ) and with a phase shifting sell ( $\varphi$ ).

The input field  $\mathbf{E}_{in}(\mathbf{r}, t)$  of interferometer is divided into two parts. These parts propagate in different arms, experience different diffraction changes and different attenuation, and acquire different phase shifts. At the end of the interferometer optical paths, two fields interact. We assume

that the attenuation of the fields in both arms is identical, as well as the lengths of the two optical paths. So the phase shift  $\varphi$  between fields is induced only by unit  $G$  and the phase shifting sell. This phase shift can be calculated as  $\varphi = \omega\delta t$ , where  $\omega$  is the cycling frequency of the field and  $\delta$  is the optical path difference induced by the sell.

Let's denote the optical field at the output of interferometer without the unit  $G$  and the phase shifting sell as  $\mathbf{E}(\mathbf{r}, t)$ . Field  $\mathbf{E}(\mathbf{r}, t)$  can be viewed as the output field of an “empty” interferometer with equal arms or as the input field  $\mathbf{E}_{in}(\mathbf{r}, t)$  recalculated to the output of such an interferometer. So without any limitations we can use field  $\mathbf{E}(\mathbf{r}, t)$  instead of  $\mathbf{E}_{in}(\mathbf{r}, t)$  and write the following equation for the output field:

$$\mathbf{E}_{\Sigma}(\mathbf{r}, t) = \left(\frac{1}{2}\right)^{1/2} (\mathbf{E}(\mathbf{r}, t) + \mathbf{E}(\mathbf{r}', t - \delta t)). \quad (3)$$

Here  $\mathbf{r}' \equiv (x', y')$  is a point in the beam cross-section at the output of element  $G$ . Let's assume that

$$\mathbf{E}(\mathbf{r}, t) = \mathbf{e}_x A(\mathbf{r}) \cos(\omega t + S(\mathbf{r})), \quad (4)$$

where  $A(\mathbf{r})$  and  $S(\mathbf{r})$  are the amplitude and phase of light-field and  $\mathbf{e}_x$  is a unit vector parallel to axis  $Ox$ . So the field at the output can be rewritten as

$$\begin{aligned} \mathbf{E}_{\Sigma}(\mathbf{r}, t) &= \mathbf{e}_x \left(\frac{1}{2}\right)^{1/2} [A(\mathbf{r}) \cos(\omega t + S(\mathbf{r})) \\ &\quad + A(\mathbf{r}') \cos(\omega t + S(\mathbf{r}') - \varphi)] \\ &\equiv A_{\Sigma}(\mathbf{r}) \cos(\omega t + S_{\Sigma}(\mathbf{r})). \end{aligned} \quad (5)$$

Taking into account the formula for the beam intensity in free space  $(\varepsilon_0/\mu_0)^{1/2} \langle \mathbf{E}^2(\mathbf{r}, t) \rangle_T$  ( $\varepsilon_0$  is the electric constant and  $\mu_0$  is the magnetic constant), we obtain the following equations describing the input and output fields:

$$\begin{aligned} I(\mathbf{r}) &= 2 \langle \mathbf{E}^2(\mathbf{r}, t) \rangle_T = A^2(\mathbf{r}), \\ I_{\Sigma}(\mathbf{r}) &= 2 \langle \mathbf{E}_{\Sigma}^2(\mathbf{r}) \rangle_T = \frac{1}{2} I(\mathbf{r}) + \frac{1}{2} I(\mathbf{r}') \\ &\quad + (I(\mathbf{r})I(\mathbf{r}'))^{1/2} \cos(S(\mathbf{r}) - S(\mathbf{r}') + \varphi) \\ &= A_{\Sigma}^2(\mathbf{r}), \end{aligned} \quad (6)$$

where  $\langle \mathbf{E}^2(\mathbf{r}, t) \rangle_T \equiv (1/T) \int_t^{t+T} \mathbf{E}^2(\mathbf{r}, t') dt'$ , and coefficient  $(1/2)(\varepsilon_0/\mu_0)^{1/2}$  was omitted to make the equation shorter. Output  $I_{\Sigma} \equiv \langle I_{\Sigma}(\mathbf{r}) \rangle_{\mathbf{r}}$  and input  $I \equiv \langle I(\mathbf{r}) \rangle_{\mathbf{r}}$  intensities averaged over the beam cross-section are

$$\begin{aligned} I &= \langle A^2(\mathbf{r}) \rangle_{\mathbf{r}}, \\ I_{\Sigma} &= I + \left\langle [I(\mathbf{r})I(\mathbf{r}')]^{1/2} \cos[S(\mathbf{r}) - S(\mathbf{r}') + \varphi] \right\rangle_{\mathbf{r}} \\ &= \langle A_{\Sigma}^2(\mathbf{r}) \rangle_{\mathbf{r}}, \end{aligned} \quad (7)$$

$\langle I(\mathbf{r}, t) \rangle_{\mathbf{r}} \equiv (1/S_b) \iint_{(S_b)} I(\mathbf{r}, t) d\mathbf{r}$ , and  $(S_b)$  is the region of square  $S$ , occupied by the beam.

The relative intensity of the output beam is possible to introduce in the following way:

$$I_r \equiv \frac{I_{\Sigma}}{I} = 1 + I^{-1} \cdot \left\langle [I(\mathbf{r})I(\mathbf{r}')]^{1/2} \cos[S(\mathbf{r}) - S(\mathbf{r}') + \varphi] \right\rangle_{\mathbf{r}}. \quad (8)$$

Obviously, this intensity is equal to the ratio of the output and input power of the beam; therefore,  $I_r$  can be registered experimentally.

Let's assume that the vortex light field incident on the input aperture of interferometer includes only one singular point positioned in the origin of coordinate system. In general, amplitude  $A(\mathbf{r})$  and phase  $S(\mathbf{r})$  profiles of the field entering (4) are the following:

$$A(\mathbf{r}) = A(r), \quad S(\mathbf{r}) = S_r(r) + V_d \cdot \vartheta(\mathbf{r}), \quad (9)$$

and  $\vartheta(\mathbf{r}) \equiv \arg(\mathbf{r})$  is an azimuth angle, while  $V_d$  is the order of a singular point. In more strict representation these profiles can be written as

$$A(\mathbf{r}) = C \exp\left(-\frac{r^2}{r_0^2}\right) \left(\frac{r}{\rho V}\right)^{|V_d|}, \quad S(\mathbf{r}) = V_d \cdot \vartheta(\mathbf{r}). \quad (10)$$

Here  $r_0$  is the radius of a Gaussian beam with zero dislocation ( $V_d = 0$ ) and  $\rho V$  is a coefficient defining the dependence of the beam amplitude on radial coordinate. Vectors  $\mathbf{r}$  and  $\mathbf{r}'$  are related by rotational transformation; modules of these vectors are equal ( $r = r'$ ), and  $\vartheta(\mathbf{r}) = \vartheta(\mathbf{r}') + M\Delta$ , so substitution of (9) into (8) gives us the relative intensity

$$I_r(V_d) \equiv \frac{I_{\Sigma}}{I} = 1 + \cos\left[\left(\frac{2\pi M V_d}{m}\right) + \varphi\right]. \quad (11)$$

Several important properties of a beam with intensity defined by (11) are recorded below.

- (1) Variations of topological charge  $V_d$  produce a discrete series of intensity  $I_r$  values,  $I_r(V_d) = I_r(V_d + im)$ , where  $i$  is an arbitrary even number.
- (2) Influence of a vortex on intensity  $I_r$  can be compensated by appropriate variations of phase shift  $\varphi$ . In the same way as it was done in (2), the phase shift is possible to be represented as  $\varphi_0 + 2\pi(LM)/m$ , where  $L$ ,  $M$ , and  $m$  are even numbers and  $\varphi_0$  is a phase shift corresponding to  $L = 0$ .
- (3) Magnitude of  $I_r$  does not depend on amplitude  $A(r)$  and phase distribution  $S_r(r)$  entering (4). Moreover, (11) is valid for a general case of rotation symmetry of  $m$ th order (in the optical system of interferometer, rotation is induced by element  $G$ ). According to this property,  $A(\mathbf{r}) = A(\mathbf{r}')$  and  $S(\mathbf{r}) - S(\mathbf{r}') = \text{const} + 2\pi i$ , that is, amplitude and phase profiles are identical in different regions of cross-section cut by rays with azimuth angles  $\vartheta = \Delta i$ .

The first and second properties strictly follow from (2). Numeration of structures is the same as earlier, but it can also be viewed as the rule of  $I_r$  discretization according to which number  $N_s$  corresponds to structure  $I_{rN_s}$ .

Obviously, if a field with the symmetry discussed in Section 3 is generated by a remote source, its properties do not change in vacuum; consequently, the distance from a source to detector is not important.

More general assumption stating that intensity  $I_r$  does not depend on the distance between the source and detector can be proved for beams propagating in vacuum or in linear homogeneous medium.

Really, diffraction of a beam in such a medium is described mathematically by a linear operator  $L_D$ . Transformations of a beam in the detector (splitting operation of the beam into three parts ( $L_{Sp1}$ ), rotation of one part by element  $G(L_G)$ , and summation of two parts ( $L_{\Sigma}$ )) are also linear. Let's rearrange these operators. Due to linearity of operator  $L_D$ , the results obtained as the sum of the fields after diffraction is the same as results of diffraction of the summed fields. Because of that, mirrors  $M_1$  and  $M_4$  can be shifted to the source of radiation, that is,  $L_{Sp1}L_D\mathbf{E} \equiv L_D\mathbf{E}_1 + L_D\mathbf{E}_2 + L_D\mathbf{E}_3 = L_D(\mathbf{E}_1 + \mathbf{E}_2 + \mathbf{E}_3) \equiv L_DL_{Sp1}\mathbf{E}$ . The order of application of operators  $L_D$  and  $L_G$  can also be changed:  $L_GL_D\mathbf{E} = L_DL_G\mathbf{E}$ , because diffraction of the field and its subsequent rotation gives the same result as rotation and diffraction of the field. Physically, this means that element  $G$  can be moved into the plane of the field generator. Using again the linearity of operator  $L_D$ , we came to a conclusion about the possibility of changing the order of operators  $L_D$  and  $L_{\Sigma}$ :  $L_{\Sigma}(L_D\mathbf{E}_1, L_D\mathbf{E}_2) = L_D\mathbf{E}_1 + L_D\mathbf{E}_2 = L_D(\mathbf{E}_1 + \mathbf{E}_2) = L_DL_{\Sigma}(\mathbf{E}_1, \mathbf{E}_2)$ . So mirrors  $M_2$  and  $M_3$  are also possible to move to the source of radiation.

As a result of all these operations, the interferometer is shifted to the source of radiation while detectors of intensity registering the fields  $\mathbf{E}_{\Sigma}$  and  $p\mathbf{E}$  remain near the receiver. Let's direct two beams of light from the source to the receiver. One of them (field  $\mathbf{E}_{\Sigma}$ ) is taken from the output of interferometer, and the other ( $p\mathbf{E}$ ) is reflected by mirror  $M_4$ . Obviously, the ratio of intensity of these two beams does not depend on the length of paths passed by them. In other words, value of  $I_r \equiv I_{\Sigma}/I$  is independent of the path length.

In analysis of the problem we should take into account aberrations of beams that are always present in real systems. To do so we insert into the phase of field described by (9) white additive noise and into its amplitude white multiplicative noise with amplitudes  $A_{nS}$  and  $A_{nA}$  correspondingly:

$$A(\mathbf{r}) = A(r)(1 + A_{nA}\xi_A(\mathbf{r})), \quad (12)$$

$$S(\mathbf{r}) = S_r(r) + V_d \cdot \vartheta(\mathbf{r}) + A_{nS}\xi_S(\mathbf{r}),$$

where  $\xi_A(\mathbf{r}) \in [-1, 1]$  and  $\xi_S(\mathbf{r}) \in [-1, 1]$  are random functions of  $\mathbf{r}$  uniformly distributed in interval  $[-1, 1]$ . This functions should meet the requirement

$$\begin{aligned} \langle \xi_A(\mathbf{r}) \rangle_{\mathbf{r}} &= 0, & \langle \xi_S(\mathbf{r}) \rangle_{\mathbf{r}} &= 0, \\ \langle \xi_A(\mathbf{r})\xi_A(\mathbf{r}') \rangle_{\mathbf{r}} &= 0, & \langle \xi_S(\mathbf{r})\xi_S(\mathbf{r}') \rangle_{\mathbf{r}} &= 0 \end{aligned} \quad (13)$$

if  $\mathbf{r}'(\mathbf{r}) \neq \mathbf{r}$ . Mathematically these conditions signify that spatial scale of noise variations is much smaller than the characteristic size of our problem, for example, lesser than the length of a ring  $2\pi r_c/m$  of radius  $r_c$ . Substituting (12) into (8), we obtain for intensity  $I_r$  the following formula:

$$I_r = 1 + I^{-1} \left\langle A(\mathbf{r})^2 (1 + A_{nA} \xi_A(\mathbf{r})) (1 + A_{nA} \xi_A(\mathbf{r}')) \times \cos \left[ \frac{2\pi V_d M}{m} + \varphi_0 + A_{nS} (\xi_S(\mathbf{r}) - \xi_S(\mathbf{r}')) \right] \right\rangle_{\mathbf{r}}. \quad (14)$$

In what follows we consider two specific cases:  $A_{nA} \neq 0$ ,  $A_{nS} = 0$  and  $A_{nA} = 0$ ,  $A_{nS} \neq 0$ . For the first situation, (14) can be written as

$$I_r = 1 + I^{-1} \left\langle A(\mathbf{r})^2 (1 + A_{nA} \xi_A(\mathbf{r})) (1 + A_{nA} \xi_A(\mathbf{r}')) \right\rangle_{\mathbf{r}} \times \cos \left( \frac{2\pi V_d M}{m} + \varphi \right). \quad (15)$$

This equation is possible to simplify with application of several mathematical operations:

- (1) transmission from Cartesian to polar coordinates in procedure of averaging  $\langle \cdot \rangle_{\mathbf{r}} = \langle \langle r \rangle_{\vartheta} \rangle_r = (1/S_b) \int_0^{\max} \int_0^{2\pi} r dr d\vartheta$ ,
- (2) calculation of integral over angle  $\vartheta$  using such properties of average values as  $\langle \xi_A(\mathbf{r}) \rangle_{\mathbf{r}} = 0$  and  $\langle \xi_A(\mathbf{r}) \xi_A(\mathbf{r}') \rangle_{\mathbf{r}} = 0$  for  $\mathbf{r}'(\mathbf{r}) \neq \mathbf{r}$  which are valid in any cross-section of the beam. When calculation of this integral is impossible, we can change averaging over angle  $\vartheta$  (this angle is analogous to some extent with a temporal variable) to averaging over the ensemble of realizations. For example,

$$\langle \xi_A(\mathbf{r})^2 \rangle_{\vartheta} = \int_{-\infty}^{\infty} \rho \{ \xi_A(\mathbf{r}) \} \xi_A(\mathbf{r})^2 d\xi_A(\mathbf{r}), \quad (16)$$

where the density of probability of random process  $\xi_A(\mathbf{r})$  is  $\rho \{ \xi_A(\mathbf{r}) \} = 1/2$  for  $\xi_A(\mathbf{r}) \in [-1, 1]$  and  $\rho \{ \xi_A(\mathbf{r}) \} = 0$  for  $\xi_A(\mathbf{r}) \notin [-1, 1]$ ,

- (3) returning to the Cartesian coordinates, for example,

$$\begin{aligned} \langle r A(r)^2 \rangle_r &= \langle r A(r)^2 \langle 1 \rangle_{\vartheta} \rangle_r = \langle r \langle A(r)^2 \rangle_{\vartheta} \rangle_r \\ &= \langle A(r)^2 \rangle_r = I. \end{aligned} \quad (17)$$

In such a way, from (15), we obtain a short formula

$$I_r = 1 + \left( 1 + \frac{A_{nA}^2}{3} \right)^{-1} \cdot \cos \left( \frac{2\pi V_d M}{m} + \varphi \right). \quad (18)$$

Amplitude of noise  $A_{nA}$  should always be less than unity, so with  $A_{nA} = 1$  we obtain the minimum value of coefficient before cosign function in (18). This coefficient is equal to  $(1 + 1/3)^{-1} = 0.75$ . The value of coefficient is close to unity, which means that influence of multiplicative

amplitude noise on intensity  $I_r$  is rather small (but only in absence of phase noise), so value  $V_d$  of topological charge is possible to detect correctly in the presence of such noise. This property will be illustrated later by results of numerical experiments.

Assuming that  $A_{nA} = 0$  and  $A_{nS} \neq 0$ , let's analyze the second problem concerning the influence of noise on the quality of vortex registration. In this assumption (14) can be rewritten in the form

$$I_r = 1 + I^{-1} \cdot \left\langle A(r)^2 \cos \left[ \frac{2\pi V_d M}{m} + \varphi + A_{nS} (\xi_S(\mathbf{r}) - \xi_S(\mathbf{r}')) \right] \right\rangle_{\mathbf{r}}. \quad (19)$$

Viewing this equation as a function of two independent random arguments and applying the operations discussed earlier, we obtain

$$I_r = 1 + \left( \frac{\sin^2(A_{nS})}{A_{nS}^2} \right) \cos \left( \frac{2\pi V_d M}{m} + \varphi \right). \quad (20)$$

According to this formula the phase noise decreases the difference between values of  $I_r$  registered for different topological charges as  $\sin^2(A_{nS})/A_{nS}^2$  making detection of the charge more difficult. For example, if  $A_{nS} = \pi$ , detection of a vortex is absolutely impossible.

The assumptions made above allow us to write for  $I_r$  a more general equation:

$$I_r = 1 + \left( 1 + \frac{A_{nS}^2}{3} \right)^{-1} \left( \frac{\sin^2(A_{nS})}{A_{nS}^2} \right) \cos \left( \frac{2\pi V_d M}{m} + \varphi \right). \quad (21)$$

### 3. Simulation of the Vortex Detector Performance and Analysis of Its Characteristics in the Presence of White Amplitude and Phase Noise

To validate conclusions made in the previous paragraph, especially properties of (21), we developed the numerical model of the detector which simulates performance of the device in the presence of additive phase noise and multiplicative amplitude noise with amplitudes  $A_{nS}$  and  $A_{nA}$ . This noise is superimposed on the field described by (10) with parameter  $\rho V = 8r_0$ . In the model of detector, the field  $\mathbf{E}_{\Sigma}(\mathbf{r}, t) = (1/2)^{1/2} (\mathbf{E}(\mathbf{r}, t) + \mathbf{E}(\mathbf{r}', t - \delta t))$  is calculated along with intensities  $I_{\Sigma} \equiv \langle I_{\Sigma}(\mathbf{r}, t) \rangle_{\mathbf{r}}$ ,  $I \equiv \langle I(\mathbf{r}, t) \rangle_{\mathbf{r}}$ , and  $I_r \equiv I_{\Sigma}/I$ . Parameter  $M$  defining the angle of rotation was taken equal unity ( $M = 1$ ), and the path length was equal zero.

The density of probability obtained in 150 realizations for relative intensity  $I_r$  is shown in Figures 2 and 3 for several fixed values of  $A_{nS}$ ,  $A_{nA}$ , and  $V_d$ . Results of numeric experiments illustrated in Figures 2 and 3 were obtained with different angles of rotation  $\Delta$  and different phase shifts  $\varphi$ . The magnitude of phase shift  $\varphi$  was specially chosen to provide maximum difference in values of intensity  $I_r(V_d)$ .

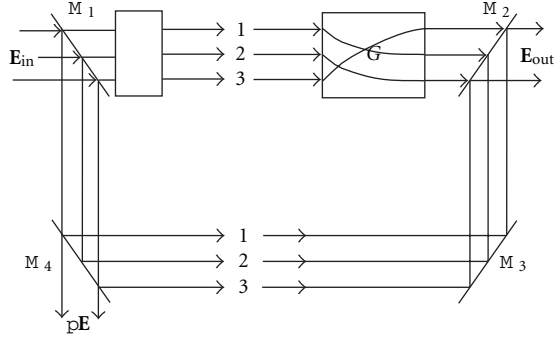


FIGURE 1: The modified Rozhdestvenskii interferometer as a detector of optical vortices. Rotation of rays 1, 2, and 3 is shown for the angle of  $120^\circ$ .

For example,  $\varphi = 0$  for  $\Delta = 180^\circ$ , and  $\varphi = -90^\circ$  for  $\Delta = 120^\circ$ .

The main properties of the detector can be systematized as follows.

- (1) Performance of the detector is influenced mainly by phase noise; influence of amplitude noise is insignificant. This thesis coincides with conclusions obtained in analysis of (18) and (20).
- (2) Detection of a vortex topological charge  $V_d$  is possible in a single realization with applications of the following rules:

$$V_d = \begin{cases} 1 + 2i, & I_r \leq 1, \\ 0 + 2i, & I_r > 1, \end{cases} \quad \text{for } \Delta = 180^\circ,$$

$$V_d = \begin{cases} 2 + 3i, & I_r < 0.94, \\ 0 + 3i, & I_r \in [0.94, 1.06] \\ 1 + 3i, & I_r > 1.06, \end{cases} \quad \text{for } \Delta = 120^\circ, \quad (22)$$

where  $i$  is an arbitrary even number. These rules are valid with  $A_{ns} \leq 0.64\pi$  (for  $\Delta = 120^\circ$ ) and with  $A_{ns} \leq 0.72\pi$  (for  $\Delta = 180^\circ$ ). The borders of their application are shown in Figures 2 and 3 by vertical dashed lines.

- (3) The averaging of results over large numbers of realizations allows one to detect value of topological charge  $V_d$  even with  $A_{ns} \leq 0.85\pi$  (for angle  $\Delta = 180^\circ$  as well as for  $\Delta = 120^\circ$ ). But in this case the value of mean intensity  $\langle I_r \rangle$  should be used instead of  $I_r$ . This result is not converse with conclusions made in analysis of (20) where  $A_{ns} < \pi$ .

In Figure 2 as well as in Figure 3 distributions of intensity  $I_r$  have finite width, and due to this fact curves corresponding to maximum and minimum values of  $I_r$  in Figure 4 do not coincide. This can be attributed to small resolution of calculation grid with only  $32 \times 32$  nodes in planes transverse relatively to the direction of propagation. So conditions ( $\langle \xi_A(\mathbf{r}) \rangle_{\mathbf{r}} = 0$ ,  $\langle \xi_S(\mathbf{r}) \rangle_{\mathbf{r}} = 0$ ,  $\langle \xi_A(\mathbf{r})\xi_A(\mathbf{r}') \rangle_{\mathbf{r}} = 0$ , and  $\langle \xi_S(\mathbf{r})\xi_S(\mathbf{r}') \rangle_{\mathbf{r}} = 0$  with  $\mathbf{r}'(\mathbf{r}) \neq r$ ,) used to obtain (18),

(20), and (21) are met only approximately. This inaccuracy can be removed completely in the process of averaging; for instance, curves representing  $\langle I_r \rangle_{N_r}$  coincide with values of  $I_r$  calculated along (21).

In the end of the paragraph we want to point out that theoretical conclusions concerning influence of white noise on performance of detector are supported by results of numerical experiments.

#### 4. Influence of Optical Axis Shifts on the Value of Relative Intensity $I_r$

As the origin of white noise, such imperfections of optical system can be taken as roughness of optical surfaces of detector and generator and some other factors. Another source of imperfections is relative shift  $S_{hx}$  of optical axes of detector and generator.

To assess the influence of  $S_{hx}$  on  $I_r$ , we have simulated field transformations in the detector. In contrast to the situation described in the previous paragraph we assumed that aberrations of field were absent. As earlier, we took  $\varphi = 0$  for  $\Delta = 180^\circ$  and  $\varphi = -90^\circ$  for  $\Delta = 120^\circ$  (Figure 1). The obtained dependencies of  $I_r$  on  $S_{hx}/r_0$  are shown in Figure 5 for different parameters of the problem.

In the numerical model, the field described by (10) can be used as distribution of radiation at the output of generator and, at the same time, as the field at the output of interferometer. This approach is valid because intensity  $I_r$  does not depend on the path length. So as a factor of normalization we used the size  $r_0$  of the beam at the output of the laser source.

The following characteristic features of the problem are seen in Figure 5. In situations where the finite size of the receiver aperture does not influence the results, relative shifts of axes induce asymptotical approach of  $I_r$  to unity. Also we observe oscillations of  $I_r$  which can be registered for topological charges different from zero ( $V_d \neq 0$ ).

In experiments performed with angle of rotation  $\Delta = 120^\circ$ , the finite size of aperture manifests itself, and with the increase of the ratio  $S_{hx}/r_0$  intensity,  $I_r$  approaches zero. This can be attributed to some properties of numerical model, namely, to the fact that due to rotation of the filed some part of interferometer input signal does not fall into the limits of the output aperture.

Oscillations of  $I_r$  induce intersections of dependences  $I_r(S_{hx}/r_0)$  obtained for different charges  $V_d$  (it should be noted that for different charges values of  $I_r(0)$  are different). This means that for some shifts of axis, detection of topological charge with rules given by (22) is impossible.

Frequency and amplitude of oscillation increase with the increase of absolute values of topological charge. So for large  $|V_d|$  intersections, points are observed for less relative shifts  $S_{hx}/r_0$ . For example, if angle  $\Delta$  equals 180 degrees ( $\Delta = 180^\circ$ ), intersection of curves corresponding to the pair  $(V_{d0}, V_{d1}) = (1, 2)$  happens earlier than for pair  $(3, 2)$  but later than for  $(V_{d0}, V_{d1}) = (3, 0)$ .

The presence of coefficient  $(r/\rho V)^{|V_d|}$  in (10) results in an increase of amplitude of oscillations and in a decrease of their

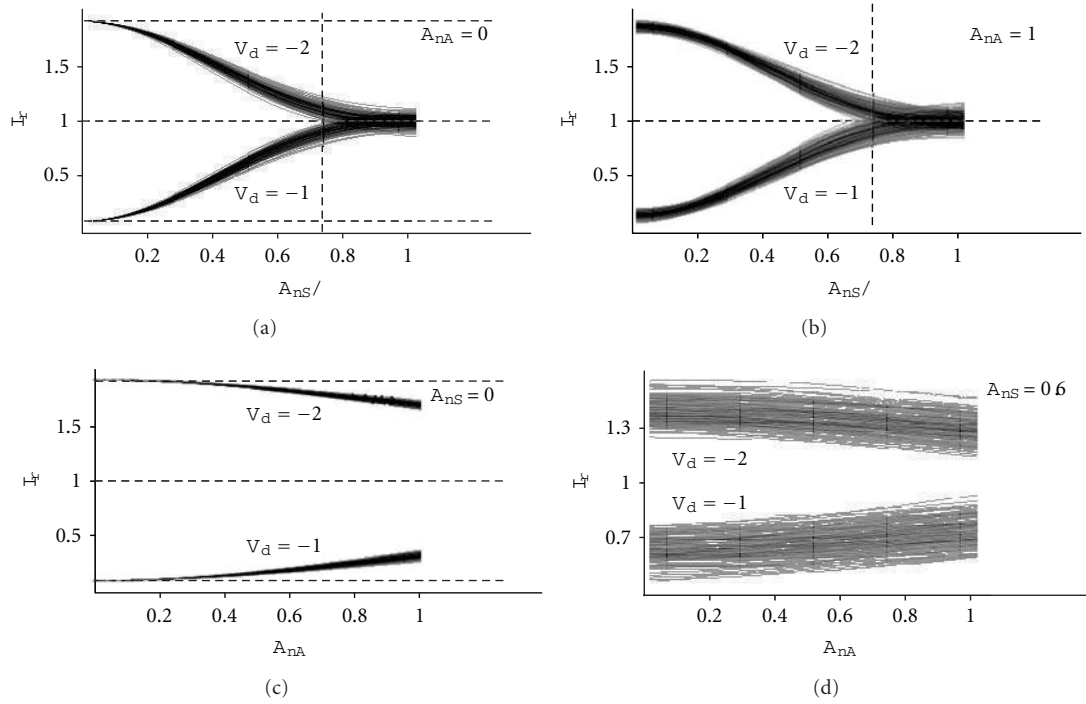


FIGURE 2: Influence of phase and amplitude noise with amplitudes  $A_{nS}$  and  $A_{nA}$  on the probability density of the intensity  $I_r$ , with  $\Delta = 180^\circ$  and  $\varphi = 0$ . The vertical dashed line corresponds to  $A_{nS} = 0.72\pi$ , while horizontal dashed lines correspond to relative intensity  $I_r$ , equal to 0, 1, and 2.

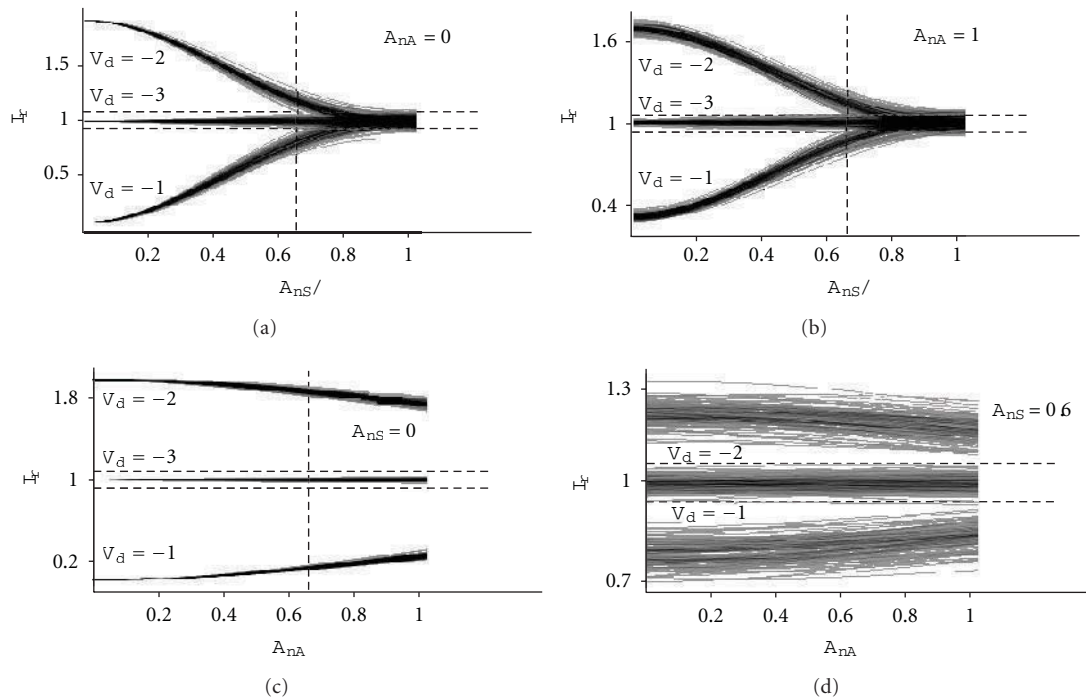


FIGURE 3: The same results as in Figure 2 obtained with  $\Delta = 120^\circ$  and  $\varphi = \pi/2$ . The vertical dashed line corresponds to  $A_{nS} = 0.64\pi$ , while horizontal dashed lines correspond to relative intensity  $I_r$ , equal to 0.94 and to 1.06.

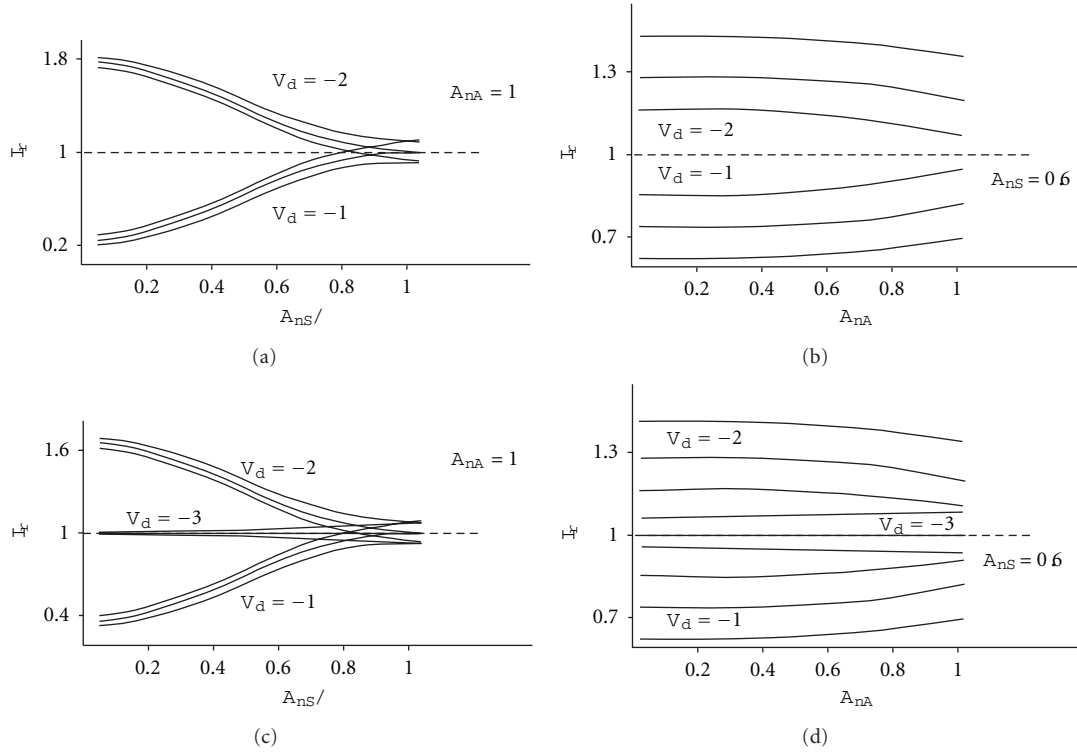


FIGURE 4: Influence of phase and amplitude noise with amplitudes  $A_{nS}$  and  $A_{nA}$  on maximum and mean values of intensity  $\langle I_r \rangle$  calculated over 150 realizations. Results were obtained with  $\Delta = 180^\circ$  and  $\varphi = 0$  (a, b) and with  $\Delta = 180^\circ$  and  $\varphi = 0$  (c, d). Amplitudes of noise were taken as  $A_{nA} = 0.5$  (a, c) and  $A_{nS} = 0.6\pi$  (b, d). The mean values of intensity calculated according to (21) coincide with curves in figures.

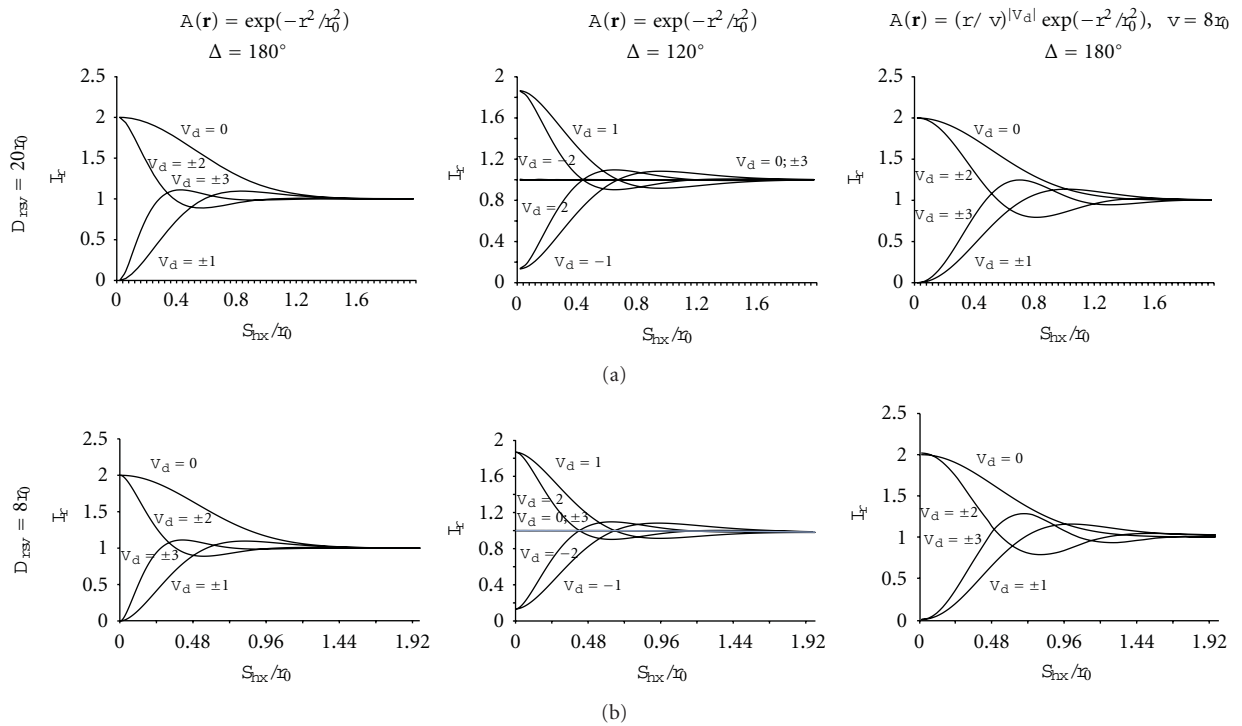


FIGURE 5: Dependence of relative intensity of interference field  $I_r(S_{hx}/r_0)$  on the shift of optical axes  $S_{hx}$  obtained for different initial amplitude profiles, angles of rotation  $\Delta$ , and topological charges  $V_d$ .

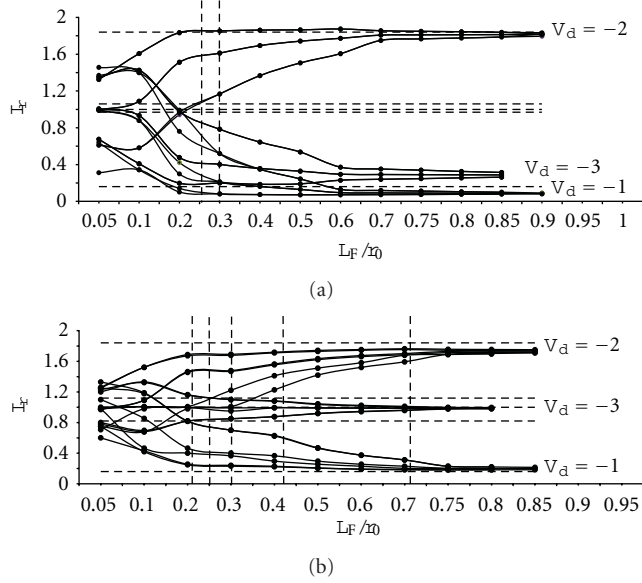


FIGURE 6: Calculated over 100 realizations, mean and maximum values of  $I_r$  obtained with different topological charges  $V_d$  for angles of rotation  $\Delta = 180^\circ$  (a) and  $\Delta = 120^\circ$  (b). Here  $L_F$  is Fried's coherence length. Horizontal dashed lines in the upper and lower parts of the pictures show the regions where values of  $I_r$  are greater and lesser than 1.84 and 0.16. In the middle part of Figure 5(a) dashed lines correspond to  $I_r = 1$  with threshold values  $I_r = 0.97$  and  $I_r = 1.06$ ; in Figure 5(b) they correspond to  $I_r = 1$  with threshold values  $I_r = 0.82$  and  $I_r = 1.12$ . Vertical dashed lines in Figure 5(a) show values of  $L_F/r_{0B}$  equal to 0.26 and 0.30, while in Figure 5(b) equal to 0.22, 0.25, 0.30, 0.43, and 0.71.

frequency. For topological charges with modulus greater than zero, this coefficient shifts points of intersection along  $S_{hx}/r_0$  axes on 25–56%, approximately from  $S_{hx} = 0, 5r_0$  up to  $S_{hx} = 0, 7r_0$ . At the same time, the curve corresponding to  $V_d = 0$  does not change its position, so the difference between curves becomes greater. This feature is especially well pronounced for the pair of charges  $(V_{d0}, V_{d1}) = (\pm 3, 0)$ .

The intersections discussed above are observed to be of relatively small values of  $S_{hx}$  ( $S_{hx} \approx 0.3r_0, \dots, 0.8r_0$ ). So it is not necessary to register the whole distribution of the beam amplitude by the receiver. Really, for  $S_{hx} \in [0, 0.8r_0]$ , the curve representing dependence  $I_r(S_{hx}/r_0)$  for the diameter of aperture  $D_{rsv} = 20r_0$  coincides with the curve obtained with the aperture  $D_{rsv} = 4r_0$ . Moreover, for  $S_{hx} = 0$ , intensity  $I_r$  is practically not influenced by the aperture diameter  $D_{rsv}$ .

## 5. Detection of a Vortex Carried by a Beam in the Turbulent Atmosphere

White noise is a source of aberrations that can easily be simulated in numerical experiments, but distortions of beams in the real atmosphere cannot be related explicitly only with noise, so we assessed the influence of turbulence on performance of the detector. Investigations were carried out for beams with Gaussian initial distribution of amplitude and with a screw dislocation in the wavefront. The beam

formed in such a way passed a thin phase screen and an optically homogeneous path of length  $L_t$ .

Intensity of turbulent distortions was characterized by the Fried coherence length  $L_F$  and by inner  $M_{inner}$  and outer  $M_{outer}$  scales of turbulence. Value of  $L_F$  was varied from  $50r_{0B}$  to  $0.05r_{0B}$ , inner and outer scales:  $M_{inner} = 0.16r_{0B} \approx 0.11r_0$ ,  $M_{outer} = 5r_{0B} \approx 3.5r_0$ , or  $M_{outer} = 20r_{0B} \approx 14.14r_0$ , where  $r_{0B} = r_0/\sqrt{2}$  is a radius of a Gaussian beam entering the equation.  $I(\mathbf{r}) = C^2 \exp(-2r^2/r_0^2) = C^2 \exp(-r^2/r_{0B}^2)$ . Path length was taken equal to 0.05 and 0.5 of diffraction length that corresponds to 5.9 and 59 kilometers for beams with radius of 10 cm and wavelength of 0.5 mkm. Averaged over 100 realizations of random phase screen, the minimum, maximum, and mean values of intensity  $I_r$  were calculated for all combinations of the physical parameters listed above.

On the path of 59 kilometers in the registration plane the distance between nodes of calculation grid was about  $r_{0B}'/16$ , where  $r_{0B}'$  is the size of beam in this plane. The error of intensity calculations was assessed by comparing the results with data obtained by processing of the etalon vortex. This error was less than 3%.

Additional errors appear at rotation of the field, but rotation on angle of  $180^\circ$  always gives zero error, and on angle  $\Delta = 120^\circ$ , the following errors: 0.0003 (0.22%) for  $V_d = -1$ , 0.0029 (0.1%) for  $V_d = -2$ , and 0.0012 (0.12%) for  $V_d = -3$ . To make numeric experiments more realistic, we introduced in the output plane of the generator relative shifts of receiver and generator optical axes:  $S_h \equiv |(S_{hx}, S_{hy})| = |-0.079r_{0B}(1, 1)| = 0.11r_{0B}$ , which results in shift of axes in the plane of receiver on the value of  $S_h' = 0.044r_{0B}'$ . These operations induced increase of errors in calculation of  $I_r$  up to 3% for angle of  $180^\circ$  and up to 10% for  $\Delta = 120^\circ$ . Nevertheless, these errors can be considered as systematic ones, and their influence on precision of vortex registration can be reduced by variations of threshold values in (22).

The obtained dependence of  $I_r$  on Fried's coherence length is shown in Figure 6 for 3 different topological charges ( $V_d = -1$ ,  $V_d = -2$ , and  $V_d = -3$ ). Under conditions of weak turbulence ( $L_F/r_{0B} \approx 50$ ) for  $\Delta = 120^\circ$  and  $V_d = -3$ , the value of  $I_r$  differs from unity on 1.4%, that is, deviation of  $I_r$  almost coincides with theoretical assessments (4%) obtained earlier.

Analysis of results obtained numerically and partially represented in Figure 6 reveals the following features of the detection system.

- (1) In weak turbulence ( $L_F > 10r_{0B}$ ) intensity,  $I_r$  does not change. Values of  $I_r$  are close to corresponding results registered in the presence of weak white noise:  $I_r = 0$  and  $I_r = 2$  in Figure 2 with  $\Delta = 180^\circ$ ;  $I_r = 0.14$  and  $I_r = 1.86$  in Figure 3 with  $\Delta = 120^\circ$ . Differences of registered values of intensity are induced mainly by shifts of optical axes and, to smaller extent, by atmospheric turbulence.
- (2) Concurrence of graphics obtained for paths of 5.9 and 59 km confirms the theoretical statement according to which the value of relative intensity  $I_r$  does not depend on the path length.

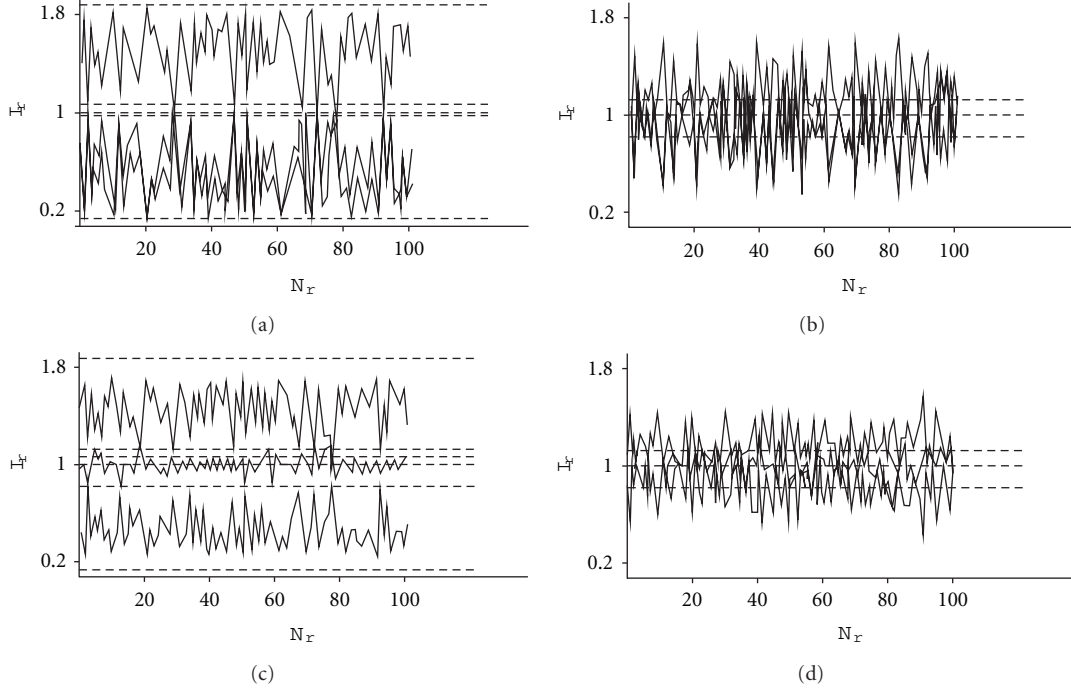


FIGURE 7: Relative intensity  $I_r$  calculated numerically with application of different phase screens  $N_r$  ( $N_r \in [0, 99]$ ). Angles of field rotation  $\Delta = 180^\circ$  (a, b) and  $\Delta = 120^\circ$  (c, d), Fried's coherence length  $L_F = 0.25r_{0B}$  (a, c) and  $L_F = 0.1r_{0B}$  (b, d). The uppermost and bottommost dashed lines correspond to values of  $I_r = 1.86$  and  $0.14$ . Dashed lines in the central part of the picture correspond to  $I_r = 1$  with threshold values of  $0.97$  and  $1.06$  (a and c) and to  $I_r = 1$  and threshold values of  $0.82$  and  $1.12$  (b and d).

(3) Analysis of topological charge detection in a single realization allows us to conclude that

(i) if the angle of field rotation is  $180^\circ$ , vortices with topological charges  $V_d = -1$  and  $V_d = -2$  can be detected when  $L_F > 0.26r_{0B}$ , with  $V_d = -2$  and  $V_d = -3$  when  $L_F > 0.26r_{0B}$  (the borders of regions are shown in Figure 6(a) by the first and third dashed lines);

(ii) if  $\Delta = 120^\circ$ , vortices with  $V_d = -1$  and  $V_d = -3$  can be detected when  $L_F > 0.71r_{0B}$ , with  $V_d = -2$  and  $V_d = -3$  when  $L_F > 0.43r_{0B}$  (the fourth and fifth dashed lines in Figure 6(b));

(4) To detect vortices with topological charges  $V_d = -1$  and  $V_d = -2$  or  $V_d = -2$  and  $V_d = -3$  and with rotation of the field on angle  $\Delta = 180^\circ$  we should change the rule of detection given by (22) to the following form:

$$V_d = \begin{cases} 1, & I_r \leq 0.97, \\ 2, & I_r > 0.97, \end{cases} \quad (23)$$

$$\text{or } V_d = \begin{cases} 3, & I_r \leq 1.063, \\ 2, & I_r > 1.063. \end{cases}$$

This rule is valid with  $L_F > 0.26r_{0B}$  or with  $L_F > 0.26r_{0B}$  (corresponding borders are shown by vertical dashed lines in Figure 6(a)).

(5) For angle of rotation  $\Delta = 120^\circ$  in (22) we can change the threshold values and obtain the new condition of vortex detection:

$$V_d = \begin{cases} 2 + 3i, & I_r < 0.818, \\ 0 + 3i, & I_r \in [0.818, 1.12], \\ 1 + 3i, & I_r > 1.12. \end{cases} \quad (24)$$

The new rule is valid for detection of vortices with  $V_d = -1$  and  $V_d = -3$  or with  $V_d = -2$  and  $V_d = -3$  when  $L_F > 0.25r_{0B}$  or  $L_F > 0.30r_{0B}$  (the regions are marked by the second and third vertical dashed lines in Figure 6(b)). But if we need to detect vortices only with charged  $V_d = -1$  and  $V_d = -2$ , then we can use the rule

$$V_d = \begin{cases} 1, & I_r \leq 0.904, \\ 2, & I_r > 0.904, \end{cases} \quad (25)$$

which is valid for  $L_F > 0.216r_{0B}$  (the first vertical dashed line in Figure 6(b)).

(6) Analysis of large samplings (100 realizations or more) allows us to detect topological charges of vortices with (22) for  $L_F = 0.1r_{0B}$  or even in stronger turbulence. Naturally, in procedure of detection we employ averaged values of intensity  $\langle I_r \rangle$  instead of  $I_r$ .

Influence of phase screen simulating turbulent distortions of radiation on detection of vortex topological charges

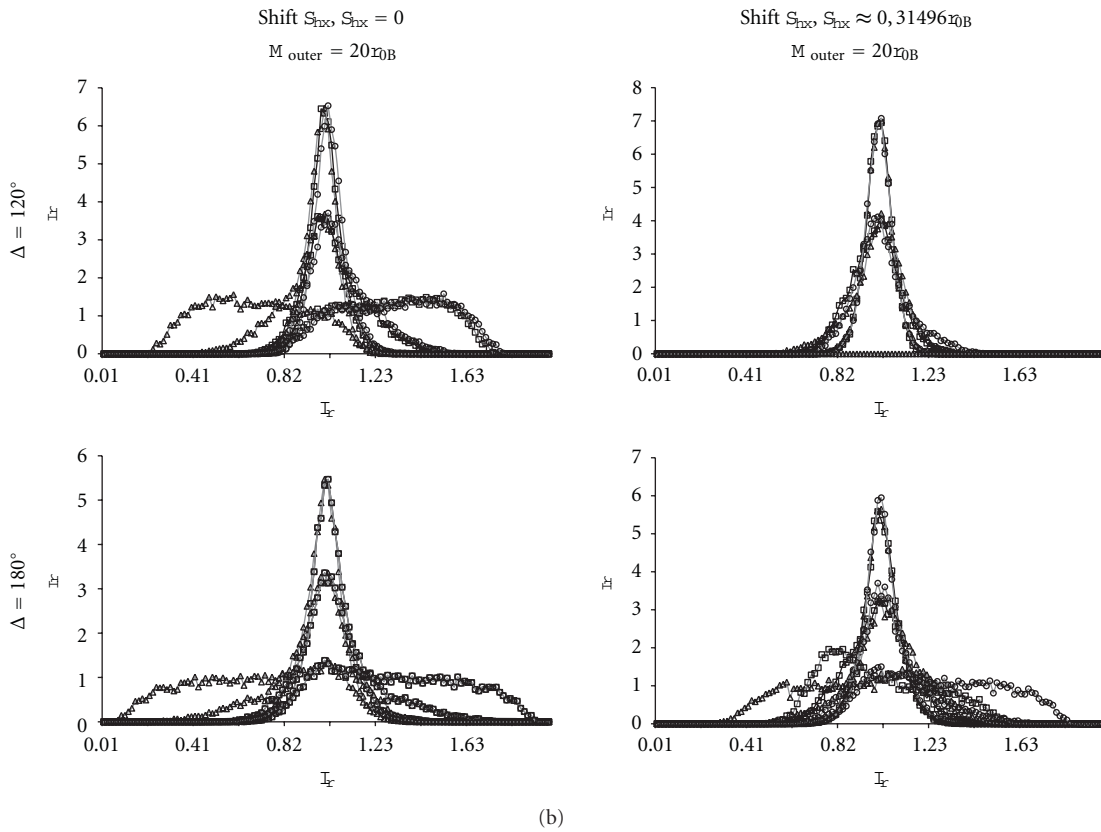
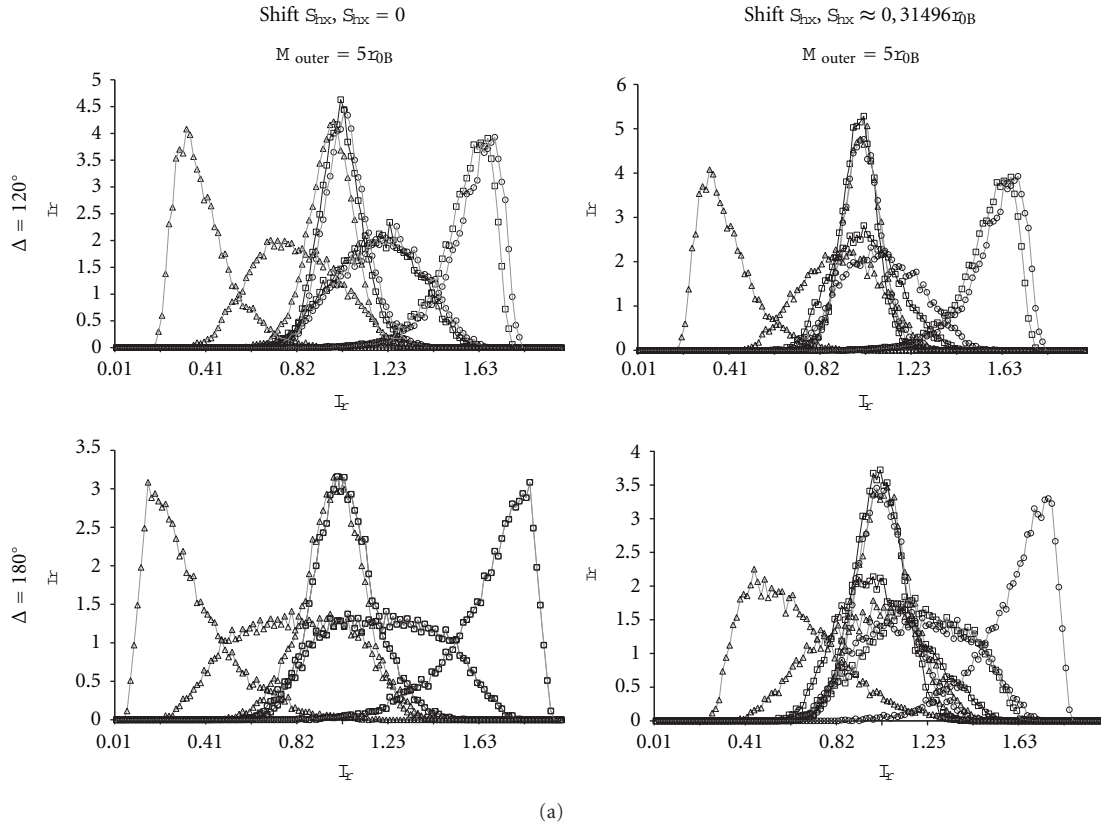


FIGURE 8: One-dimensional distributions of probability density  $\rho_r \equiv \rho(I_r)$  obtained with different values of  $M_{outer}$  and  $S_{hx}$ . The values of Fried's coherence length are 0.25, 0.1, and 0.05. Curves marked by symbols “ $\Delta$ ”, “ $\square$ ”, and “ $o$ ” were obtained for topological charges  $-1$ ,  $-2$ , and  $0$  correspondingly.

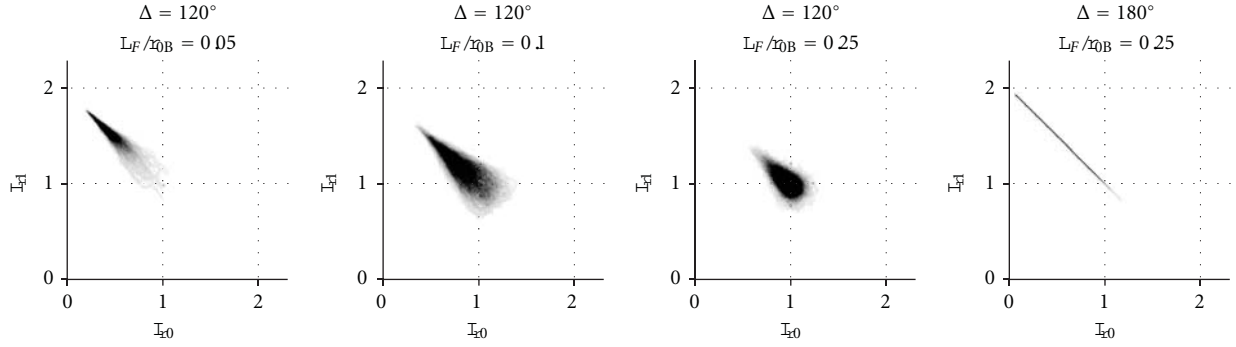


FIGURE 9: Two-dimensional probability density  $\rho(I_{r0}, I_{r1})$  obtained with  $(V_{d0}, V_{d1}) = (-1, -2)$ ,  $S_{hx} = 0$ ,  $M_{outer} = 5r_{0B}$ , and different values of  $L_F$  and  $\Delta$ .

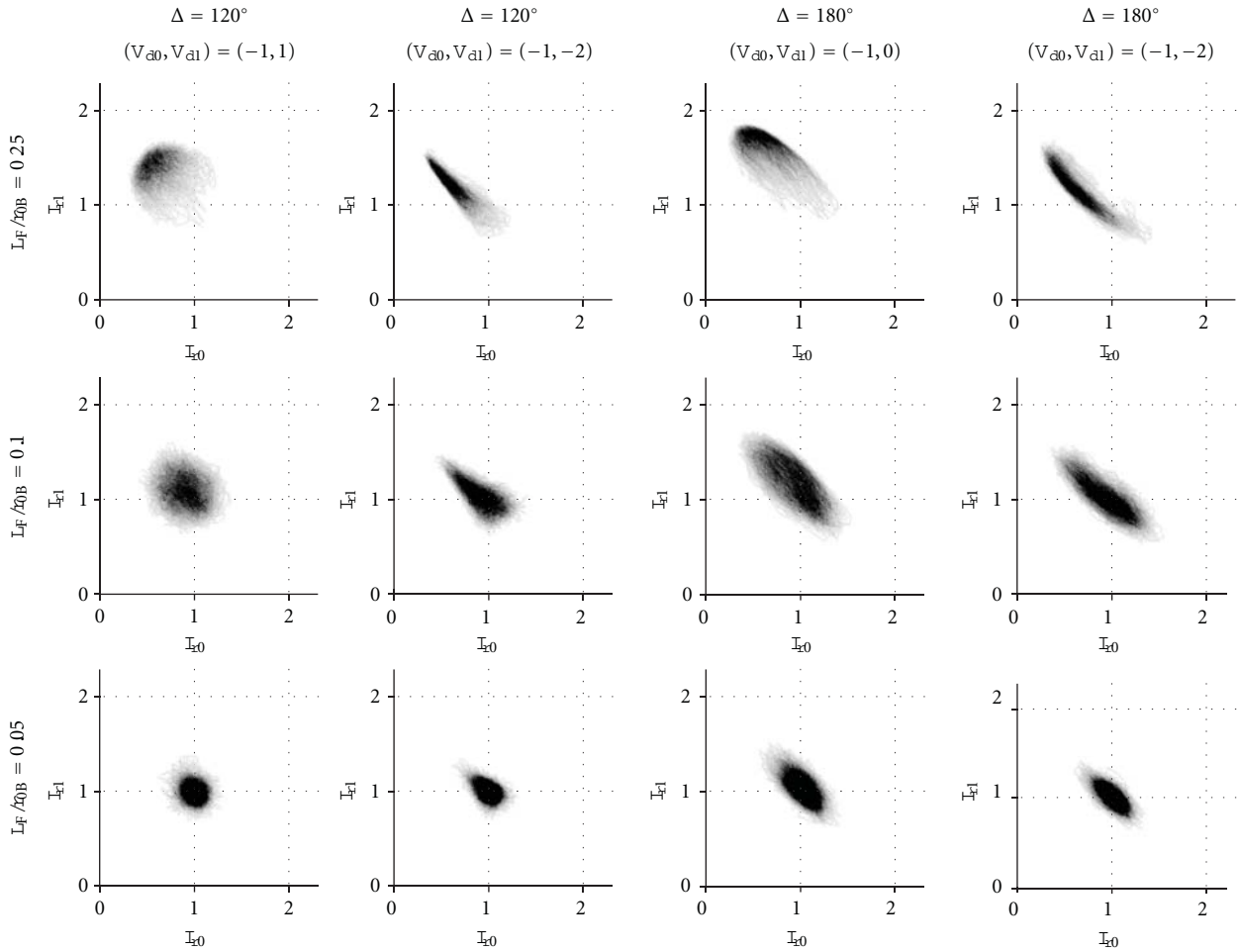


FIGURE 10: Two-dimensional probability density  $\rho(I_{r0}, I_{r1})$  obtained with  $S_{hx} \approx 0.314r_{0B}$ ,  $M_{outer} = 5r_{0B}$ , and different values of  $V_{d0}$ ,  $V_{d1}$ ,  $L_F$ , and  $\Delta$ .

is illustrated in Figure 7. Different curves in this picture correspond to vortices with different charges ( $V_d = -2$ ,  $V_d = -1$ , and  $V_d = -3$ ). In Figures 7(b) and 7(d), curves cannot be separated which indicates large strength of turbulence.

Also in Figure 7 we observe mirror symmetry between curves  $I_r(N_r)$  related with different charges, for example, with  $V_d = -2$  and  $V_d = -1$ ;  $V_d = -2$  and  $V_d = -3$ .

The exact reflection of curves is possible to expect when optical axis of receiver and detector coincide and angle of rotation is  $180^\circ$ , but development of symmetry for  $\Delta = 120^\circ$  is unachievable (Figures 7(c) and 7(d)).

One more characteristic feature observed in these pictures is the following: normally,  $I_r(N_r, V_{d0}) \neq I_r(N_r, V_{d1})$  for  $V_{d0} \neq V_{d1}$ . This attribute and the symmetry of curves are also

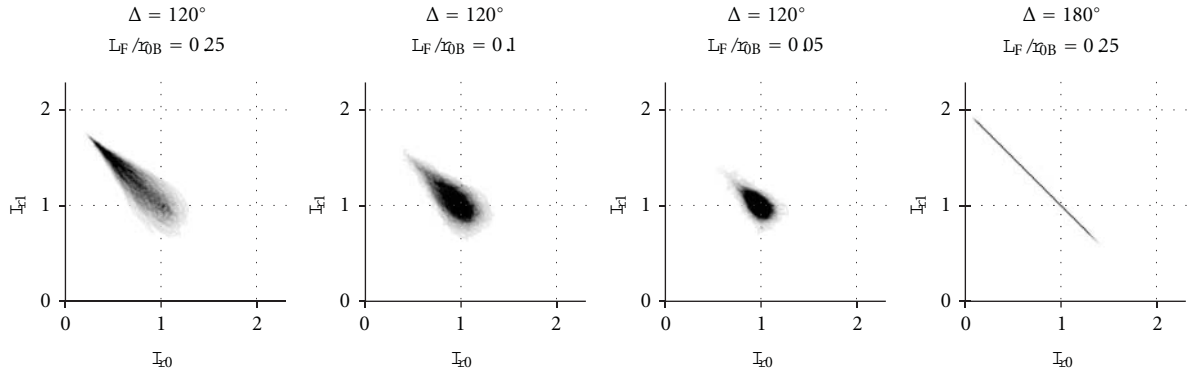


FIGURE 11: The same data as in Figure 8 but obtained with  $M_{\text{outer}} = 20r_{0B}$ .

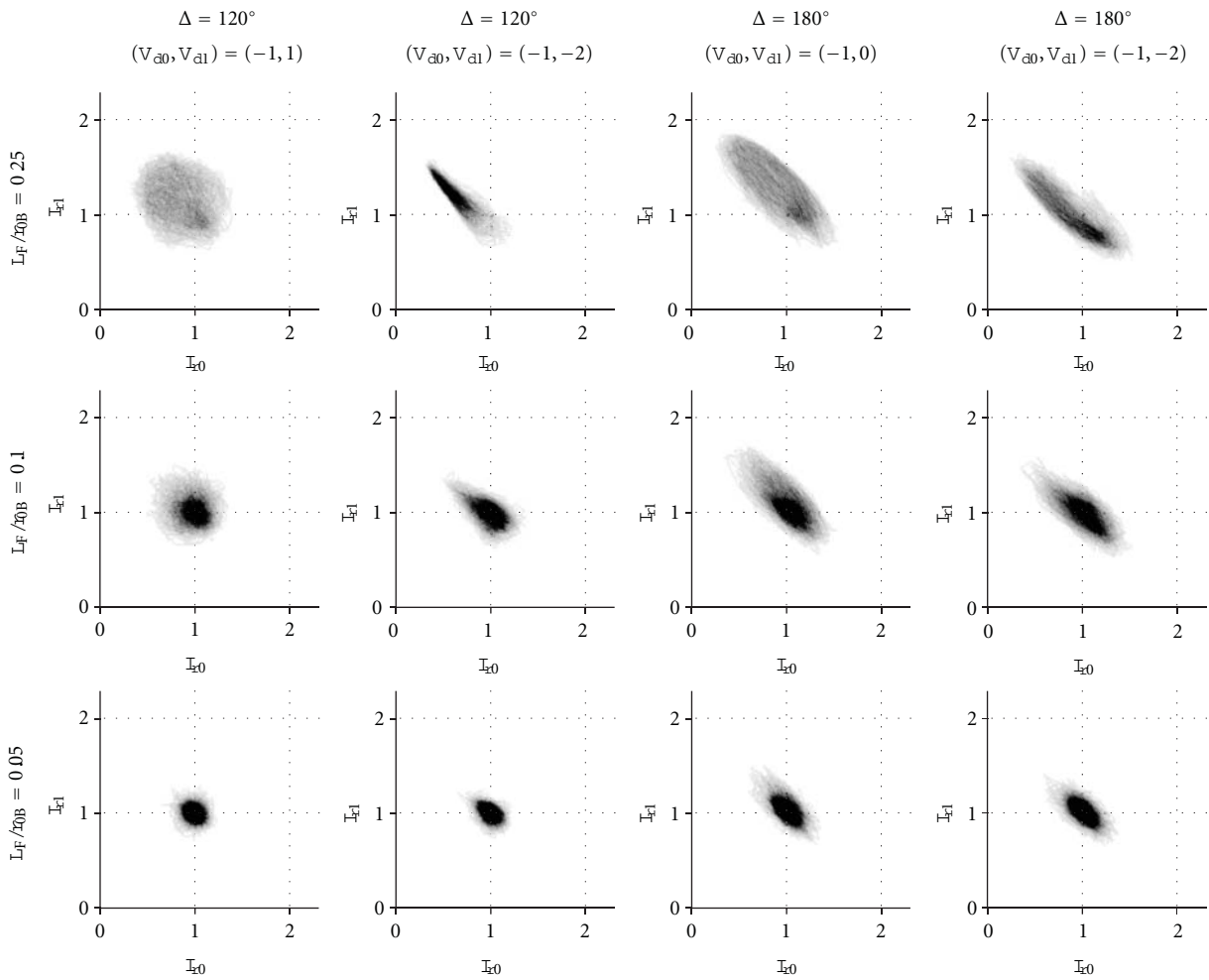


FIGURE 12: The same data as in Figure 9 but obtained with  $M_{\text{outer}} = 20r_{0B}$ .

illustrated by distributions  $\rho(I_r)$ ,  $\rho(I_{r0}, I_{r1})$  of probability density presented in Figures 8, 9, 10, and 11 for different values of  $L_F$ ,  $M_{\text{outer}}$ ,  $S_{hx}$ , and  $V_d$ .

Graphs representing the results of numeric experiments with zero shifts of optical axes show that differences in probability density  $\rho(I_{r0}, I_{r1})$  for triplets  $(120^\circ, -1, 1)$  and

$(120^\circ, -1, -2)$  cannot be distinguished visually. The same is true for triplets  $(180^\circ, -1, 0)$  and  $(180^\circ, -1, -2)$ .

According to Figures 9, 10, 11, and 12 with increase of turbulence strength (with decrease of  $L_F$ ), distribution of probability density initially localized in vicinity of point  $(1, 1)$  moves out of the second quadrant in direction of

TABLE 1: Averaged over 13000 realizations mean values of  $\langle I_{r1} - I_{r0} \rangle$  and maximum amplitudes  $I_{r0 \max} - I_{r1 \min}$  obtained for pairs  $(V_{d0}, V_{d1})$  with different Fried's coherence lengths  $L_F/r_{0B}$ , angles of field rotation  $\Delta$ , shifts of optical axes  $S_{hx}$ , and different outer scales  $M_{\text{outer}}$ .

$L_F/r_{0B}$	$V_{d0}$	$\Delta = 180^\circ$				$\Delta = 120^\circ$			
		$S_{hx} = 0$		$S_{hx} \approx 0.314r_{0B}$		$S_{hx} = 0$		$S_{hx} \approx 0.314r_{0B}$	
		$-1;$	$-1;$	$-1;$	$-1;$	$-1;$	$-1;$	$-1;$	$-1;$
	$V_{d1}$	0	-2	0	-2	+1	-2	+1	
$M_{\text{outer}} = 5r_{0B}$									
0.25	$\langle I_{r1} - I_{r0} \rangle$	1.35	0.997	0.56	1.16	1.20	0.60	0.79	
	$I_{r0 \max} - I_{r1 \min}$	0.35	0.57	0.83	0.20	0.18	0.55	0.45	
0.10	$\langle I_{r1} - I_{r0} \rangle$	0.39	0.24	0.08	0.35	0.38	0.11	0.19	
	$I_{r0 \max} - I_{r1 \min}$	1.01	1.00	1.02	0.75	0.72	0.80	0.76	
0.05	$\langle I_{r1} - I_{r0} \rangle$	0.06	0.01	-0.02	0.05	0.07	-0.01	0.01	
	$I_{r0 \max} - I_{r1 \min}$	0.82	0.79	0.80	0.59	0.57	0.60	0.59	
$M_{\text{outer}} = 20r_{0B}$									
0.25	$\langle I_{r1} - I_{r0} \rangle$	0.59	0.36	0.08	0.58	0.62	0.19	0.32	
	$I_{r0 \max} - I_{r1 \min}$	0.82	0.91	1.03	0.61	0.59	0.82	0.78	
0.10	$\langle I_{r1} - I_{r0} \rangle$	0.11	0.03	-0.03	0.12	0.13	-0.01	0.02	
	$I_{r0 \max} - I_{r1 \min}$	0.99	0.98	1.02	0.72	0.71	0.74	0.71	
0.05	$\langle I_{r1} - I_{r0} \rangle$	0.03	0.01	-0.00	0.02	0.04	-0.00	0.00	
	$I_{r0 \max} - I_{r1 \min}$	0.75	0.72	0.73	0.60	0.57	0.51	0.54	

TABLE 2: Influence of optical axes shift  $S_{hx}$  and outer scale  $M_{\text{outer}}$  of turbulence on difference  $I_{r0 \max} - I_{r1 \min}$  and mean difference  $\langle I_{r1} - I_{r0} \rangle$  of functions  $I_{r1}(N_r)$  and  $I_{r0}(N_r)$ .

Difference	Shift of axes $S_{hx}/r_{0B}$				Outer scale of turbulence $M_{\text{outer}}/r_{0B}$			
	0	0.315	Increase: 0 $\rightarrow$ 0.315		5	20	Increase: 5 $\rightarrow$ 20	
			Variations, %	Interval			Mean	Variations, %
$\langle I_{r1} - I_{r0} \rangle$	0.41	0.188 $\approx$ $\approx (1 - 0.54) \cdot 0.41$	-131 $\dots$ -26	-77	0.432	0.164 $\approx$ $\approx (1 - 0.62) \cdot 0.432$	-144 $\dots$ -31.7	-70
$I_{r0 \max} - I_{r1 \min}$	0.68	0.76 $\approx$ $\approx (1 + 0.11) \cdot 0.68$	-17 $\dots$ 63	12	0.77	0.67 $\approx$ $\approx (1 - 0.14) \cdot 0.77$	-229 $\dots$ +15	-34

the fourth one and acquires symmetric shape relatively to this point. As a result distribution of function  $\rho(I_{r0}, I_{r1})$  for  $L_F/r_{0P} = 0.05$  looks like a distribution of the Gaussian function.

Relative shift of the generator and receiver optical axes  $S_{hx} \approx 0.314r_{0B}$  in the presence of weak turbulence ( $L_F = 0.25r_{0P}$ ) results in the broadening of distribution and transport of its gravity center to the first and third quadrants. These changes are clearly seen in graphics corresponding to  $\Delta = 180^\circ$ . With increase of turbulence, intensity increases the speed of transformation of  $\rho(I_{r0}, I_{r1})$  distribution to a Gaussian form.

Symmetry of  $\rho(I_{r0}, I_{r1})$  distribution guarantees correct data transfer by a system even on realizations when the topological charge of vortex is incorrectly detected. Due to symmetry an error of vortex identification is possible to consider as a regular event; therefore, it can be taken into account in the algorithm of detection. Another property of the system, namely, the difference of intensities  $I_r(N_r, V_{d0}) \neq I_r(N_r, V_{d1})$  observed when  $V_{d0} \neq V_{d1}$  suggests application of adaptive thresholds in the algorithm, with the use of which the errors can be reduced.

The above-presented conclusions based on visual analysis of results are supported by the data of Table 1, where the influence of phase screen, detector, and order of a singular points on difference  $\langle I_r(N_r, V_{d1}) - I_r(N_r, V_{d0}) \rangle_{N_r} \equiv \langle I_{r1} - I_{r0} \rangle$  is illustrated. Obviously, identification of vortices is easier if the difference of intensities  $\langle I_{r1} - I_{r0} \rangle$  is greater. According to Table 1 detection of vortices is not always possible even with small intensity of turbulence, for example, with  $L_F = 0.25r_{0B}$ . This notion does not conflict with conclusions 3–5 drawn for  $S_h = 0.11r_{0B}$  and  $M_{\text{outer}} = 5r_{0PB}$  in contrast with the thesis about possible application of (25) for  $L_F > 0.216r_{0P}$  which seems rather doubtful. The cause of disagreement can be explained as follows: according to our estimates, probability of the event appearance is rather small (about 1.6%) for a random phase screen with  $L_F = 0.25r_{0B}$  and  $M_{\text{outer}} = 5r_{0B}$  which guarantees fulfillment of inequality  $I_r(V_{d1} = -2) < I_r(V_{d0} = -1)$ . But we used only 100 realizations to obtain data shown as graphs in Figure 6, so it is possible to expect that the screen is absent in this sampling, while results in Table 1 were averaged over 13000 realizations.

The results of Table 1 also allow one to conclude that with  $\Delta = 180^\circ$  and  $S_{hx} = 0$ , values of  $\langle I_{r1} - I_{r0} \rangle$  and  $I_{r0\max} - I_{r1\min}$  obtained for different pairs of  $(V_{d0}, V_{d1})$  coincide precisely. This property can be attributed to mirror symmetry of corresponding curves representing functions  $I_r(N_r)$ . With  $\Delta = 120^\circ$  and  $S_{hx} = 0$ , between values of  $\langle I_{r1} - I_{r0} \rangle$  and  $I_{r0\max} - I_{r1\min}$  we registered only small difference. If the optical axes are shifted, mirror symmetry of curves is broken as well as correlation between values of  $\langle I_{r1} - I_{r0} \rangle$  and  $I_{r0\max} - I_{r1\min}$ .

Additionally, increase of  $S_{hx}$  and of the outer scale  $M_{\text{outer}}$  results in decrease of  $\langle I_{r1} - I_{r0} \rangle$  (Table 2). Obviously, in this case, performance of the detector can be improved with application of an adaptive optics system compensating for large-scale aberrations of radiation.

## 6. Conclusions

The main results of theoretical analysis can be summarized as follows.

- (1) Due to optical field transformation in an interferometer, the magnitude of the output intensity depends on the order of a vortex carrying by the field. This magnitude can be used to detect presence and order  $V_d$  of the vortex.
- (2) The influence of white amplitude and phase noise was assessed on precision of vortex identification. It was shown that precision of vortex identification is influenced mainly by amplitude white noise.
- (3) Invariance of detector characteristics under path length was proved in linear homogeneous medium.
- (4) The mirror symmetry of the output field intensity  $I_r$  relatively to the level  $I_r = 1$  for specific angles of rotation, and specific differences of topological charges was demonstrated.

With the use of numerical simulation, it was shown that

- (1) Assessments of white noise and turbulence influence on precision of a vortex detection support theoretical results.
- (2) The simple criteria are possible to introduce in the model of a detector to distinguish presence and order of optical vortex.
- (3) Magnitude of relative intensity  $I_r$  and precision of vortex detection depend noticeably on shifts of receiver and source optical axes.

The main characteristics are also found of 1D and 2D probabilities of vortex detection as functions of Fried's coherence length, inner and outer scales of turbulence, and relative shifts of optical axes.

## References

- [1] L. Allen, M. W. Beijersbergen, R. J. C. Spreeuw, and J. P. Woerdman, "Orbital angular momentum of light and the transformation of Laguerre-Gaussian laser modes," *Physical Review A*, vol. 45, no. 11, pp. 8185–8189, 1992.
- [2] G. Molina-Terriza, J. P. Torres, and L. Torner, "Management of the angular momentum of light: preparation of photons in multidimensional vector states of angular momentum," *Physical Review Letters*, vol. 88, no. 1, pp. 136011–136014, 2002.
- [3] G. Gibson, J. Courtial, M. J. Padgett et al., "Free-space information transfer using light beams carrying orbital angular momentum," *Optics Express*, vol. 12, no. 22, pp. 5448–5456, 2004.
- [4] C. Paterson, "Atmospheric turbulence and orbital angular momentum of single photons for optical communication," *Physical Review Letters*, vol. 94, no. 15, Article ID 153901, 2005.
- [5] V. Aksenov, I. Izmailov, F. Kanev, and B. Poizner, "Detector of topological charges of optical vortices," in *Proceedings of the International Conference "Laser Optics '10"*, p. 21, St. Petersburg, Russia, 2010.
- [6] R. B. Shack and B. C. Platt, "Production and use of a lenticular hartmann screen," *Journal of the Optical Society of America*, vol. 61, pp. 656–662, 1971.
- [7] F. A. Starikov, V. P. Aksenov, F. Y. Kanev et al., "Wavefront reconstruction of an optical vortex by a Hartmann-Shack sensor," *Optics Letters*, vol. 32, no. 16, pp. 2291–2294, 2007.
- [8] V. Voitikhovich, L. Sanchez, V. Orlov, and S. Cuevas, "Efficiency of the Hartmann test with different subpupil forms for the measurement of turbulence-induced phase distortions," *Applied Optics*, vol. 40, no. 9, pp. 1299–1304, 2001.
- [9] R. Ragazzoni, "Pupil plane wavefront sensing with an oscillating prism," *Journal of Modern Optics*, vol. 43, no. 2, pp. 289–293, 1996.
- [10] R. Ragazzoni, A. Ghedina, A. Baruffolo et al., "Testing the pyramid wavefront sensor on the sky," in *The International Society for Optics and Photonics*, vol. 4007 of *Proceedings of the SPIE*, pp. 423–429, March 2000.
- [11] M. Ghigo, G. Crimi, and F. Perennes, "Construction of a pyramidal wavefront sensor for adaptive optics compensation," in *Proceedings of the International Conference "Beyond Conventional Adaptive Optics"*, pp. 465–472, 2001.
- [12] F. Y. Kanev, V. P. Lukin, and N. A. Makenova, "Detection of dislocations as branching points of interference pattern," in *The International Society for Optics and Photonics*, vol. 4357 of *Proceedings of the SPIE*, pp. 231–235, June 2001.
- [13] C. Rockstuhl, A. A. Ivanovskyy, M. S. Soskin, M. G. Salt, H. P. Herzig, and R. Dändliker, "High-resolution measurement of phase singularities produced by computer-generated holograms," *Optics Communications*, vol. 242, no. 1–3, pp. 163–169, 2004.
- [14] M. V. Berry, "Coloured phase singularities," *New Journal of Physics*, vol. 4, pp. 66.1–66.14, 2002.
- [15] M. V. Berry, "Exploring the colours of dark light," *New Journal of Physics*, vol. 4, pp. 74.1–74.14, 2002.
- [16] G. V. Bogatryyova, C. V. Felde, P. V. Polyanskii, S. A. Ponomarenko, M. S. Soskin, and E. Wolf, "Partially coherent vortex beams with a separable phase," *Optics Letters*, vol. 28, no. 11, pp. 878–880, 2003.
- [17] D. L. Fried, "Adaptive optics wave function reconstruction and phase unwrapping when branch points are present," *Optics Communications*, vol. 200, no. 1–6, pp. 43–72, 2001.
- [18] V. P. Aksenov, I. V. Izmailov, F. Y. Kanev, and F. A. Starikov, "Algorithms for the reconstruction of the singular wave front of laser radiation: analysis and improvement of accuracy," *Quantum Electronics*, vol. 38, no. 7, pp. 673–677, 2008.
- [19] I. V. Izmailov, A. L. Magazinnikov, and B. N. Poizner, "Identification of a screw wave-front dislocation and compensation for its influence on structuration in models of a ring interferometer," *Atmospheric and Ocean Optics*, vol. 13, pp. 805–812, 2000.

## Research Article

# Fresnel Lens with Embedded Vortices

Sunil Vyas,<sup>1</sup> Rakesh Kumar Singh,<sup>1</sup> Devinder Pal Ghai,<sup>2</sup>  
and P. Senthilkumaran<sup>1</sup>

<sup>1</sup>Department of Physics, Indian Institute of Technology Delhi, New Delhi 110016, India

<sup>2</sup>Laser Science and Technology Centre, Metcalfe House, Delhi 110054, India

Correspondence should be addressed to P. Senthilkumaran, psenthilk@yahoo.com

Received 25 March 2011; Accepted 20 June 2011

Academic Editor: Jan Masajada

Copyright © 2012 Sunil Vyas et al. This is an open access article distributed under the Creative Commons Attribution License, which permits unrestricted use, distribution, and reproduction in any medium, provided the original work is properly cited.

Vortices of different charges are embedded in a wavefront that has quadratic phase variation, and the intensity distribution near the focal plane is studied. This method may be useful in realizing complicated beam profiles. We have experimentally demonstrated the generation of vortex arrays having integer as well as fractional topological charges that produce different intensity profiles at the focal plane. The phase variation realized on a spatial light modulator (SLM) acts as a Fresnel lens with embedded vortices.

## 1. Introduction

A modulo  $2\pi$  operation carried out on a spherical wavefront results in concentric zones called Fresnel zones. A Fresnel lens is formed by segmenting the continuous surface of a conventional lens into a set of surfaces of the same curvature. This process allows fabrication of a large diameter lens with very short focal length thereby ensuring substantial increase in its numerical aperture. Further, there is a significant reduction in the thickness and weight of the lens. Thus, a plane wave incident on a Fresnel lens is split into multiple segments (zones), and the combination of multiple successive wavefront zones reconstructs the spherical wavefront.

An optical beam with phase singularity also called optical vortex or a screw dislocation is a helical phase ramp which focuses to a ring-like intensity pattern [1]. An optical vortex is characterized by azimuthal phase dependence of the type  $\exp(im\theta)$  where  $m$  is the topological charge. The magnitude of topological charge represents the total phase accumulated by the helical wave in one complete revolution around the vortex point. The sign of topological charge represents left- or right-handed helicity. When the topological charge has a noninteger value, it results in the formation of a fractional vortex. Wavefront containing fractional charge vortex exhibits a half-cut (low-intensity radial opening in the doughnut structure), corresponding to a mixed edge-screw

dislocation [2]. Such vortices, on propagation, transform into several opposite-sign screw dislocations which disappear on the beam periphery [3].

Optical vortices find applications in particle trapping [4], data encryption [5], phase contrast microscopy [6], image processing [7], collimation testing [8], vortex coronagraphy, [9] and in various other areas. Recently, optical vortex arrays which are regular nets of vortices have generated an enormous interest among many research groups [10, 11]. Optical vortex arrays, also called vortex lattices, find applications in multiple trap optical tweezers [12], spatial solitons [13], microfluidic sorting [14], metrology [15], micromechanics [16], and atom optics [17]. Vortex arrays are generated using interferometry [18–20], Talbot imaging [21], and spatial filtering [22]. In this paper, we present a simple and effective method of generating array of vortices by embedding vortex phase distribution in the Fresnel lens. Specially designed phase masks are produced which are encoded onto the SLM to achieve array of vortices near the focal plane. A vortex array of integer as well as fractional topological charge can be produced by this method. As this method uses a single lens function, there is no cross-talk and overlapping of different beams. The method offers flexibility in the selection of location, number density, and topological charge of vortices in the beam.

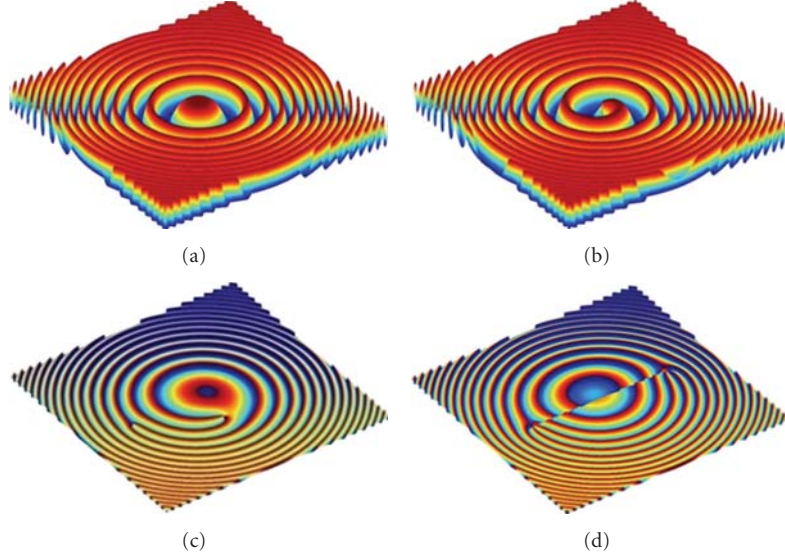


FIGURE 1: (a) Surface profile of a conventional Fresnel lens. (b) Surface profile of a Fresnel vortex lens. (c) Surface profile of a Fresnel lens with vortices embedded at off-axis locations. (d) Surface profile of a Fresnel lens with half-integer vortices embedded at off-axis locations.

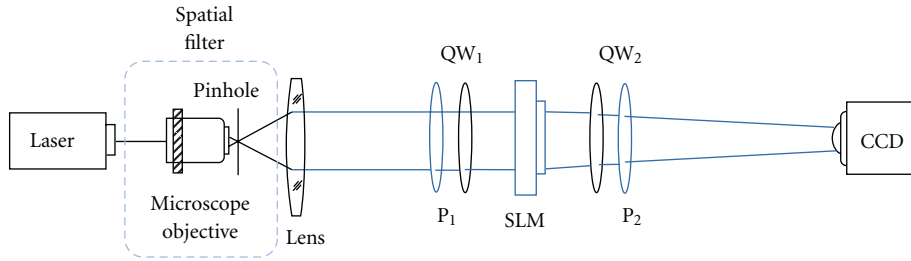


FIGURE 2: Experimental setup of Fresnel lens with embedded vortices;  $P_1$  and  $P_2$ : Polarizers,  $QW_1$  and  $QW_2$ : Quarter wave plates, SLM: Spatial light modulator, and CCD: Camera.

## 2. Theory

A convex lens brings a collimated incident beam to a focus at a distance  $f$  from the lens. The phase delay  $\Delta\psi(\rho, \theta)$  suffered by the beam due to lens is

$$\Delta\psi(\rho, \theta) = \frac{-k\rho^2}{2f}, \quad (1)$$

where  $f$  is the focal length,  $k = 2\pi/\lambda$ , and  $\lambda$  is the wavelength of light used. The polar coordinates in the element plane  $\rho, \theta$  are related to Cartesian coordinates by  $\rho^2 = x^2 + y^2$ ,  $\theta = \tan^{-1}(y/x)$ . A thin lens can be considered equivalent to a transparency with a complex amplitude transmittance given by

$$t_1(x, y) = \exp(i\Delta\psi(\rho, \theta)). \quad (2)$$

Fresnel zone sectioning of this transmittance function leads to a Fresnel lens. The radius of the  $n$ th zone is  $\rho_n \approx \sqrt{2fn\lambda}$ . Figure 1(a) shows the profile of a conventional Fresnel lens.

A vortex or phase singularity in the wave field can be implanted by using a phase mask or by a spiral phase plate. The transmission function of such a phase mask is given by

$$t_2(\rho, \theta) = \begin{cases} \exp(im\theta), & \text{for } 0 \leq \rho \leq 1, \\ 0, & \text{otherwise,} \end{cases} \quad (3)$$

where  $m$  is the topological charge of vortex. A vortex lens [23] has the transmission function given by

$$t_3(\rho, \theta) = t_1(\rho, \theta)t_2(\rho, \theta) = \exp\left(i\left(m\theta - \frac{k}{2f}\rho^2\right)\right). \quad (4)$$

A phase mask having this transmittance function transforms incident plane wave into converging helicoidal wave  $E(\rho, \theta, z)$ . Presence of Fresnel lens factor in a wave field  $e^{im\theta}$  gives desired curvature to the beam. When the topological charge  $m$  is a fraction, it is called fractional vortex lens [24]. This specific transmittance imparts an on-axis vortex on the incident optical field. Phase variation corresponding to

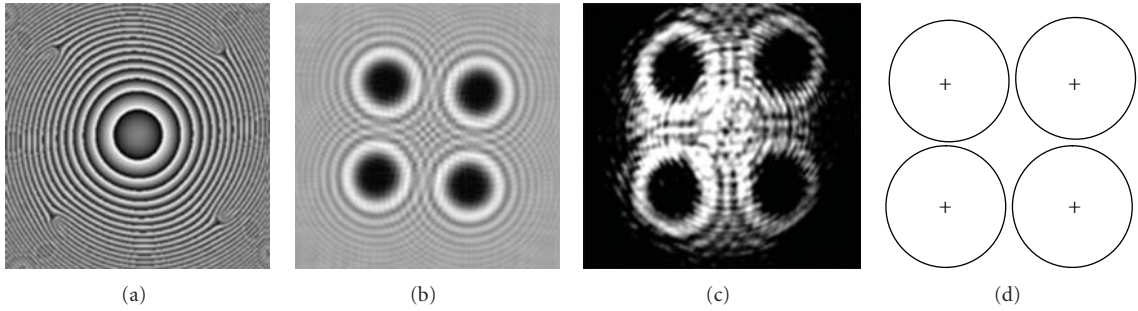


FIGURE 3: Fresnel lens with four vortices, each of topological charge 2 embedded at off-axis locations. (a) Phase distribution displayed on SLM. (b) Simulated intensity distribution near the focal plane. (c) Experimentally observed intensity distribution near the focal plane. (d) Distribution of topological charge in the intensity pattern.

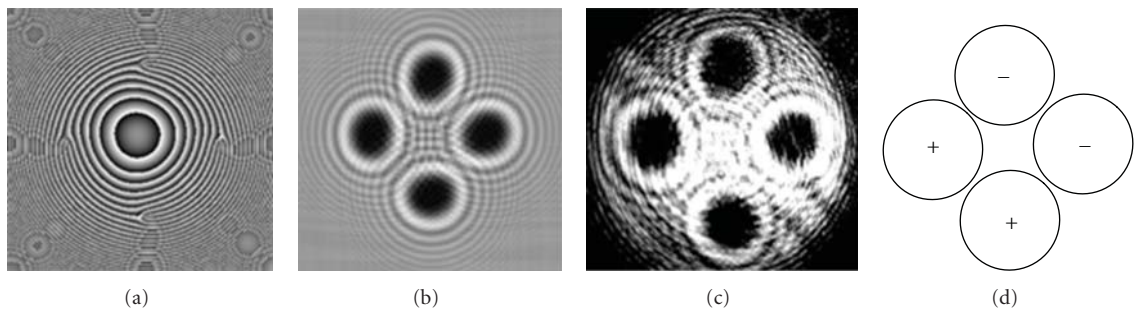


FIGURE 4: Fresnel lens with two positive and two negative charge vortices embedded at off-axis locations. (a) Phase distribution displayed on SLM. (b) Simulated intensity distribution near the focal plane. (c) Experimentally observed intensity distribution near the focal plane. (d) Distribution of topological charge in the intensity pattern.

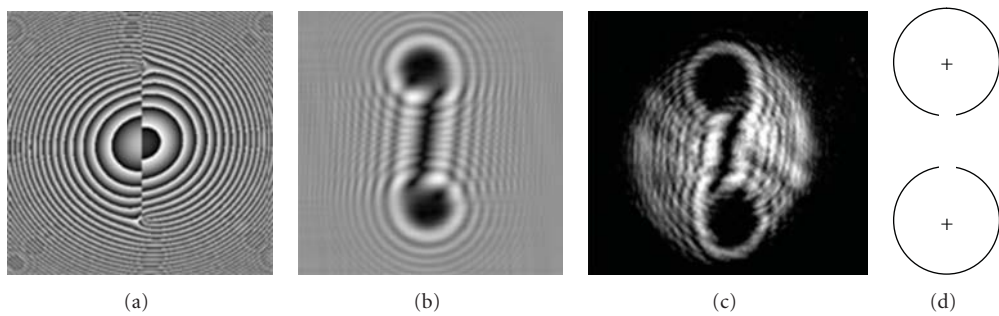


FIGURE 5: Fresnel lens with fractional vortices of the same charge (3.5) embedded at off-axis locations. (a) Phase distribution displayed on SLM. (b) Simulated intensity distribution near the focal plane. (c) Experimentally observed intensity distribution near the focal plane. (d) Distribution of topological charge in the intensity pattern.

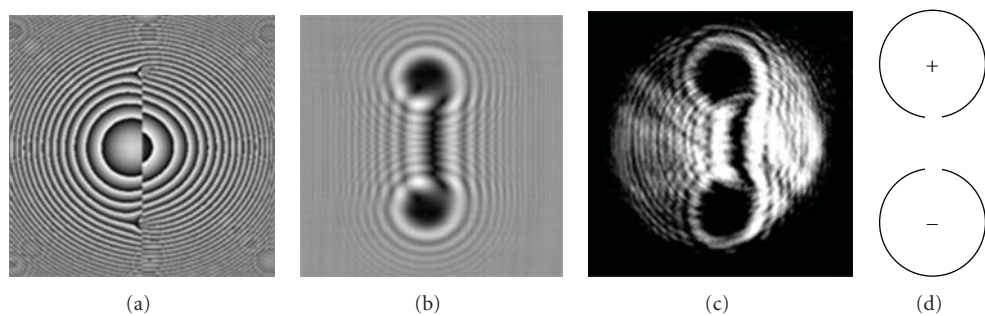


FIGURE 6: Fresnel lens with fractional vortices of opposite charge (3.5) embedded at off-axis locations. (a) Phase distribution displayed on SLM. (b) Simulated intensity distribution near the focal plane. (c) Experimentally observed intensity distribution near the focal plane. (d) Distribution of topological charge in the intensity pattern.

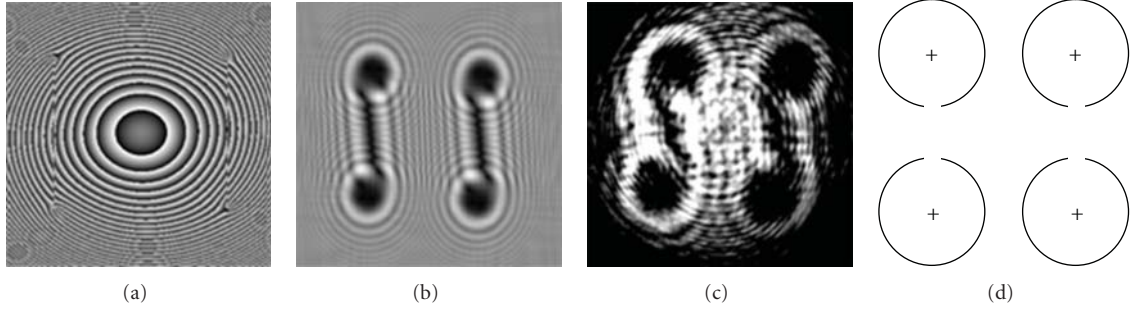


FIGURE 7: Fresnel lens with  $2 \times 2$  lattice of fractional vortices of the same charge  $m = 3.5$  embedded at off-axis locations. (a) Phase distribution displayed on SLM. (b) Simulated intensity pattern near the focal plane. (c) Experimentally observed intensity distribution near the focal plane. (d) Distribution of topological charge in the intensity pattern.

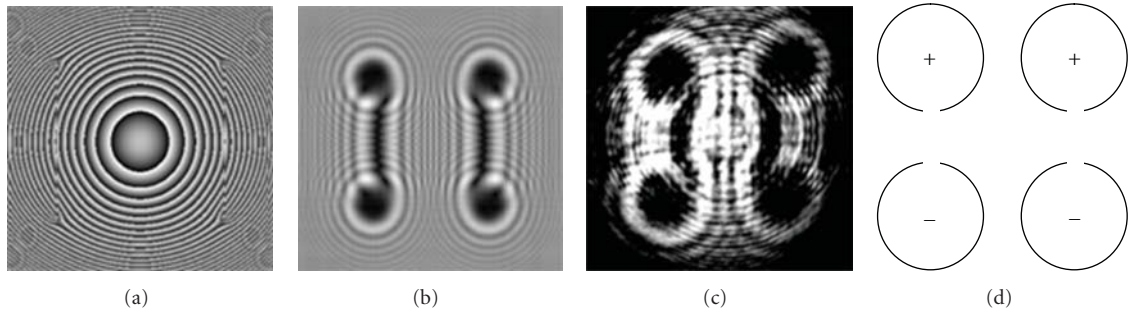


FIGURE 8: Fresnel lens with  $2 \times 2$  lattice of fractional vortices with two positive and two negative topological charge vortices, each of magnitude 3.5 embedded at off-axis locations. (a) Phase distribution displayed on SLM. (b) Simulated intensity pattern near the focal plane. (c) Experimentally observed intensity distribution near the focal plane. (d) Distribution of topological charge in the intensity pattern.

multiple vortices can be embedded into the wavefront by using the expression

$$t_4(\rho, \theta) = \exp \left[ i \sum_{j=1}^N m_j \theta(\rho_j, \theta_j) \right], \quad (5)$$

where  $m_j$  is the topological charge of  $j$ th vortex, and  $\theta$  is helical phase variation corresponding to the  $j$ th vortex. The position of the core of the  $j$ th vortex is  $(\rho_j, \theta_j)$ , where

$$\begin{aligned} \rho_j &= \sqrt{x_j^2 + y_j^2}, \\ \theta_j &= \tan^{-1} \left( \frac{y - y_j}{x - x_j} \right), \end{aligned} \quad (6)$$

where  $x_j, y_j$  are the Cartesian coordinates of the  $j$ th vortex core. Similar method of embedding vortices at desired locations is used in the iterative computational phase synthesis algorithms for diffractive elements, in wave optical engineering [25, 26]. This process is used to annihilate stagnation causing vortices, in the iterative algorithms.

When the extremum of a quadratic phase variation of a lens  $\Delta\psi(\rho, \theta)$  coincides with the position of the core of the vortex, spiral zones are formed. Figure 1(b) shows the profile of a vortex Fresnel lens. When the position of the vortex  $(\rho_j, \theta_j)$  does not coincide with the extremum of

$\Delta\psi(\rho, \theta)$ , branching of the zone boundary occurs as can be seen from Figure 1(c). The number of branches is equal to the magnitude of the charge of the vortex. The sign of the vortex decides the sense (clockwise or anticlockwise) in which the branching occurs. Figure 1(d) shows profile of a vortex Fresnel lens in which opposite vortices of unequal fractional charges are embedded at two different locations.

The complex amplitude at the focal plane can be evaluated by using the Fresnel-Kirchhoff diffraction integral which can be written [27] as

$$\begin{aligned} E(r, \phi, f) &= A \int_0^1 \int_0^{2\pi} E(\rho, \theta, z=0) \\ &\times \exp \left[ -i \frac{2\pi}{\lambda f} r \rho \cos(\theta - \phi) \right] \rho d\rho d\theta, \end{aligned} \quad (7)$$

where

$$A = \frac{1}{i\lambda f} e^{ikf} \exp \left( \frac{i\pi r^2}{\lambda f} \right). \quad (8)$$

$(\rho, \theta, z)$  and  $(r, \phi, f)$  correspond to object and diffracted field planes expressed in cylindrical coordinates.  $\lambda$  is the wavelength of light used, and  $f$  is the focal length of the lens. The multiplicative factor  $A$  is ignored since the amplitude  $1/\lambda f$  is only a scale factor, and the phase  $(kf + (\pi r^2/\lambda f - \pi/2))$

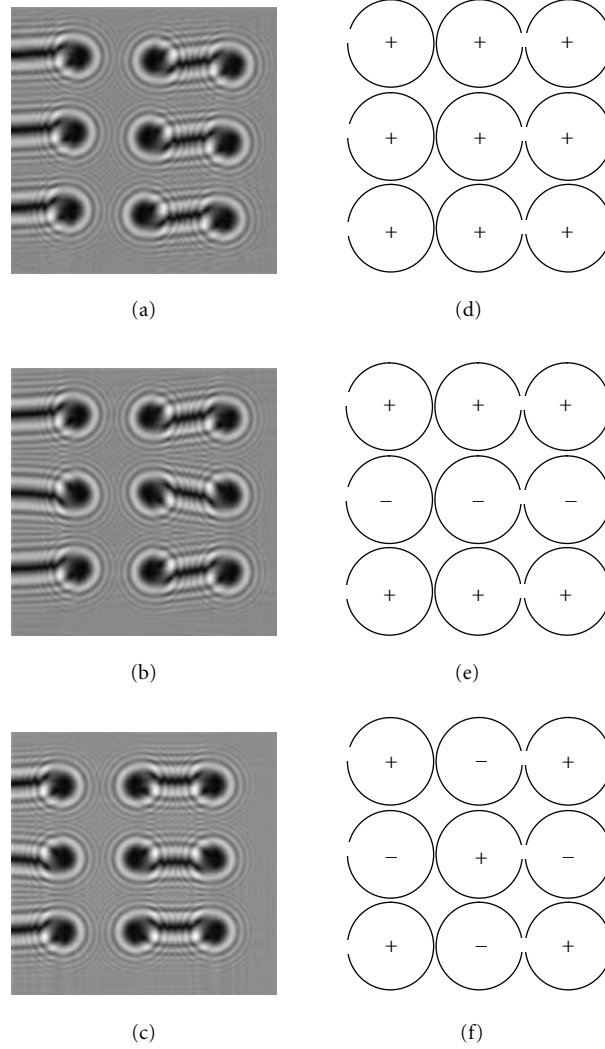


FIGURE 9:  $3 \times 3$  lattices of fractional vortices each of charge  $\pm 3.5$  embedded in a Fresnel lens. Simulated intensity distributions (a–c) and the corresponding charge distributions (d–f) are shown.

has no effect on the intensity. The field at the focal plane is proportional to the Fourier transform of the transmittance function given in (7). Intensity distribution at the observation plane is then given by

$$I(r, \phi, f) = |E(r, \phi, f)|^2. \quad (9)$$

Here, the intensity distribution refers to the far-field image of the object. We have carried our simulation studies to find the distribution of intensity in the focal plane.

### 3. Experimental Setup

A phase-only SLM can impose an azimuthal phase term directly on the incident beam converting it into a helical beam. The method of generating optical vortices using phase mask is more versatile because it allows precise and dynamic control over vortex parameters and possibility of generating specific patterns of optical vortices. The

experimental arrangement is shown in Figure 2. A linearly polarized light from a He-Ne laser ( $\lambda = 632.8 \text{ nm}$ ) is spatially filtered, expanded, and collimated to form a plane wave. The collimated beam of light is directed on the SLM (Holoeye LC-2002 with  $832 \times 624$  pixels, pitch =  $32 \mu\text{m}$ ). By using properly oriented linear polarizer or by generating appropriate elliptically polarized light, one can modulate the phase while keeping the amplitude constant. We have used elliptically polarized light to achieve phase-only modulation for the SLM using a combination of two polarizers and two quarter wave plates, as shown in Figure 2. This architecture consists of a combination of an input polarizer P and a quarter wave plate  $\text{QW}_1$  in front of the SLM and an output quarter wave plates  $\text{QW}_2$  and polarizer  $\text{P}_2$  behind the SLM. We adjust the polarizers and wave plates such that the SLM modulates only the phase, leaving the amplitude constant. A gray-scale phase mask corresponding to the transmittance of a lens, embedded with

required vortex phase distributions, is displayed on SLM, and the corresponding intensity distribution is recorded on a CCD.

#### 4. Results and Discussion

The Airy pattern at the focal plane of a lens is replaced by a doughnut pattern in a vortex lens. In a Fresnel vortex lens, the vortex phase is embedded at the extremum of the lens phase distribution that can produce a ring focus. By embedding multiple vortices in different locations in a Fresnel lens, vortex lattices can be realized at the focal plane [28]. Figure 3(a) shows the phase distribution of the modified Fresnel lens that can generate a  $2 \times 2$  vortex lattice of four vortices with positive topological charge. Figures 3(b) and 3(c) depict the simulation and experimental results of the intensity pattern in the focal plane of the Fresnel lens embedded with  $2 \times 2$  vortex lattice, as described above. The position and the charge of each of the vortices can be modified. Figure 4 shows one such configuration where two positive charge and two negative charge vortices are formed. The phase distributions are similar to that of a conventional Fresnel lens with branching of zones occurring at off-axis locations [29]. For positive (negative) vortex, the branch or fork occurs in anticlockwise (clockwise) sense as we move along the zone boundary. For a diverging Fresnel lens, the sense of fork formation is opposite to that of a positive lens. Similarly, vortex phase of fractional charge can also be embedded in a Fresnel lens. Figure 5 shows two positively charged fractional vortices of magnitude 3.5, embedded at off-axis locations. In this case, apart from branching of zones at vortex points, there is an additional edge dislocation connecting the two vortices. In the intensity distribution near the focal plane, the two dark cores are connected by a curved dark line. The two dark cores and the connecting dark curved line are surrounded by bright intensity pattern. In Figure 6, oppositely charged fractional vortices are embedded in the phase distribution of Fresnel lens. The dark cores in this case are connected by the dark line that has different geometry. These intensity patterns are unique. Two fractional vortices are connected to each other, irrespective of the charge of the individual vortex. Figures 7 and 8 depict  $2 \times 2$  arrays of vortices with fractional topological charges. The dark line that connects two vortices is decided by the manner, the edge dislocation connecting the two fractional vortices, appears in the phase distribution. If the edge dislocation line starting from one fractional vortex is not connected to another fractional vortex, it runs towards the boundary of the intensity pattern and terminates. Simulations are carried out to see the focal plane intensity distributions of such lenses. In all the Figures 3–8, it can be clearly seen that the experimental and simulation results match exactly. Figure 9 depicts vortex lattices of  $3 \times 3$  arrays of the vortices with fractional topological charges. The charge distributions of the vortices in each of the lattices are different. Simulated intensity distributions at the focal plane corresponding to these lattices reveal that all the vortices are not connected by dark lines to form pairs. Only three pairs are connected, and

in the remaining three fractional vortices, the dark lines from their cores are diverging outward.

#### 5. Conclusion

Array of vortices of different charges are embedded in a wavefront with quadratic phase variation and the intensity distribution near the focal plane is studied. The intensity patterns, when fractional vortices are embedded in the Fresnel lens, possess unique interesting features. The intensity patterns produced by any two fractional charge vortices are connected by dark line, irrespective of the sign of the vortices. The geometry of this dark line is decided by the manner in which the edge dislocation line appears in the phase distribution of the Fresnel lens.

#### References

- [1] J. F. Nye and M. V. Berry, "Dislocations in wave trains," *Proceedings of the Royal Society A*, vol. 336, pp. 165–190, 1974.
- [2] W. M. Lee, X.-C. Yuan, and K. Dholakia, "Experimental observation of optical vortex evolution in a Gaussian beam with an embedded fractional phase step," *Optics Communications*, vol. 239, no. 1–3, pp. 129–135, 2004.
- [3] M. V. Berry, "Optical vortices evolving from helicoidal integer and fractional phase steps," *Journal of Optics A*, vol. 6, no. 2, pp. 259–268, 2004.
- [4] K. T. Gahagan and G. A. Swartzlander, "Optical vortex trapping of particles," *Optics Letters*, vol. 21, no. 11, pp. 827–829, 1996.
- [5] A. Jesacher, S. Furhapter, S. Bernet, and M. Ritsch-Marte, "Spiral interferometry," *Optics Letters*, vol. 30, pp. 1953–1955, 2006.
- [6] G. Gibson, J. Courtial, M. J. Padgett et al., "Free space information transfer using light beams carrying orbital angular momentum," *Optics Express*, vol. 12, no. 22, pp. 5448–5456, 2004.
- [7] J. A. Davis, I. Moreno, and K. Crabtree, "Optical processing with vortex-producing lenses," *Applied Optics*, vol. 43, no. 6, pp. 1360–1367, 2004.
- [8] P. Senthilkumaran, "Optical phase singularities in detection of laser beam collimation," *Applied Optics*, vol. 42, no. 31, pp. 6314–6320, 2003.
- [9] G. A. Swartzlander Jr., "Peering into darkness with a vortex spatial filter," *Optics Letters*, vol. 26, no. 8, pp. 497–499, 2001.
- [10] J. Leach, M. R. Dennis, J. Courtial, and M. J. Padgett, "Knotted threads of darkness," *Nature*, vol. 432, no. 7014, p. 165, 2004.
- [11] D. P. Ghai, S. Vyas, P. Senthilkumaran, and R. S. Sirohi, "Vortex lattice generation using interferometric techniques based on lateral shearing," *Optics Communications*, vol. 282, no. 14, pp. 2692–2698, 2009.
- [12] M. M. Burns, J. M. Fournier, and J. A. Golovchenko, "Optical matter: crystallization and binding in intense optical fields," *Science*, vol. 249, no. 4970, pp. 749–754, 1990.
- [13] G. A. Swartzlander Jr. and C. T. Law, "Optical vortex solitons observed in Kerr nonlinear media," *Physical Review Letters*, vol. 69, no. 17, pp. 2503–2506, 1992.
- [14] M. P. MacDonald, G. C. Spalding, and K. Dholakia, "Microfluidic sorting in an optical lattice," *Nature*, vol. 426, no. 6965, pp. 421–424, 2003.

- [15] J. Masajada, "Small-angle rotations measurement using optical vortex interferometer," *Optics Communications*, vol. 239, no. 4–6, pp. 373–381, 2004.
- [16] K. Ladavac and D. G. Grier, "Micro-opto-mechanical pumps assembled and driven by holographic optical vortex arrays," *Optics Express*, vol. 12, no. 6, pp. 1144–1149, 2004.
- [17] N. Chattaripiban, E. A. Rogers, I. V. Arakelyan, R. Roy, and W. T. Hill, "Laser beams with embedded vortices: tools for atom optics," *Journal of the Optical Society of America B*, vol. 23, no. 1, pp. 94–103, 2006.
- [18] J. Masajada and B. Dubik, "Optical vortex generation by three plane wave interference," *Optics Communications*, vol. 198, no. 1–3, pp. 21–27, 2001.
- [19] S. Vyas and P. Senthilkumaran, "Interferometric optical vortex array generator," *Applied Optics*, vol. 46, no. 15, pp. 2893–2898, 2007.
- [20] J. Masajada, A. Popiołek-Masajada, and M. Leniec, "Creation of vortex lattices by a wavefront division," *Optics Express*, vol. 15, no. 8, pp. 5196–5207, 2007.
- [21] G. X. Wei, L. L. Lu, and C. S. Guo, "Generation of optical vortex array using Talbot array illuminators," *Optics Communications*, vol. 282, pp. 2665–2669, 2009.
- [22] C. S. Guo, Y. Zhang, Y. J. Han, J. P. Ding, and H. T. Wang, "Generation of optical vortices with arbitrary shape and array via helical phase spatial filtering," *Optics Communications*, vol. 259, no. 2, pp. 449–454, 2006.
- [23] G. A. Swartzlander Jr., "Achromatic optical vortex lens," *Optics Letters*, vol. 31, no. 13, pp. 2042–2044, 2006.
- [24] S. Vyas, R. Kumar Singh, and P. Senthilkumaran, "Fractional vortex lens," *Optics and Laser Technology*, vol. 42, no. 6, pp. 1150–1159, 2010.
- [25] P. Senthilkumaran and F. Wyrowski, "Phase synthesis in wave-optical engineering: mapping and diffuser type approaches," *Journal of Modern Optics*, vol. 49, no. 11, pp. 1831–1850, 2002.
- [26] P. Senthilkumaran, F. Wyrowski, and H. Schimmel, "Vortex Stagnation problem in iterative Fourier transform algorithms," *Optics and Lasers in Engineering*, vol. 43, no. 1, pp. 43–56, 2005.
- [27] J. W. Goodman, *Introduction to Fourier Optics*, McGraw-Hill Companies, New York, NY, USA, 2nd edition, 1996.
- [28] X. Gan, J. Zhao, S. Liu, and L. Fang, "Generation and motion control of optical multi-vortex," *Chinese Optics Letters*, vol. 7, no. 12, pp. 1142–1145, 2009.
- [29] F. S. Roux, "Diffractive lens with a null in the center of its focal point," *Applied Optics*, vol. 32, no. 22, pp. 4191–4192, 1993.

## Research Article

# Generation of Optical Vortex Arrays Using Single-Element Reversed-Wavefront Folding Interferometer

Brijesh Kumar Singh,<sup>1</sup> G. Singh,<sup>2</sup> P. Senthilkumaran,<sup>1</sup> and D. S. Mehta<sup>2</sup>

<sup>1</sup>Department of Physics, Indian Institute of Technology Delhi, Hauz Khas, New Delhi 110016, India

<sup>2</sup>Laser Applications and Holography Laboratory, Instrument Design Development Centre, Indian Institute of Technology Delhi, Hauz Khas, New Delhi 110016, India

Correspondence should be addressed to Brijesh Kumar Singh, brijeshsingh831@gmail.com

Received 15 April 2011; Revised 7 June 2011; Accepted 8 June 2011

Academic Editor: Shunichi Sato

Copyright © 2012 Brijesh Kumar Singh et al. This is an open access article distributed under the Creative Commons Attribution License, which permits unrestricted use, distribution, and reproduction in any medium, provided the original work is properly cited.

Optical vortex arrays have been generated using simple, novel, and stable reversed-wavefront folding interferometer. Two new interferometric configurations were used for generating a variety of optical vortex lattices. In the first interferometric configuration one cube beam splitter (CBS) was used in one arm of Mach-Zehnder interferometer for splitting and combining the collimated beam, and one mirror of another arm is replaced by second CBS. At the output of interferometer, three-beam interference gives rise to optical vortex arrays. In second interferometric configuration, a divergent wavefront was made incident on a single CBS which splits and combines wavefronts leading to the generation of vortex arrays due to four-beam interference. It was found that the orientation and structure of the optical vortices can be stably controlled by means of changing the rotation angle of CBS.

## 1. Introduction

Optical vortices (OVs) are point phase defects, also called phase singularities in the distribution of optical wave-fields where both real and imaginary values of the optical fields are zero [1]. An interesting peculiarity of point phase defects is the helicoidal structure of the wave front around the defect axis and is described as  $\exp(il\Phi)$ , where  $l$  is the topological charge and  $\Phi$  is the azimuthal angle around the defect axis. The magnitude of topological charge determines the degree of circulation, that is, the number of  $2\pi$  cycles of phase accumulation around the vortex point. The sign of topological charge defines the handedness or helicity of the phase singular beam along the propagation direction of the  $z$ -axis. An interesting aspect of a vortex beam is that it possesses orbital angular momentum (OAM). Optical vortices play significant role for studying OAM of light fields [2, 3] and have been widely used in the area of optical tweezers [4], singular optics [5], optical solitons [6], and optical metrology [7, 8]. The most commonly used methods for generating OVs with single or multiple charge are synthetic holograms [9], spiral phase plates [10], liquid-crystal cells [11], dielectric wedge [12], and higher-order

laser beams [13]. An alternative method for generating OVs efficiently is the use of optical fibers [14] such as, a hollow-core optical fiber for generating doughnut-shaped beam and a holey fiber for generating hollow beam.

Recently, there has been great interest for generating optical vortex arrays (OVAs) also called vortex lattices using multiple beam interference [15, 16]. It has been demonstrated that when three or more plane waves overlap in space, complete destructive interference occurs on nodal lines, also called phase singularities or optical vortices leading to the generation of regular net of vortex lattices. Various optical interferometric configurations have been implemented for generating vortex lattices. Generation of OVAs by three-, four- and five- plane wave interference [17], interferometric optical vortex array generator [18, 19], creation of OV lattices by wavefront division [20], using couple of Wollaston prisms [21, 22], and lateral shearing interferometers [23] have been reported. Such periodic arrays of optical vortices have been used as phase markers [22], in optical metrology for the measurements of small-angular rotations, tilt, orientation [24–26], and birefringence [27]. But most of the aforementioned interferometric techniques used for generating vortex lattices are based on modified Mach-Zehnder

interferometer and multiple Michelson interferometers to generate and recombine three-, four-, or five-wave fronts. This requires the use of multiple beam-splitters, mirrors, attenuation plates, and vibration isolation table which makes the experimental setup complicated and demands tedious and precise alignment procedure. The existing systems for generating OVAs are bulky, expensive, and require alignment of multiple components and hence are not robust. The essential requirement of optical vortex interferometry is the generation of highly stable regular optical vortex lattice for improving the accuracy in measurement.

In this paper, we demonstrate the generation of optical vortex arrays using a novel reversed-wavefront folding interferometer. Multiple wavefronts are generated and combined by means of simple interferometric configurations. Similar situation of CBS was used earlier for measuring the degree of coherence [28], optical metrology [29], and digital holographic microscopy [30]. Two new interferometric configurations were used for generating a variety of vortex lattices. We demonstrate that the orientation and structure of the optical vortices can be stably controlled by means of changing the rotation angle of CBS. The main advantages of the present system are simple, robust, and inexpensive method for generating OVAs. The system can generate multiple wavefronts, interferograms, and one can change the orientation, structure, and spatial carrier frequency of OVAs by means of changing the angle of the CBS. The first interferometric configuration as shown in Figure 1(a) requires less vibration isolation table in comparison to second interferometric configuration (Figure 1(b)) and precise control, adjustment, and alignment of multiple optical components which are an essential requirement in the existing systems for generating OVAs [15–27].

## 2. Optical Vortex Array Generation

The schematic diagram of the modified Mach-Zehnder interferometer by two CBSs for generating optical vortex lattices using collimated beam is shown in Figure 1(a). Gaussian beam ( $TEM_{00}$  fundamental mode) from a CW green laser having power 30 mW and wavelength  $\lambda = 532$  nm was expanded and spatially filtered. A collimated beam is then made to incident onto a 50/50 CBS<sub>1</sub> (size 50 mm  $\times$  50 mm). Two CBSs are used to modify the Mach-Zehnder interferometer. CBS<sub>2</sub> is used in first arm, while the CBS<sub>3</sub> is used to replace the mirror in second arm of the interferometer. The transmitted wavefront in the first (upper) arm of the interferometer is divided into two parts called input 1 and input 2. When input 1 is incident on the CBS<sub>2</sub>, it will be reflected and transmitted through semireflecting layer. Reflected part will be the reverted replica of the input 1, and it will get an extra phase shift of  $\pi/2$  (rad). The transmitted part will be the translated replica of the input 1. Similarly when input 2 is incident on CBS<sub>2</sub> two replicas of itself at the output of the CBS<sub>2</sub> will be available. Hence at one of the outputs of the CBS<sub>2</sub> reflected replica of input 1 and transmitted replica of input 2 will interfere with each other and generate interference fringe pattern 1 (IFP1). Similarly interference of reflected replica of input 2 and transmitted replica of

input 1 will generate interference fringe pattern 2 (IFP2) at the other output of CBS<sub>2</sub> as shown in Figure 1(a). The ray diagram for the input 1 and 2 in the CBS<sub>2</sub> is shown in the left bottom of Figure 1(a). A detailed analysis of generating two interferograms using single CBS in presence of collimated beam is given in [29]. The rotation of the CBS<sub>2</sub> is also shown. The CBS<sub>2</sub> rotates about the  $x$ -axis which is normal to the paper, and angle  $\theta$  is measured between  $z$ -axis (propagation direction of the incident beam) and semireflecting plane of the CBS<sub>2</sub>. As the angle  $\theta$  is increased, both the orientation and number of straight line fringes of IFP 1 and 2 increase.

In the case of collimated beam, both IFP 1 and IFP 2 propagate parallel to each other and will not overlap. Both IFP 1 and 2 propagate in space and reflected by mirror M<sub>1</sub> and again transmitted through CBS<sub>4</sub>. The beam input 3 in the second (lower) arm of the interferometer is reflected by CBS<sub>3</sub> and after propagation in space again reflected by CBS<sub>4</sub> where it interferes with IFP 1 and IFP 2 at the output. At the end of the interferometer, optical vortex arrays are generated by interference of three beams. Two beams come from first arm and one beam comes from second arm of the modified Mach-Zehnder interferometer. CBS<sub>3</sub> is used to make the amplitude of the interference beam equal for vortex lattices generation. Interference of beam input 3 with IFP 1 and 2 generate the optical vortex arrays 1 (OVAs 1) and OVAs 2 at the output of the interferometer as shown in Figure 1(a).

Second configuration for generating the vortex lattices by using a single CBS is shown schematically in Figure 1(b). Gaussian beam ( $TEM_{00}$  fundamental mode) from a CW green laser having power 30 mW and wavelength  $\lambda = 532$  nm was expanded and spatially filtered (BE/SF) and a divergent beam was then made incident on to the 50/50 CBS (size 50 mm  $\times$  50 mm). The CBS was kept in unconventional position so as to both split and combine the diverging spherical wave fronts [29, 30]. A light beam having spherical wave front (diameter 20 mm) traveling along the  $z$ -axis was made incident on the CBS with its central semireflecting layer placed along the propagation direction. The wavefront is divided into two parts called input 1 and input 2, and each beam generates two respective replicas of itself. The input beam 1 incident on the top front cube wall changes the direction of propagation inside the CBS and is divided into two parts, first is reflected and second is transmitted and finally exit from the CBS as shown in Figure 1(b). Because of the reflection that occurs at the internal semireflecting surface of the CBS, one of the two replicas will acquire an extra phase-shift of  $\pi/2$  (rad), as required by symmetry and energy conservations [29]. Similarly, the other beam input 2 incident on the bottom front cube wall generates two replicas of the beam, one transmitted and other reflected with an extra phase-shift of  $\pi/2$  (rad). The two spherical beams generated by transmission through the beam-splitter will be simply translated replicas of the input fields, while the reflected beams will be translated and reverted replicas. In this way, there are four diverging spherical beams at the output of the CBS. Two output beams exiting on the top of CBS generate interference fringe pattern 1 (IFP 1), and the two beams exiting at the bottom generate interference fringe pattern 2 (IFP 2). As it is a common-path interferometer, all

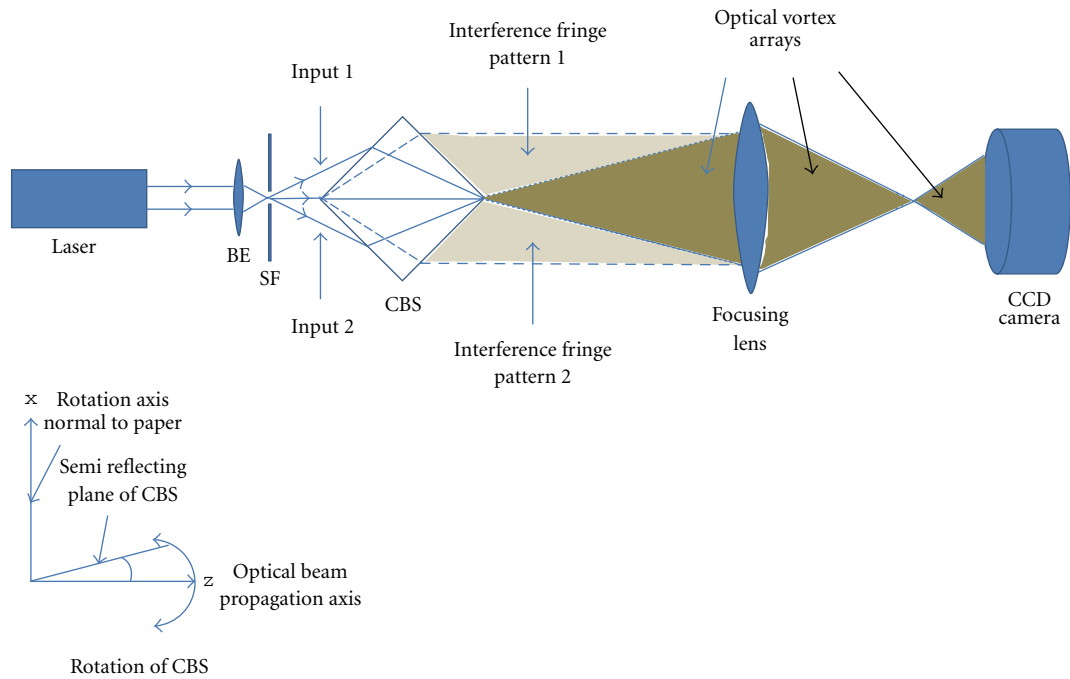
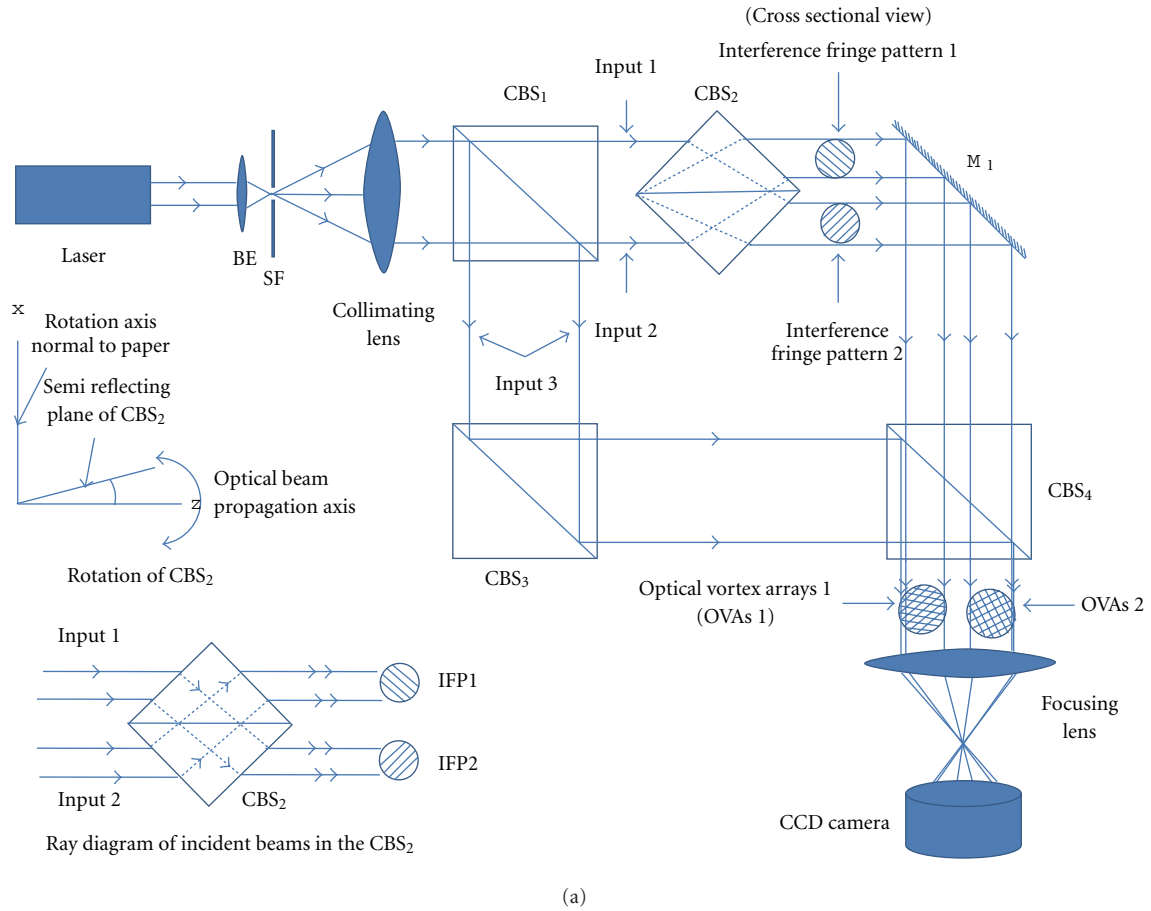


FIGURE 1: Schematic diagrams for generating optical vortex arrays: (a) by using collimated beams in modified Mach-Zehnder interferometer; (b) by using spherical wavefronts in single element common path interferometer. BE: beam expander, SF: spatial filter, CBS: cubic beam splitter, CCD: charge-coupled device, IFP: interference fringe pattern.

the four beams generated by input 1 and 2 travel the same distance and the interference fringes can be obtained. The CBS was mounted on a rotating table, and a small angle  $\theta$  was introduced between the light propagation direction and the central semireflecting layer (Figure 1(b)). Due to this, a wedge-shaped optical path difference is introduced to the reflected light and the transmitted light which results in interferograms with straight line fringes. The rotation axis and the orientation of CBS are the same as for the CBS<sub>2</sub> in Figure 1(a). The orientation of fringes in IFP 1 and IFP 2 is opposite to each other (Figure 1(b)). If the orientation angle of the IFP 1 is changed, orientation angle of the IFP 2 will also change accordingly. The orientation and the spatial carrier frequency of the IFP 1 and 2 can be easily controlled by means of changing angle  $\theta$  [29, 30]. The two interferograms IFP 1 and 2 are highly diverging and as the distance of propagation increases they start overlapping to each other. In the region of overlap, they produce optical vortex arrays due to destructive interference among the four spherical waves. In Figure 1(a), we used the collimated beam while in Figure 1(b) diverging beam is used. In both cases (in Figures 1(a) and 1(b)), a focusing lens was used to reduce the size of the beams so that both the output interference patterns can be recorded using a single CCD camera. The main advantages of the proposed setup are its simplicity and insensitive to vibration, and hence the interferometer generates stable optical vortex lattices.

**2.1. Reconstruction of Phase Map.** This interference due to the superposition of three plane waves  $a_1 e^{i2\pi(f_{1x}x + f_{1y}y)}$ ,  $a_2 e^{i2\pi(f_{2x}x + f_{2y}y)}$ , and  $a_3 e^{i2\pi(f_{3x}x + f_{3y}y)}$  gives rise to a two-dimensional fringe pattern that contains vortices. The superposition of above three-plane waves can be written as

$$a_1(x, y)e^{i2\pi(f_{1x}x + f_{1y}y)} + a_2(x, y)e^{i2\pi(f_{2x}x + f_{2y}y)} + a_3(x, y)e^{i2\pi(f_{3x}x + f_{3y}y)} = b(x, y)e^{i\varphi}. \quad (1)$$

And the interference intensity distribution is

$$\begin{aligned} g(x, y) &= a_1^2(x, y) + a_2^2(x, y) + a_3^2(x, y) \\ &+ 2a_1(x, y)a_2(x, y) \\ &\times \cos\left[2\pi\left((f_{1x} - f_{2x})x + (f_{1y} - f_{2y})y\right)\right] \\ &+ 2a_2(x, y)a_3(x, y) \\ &\times \cos\left[2\pi\left((f_{2x} - f_{3x})x + (f_{2y} - f_{3y})y\right)\right] \\ &+ 2a_1(x, y)a_3(x, y) \\ &\times \cos\left[2\pi\left((f_{1x} - f_{3x})x + (f_{1y} - f_{3y})y\right)\right]. \end{aligned} \quad (2)$$

For convenience, we write

$$\begin{aligned} g(x, y) &= b^2 = a_1^2(x, y) + a_2^2(x, y) + a_3^2(x, y) \\ &+ 2a_1(x, y)a_2(x, y)\cos(\theta_1 - \theta_2) \\ &+ 2a_2(x, y)a_3(x, y)\cos(\theta_2 - \theta_3) \\ &+ 2a_1(x, y)a_3(x, y)\cos(\theta_1 - \theta_3). \end{aligned} \quad (3)$$

Equation (3) can be written in generalized form as

$$g(x, y) = \sum_{j=1}^3 a_j^2(x, y) + 2 \sum_{j=1}^3 \sum_{k>j}^3 a_{jk}(x, y) \cos(\Delta\theta_{jk}(x, y)), \quad (4)$$

where  $a_j^2(x, y)$  and  $a_{jk}(x, y) = a_j a_k$  (for  $j, k = 1, 2, 3$ ) are the background intensity and fringe amplitude for the three-beam interference.  $\Delta\theta_{jk} = \theta_j - \theta_k$ ,  $\theta_j = 2\pi(f_{jx}x + f_{jy}y)$  and  $\theta_k = 2\pi(f_{kx}x + f_{ky}y)$ , where  $f_{jx}$ ,  $f_{kx}$ ,  $f_{jy}$ ,  $f_{ky}$  (for  $j, k = 1, 2, 3$ ) are the spatial frequency of the first, second, and third beam in the  $x$  and  $y$  directions, respectively.

The Fourier transform of the intensity distribution is consisting of nine spots, further

$$\begin{aligned} \mathcal{F}\{b^2(x, y)\} &= \mathcal{F}\{b(x, y)e^{i\varphi}\} \otimes \mathcal{F}\{b(x, y)e^{-i\varphi}\} \\ &= \{A_1(f_x, f_y) \otimes \delta(f_x - f_{1x}, f_y - f_{1y}) \\ &\quad + A_2(f_x, f_y) \otimes \delta(f_x - f_{2x}, f_y - f_{2y}) \\ &\quad + A_3(f_x, f_y) \otimes \delta(f_x - f_{3x}, f_y - f_{3y})\} \\ &\otimes \{A_1^*(f_x, f_y) \otimes \delta(f_x + f_{1x}, f_y + f_{1y}) \\ &\quad + A_2^*(f_x, f_y) \otimes \delta(f_x + f_{2x}, f_y + f_{2y}) \\ &\quad + A_3^*(f_x, f_y) \otimes \delta(f_x + f_{3x}, f_y + f_{3y})\}, \end{aligned} \quad (5)$$

where  $A_j(f_x, f_y) = \mathcal{F}\{a_j(x, y)\}$ , for  $j = 1, 2, 3$ . This can be seen from (3) by writing  $\cos(\Delta\theta) = (1/2)[e^{i\Delta\theta} + e^{-i\Delta\theta}]$  and noting that the FT consists of  $3\delta$  functions overlapping at the origin and six  $\delta$  functions at the locations given by  $f_x, f_y = f_{jx} \mp f_{kx}, f_{jy} \mp f_{ky}$  ( $k > j$ ,  $j, k = 1, 2, 3$ ).

By selecting three of the  $\delta$  functions (at  $(f_{1x} - f_{2x}, f_{1y} - f_{2y})$ ,  $(f_{2x} - f_{3x}, f_{2y} - f_{3y})$ ,  $(f_{1x} - f_{3x}, f_{1y} - f_{3y})$ ), and taking inverse Fourier transform (IFT), the phase distribution of the intensity modulated fringes can be obtained. This phase distribution can be extracted by separating out the imaginary part of the logarithm complex function obtained by IFT operation.

This is actually the phase distribution corresponding to

$$\begin{aligned} &2a_1(x, y)a_2(x, y)\cos(\theta_1 - \theta_2) \\ &+ 2a_2(x, y)a_3(x, y)\cos(\theta_2 - \theta_3) \\ &+ 2a_1(x, y)a_3(x, y)\cos(\theta_1 - \theta_3), \end{aligned} \quad (6)$$

which are the modulation terms in the intensity pattern.

### 3. Experimental Results

Figure 2 is the interference pattern obtained from the experimental setup shown in Figure 1(a) in which we record the formation of optical vortex arrays (OVAs) using the interference of three plane waves. At the exit of CBS<sub>4</sub> as shown in the Figure 1(a), we obtain two optical vortex arrays

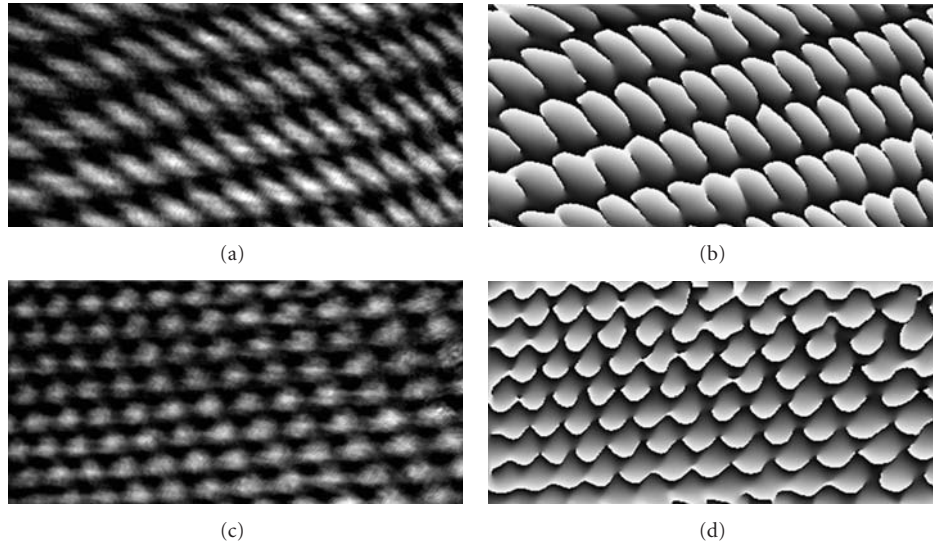


FIGURE 2: (a) and (c) are the recorded interferograms of generated vortex arrays at the rotation angles  $0.25^\circ$  and  $0.30^\circ$  of  $\text{CBS}_2$  by using experimental set-up Figure 1(a) and (b) and (d) are the corresponding phase-maps due to the superposition of three plane wavefronts respectively.

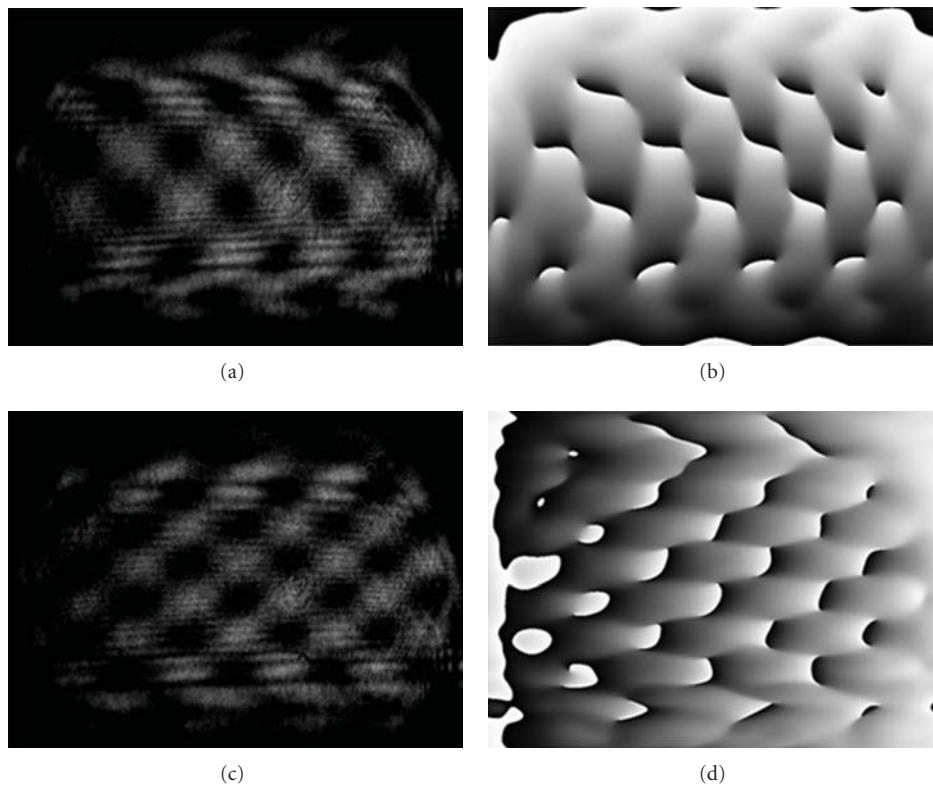


FIGURE 3: (a) and (c) are the recorded interferograms of generated vortex arrays at the rotation angles  $0.25^\circ$  and  $0.40^\circ$  of CBS by using experimental set-up Figure 1(b) and (b) and (d) are the corresponding phase-maps due to the superposition of four spherical wavefronts respectively.

(OVAs 1 and OVAs 2) side-by-side in the transverse plane. The generation of OVAs are due to the interference of three beams in which two beams are coming from first (upper) arm while third beam is coming from second (lower) arm of

the interferometer. Figures 2(a) and 2(c) show the recorded interferogram of three beam interference where the OVAs is present while Figures 2(b) and 2(d) show the phase-map corresponding to Figures 2(a) and 2(c), respectively.

First, we put the CBS<sub>2</sub> in the experimental setup (Figure 1(a)) in this way that the transmitted beam from CBS<sub>1</sub> and the central line of CBS<sub>2</sub> are nearly parallel to each other. The CBS<sub>2</sub> was then rotated around an axis which is normal to the optical table and optical axis, in either direction with the rotation angle incremented by  $\sim 0.05^\circ$ . On increasing the rotation angle  $\theta$  with a step of  $\sim 0.05^\circ$ , both the orientation as well as the spatial carrier frequency of the individual interferograms (IFP 1 and IFP 2) increase by equal amount. The orientation of the fringes is opposite in the two fields IFP 1 and IFP 2. By interfering these fringes with third plane beam coming from lower arm of the interferometer, a perfectly knitted pattern of vortex lattices was observed as can be seen from Figures 2(a) and 2(c). Another point is that in the present setup a variety of vortex lattices can be generated by means of changing the small rotation angle of CBS<sub>2</sub>. The density of the optical vortices was further increased on increasing the rotation angle of the CBS<sub>2</sub> as can be seen from Figure 2(c). It can also be seen from Figures 2(a) and 2(c) that dark spots appear in the overlap region, and in each dark spot a phase dislocation is present. This can be seen from the constructed phase maps (Figures 2(b) and 2(d)). The vortex lattice generation using the collimated beam (Figure 1(a)) is similar to the generation of vortex lattices by four or more plane waves as has been demonstrated previously using multiple beam interferometers [15–17].

Figures 3(a) and 3(c) show the recorded interferograms using divergent beam in the experimental setup as shown in Figure 1(b). A divergent beam incident on a CBS gives two interferograms (IFP 1 and IFP 2) side-by-side as shown in Figure 1(b). They overlap as the distance of propagation increases as shown in Figure 1(b). When the central line of CBS is perfectly parallel to optical axis, the fringes in both the interferograms IFP 1 and IFP 2 are vertical straight lines in the overlap region. As shown in Figure 1(b), the CBS was then rotated around an axis which is normal to the optical table and optical axis, in either direction with the rotation angle incremented by  $\sim 0.05^\circ$ . On increasing the rotation angle  $\theta$  with a step of  $\sim 0.05^\circ$  both the orientation as well as the spatial carrier frequency of the individual interferograms (IFP 1 and IFP 2) increases with equal amount and the orientation of the fringes is in the opposite direction. In the region where all the four beams overlap, optical vortices are generated. It is visible from Figures 3(a) and 3(c) that dark spots appear in the overlap region, and corresponding to each dark spot phase dislocations can be seen from the corresponding phase map as shown in Figures 3(b) and 3(d), respectively. The density of optical vortices was further increased on increasing the rotation angle of the CBS as can be seen from Figure 3(c). Extraction of the phase distributions from the interferograms is done by Fourier transform fringe analysis method [31]. So in this way, the vortex arrays can be generated using a stable single element optical interferometer as shown in Figure 1(b). The orientation and the spatial-carrier frequency can be easily controlled by simply changing the rotation angle of the CBS. The main advantage of the present system is that the vortex lattices are stable due to the common path interferometer.

This kind of setup is highly useful for multiple trapping of microparticles and biological cells in the optical tweezers.

#### 4. Conclusions

In conclusion, we have demonstrated an efficient, simple, and cost-effective method for generating optical vortex arrays using simple and highly stable reversed-wavefront folding interferometer. Two new interferometric configurations have been used for generating a variety of vortex lattices. In the first interferometric configuration, two CBSs were then used to modify the Mach-Zehnder interferometer and then by interference of three beams optical vortex arrays are generated. In second configuration, a divergent wavefront was made incident on a single CBS which splits and combines wavefronts leading to the generation of vortex arrays due to four-beam interference. It was found that the orientation and structure of the optical vortices can be stably controlled by means of changing the rotation angle of CBS. Further, the spatial-carrier frequency and the orientation of the interference fringes can be stably controlled. The present systems have potential applications in multiple trapping and optical metrology. The most important advantages of the proposed setups for generating vortex lattices are their simplicity, minimal number of optical elements, and insensitivity to external vibrations.

#### Acknowledgment

B. K. Singh thankfully acknowledges University Grant Commission (UGC) of India for junior research fellowship.

#### References

- [1] J. E. Nye and M. V. Berry, "Dislocation in wave trains," *Proceedings of the Royal Society A*, vol. 336, pp. 165–190, 1974.
- [2] L. Allen, M. J. Padgett, and M. Babiker, "The orbital angular momentum of light," *Progress in Optics*, vol. 39, pp. 291–372, 1999.
- [3] C.-S. Guo, S.-J. Yue, and G.-X. Wei, "Measuring the orbital angular momentum of optical vortices using a multipinhole plate," *Applied Physics Letters*, vol. 94, no. 23, Article ID 231104, 3 pages, 2009.
- [4] K. T. Gahagan and G. A. Swartzlander Jr., "Optical vortex trapping of particles," *Optics Letters*, vol. 21, no. 11, pp. 827–829, 1996.
- [5] M. S. Soskin, V. N. Gorshkov, M. V. Vasnetsov, J. T. Malos, and N. R. Heckenberg, "Topological charge and angular momentum of light beams carrying optical vortices," *Physical Review A*, vol. 56, no. 5, pp. 4064–4075, 1997.
- [6] C. T. Law and G. A. Swartzlander, "Optical vortex solitons and the stability of dark soliton stripes," *Optics Letters*, vol. 18, no. 8, pp. 586–588, 1993.
- [7] W. Wang, T. Yokozeki, R. Ishijima et al., "Optical vortex metrology for nanometric speckle displacement measurement," *Optics Express*, vol. 14, no. 1, pp. 120–127, 2006.
- [8] W. Wang, T. Yokozeki, R. Ishijima, M. Takeda, and S. G. Hanson, "Optical vortex metrology based on the core structures of phase singularities in Laguerre-Gauss transform of a speckle pattern," *Optics Express*, vol. 14, no. 22, pp. 10195–10206, 2006.

- [9] N. R. Heckenberg, R. McDuff, C. P. Smith, and A. G. White, "Generation of optical phase singularities by computer-generated holograms," *Optics Letters*, pp. 221–223, 1992.
- [10] K. J. Moh, X.-C. Yuan, W. C. Cheong et al., "High-power efficient multiple optical vortices in a single beam generated by a kinoform-type spiral phase plate," *Applied Optics*, vol. 45, no. 6, pp. 1153–1161, 2006.
- [11] D. Ganic, X. Gan, M. Gu et al., "Generation of doughnut laser beams by use of a liquid-crystal cell with a conversion efficiency near 100%," *Optics Letters*, vol. 27, no. 15, pp. 1351–1353, 2002.
- [12] Y. Izdebskaya, V. Shvedov, and A. Volyar, "Generation of higher-order optical vortices by a dielectric wedge," *Optics Letters*, vol. 30, no. 18, pp. 2472–2474, 2005.
- [13] C. Tamm and C. O. Weiss, "Bistability and optical switching of spatial patterns in a laser," *Journal of the Optical Society of America B*, vol. 7, pp. 1034–1038, 1990.
- [14] R. Kumar, D. Singh Mehta, A. Sachdeva, A. Garg, P. Senthilkumaran, and C. Shakher, "Generation and detection of optical vortices using all fiber-optic system," *Optics Communications*, vol. 281, no. 13, pp. 3414–3420, 2008.
- [15] J. Masajada and B. Dubik, "Optical vortex generation by three plane wave interference," *Optics Communications*, vol. 198, no. 1–3, pp. 21–27, 2001.
- [16] J. Masajada, A. Popiołek-Masajada, E. Frączek, and W. Frączek, "Vortex points localization problem in optical vortices interferometry," *Optics Communications*, vol. 234, no. 1–6, pp. 23–28, 2004.
- [17] K. O'Holleran, M. J. Padgett, and M. R. Dennis, "Topology of optical vortex lines formed by the interference of three, four, and five plane waves," *Optics Express*, vol. 14, no. 7, pp. 3039–3044, 2006.
- [18] S. Vyas and P. Senthilkumaran, "Interferometric optical vortex array generator," *Applied Optics*, vol. 46, no. 15, pp. 2893–2898, 2007.
- [19] S. Vyas and P. Senthilkumaran, "Vortex array generation by interference of spherical waves," *Applied Optics*, vol. 46, no. 32, pp. 7862–7867, 2007.
- [20] J. Masajada, A. Popiołek-Masajada, and M. Leniec, "Creation of vortex lattices by a wavefront division," *Optics Express*, vol. 15, no. 8, pp. 5196–5207, 2007.
- [21] P. Kurzynowski, W. A. Wozniak, and E. Frączek, "Optical vortices generation using the Wollaston compensator," *Applied Optics*, vol. 45, pp. 7898–7903, 2006.
- [22] P. Kurzynowski and M. Borwińska, "Generation of vortex-type markers in a one-wave setup," *Applied Optics*, vol. 46, no. 5, pp. 676–679, 2007.
- [23] D. P. Ghai, S. Vyas, P. Senthilkumaran, and R. S. Sirohi, "Vortex lattice generation using interferometric techniques based on lateral shearing," *Optics Communications*, vol. 282, no. 14, pp. 2692–2698, 2009.
- [24] J. Masajada, "Small-angle rotations measurement using optical vortex interferometer," *Optics Communications*, vol. 239, no. 4–6, pp. 373–381, 2004.
- [25] A. Popiołek-Masajada, M. Borwińska, and W. Frączek, "Testing a new method for small-angle rotation measurements with the optical vortex interferometer," *Measurement Science and Technology*, vol. 17, no. 4, pp. 653–658, 2006.
- [26] A. Popiołek-Masajada, M. Borwińska, and B. Dubik, "Reconstruction of a plane wave's tilt and orientation using an optical vortex interferometer," *Optical Engineering*, vol. 46, no. 7, Article ID 073604, 2007.
- [27] M. Borwińska, A. Popiołek-Masajada, and P. Kurzynowski, "Measurements of birefringent media properties using optical vortex birefringence compensator," *Applied Optics*, vol. 46, no. 25, pp. 6419–6426, 2007.
- [28] M. Santarsiero and R. Borghi, "Measuring spatial coherence by using a reversed-wavefront Young interferometer," *Optics Letters*, vol. 31, no. 7, pp. 861–863, 2006.
- [29] J. A. Ferrari and E. M. Frins, "Single-element interferometer," *Optics Communications*, vol. 279, no. 2, pp. 235–239, 2007.
- [30] Q. Weijuan, Y. Yingjie, C. O. Choo, and A. Asundi, "Digital holographic microscopy with physical phase compensation," *Optics Letters*, vol. 34, no. 8, pp. 1276–1278, 2009.
- [31] M. Takeda, H. Ina, and S. Kobayashi, "Fourier-transform method of fringe-pattern analysis for computer-based topography and interferometry," *Journal of the Optical Society of America*, vol. 72, no. 1, pp. 156–160, 1982.